



HAL
open science

Polarisation dynamics and force generation at the B cell immune synapse

Judith Pineau

► **To cite this version:**

Judith Pineau. Polarisation dynamics and force generation at the B cell immune synapse. Cellular Biology. Université Paris Cité, 2021. English. NNT : 2021UNIP5151 . tel-04522524

HAL Id: tel-04522524

<https://theses.hal.science/tel-04522524>

Submitted on 26 Mar 2024

HAL is a multi-disciplinary open access archive for the deposit and dissemination of scientific research documents, whether they are published or not. The documents may come from teaching and research institutions in France or abroad, or from public or private research centers.

L'archive ouverte pluridisciplinaire **HAL**, est destinée au dépôt et à la diffusion de documents scientifiques de niveau recherche, publiés ou non, émanant des établissements d'enseignement et de recherche français ou étrangers, des laboratoires publics ou privés.

Université de Paris

École doctorale Frontières de l'Innovation en Recherche et Education ED 474

Laboratoire Immunité et Cancer INSERM U932

Polarisation dynamics and force generation at the B cell immune synapse

Par Judith Pineau

Thèse de doctorat de Biologie cellulaire et biologie du
développement

Dirigée par Paolo Pierobon
Et par Ana-Maria Lennon-Duménil

Présentée et soutenue publiquement le 2 décembre 2021

Devant un jury composé de :

Dr Paolo Pierobon

CR CNRS, Université de Paris

Dr Ana-Maria Lennon-Duménil

DR INSERM, Université de Paris

Prof Gillian Griffiths

Professor, University of Cambridge

Dr Katelyn Spillane

Senior Lecturer, King's College London

Prof Julien Husson

Professeur associé HDR, Ecole Polytechnique

Dr Manuel Théry

DR CEA, Université Grenoble-alpes

Directeur de thèse

Co-Directrice de thèse

Rapportrice

Rapportrice

Examineur

Examineur

“When one tries continuously, one ends up succeeding. Thus, the more one fails, the greater the chance that it will work.”

Shadok saying, Jacques Rouxel

Abstract

B lymphocytes initiate the humoral adaptive immune response upon engagement of their B cell receptor with a cognate antigen. In lymphoid organs, this event mainly involves antigens that are exposed at the surface of neighboring cells. It thus leads to the formation of an immune synapse, i.e. a zone of tight contact between the two cell types, which facilitates their communication by orchestrating distinct events of signaling, vesicle trafficking and cytoskeleton rearrangements. Immune synapse formation further allows antigen extraction for later presentation to helper T cells, an essential step for the generation of high-affinity antibodies and immune memory. Antigen extraction occurs through two main pathways: direct mechanical pulling on the antigen or polarised secretion of protease-containing lysosomes at the immune synapse, which helps chopping antigens for internalisation. Both pathways are intimately linked with the cell cytoskeleton, with mechanical extraction relying on actomyosin contractility and protease secretion requiring the polarised reorganisation of the microtubule network. How the distinct cellular and molecular events involved in synapse formation are coordinated to facilitate B lymphocyte activation has not been studied. My PhD work focuses on the respective roles of the actin and microtubule networks in the formation of the B cell immune synapse. More specifically, I addressed the following questions:

(1) *How are forces and F-actin organised and regulated at the immune synapse?* My work helped showing that mechanical forces that build up at the immune synapse are patterned, with centripetal tangential forces appearing at the synapse periphery and local 3D forces emerging at the synapse center. Tangential forces rely on myosin II contractility and are needed for local 3D forces to be built at the synapse center. Noticeably, I found that 3D forces are associated to invadosome-like actin protrusions, which are responsible for antigen extraction.

(2) *How are the molecular and cellular events that operate at different time scales during synapse formation coordinated in space and time?* To address these questions, I built a custom droplet-based microfluidic system that allowed me to define the characteristic timescales of the main signaling and trafficking events associated to synapse formation. By doing so I was able to divide these events in two distinct phases: an early phase that includes reorganisation of the F-actin cytoskeleton and of antigen receptor signaling at the cell-droplet interface and a late phase where additional components such as the centrosome, Golgi and lysosomes reach the synapse, which is also accompanied by nucleus repositioning towards the back of the cell. Remarkably, I found that this second phase, which is driven by microtubules, occurs independently of the actin polymerisation. In contrast, microtubule depolymerisation deeply affects the early phase of synapse formation, with a loss of F-actin polarity, which is now nucleated all around the cell cortex. My work further shows that this feedback loop relies on the small GTPase RhoA, which is activated upon GEF-H1 release from microtubules.

We propose that such coordination of early and late events of synapse formation might contribute to enhance the robustness of antigen extraction by B lymphocytes. First, the independency of the late phase on the early one allows proteolytic antigen extraction (microtubule-dependent) to occur, even in case the mechanical antigen extraction (actin-dependent) fails. Second, the feedback regulatory loop exerted by microtubules on restricting actin cytoskeleton polarity might help the cell mechanically extracting antigens at various cell locations in case proteolytic extraction is compromised.

Dedicated to B.Cs

Contents

| | | |
|----------|--|-----------|
| 1 | Introduction | 1 |
| 1.1 | The immune system | 1 |
| 1.1.1 | The innate immune system | 4 |
| 1.1.2 | The adaptive immune system | 4 |
| 1.2 | The B lymphocyte | 6 |
| 1.2.1 | Generation of B lymphocytes | 7 |
| 1.2.2 | B lymphocyte activation by antigen encounter | 9 |
| 1.2.3 | Antigen internalisation, processing and presentation by B lymphocytes | 11 |
| 1.3 | The cell cytoskeleton and polarity | 13 |
| 1.3.1 | The cell cytoskeleton | 13 |
| 1.3.1.1 | Cytoskeletal filaments assembly | 14 |
| 1.3.1.2 | Shaping the cell cytoskeleton | 18 |
| 1.3.1.3 | Molecular motors | 23 |
| 1.3.1.4 | Interactions between cytoskeletal networks | 24 |
| 1.3.2 | Cell polarity | 29 |
| 1.3.3 | Nucleus-cytoskeleton interactions | 33 |
| 1.4 | The B cell immune synapse: a highly organised structure | 36 |
| 1.4.1 | Plane of the synapse: a concentric organisation | 36 |
| 1.4.1.1 | B cell antigen affinity discrimination and antigen extraction | 40 |
| 1.4.2 | Transversal plane: polarisation of the B lymphocyte | 42 |
| 1.5 | Model systems of the immune synapse | 45 |
| 1.5.1 | Antigen presentation substrates | 45 |
| 1.5.2 | Imaging the immune synapse | 46 |
| 1.5.3 | Measuring forces at the immune synapse | 49 |
| 1.6 | Objectives and outline of the thesis | 52 |
| 2 | Actomyosin-driven force patterning controls endocytosis at the immune synapse | 53 |
| 2.1 | Introduction | 53 |
| 2.2 | Results | 57 |

| | | |
|----------|--|------------|
| 2.2.1 | Actin protrusions generate non-planar forces at the immune synapse | 57 |
| 2.2.2 | Actin patches are antigen-dependent dynamic structures that resemble invadosome-like protrusions | 58 |
| 2.2.3 | Actin patches stability, force generation and antigen extraction are modulated by actomyosin contractility | 61 |
| 2.3 | Conclusion | 64 |
| 3 | Dynamics of immune synapse formation in B lymphocytes | 65 |
| 3.1 | A microfluidic system for the systematic study of immune synapse formation | 67 |
| 3.2 | Characteristic timescales at the B lymphocyte immune synapse | 71 |
| 3.3 | Cytoskeletal networks and synapse formation | 75 |
| 3.3.1 | The actin cytoskeleton is necessary for antigen clustering and signaling at the immune synapse | 75 |
| 3.3.2 | The actin cytoskeleton does not impact later events of synapse formation | 77 |
| 3.3.3 | Microtubules are essential for the formation of the centrosome-nucleus polarity axis | 79 |
| 3.3.4 | Microtubules restrict actin nucleation to the immune synapse and prevent polarity loss | 81 |
| 3.4 | Conclusion | 87 |
| 4 | Discussion | 89 |
| 4.1 | Role of actomyosin contractions and structures at the immune synapse . | 90 |
| 4.2 | Control of immune synapse formation by actin and microtubule interactions | 93 |
| 4.3 | Implications in primary cells and physiological conditions | 98 |
| 4.4 | Concluding remarks and perspectives | 103 |
| 5 | Materials and Methods | 105 |
| 5.1 | For Chapter 2 | 105 |
| 5.1.1 | Cells and cell culture | 105 |
| 5.1.2 | Reagents | 105 |
| 5.1.3 | Experimental protocols | 106 |
| 5.2 | For Chapter 3 | 109 |
| 5.2.1 | Cells and cell culture | 109 |
| 5.2.2 | Reagents | 109 |

| | | |
|---|--|------------|
| 5.2.3 | Experimental protocols | 111 |
| 5.2.4 | Image analysis | 114 |
| Bibliography | | 117 |
| A Co-first author Research article | | 139 |
| B Published Protocol article | | 155 |
| C Collaborative Research articles | | 171 |
| C.1 | Collaborative Research article 1 | 171 |
| C.2 | Collaborative Research article 2 | 187 |
| C.3 | Collaborative Research article 3 | 206 |
| D Résumé en Français | | 219 |

List of Figures

| | | |
|------|---|----|
| 1.1 | Barriers against pathogens | 2 |
| 1.2 | Generation of immune cells | 3 |
| 1.3 | Innate and Adaptive Immunity | 5 |
| 1.4 | The B cell receptor | 7 |
| 1.5 | Generation of B lymphocytes | 8 |
| 1.6 | B lymphocyte activation by encounter of surface-tethered antigens. . . . | 10 |
| 1.7 | Antigen internalisation, processing and presentation by B lymphocytes . | 12 |
| 1.8 | Cell cytoskeleton microscopy | 14 |
| 1.9 | Assembly of cytoskeletal filaments | 17 |
| 1.10 | Regulation of actin filament assembly | 19 |
| 1.11 | Regulation of microtubule assembly | 21 |
| 1.12 | Interactions between cytoskeletal networks | 25 |
| 1.13 | Effectors of GTPases | 28 |
| 1.14 | Cell polarity: interactions between Par proteins and small GTPases . . . | 31 |
| 1.15 | Nucleus-cytoskeleton interactions: the LINC complex | 34 |
| 1.16 | B cell immune synapse formation | 39 |
| 1.17 | B cell polarisation at the immune synapse | 44 |
| 1.18 | Model substrates for antigen presentation | 45 |
| 1.19 | Systems to image B lymphocyte-antigen encounter | 48 |
| 1.20 | Measuring forces at the immune synapse | 51 |
| 2.1 | B lymphocytes generate antigen-specific forces at the immune synapse . | 54 |
| 2.2 | Myosin II is essential for force generation, actin patch formation and antigen extraction in B cells | 56 |
| 2.3 | B lymphocytes exert forces orthogonal to the substrate at the center of the immune synapse | 57 |
| 2.4 | Actin patches are similar to invadosome-like protrusions | 59 |
| 2.5 | Actin patches are promoted and stabilized in the presence of antigen . . | 60 |
| 2.6 | Actomyosin contractility regulates forces, actin patches and antigen ex- traction | 62 |

| | | |
|------|---|-----|
| 2.7 | Model: Actomyosin-driven force patterning controls endocytosis at the immune synapse | 63 |
| 3.1 | Microfluidic system to study dynamics of B lymphocyte polarisation and immune synapse formation | 66 |
| 3.2 | Timescales of B lymphocyte polarisation | 71 |
| 3.3 | The nucleus undergoes a rotation followed by rearward transport | 73 |
| 3.4 | F-actin is essential for antigen recruitment and signaling amplification, but not for the establishment of the polarity axis | 74 |
| 3.5 | Myosin II activity does not have a significant impact on immune synapse formation and B cell polarisation | 76 |
| 3.6 | Centrosome and nucleus reorientation are correlated, and actin-independent | 78 |
| 3.7 | Microtubule disruption leads to intense cell and nucleus deformation, and impairs the establishment and maintenance of a polarised organisation | 80 |
| 3.8 | Controlled RhoA activation regulates actin patterning and polarisation . | 82 |
| 3.9 | GEF-H1 is responsible for cell shape and actin patterning defects upon microtubule depletion, independently of myosin II | 84 |
| 3.10 | Microtubules control the polarised enrichment in F-actin via GEF-H1 . . | 86 |
| 3.11 | Immune synapse formation has two phases, with different dependencies on actin and microtubules | 88 |
| 4.1 | Phase 1 corresponds to an attempt at mechanical extraction of the antigen, and Phase 2 to the reorganisation of intracellular components for proteolytic extraction | 93 |
| 4.2 | Model for the polarised activation of mDia1 | 95 |
| 4.3 | Nocodazole-treated cells can form multiple immune synapses | 96 |
| 4.4 | Primary B lymphocytes complete Phase 1, but not Phase 2 of immune synapse formation | 99 |
| 4.5 | Primary B lymphocytes form actomyosin-rich punches at the immune synapse, promoted by actomyosin contractility | 102 |

Chapter 1

Introduction

1.1 The immune system

Humans, like most organisms, are constantly in contact with billions of pathogens and foreign bodies through surrounding objects, food, or even air. While some bacteria and fungi live peacefully with their host, the most well known being the gut microbiota that participates in food processing, other foreign bodies can be extremely dangerous for the organism. Humans have evolved to implement various layers of protection against infection (Figure 1.1).

The first layer is purely mechanical: the **epithelium**. Any contact with external elements is made with the protection of the skin or through densely packed epithelial cells, the mouth and gut epithelia for example. The commensal flora living on these surfaces are also crucial to avoid opportunistic pathogens populating these territories. If this first layer fails, because of a defect in the epithelium for example, and cells are infected, a second layer shields the organism: **cell-intrinsic responses**. Indeed, if an infected cell detects that it has ingested a pathogen, it tries to degrade it with lysosomes, and degrades foreign DNA by processes that detect cytoplasmic DNA. This cellular damage triggers tissue repair responses, as well as a local inflammation to call the third layer: immune responses.

Only then will the specialised immune cells take action, through two types of responses: **the innate and adaptive immune responses**. The innate immune response is a fast, non-specific response that targets anything presenting patterns associated with foreign antigens. If this does not clear the infection fully and quickly, adaptive immunity processes intervene. This last type of immune response is slower to mount and can therefore only be activated in later phases, but it allows stronger and pathogen-specific responses, and keeps memory of previous infections.

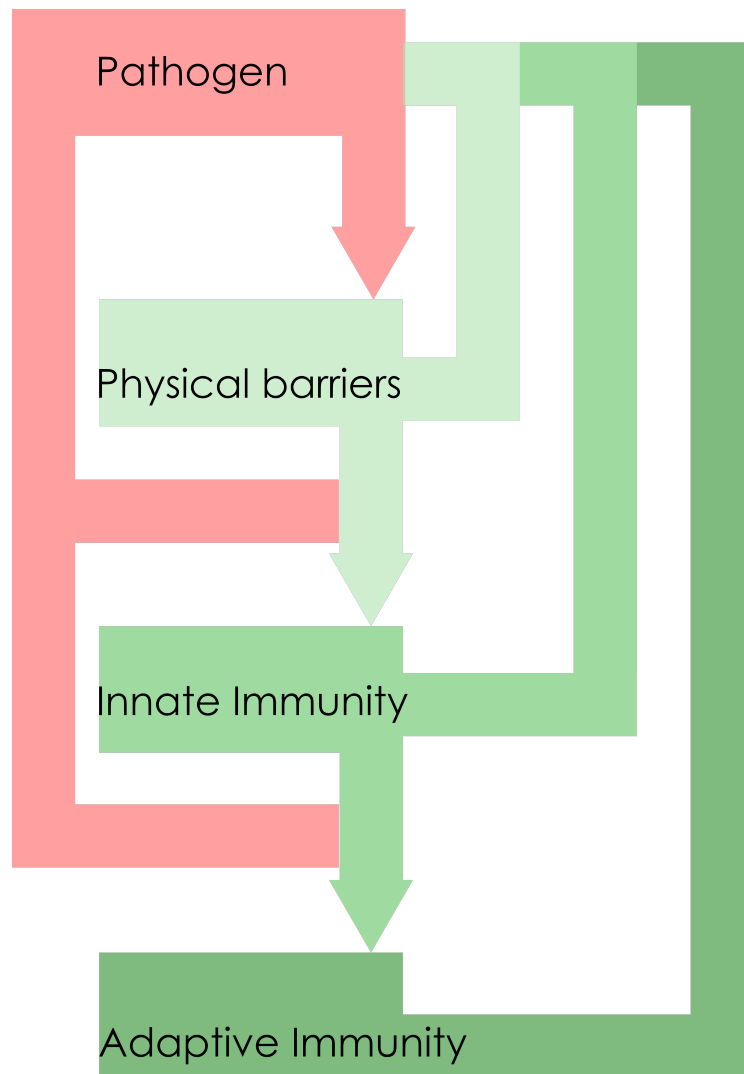


FIGURE 1.1: **Barriers against pathogens.** The body has three layers of protection against pathogens: physical barriers and intrinsic cell response, the innate immune response if the pathogen can go through the physical barriers, and the adaptive immune response if the innate immune response failed to clear the infection.

Interestingly, those two aspects of immunity, innate and adaptive, were envisioned at the same time by two different scientists, Elie Metchnikoff and Paul Ehrlich, at the end of the 19th Century. They eventually got the Nobel Prize in Physiology and Medicine together in 1908, Elie Metchnikoff for discovering that specialised cells could be recruited to the site of infection and phagocyte microbes, and Paul Ehrlich for offering the first theory of production of "side chains" that would target specific toxins after a first encounter. Elie Metchnikoff set the path for innate immunity, and Paul Ehrlich for adaptive immunity.

Both the innate and adaptive immune systems arise from precursor cells in the bone marrow called hematopoietic stem cells (Figure 1.2A). Immune cells are all generated in primary lymphoid organs (bone marrow and thymus), and can then travel to tissues and secondary lymphoid organs (lymph nodes, spleen) through the blood vessel network and a specific parallel network of lymphatic vessels (Figure 1.2B).

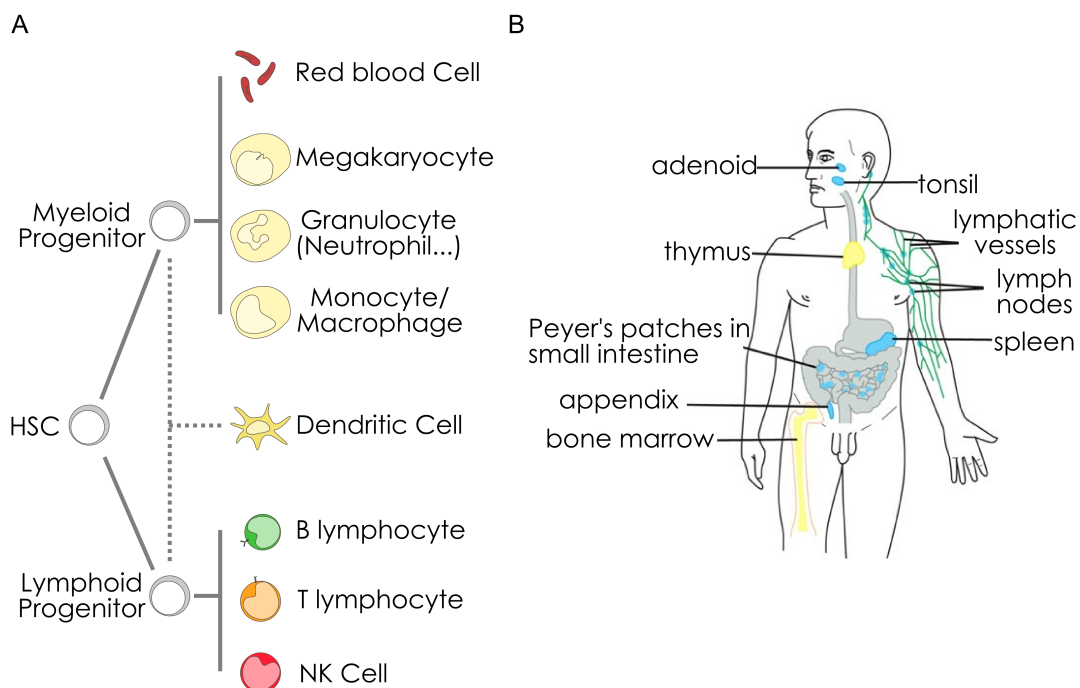


FIGURE 1.2: **Generation of immune cells.** (A) Overview of hematopoiesis, occurring in primary lymphoid organs. HSC, hematopoietic stem cell. (B) The lymphatic system: in yellow are primary lymphoid organs, in blue secondary lymphoid organs. Taken from *Molecular Biology of the Cell* 5th edition Alberts et al., 2008

1.1.1 The innate immune system

When a pathogen manages to break the first physical barriers, the damaged tissue or infected cells trigger an inflammatory response to start fighting the infection and launch the processes of tissue repair. Inflammation induces very typical external signs that were identified in the 1st Century by the Romans: swelling, redness, heat and pain. These events are all the consequences of a strong vasodilatation within minutes of injury, that results in a rise in blood volume in the inflamed area. The increased amount of blood gives the reddish colour to the area, and heats the tissue. Blood vessels not only enlarge but also become more permeable, letting fluid enter the tissue, especially from capillaries. This accumulation of fluid results in local swelling that can apply pressure to nerves, generating pain signals. But why the need for increased blood volume and fluid leakage ?

This mechanism allows the recruitment of leukocytes, that extravasate from the blood vessel to the tissue more easily due to increased permeability of local blood vessels in the inflamed area. Leukocytes release pro-inflammatory cytokines to attract more immune cells, and phagocyte pathogens to clear the infection. Phagocytes such as neutrophils will be recruited first, followed by macrophages and dendritic cells to help the clearing of infection (Figure 1.3).

In homeostasis, tissue-resident macrophages and dendritic cells are responsible for clearing dead cells or debris, and patrolling in search of potential pathogens. These two cell types constitutively engulf large amount of extracellular material by phagocytosis (internalisation of large particles) or macropinocytosis (engulfment of extracellular fluids). Upon encounter of a danger signal, they become activated and clear the area while recruiting other phagocytes to fight the pathogen.

In addition, activated dendritic cells down-regulate their macropinocytic activity, migrate to the closest lymph node to present particles acquired from the tissue to T lymphocytes and trigger the adaptive, antigen-specific immune response (Figure 1.3). Dendritic cells are the main link between the innate and the adaptive immune system, that will be described in the next section.

1.1.2 The adaptive immune system

The adaptive immune response is an antigen-specific response, and therefore needs the encounter between a specific lymphocyte and its cognate antigen to be triggered. To increase this chance of encounter, naive B and T lymphocytes circulate between secondary lymphoid organs (lymph nodes, spleen), where antigens are transported by

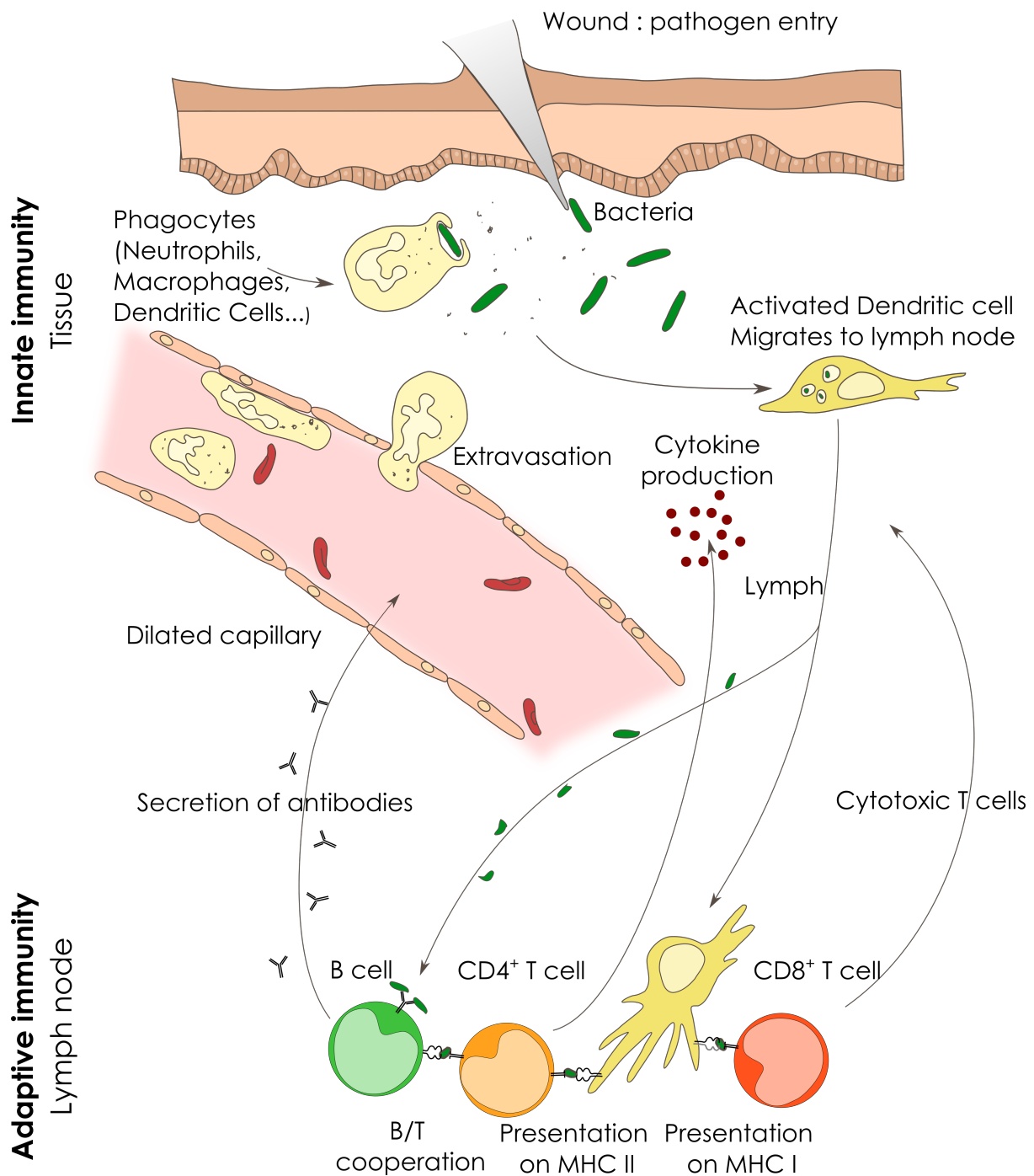


FIGURE 1.3: Innate and Adaptive Immunity. Upon breaking of physical barriers and pathogen entry into the tissue, inflammation signals are sent to trigger the innate immune response. Phagocytes (neutrophils, then macrophages and dendritic cells) are recruited to clear the infection. Activated dendritic cells migrate to the closest lymph node to trigger the adaptive immune response by presenting antigen to T lymphocytes, while pathogenic particles are brought to the lymph node for B lymphocyte activation. The activation of CD8⁺ T lymphocytes leads to their migration to the tissue for target killing, while the activation of CD4⁺ T lymphocytes supports cellular immunity by secreting cytokines, and allows together with B lymphocyte activation the production of high affinity antibodies.

the blood, lymph, or activated dendritic cells.

Lymph nodes contain a wide variety of naive B and T lymphocytes, each carrying a specific receptor (called B cell receptor BCR, T cell receptor TCR) capable of recognizing a specific epitope of a foreign antigen. Activated dendritic cells partially degrade the material they internalise, and present the resulting peptides on Major Histocompatibility Complex Class II (MHC II) to CD4⁺ T cells, or on Major Histocompatibility Complex Class I (MHC I) to CD8⁺ T cells. Upon antigen recognition, activated CD8⁺ T cells migrate directly to the site of infection and kill the infected cells, while activated CD4⁺ T cells become Helper T cells that secrete cytokines at the site of infection to support recruitment and activation of NK cells, CD8⁺ T cells and phagocytes at the site of infection, but also ensure the proper activation of B lymphocytes (Figure 1.3).

B lymphocytes also encounter antigens in the lymph node, but as whole non-processed particles. B lymphocytes become activated upon encounter with their cognate antigen, which allows them to internalise the antigen, process it and present the resulting peptides on MHC II to the Helper T cells for confirmation: this process is called B/T cooperation and is essential for the B lymphocyte to be fully activated. Activated B lymphocytes are then able to proliferate and produce high affinity antibodies against the antigen (Figure 1.3), eventually differentiating into plasma cells for secretion of high affinity antibodies, and memory B cells to mount a faster adaptive immune response against this antigen in the future.

This process of immune memory allows humans to be trained and resistant to some diseases, and is at the basis of vaccination.

1.2 The B lymphocyte

B lymphocytes are widely preserved across all jawed vertebrates, from sharks to humans (Cooper, 2015), and set the foundation of adaptive immunity and immune memory. Antibodies were first identified at the end of the 19th century by Paul Ehrlich and set the path to the study of adaptive immunity. Researchers followed the track leading to antibody production sites, plasma cells, in the 1960s, and then up to naive B cells and beyond, with all these cells having something in common: B lymphocytes all carry a unique immunoglobulin (Ig) surface receptor, recognizing a single antigen epitope (Lebien and Tedder, 2008). The basic structure of an immunoglobulin composed of two identical heavy (H) chains with two identical light (L) chains (Figure 1.4). These four chains assemble to form a symmetrical structure with two identical antigen-binding

sites, each formed by the combination of a light and a heavy chain. It is the nature of the heavy chain that determines the type and level of differentiation of a B lymphocyte (IgM in immature B cells, IgM and IgD in mature naive B cells, IgG in activated B cells). All immunoglobulins except IgD are also found in a secreted form, with IgM complexes being secreted in the early stages of the primary antibody response to bind antigens and activate complements, and IgG, IgA and IgE in the secondary antibody response. IgA is found in secretions (saliva, tears, feces) while IgG and IgE are found in the blood and are responsible for antibody-mediated phagocytosis by phagocytes (Schroeder and Cavacini, 2010). The association of the membrane immunoglobulin and a signal transduction region (Ig α /Ig β) forms the B Cell Receptor (BCR) (Figure 1.4).

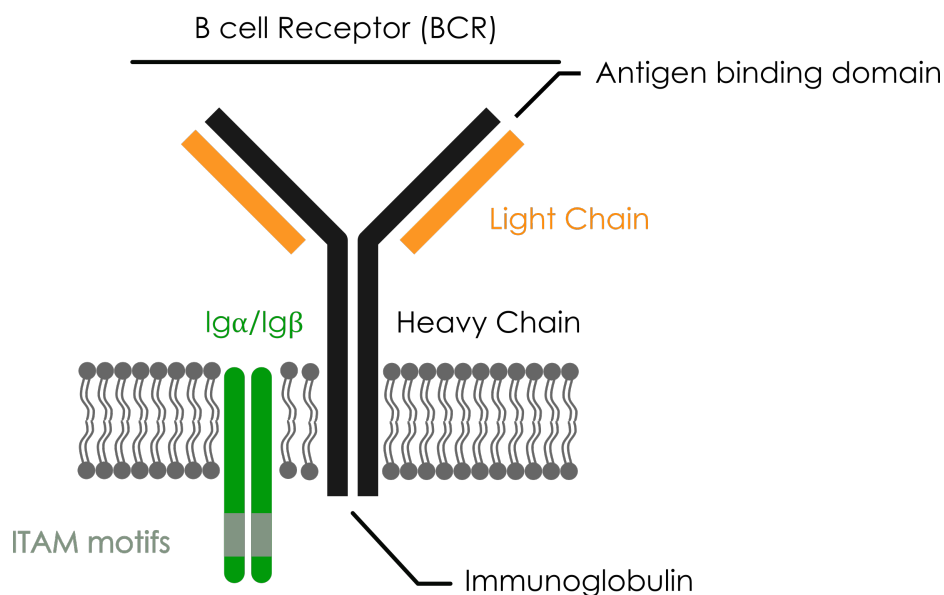


FIGURE 1.4: **The B cell receptor** is composed of a membrane immunoglobulin and a signal transduction region (Ig α /Ig β). The membrane immunoglobulin itself comprises two identical heavy chains and two identical light chains, that assemble to form a symmetrical structure with two identical antigen-binding sites.

1.2.1 Generation of B lymphocytes

In the bone marrow, hematopoietic stem cells (HSCs) are initially able to differentiate into any immune cell type. A subpopulation will start differentiating into common lymphoid progenitors (CLPs), precursors of B and T lymphocytes. Commitment to the B cell lineage is then triggered by the transcription factor Pax5, that differentiates the CLP into a pro-B cell and induces the expression of B220 (also called CD45R), a typical B cell marker. Further differentiation into pre-B cell induces the expression of the first form of surface immunoglobulin, the pre-BCR, that contains two μ heavy chains like

the future BCR, but temporary surrogate light chains (Figure 1.5).

Only pre-B cells that are able to assemble heavy chains and surrogate light chains into a signaling-competent pre-BCR continue their development into immature B cells. At this stage, the pre-BCR is replaced by a BCR containing a membrane IgM (immunoglobulin with a μ -class heavy chain) with a κ or λ light chain (Nagasawa, 2006).

To be able to recognize any unknown antigen, the immune system needs to generate a huge diversity of BCRs. This is achieved through random mutations in BCR binding sites, and can result in the presence of BCRs that recognize epitopes naturally present in the body: self-antigens. Self-reactive B cells are eliminated at the immature B cell stage, and the remaining cells migrate from the bone marrow to the spleen to undergo a maturation process. After these repeated gene rearrangements and selection steps, only 10% of the initial pool of B cell progenitors reaches maturity, with $\sim 5 \cdot 10^6$ mature B cells reaching the spleen every day (Kindt, Goldsby, and Osborne, 2007). Mature B cells eventually exit the spleen and travel through the blood and lymphatic network to settle in secondary lymphoid organs follicles (lymph node and spleen), offering a broad immune coverage to the whole body. These mature B cells that have never encountered their cognate antigen are termed naive B cells (Figure 1.5).

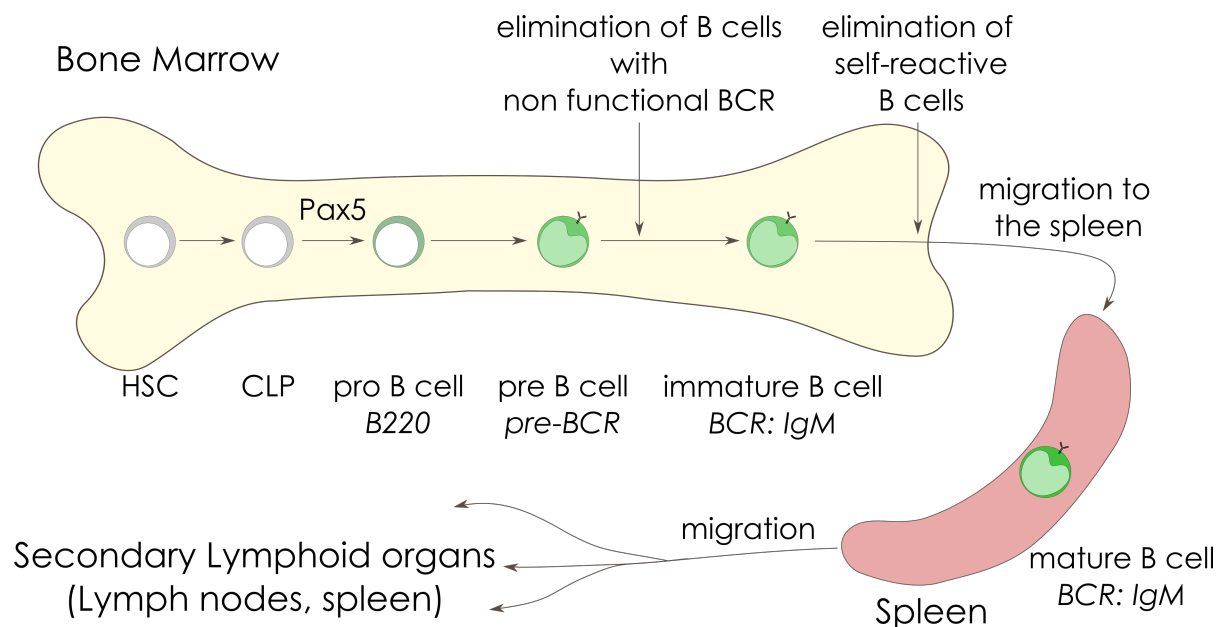


FIGURE 1.5: **Generation of B lymphocytes.**

1.2.2 B lymphocyte activation by antigen encounter

The activation of a naive B lymphocyte occurs through the engagement of the B cell Receptor (BCR) with its cognate antigen. Naive B cells are located in the B cell follicles of lymph nodes, and encounter antigens either in a soluble form, if the antigen is small enough to diffuse to the B cell follicle (<70kDa), or tethered at the surface of other immune cells in the case of large particulate antigens (Pape et al., 2007). Indeed, large antigens are unable to freely diffuse in the lymph node and get stuck at the surface of subcapsular macrophages, follicular dendritic cells or are brought by migrating dendritic cells (Figure 1.6) (Obino and Lennon-Duménil, 2014; Batista and Harwood, 2009; Carrasco and Batista, 2007; Junt et al., 2007; Suzuki et al., 2009).

In B cell follicles, naive B cells express the chemokine receptor CXCR5 that binds the chemokine CXCL13, which allows them to constantly migrate and scan their surroundings for antigen (K.M. et al., 2000). Upon recognition of an antigen at the surface of another cell, the naive B cell stops migrating and forms a structure called the immune synapse with the opposing cell. This structure is similar to immune cell-cell contacts initially described in T lymphocytes.

The engagement of the BCR by the antigen triggers a very fast signaling pathway and dramatic cell rearrangements that ultimately lead to the activation of the B lymphocyte. The first step is the activation of Lyn, a Src kinase, that phosphorylates the immunoreceptor tyrosine-based activation motifs (ITAM) on the cytoplasmic tail of the $Ig\alpha/Ig\beta$ heterodimer. This event allows the docking of Syk to the ITAMs and its phosphorylation, eventually leading to the phosphorylation of Btk and Vav. This first wave of signaling results in a burst of calcium released from Endoplasmic Reticulum stores, and the production of DAG (Diacylglycerol) and IP3 that allow further B cell activation.

IP3 helps maintaining a sustained calcium release from the Endoplasmic Reticulum, while DAG induces the translocation of the transcription factors $Erk^{1/2}$ and $NF-\kappa B$, via the activation of PKC, to the nucleus (Figure 1.6).

The activation of DAG and the phosphorylation of Lyn, Syk and Btk also induce drastic cytoskeletal remodelling and the polarisation of the B cell, both being described more in-depth in section 1.4. This remodelling has proven essential for proper activation of B cells, and for further antigen internalisation, processing and presentation to Helper T cells.

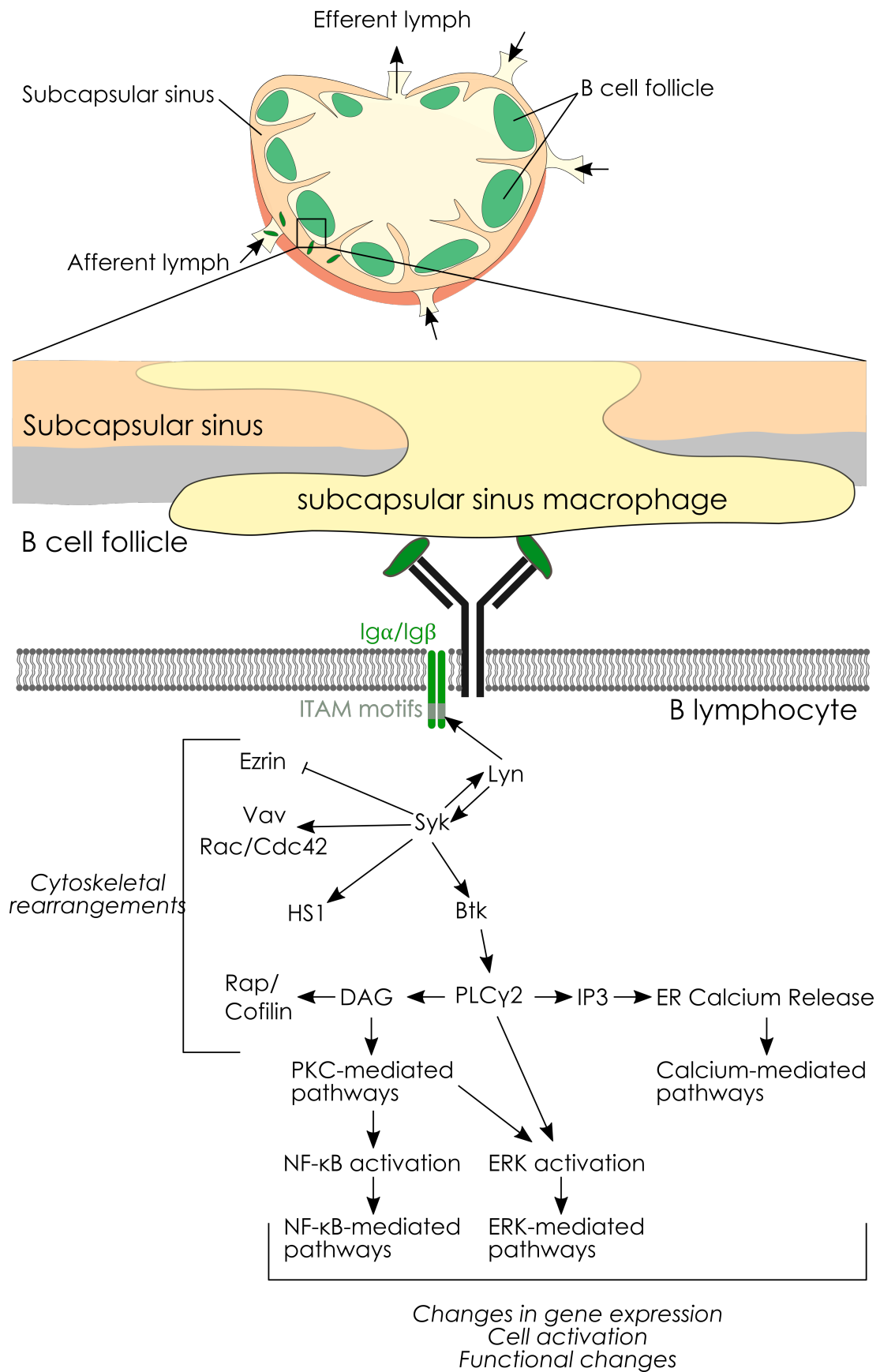


FIGURE 1.6: B lymphocyte activation by encounter of surface-tethered antigens.

1.2.3 Antigen internalisation, processing and presentation by B lymphocytes

The activation of naive B cells through BCR-induced signaling results in an initial activation state of the cell, but the continuation of the adaptive immune response requires the internalisation and processing of antigens by B cells, and their presentation to Helper T cells on MHC II for B/T cooperation. If the B cell fails to present to a corresponding Helper T cell, it undergoes apoptosis and this adaptive immune response is terminated.

The extraction of the antigen from the surface of the antigen-loaded cell can be achieved via direct mechanical pulling on the antigen through the BCR, or via the release of proteases at the immune synapse by B lymphocytes (Batista, Iber, and Neuberger, 2001; Spillane and Tolar, 2016). Antigen-BCR complexes are then internalised through clathrin-mediated endocytosis and converge together with Cathepsin S, H2-DM and Lamp1⁺-MHC II⁺ endolysosomes into multivesicular bodies for antigen processing (Roberts et al., 2020; Obino and Lennon-Duménil, 2014). Premature binding of endogenous peptides on MHC II is prevented by the presence of a chaperone, the invariant chain Ii, on its peptide-binding domain. The invariant chain also plays a role in guiding MHC II molecules to endolysosomes, through the interaction of its cytoplasmic tail with myosin II (Figure 1.7 steps 1-2) (Vascotto et al., 2007). In the antigen processing compartment, the invariant chain is partially cleaved by Cathepsin S, leaving only its CLIP portion to protect the peptide-binding domain. Meanwhile, the antigen undergoes partial proteolysis to obtain small antigenic peptides that are exchanged with the CLIP peptide with the help of the chaperone H2-DM (Figure 1.7 steps 3-5) (Yuseff et al., 2013; Obino and Lennon-Duménil, 2014; Adler et al., 2017).

The MHC II - peptide complex is transported to the cell surface to be presented to Helper T cells primed by dendritic cells (Figure 1.7 step 6). A successful B/T cooperation ultimately allows the activated B cell to survive and form germinal centers in the lymph node. In germinal centers, activated B cells undergo somatic hypermutation (repeated mutations of their antigen-binding domains) to optimise their antigen-binding capacities, leading to the production of high-affinity antibodies.

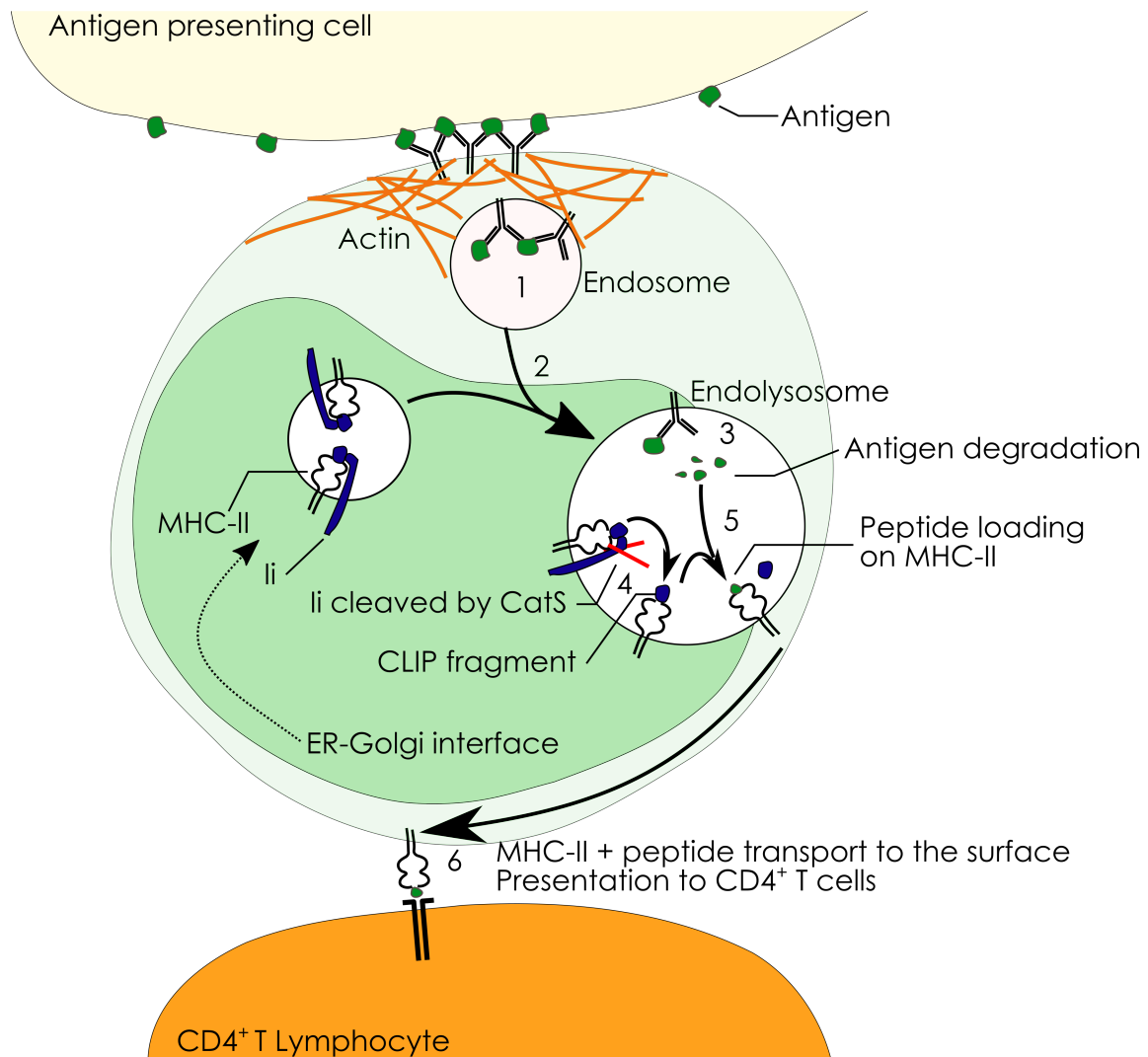


FIGURE 1.7: Antigen internalisation, processing and presentation by B lymphocytes. 1. Ag-BCR complexes are internalised. 2. Endosomes containing Ag-BCR complexes and compartments containing MHC-II with the invariant chain Ii are merged in a Myosin II dependent manner. 3. Antigen is partially degraded to obtain antigenic peptides. 4. Ii is cleaved by Cathepsin S, leaving only the CLIP fragment on the peptide-binding site of MHC II. 5. The antigenic peptide is loaded on MHC II, replacing CLIP with the help of the chaperone H2-DM. 6. MHC II + peptide complexes are transported to the cell surface for presentation to CD4⁺ T cells.

1.3 The cell cytoskeleton and polarity

1.3.1 The cell cytoskeleton

Cells are plastic units that are able to adapt their shape and properties to specific functions and environmental cues, as illustrated by dendritic cells that switch from a macropinocytic phenotype to a fast migrating phenotype to go to the closest lymph node upon activation. To tune their internal organisation and physical properties, all cells use the same versatile set of filaments: the cell cytoskeleton.

The cell cytoskeleton is composed of three types of filaments with complementary roles: **(1) actin filaments** control cell shape and migratory capabilities, while **(2) microtubules** act as a network for intracellular transport and organelle positioning and **(3) intermediate filaments** provide mechanical strength and a scaffold to control intracellular organisation (Figure 1.8).

(1) Actin filaments and (2) microtubules are conserved in some form amongst both eukaryotes and prokaryotes, and in all cell types (Wickstead and Gull, 2011), making actin one of the most abundant protein on earth. Actin was identified for the first time in the 1940s in muscle cells by F.B. Straub, shortly followed by the discovery of microtubules in the 1950s with the advent of transmission electron microscopy (Brinkley, 1997). Actin filaments and microtubules are both formed of globular subunits, globular actin (G-actin) and tubulin respectively, that assemble to form polarized filaments. However, their properties differ widely: while (2) microtubules are wide (25nm), stiff (persistence length of several millimeters), hollow tubes, usually nucleating from a unique microtubules organising center (MTOC), (1) actin filaments are thin ($\sim 5\text{-}9\text{nm}$), more flexible (persistence length $\sim 10\mu\text{m}$) and generate various higher-order structures all across the cell, from stiff bundles to gels or 2D sheets, but also the cortex under the plasma membrane that defines cell shape.

(3) Intermediate filaments are sensibly different from the other types of cytoskeletal filaments, as this term encompasses a broad variety of filaments from lamin in the nucleus to keratin or vimentin. This term was initially coined in 1968 to describe intermediate-sized filaments that were neither actin nor microtubules (Ishikawa, Bischoff, and Holtzer, 1968), and the notion of a family of filaments with shared characteristics emerged only later. Although intermediate filaments are present in almost all eukaryotic cells, they are expressed in different forms and amounts, making them hard to identify and study. Indeed, more than 70 genes coding for different intermediate filaments evolved from the ancestral lamin-like gene and are differentially expressed in different cell types (Etienne-Manneville, 2018).

Contrary to actin filaments and microtubules, intermediate filaments are composed of

elongated apolar subunits assembling to form a very deformable filament (persistence length $< 1\mu\text{m}$) with a diameter of $\sim 10\text{nm}$. Their compliance and the ability of the network to adapt under stress make intermediate filaments a key asset for cells experiencing mechanical constraints.

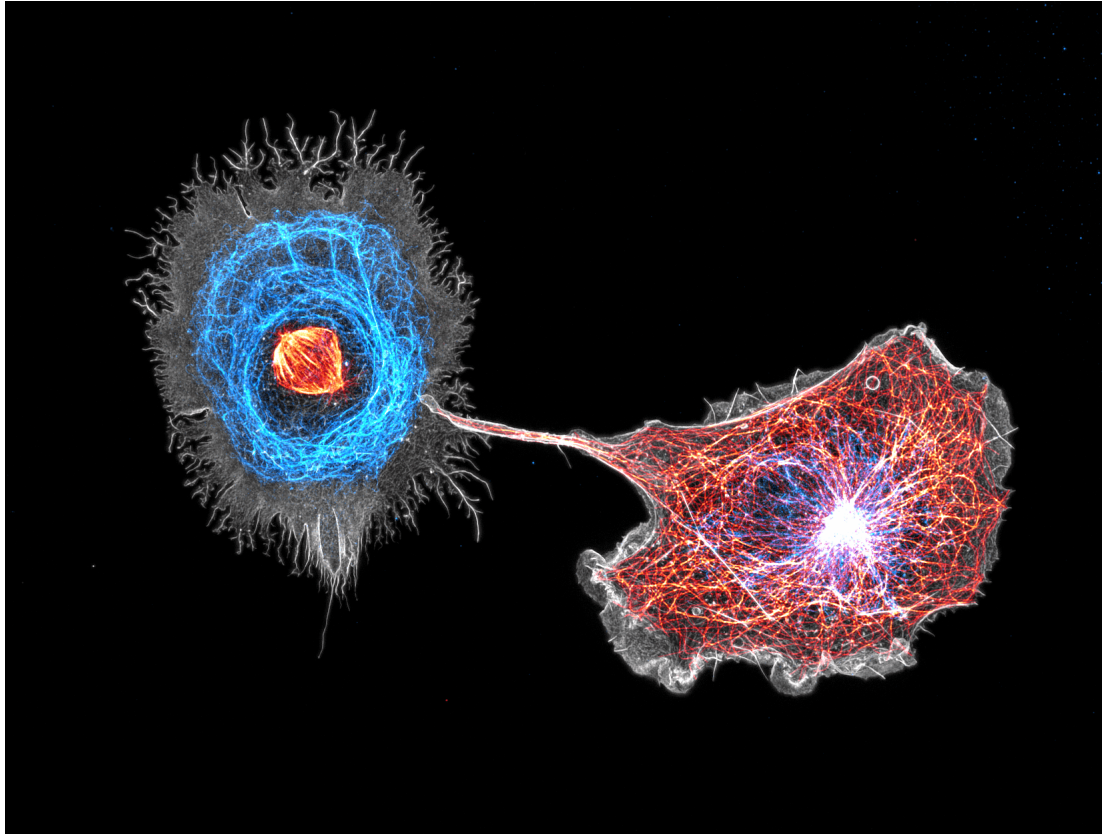


FIGURE 1.8: Cytoskeletal networks in COS-7 Cells. Grey: Actin. Red: Microtubules. Blue: Vimentin (intermediate filaments). Credits Christophe Leterrier, NeuroCyto, INP, Marseille.

1.3.1.1 Cytoskeletal filaments assembly

All types of cytoskeletal filaments are composed of several protofilaments made of the soluble subunits, that are assembled laterally into helical structures. Unlike in long-lived polymers like DNA, the subunits are not covalently bound together, making filaments prompt to dynamic assembly and disassembly, while the multiple interactions of each subunit with subunits from the same protofilament and from neighbouring protofilaments confer to cytoskeletal filaments a good resistance against breaking (Alberts et al., 2008).

Actin filaments are made from small subunits called Globular Actin (G-actin, actin monomers). Actin monomers assemble in a head-to-tail fashion into filaments formed

of two protofilaments twisted around each other. This results in polar filaments with two different extremities: the pointed end (also termed minus end) and the barbed end (plus end), where new ATP-bound G actin can bind to elongate the filament. As the filament ages, ATP gets hydrolyzed into ADP, and the polymer is destabilised (Figure 1.9). This results in continuous polymerisation at the barbed end and depolymerisation at the pointed end, a phenomenon known as actin filament treadmilling (Pollard and Cooper, 2009) that generates actin flows often seen in migrating cells.

Microtubules are composed of tubulin subunits, that are heterodimers of α - and β -tubulin molecules. Tubulin subunits interact longitudinally to form protofilaments with α - β interactions, and laterally with α - α and β - β interactions to combine, on average, 13 protofilaments into a polarized microtubule (Figure 1.9) (Gall, 1966). The unidirectional assembly of the tubulin heterodimers confers a polarity to the microtubules, with the minus end presenting only α -tubulin, and the plus end only β -tubulin, and allowing the binding of GTP-tubulin to for protofilament elongation. Protofilaments grow from the microtubule extremity, first in a bent conformation, then straighten to properly interact with their neighbours and elongate the microtubule (McIntosh et al., 2018). Eventually, the GTP-tubulin incorporated in the microtubule is hydrolyzed into GDP-tubulin and induces a slight change in conformation (Alushin et al., 2014). When enough new GTP-tubulin subunits arrive at the plus end, maintaining a GTP cap, the microtubule is stable and able to grow. However, if all tubulin subunits of the microtubule are in the GDP-bound form, the conformational change in subunits induces a strain in the filaments that leads to disassembly from the plus end and filament shrinkage. Alternating phases of growth and shrinkage is a characteristic feature of microtubules called dynamic instability, and the balance between the two states plays a crucial role in many cell functions, especially in the establishment of polarity or in chromosome segregation during cell division.

Intermediate filaments subunits are elongated tetramers formed of two anti-parallel coiled-coil dimers, making them an apolar subunit. The longitudinal assembly of tetramers results in the formation of protofilaments that in turn interact laterally and form bundles of eight protofilaments, reaching the final form of intermediate filaments (Figure 1.9). Unlike in polarized actin filaments and microtubules, the extremities do not have any known characteristics and assembly does not occur from ATP/GTP-dependent addition of subunits. Instead, tetramers at the periphery of the cell are pre-assembled into unit-length-filaments (ULF, composed of 8 tetramers), particles of

a few ULFs, and squiggles (short filaments). ULFs and short filaments are transported towards the center of the cell to assemble and form intermediate filament that will be integrated in the existing network (Robert, Hookway, and Gelfand, 2016). Remodelling of intermediate filaments is not fully understood yet, but disassembly upon phosphorylation, severing of filaments and end-to-end annealing have been described (Robert, Hookway, and Gelfand, 2016; Etienne-Manneville, 2018). Drastic intermediate filaments rearrangements have been observed in fibroblasts (Alberts et al., 2008) and in B lymphocytes, where this remodelling is essential for proper B lymphocyte function (Tsui et al., 2018).

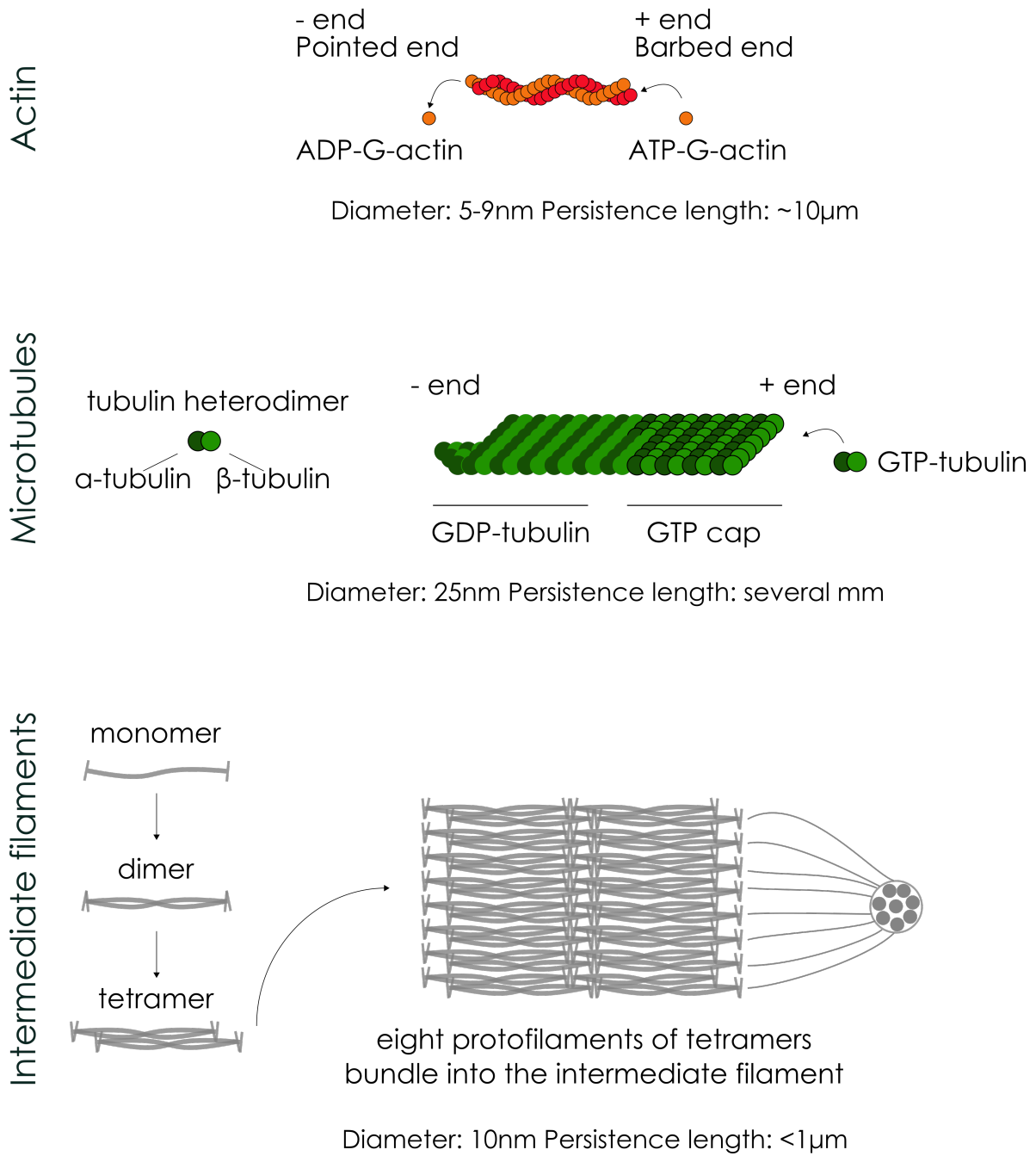


FIGURE 1.9: **Assembly of cytoskeletal filaments**

1.3.1.2 Shaping the cell cytoskeleton

If cytoskeletal filaments were left to grow freely, the cell would be filled with filaments and have very little monomer backup and intracellular organisation. Yet, cells show highly organised pools of cytoskeletal filaments, are able to establish a polarity and induce bursts of filament polymerisation when needed, as 50% of actin is kept in a monomeric form in a resting cell (Alberts et al., 2008). This tight control of localisation, organisation and growth rate of cytoskeletal filaments is operated through hundreds of accessory proteins that interact with subunits and filaments.

FILAMENT NUCLEATION sites and extent are controlled by specific nucleators of actin filaments and microtubules. Small nuclei of few subunits are very unstable and cannot be maintained long enough to grow a filament, making nucleators necessary to stabilise new emerging filaments. Nucleation strategies are either to concentrate and sequester subunits locally, or to offer a template for filament assembly by mimicry.

Actin filaments have three families of nucleators: Formins, the Arp2/3 complex and WH2-containing proteins. Those families generate different types of actin networks and can collaborate or compete in cellular processes (Figure 1.10).

- *The Arp2/3 complex* is a nucleator of branched actin. It docks on a pre-existing actin filament -the mother filament- and nucleates a new actin filament -the daughter filament- with an angle of 70°. The Arp2/3 complex uses mimicry to nucleate a daughter filament through its Arp2 and Arp3 subunits. It benefits from numerous nucleation promoting factors (WASp/SCAR/WAVE-family proteins) that induce a conformational change of Arp2 and Arp3 and recruit the actin monomers necessary for filament nucleation (Chesarone and Goode, 2009). Arp2/3-mediated actin nucleation is found not only in dense actin networks and flat structures, like lamellipodia or macropinosomes, but also in the actin cortex (Figure 1.12).
- *Formins* are a family of linear actin nucleators that also act as actin filament elongation factors. Unlike Arp2/3 that remains at the pointed end of the filament, formins are processively displaced and maintained at the barbed end. They possess a "doughnut-shaped" FH2 domain that acts as an anchor and a template, and a long diffusing FH1 domain that captures free actin monomers and transfers them to the FH2 domain at the barbed end (Pollard and Cooper, 2009; Chesarone and Goode, 2009). Linear actin fibers resulting from formin-mediated actin polymerisation can form bundles and are found in stress fibers, filopodia, or cytokinesis rings (Figure 1.12).

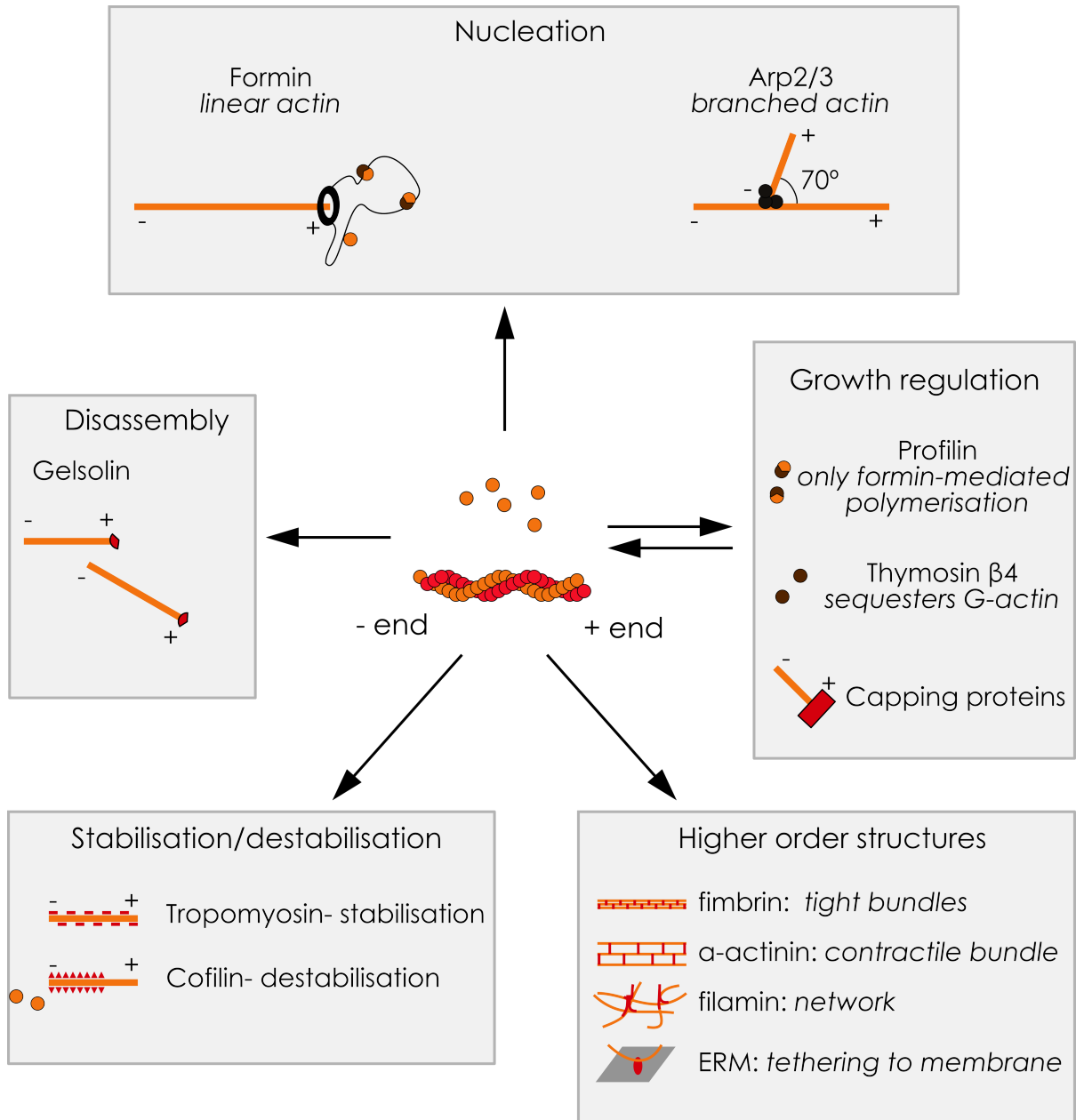


FIGURE 1.10: Regulation of actin filament assembly.

- *WH2-containing* actin nucleators are a less described nucleator family associated to linear actin. This family contains Spire (Baum and Kunda, 2005), Cordon-bleu (COBL) and Leiomodin (Lmod) (Chesarone and Goode, 2009). These proteins all have several actin monomer binding domains, and would use them to assemble actin monomers into a nascent complex serving as a nucleation platform. The different members of this family are implicated in various structures: Spire has been shown to interact with formins and microtubules and might play a role in membrane transport and cytoskeletal interactions (Campellone and Welch, 2010) while Cordon-Bleu expression has been linked to the formation of highly dynamic microvilli (Grega-Larson, Crawley, and Tyska, 2016) (Figure 1.12).

The activity of these different actin nucleators can be tuned locally, as the Arp^{2/3} promoting factors and formins are initially in an inhibited state. Rho-GTPases allow the cell to differentially promote the activity of actin nucleators. Classically, Rac1 and Cdc42 promote Arp^{2/3} activity (by releasing the inhibition of its promoting factors), and RhoA promotes formin activity as well as contractility (Suarez and Kovar, 2016).

Microtubules, in contrast, nucleate in most cell types from a unique MicroTubule Organising Center (MTOC): the centrosome (Figure 1.11). The centrosome is usually located at the geometrical center of the cell in non-polarized cells, and is composed of two centrioles (short tubes of modified tubulin) and an ensemble of proteins called the peri-centriolar material (PCM). The peri-centriolar material contains hundreds of γ -Tubulin ring Complexes (γ TurC) that nucleate microtubules. γ TurC is mainly composed of copies of γ -tubulin arranged in a ring-shaped structure that acts as a template for microtubule growth (Moritz et al., 2000). Microtubules grow radially from the centrosome, with the minus end attached to γ TurC, forming an aster.

FILAMENT GROWTH REGULATION is crucial to obtain different types of cytoskeletal structures: long or short filaments, dense or scattered networks. Two main strategies have been described to regulate filament growth: modulation of subunits availability or modification of the growing end.

In addition to limiting the growth of filaments, the sequestration of subunits also maintains a non-polymerized pool that can be made available in case of fast remodelling, as in the case of local actin polymerisation bursts during endocytosis. Microtubule subunits can be sequestered by stathmin (Figure 1.11), that binds two tubulin heterodimers (Jourdain et al., 1997), and G-actin can be bound by thymosin β 4 or by profilin (Figure 1.10). Thymosin β 4, like stathmin, completely prevents the addition of the monomer

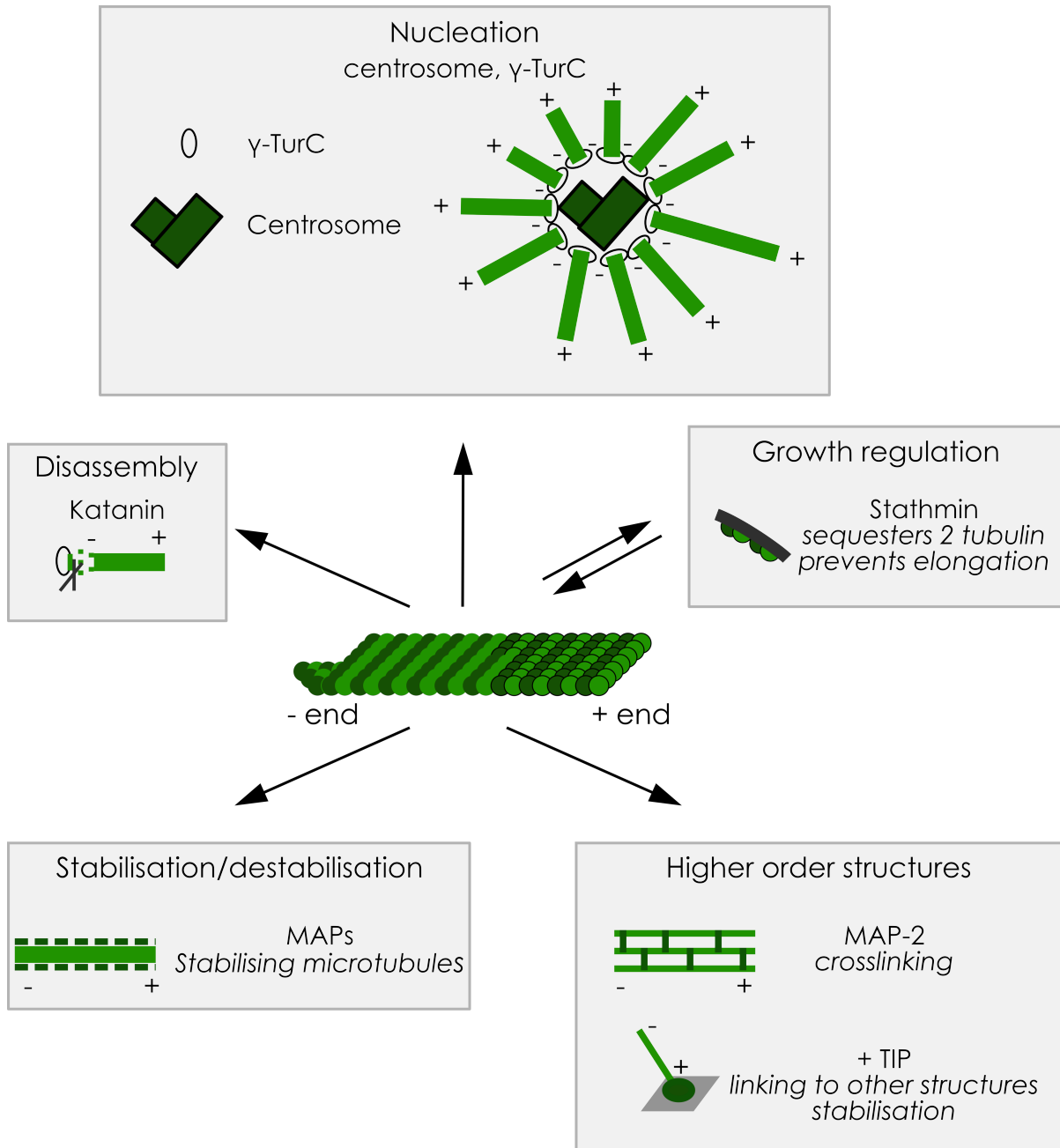


FIGURE 1.11: Regulation of microtubule assembly

to a filament, but profilin still allows the addition of monomers to filaments through formins and only decreases Arp2/3-mediated actin polymerisation (Suarez et al., 2015; Chesarone and Goode, 2009; Alberts et al., 2008).

Filament growth can be promoted or stopped by end-binding proteins that alter the state of the growing end. Formins and Ena/VASp bind to the growing end of actin filaments and act as elongation factors, increasing the growth rate, while capping proteins stop elongation (Figure 1.10) (Chesarone and Goode, 2009). The growth/shrinking balance of microtubules can be balanced by numerous plus end binding proteins. Widely known examples are kinesin 13 that induces shrinking, and XMAP215 that stabilises microtubules and promotes their growth (Figure 1.11) (Alberts et al., 2008). Regulation of filament growth is crucial to ensure availability of monomers for the different pools of filaments, but also to form specific structures. In the case of F-actin networks, availability of monomers appears to be a factor regulation actin organisation through the competition of different networks regulated by formins or Arp2/3. An important concentration of G-actin has been shown to favor the formation of Arp2/3-mediated branched actin networks, while low G-actin levels or increased profilin-1 leads to the preferential formation of contractile rings and actin bundles, and a decrease in Arp2/3 activity (Burke et al., 2014; Rotty et al., 2015). Ultimately, the availability of monomers, the profilin/G-actin balance will determine the preferential actin nucleators, while the proportion of elongation factors and capping proteins will determine filament length and the final structure of the actin pool: while filopodia require long actin filaments, a dense mesh of actin as found in a lamellipodium requires numerous short and branched actin filaments (Chhabra and Higgs, 2007).

FILAMENT STABILITY is also regulated by many accessory proteins, as some structures need to be preserved in the long term (epithelial cells for example) while others are only transient and are constantly disassembled to allow cell reorganisation (random cell migration). Filament disassembly can be induced by severing of filaments, which exposes minus ends and destabilises filament structure, resulting in a rapid depolymerisation. Severing proteins include the Gelsolin-superfamily proteins for actin (Figure 1.10), and katanin for microtubules (Figure 1.11) (Alberts et al., 2008). More subtle regulation of filament stability can be operated by proteins binding along filaments to stabilise or destabilise them, such as Microtubule-Associated Proteins (MAPs) that bind to and stabilise microtubules, or tropomyosin and cofilin (Actin Depolymerising Factor ADF) that bind to and respectively stabilise and destabilise actin filaments. Cofilin specifically binds along ADP-actin filaments, and applies a strain that leads to filament depolymerisation (Alberts et al., 2008).

No specific severing or stabilising proteins have been identified for intermediate filaments, but regulation of filament stability by phosphorylation or post-translational modifications has been described for vimentin and keratin (Etienne-Manneville, 2018).

HIGHER-ORDER STRUCTURES of the cytoskeleton, like meshes or spindles, are formed through the interaction of crosslinkers with cytoskeletal filaments. The growth of microtubules from a single centrosome offers a primary structure to this network, but additional structures can be created through bundling of filaments by Microtubule-Associated Proteins (MAPs), creating ensembles of microtubules of various densities. Microtubules can also be tethered or captured at specific sites of the plasma membrane by plus end tracking proteins (plus TIPs) (Figure 1.11). Actin filaments have a wide variety of crosslinkers generating different structures: contractile bundles with antiparallel filaments, tight parallel bundles, or gel-like networks. Contractile bundles are typically formed by α -actinin that allows the insertion of myosin II to generate contractility, while tight parallel bundles are formed mostly by fimbrin and are too tight for myosin II to be inserted. Actin gels can be generated by spectrin or filamin in the actin cortex, the latter being enriched in lamellipodial structures. Finally, the actin cortex is tethered to the plasma membrane by ERM proteins (ezrin, radixin, moesin) that are activated through phosphorylation or PIP₂ binding (Figure 1.10). The regulation of actin cortex tethering to the membrane is crucial for cell polarity and endo/exocytic capacities of the cell (Marion et al., 2011; Nomachi et al., 2013; Alberts et al., 2008). Intermediate filaments also present higher-order structures, associating into bundles through spontaneous lateral association or crosslinkers. The most widely known crosslinker of intermediate filaments is plectin, that does not only bundle intermediate filaments but can also link them to the rest of the cytoskeleton to the plasma membrane.

1.3.1.3 Molecular motors

In addition to accessory proteins that regulate filament growth and network structure, a specific type of filament-binding proteins brings movement to the cytoskeleton: molecular motors. Molecular motors have one or several heads that interact with polarized filaments (actin filaments or microtubules) and move along the filament through subsequent steps of ATP-hydrolysis-dependent binding and unbinding of the head. Various types of molecular motors exist, differing in ability to transport a cargo, processivity, speed, and minus or plus directionality.

Myosins are the only family of molecular motors binding to actin filaments. Most myosins travel to the barbed end (except myosin VI that moves toward the pointed

end), but all have different roles and properties. For example, myosin V has two heads and participates in vesicle transport, while myosin I has a single head and is poorly processive, but binds the plasma membrane or actin filaments with its tail and participates in intracellular organisation (O'Connell, Tyska, and Mooseker, 2007). The most widely known myosin is myosin II, that is able to form filaments and bind to antiparallel actin filaments to generate contractility. Myosin II also acts as an actin network regulator, as it can promote the formation of stress fibers, actin bundles or asters (Lehtimäki et al., 2021; Köster et al., 2016), or selectively collapse pools of linear actin by pulling when over-activated, while preserving branched actin networks (Reymann et al., 2012).

Microtubules are experts in intracellular transport and have many processive molecular motors separated in two distinct families: dyneins and kinesins. Kinesins are targeted to the plus end and have a binding site for other organelles or microtubules. Dyneins are much faster than kinesins and transport various cargoes and vesicles to the minus end. Microtubule-dependent molecular motors are notably implicated in the maintenance of the Golgi apparatus structure (maintained at the centrosome by dyneins) and the Endoplasmic Reticulum structure (prevented from collapse by kinesins) (Burkhardt, 1998; Woźniak et al., 2009).

Molecular motor activities are regulated by different factors, including phosphorylation, but differently depending on the motor. Indeed, while phosphorylation inactivates kinesins, phosphorylation of the Myosin Light Chain (MLC) induces an increase in myosin II contractility.

1.3.1.4 Interactions between cytoskeletal networks

Although they form separate networks, actin filaments, microtubules and intermediate filaments collaborate to increase the versatility of the cytoskeleton, and numerous interactions and co-regulations exist in addition to the external accessory proteins described above. The most striking illustration of this cooperation is the fact that no molecular motor is yet known for intermediate filaments, which rely on microtubules and actin filaments for transport of both fully formed filaments and small particles for filament assembly (Hohmann and Dehghani, 2019).

Cytoskeletal filaments interact in many different ways, directly or indirectly, promoting or impeding filament formation, influencing structures, and displacing each other (Figure 1.12) (Hohmann and Dehghani, 2019; Dogterom and Koenderink, 2019).

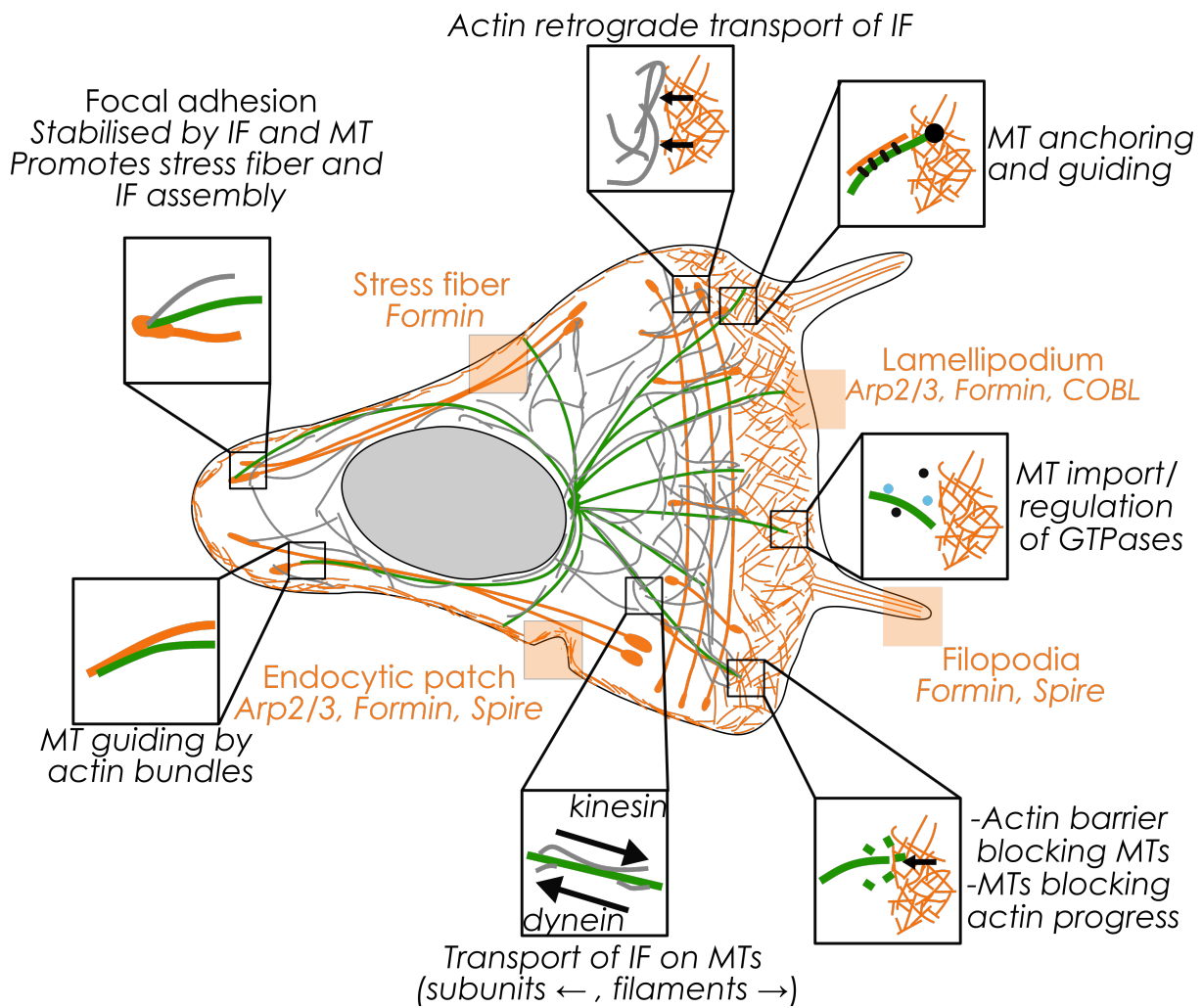


FIGURE 1.12: **Interactions between cytoskeletal networks.** Orange: actin. Green: Microtubules. Grey: Intermediate filaments (Vimentin here).

Intuitively, one can picture steric interactions between networks inducing stabilising, guiding or blocking effects.

Guiding of filament has been described mainly for microtubules. Microtubule growth can be guided along actin bundles through plus TIP proteins at the plus end of microtubules. The most widely known proteins regulating this interaction are CLIP170, that binds microtubules and their plus end, and IQGAP1, that interacts with actin filaments and CLIP170 but also with RhoGTPases like Cdc42 and Rac1 (Fukata et al., 2002; Dogterom and Koenderink, 2019). Growing microtubules can also be guided by vimentin templates (Hohmann and Dehghani, 2019), as described in migrating cells where vimentin orients microtubules to ensure the directionality and persistence of migration (Gan et al., 2016).

The spatial organisation of the cytoskeleton is also influenced by interactions between the different networks, for example by inducing **filament disassembly**. Indeed, actin networks such as the actin cortex or lamellipodial actin are very dense and contractile, and can induce an increase in the rate of catastrophes in microtubules (Colin et al., 2018). This limits the ability of microtubules to penetrate some areas, to prevent interaction with certain membrane-bound proteins for example, but also limits the microtubule-mediated transport of intermediate filaments to these regions. Interestingly dynamic microtubules can in turn negatively regulate actin flows (Hui and Upadhyaya, 2017).

Conversely, some structures or intermediates can **stabilise or anchor** cytoskeletal networks. A loose, unbranched actin network or anchoring to cortical actin through plus TIP proteins like Ezrin/Radixin/Moesin can increase microtubule stability instead of inducing catastrophes (Solinet et al., 2013; Dogterom and Koenderink, 2019; Colin et al., 2018). Focal adhesions are rich in interactions between cytoskeletal networks, and locally promote actin stress fiber formation and intermediate filament assembly. Intermediate filaments in turn promote the stability of focal adhesions, while microtubules interact with focal adhesions to promote their turnover (Dogterom and Koenderink, 2019).

In addition to stabilising each other, the different cytoskeletal networks can promote **filament nucleation**. As described earlier, some plus TIP proteins can interact with actin, and in particular with the formin mDia1. This not only results in a stabilising actin-microtubule interaction, but also in the promotion of actin filament nucleation at the plus end of microtubules (Henty-Ridilla et al., 2016). Conversely, actin has recently been shown to interact strongly with the centrosome, with actin-like proteins identified at the γ TurC complex (Liu et al., 2020), and even actin-like filaments inside the lumen

of microtubules (Paul et al., 2020). Moreover, the centrosome is an actin-nucleating center surrounded by a pool of branched actin (Farina et al., 2016) that regulates microtubule growth by physically limiting the chances of growing microtubules to exit this area (Inoue et al., 2019).

Finally, the morphology of the different cytoskeletal networks can be linked through their **shared regulators**. Indeed, various cross-talks exist between cytoskeletal filaments and GTPases (mainly Rap, Rho, Rac, Cdc42). GTPases can be activated or inhibited by specific GEFs (Guanine exchange factors) and GAPs (GTPase activating proteins), respectively. Their main regulatory activity is the control of actin nucleation and actomyosin contractility (RhoA induces increased formin and myosin II activity, Rac1 and Cdc42 induce formin and Arp2/3 activity, Rap results in cofilin-mediated actin severing) (Figure 1.13). Small Rho-GTPases also impact microtubules through the regulation of microtubule-binding proteins, molecular motor activity and actin nucleators (Peglion and Goehring, 2019; Wojnacki et al., 2014). Cdc42 is implicated in the reorientation of the centrosome in numerous systems including the B cell immune synapse, and RhoA-mediated activation of mDia1 at the T cell immune synapse has been shown to promote centrosome polarisation through anchoring and stabilisation of microtubules at the cortex (Gomez et al., 2007; Andrés-Delgado et al., 2012). Interestingly, microtubules and vimentin are in turn able to regulate Rho-GTPases activity through the modulation of certain GEFs (Chang et al., 2008; Heck et al., 2012; Jiu et al., 2017). In particular, GEF-H1 is a RhoA-specific GEF whose activity is inhibited when bound to microtubules, and decreased by microtubule-associated vimentin (Jiu et al., 2017). The release and activation of GEF-H1, upon microtubule disassembly for example, leads to RhoA activation, increased actomyosin contractility and actin fiber formation. In the presence of PAK4, GEF-H1 can also activate Rac1, promoting lamellipodium formation (Siegrist and Doe, 2007; Chang et al., 2008). This regulation of contractility by microtubules and vimentin could explain the increase in vimentin expression during epithelial to mesenchymal transition, as a decrease in stress fiber and adhesion is needed to initiate an efficient migration.

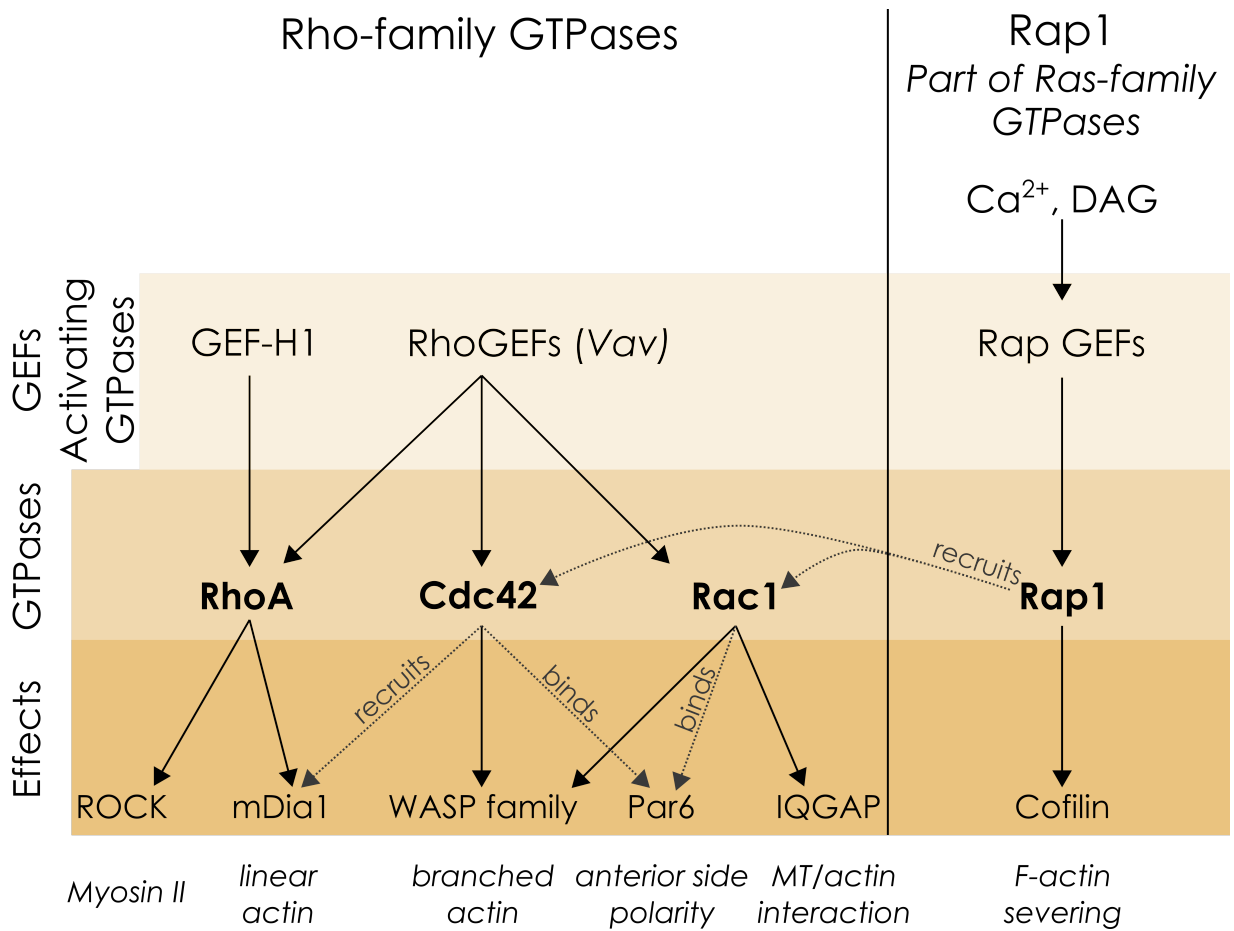


FIGURE 1.13: **Effectors of GTPases.**

1.3.2 Cell polarity

A polarised cell is characterised by the non-symmetrical organisation of its organelles and cytoskeletal networks along an axis, usually defined by the centrosome-nucleus axis. Polarity is a widely observed feature in healthy cells and allows to organise organelles and cytoskeletal networks for specific functions, like the apico-basal polarisation of epithelial cells or the front-back polarisation of migrating cells. Loss of polarity often corresponds to a loss of function, and is one of the characteristics associated with the development of cancers (Wodarz and Näthke, 2007).

Polarity takes very different forms and can be induced by a variety of stimuli. It is most of the time regulated by the widely conserved PAR (Partitioning defective) polarity complex. Other polarity complexes exist but are more context-specific, with the Crumb complex regulating apical polarity in drosophila, or the Scribble complex regulating basolateral polarity (Peglion and Goehring, 2019). In this part, I will only focus on the PAR polarity complex and its interaction with small GTPases.

The PAR polarity complex was discovered in the late 1980s while studying *C.Elegans* embryos with a defect in asymmetric division (Kemphues et al., 1988). This complex can be separated into two groups associated to the anterior (Par3, Par6, atypical PKC - aPKC) or the posterior (Par1, Par2) side. The activity of the PAR pathway is regulated by the small GTPase Cdc42, and can be opposed by posterior-side proteins or by the Scribble pathway for example (Peglion and Goehring, 2019). The local activation of Cdc42 either arises specifically from signaling and activation of Cdc42-targeted GEFs (Vav, or other Rho-GEF), results from the import of activating proteins like IQGAP1 (Siegrist and Doe, 2007), or occurs in a spontaneous manner as in the case of random migration, which implies the existence of a positive feedback loop following a small accumulation of activated Cdc42 (Woods and Lew, 2019).

How is the initial accumulation generated, and how is it maintained ? Several mechanisms exist to generate polarisation, allowing its establishment and maintenance in very different contexts.

1. **Active, directed transport by actin and microtubules.** Polarity proteins and small GTPases are able to alter the state of molecular motors and control their activity. Polarity proteins can use this directly to be targeted to the right sites and enhance or maintain their patterning. This mechanism has been described for Par3, that selectively uses dynein to be transported to cell junctions during collective fibroblast migration (Schmoranzler et al., 2009). More generally, small GTPases and polarity proteins (Cdc42/aPKC) modulate the relative activity of dyneins and kinesins in migrating cells to promote forward transport of material to the leading edge (Leduc and

Etienne-Manneville, 2017). Independently of cues, the presence of microtubules and their stability can also generate polarity by local delivery of IQGAP1 (activates and stabilises Rac1/Cdc42) or GEF-H1 (RhoA activation) (Siegrist and Doe, 2007).

2. **Bulk flows** of actin, often generated by difference in contractility or actin polymerisation, also create gradients of molecules. This phenomenon has been described in the lamellipodium of migrating cells (Illukkumbura, Bland, and Goehring, 2019).

3. **Local retention** of polarity proteins. Differences in membrane binding (through activation by GEFs for example) or in diffusion coefficient (by formation of complexes or binding to mRNA) can drive the polarised accumulation of proteins by trapping proteins locally, and inducing a flow of free proteins to equilibrate the cytosolic concentration (Peglion and Goehring, 2019).

The patterning of polarity proteins induces, and is reinforced by, a polarisation of the cytoskeleton via interactions between polarity proteins and small GTPases (Figure 1.14) (Iden and Collard, 2008). The differential activation of Rho-GTPases at the back and at the front results in very different cytoskeletal structures, classically starting with a rearrangement of the actin cytoskeleton network, followed by the polarisation of microtubules.

At the front, Cdc42 and Rac, that is recruited by Cdc42 via the PAR proteins, are associated to increased actin polymerisation. Indeed, Cdc42 activates WASP and recruits mDia1 and, together with Rac, induces the formation of lamellipodial and filopodial structures (Etienne-Manneville, 2004).

Microtubules are affected by both this dense actin network and the activity of Cdc42 and its effectors, resulting in one of the hallmarks of polarisation: the formation of a nucleus-centrosome polarity axis. This polarisation event is widely conserved, but different pathways have been described depending on cell types. In astrocytes, the centrosome is displaced in a Par6- and PKC ζ -dependent manner, while in fibroblasts the centrosome is immobilised by Cdc42, dynein and dynactin, and the polarity axis is generated by the rearward transport of the nucleus (Wojnacki et al., 2014).

Many pathways have been described in immune synapses, depending on the cell type (T cell immune synapse, B cell immune synapse, NK and CD8⁺ T cell cytotoxic synapse), and many are certainly coexisting. At the CD8⁺T lymphocyte immune synapse, the recruitment of Cdc42 and Rac induces the inhibition of stathmin, increasing the growth and stability of microtubules to allow the recruitment of the centrosome (Filbert et al., 2012). In B lymphocytes, the polarisation of the centrosome relies on the accumulation of Par3, the remodeling of actin at the immune synapse by Rap1, Cdc42 and its effectors, as well as microtubule-actin interactions mediated by IQGAP1 (Wang

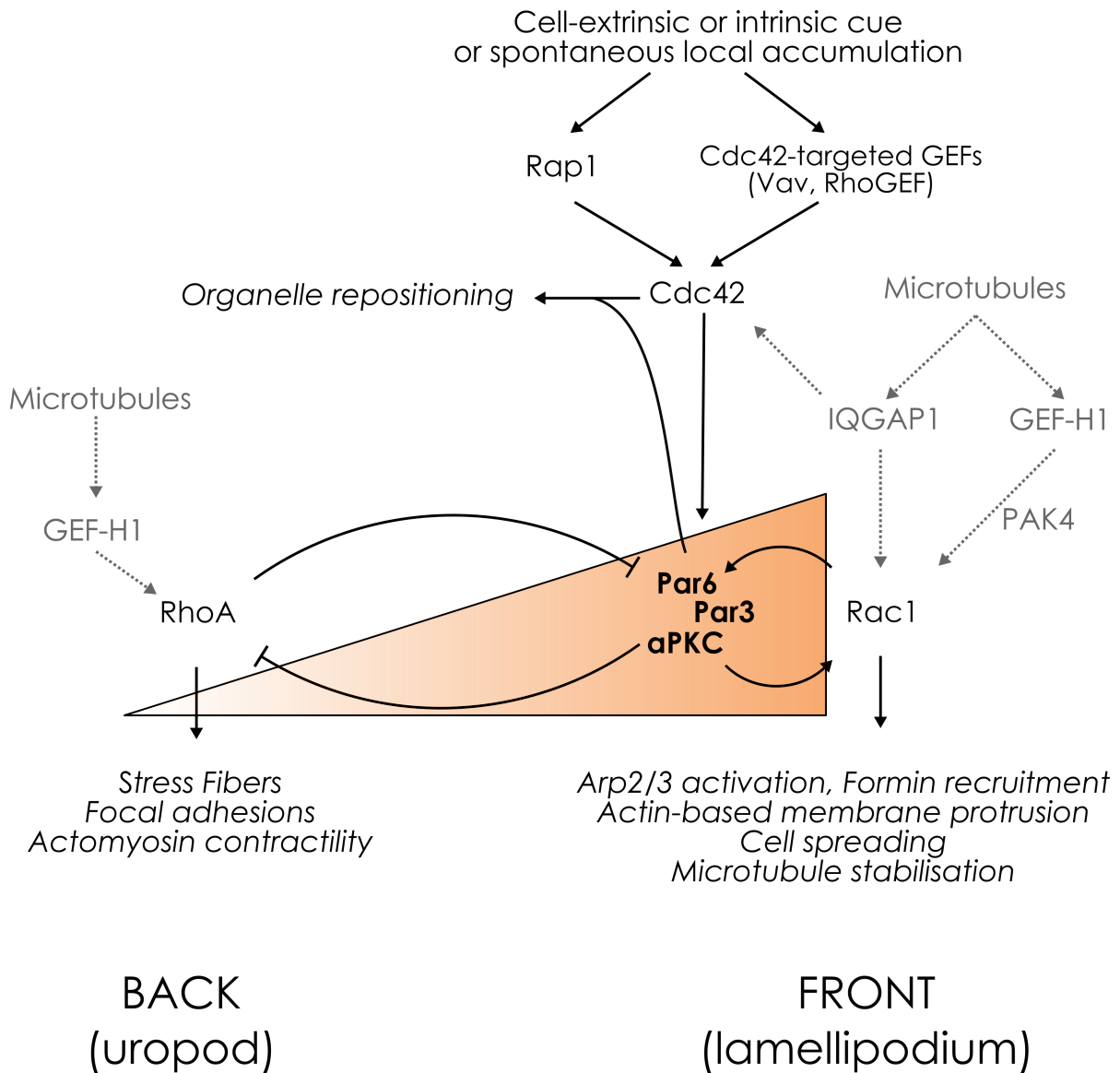


FIGURE 1.14: **Cell polarity: main interactions between PAR proteins and small GTPases.** Bold: PAR polarity proteins Par3, Par6 and atypical PKC, accumulated at the front. Normal: small GTPases. Grey: additional microtubule-mediated regulation. Italic: effects.

et al., 2017; Reversat et al., 2015; Yuseff et al., 2011).

The polarisation of intermediate filaments is thought to be mainly indirect and caused by the remodeling of the actin and microtubule cytoskeleton. Typically, vimentin is recruited to the front, as has been described both in the B cell immune synapse (Tsui et al., 2018) and in migrating cells (Dupin, Sakamoto, and Etienne-Manneville, 2011). In migrating cells, Cdc42 and aPKC inhibit dynein at the leading edge and allow the forward transport of perinuclear vimentin, where it remains excluded from the lamellipodia by actin-dependent retrograde transport (Leduc and Etienne-Manneville, 2017). Although the accumulation of vimentin at the leading edge is not necessary for lamellipodia formation, it promotes the persistence of large protrusions for steady migration (Thievensen et al., 2015).

1.3.3 Nucleus-cytoskeleton interactions

The establishment of polarity often corresponds to the generation of a centrosome-nucleus axis, and can imply the displacement of the nucleus towards a pole. Since the nucleus itself does not have any motors, its shape and positioning is instead controlled by nucleus-cytoskeleton interactions.

The nuclear membrane defines the border between the nucleus and the cytoplasm and is therefore a hotspot for their chemical and physical exchanges. Communication takes place through Nuclear Pore Complexes (NPCs) that allow the exchange of molecules (messenger RNA -mRNA, Transcription factors, proteins for the nucleus), and through the LINC complex (Linkers of the Nucleus and the Cytoskeleton) that allows a physical connection and the transmission of mechanical signals (Figure 1.15) (Jahed et al., 2016).

Nucleus-cytoskeleton interactions are not restricted to interactions between the surface of the nucleus and cytoplasmic filaments, but extend to the nucleoplasm with the presence of a nuclear cytoskeleton. Although I previously focused on cytoplasmic cytoskeletal filaments, actin, myosin and intermediate filaments are also present in the nucleus. Most importantly, a family of intermediate filaments called lamins are the main anchors of the LINC complex in the nucleus and form a network lining the inner nuclear membrane. Lamins are the most ancient form of intermediate filaments and can be separated in A-type Lamins (Lamin A and C) and B-type Lamins (Lamin B1 and B2) which form distinct networks (Leeuw, Gruenbaum, and Medalia, 2018). This layer of filaments ensures nuclear integrity, controls the mechanical properties of the nucleus and allows the tethering of heterochromatin to the nucleus periphery (Leeuw, Gruenbaum, and Medalia, 2018). The two families of lamins play different roles and are present in different proportions: Lamin A/C is associated with nuclear stiffness and adaptation to the mechanical environment, while Lamin B1 maintains nuclear integrity (Lammerding et al., 2006) and regulates transcription, RNA synthesis and signaling pathways (Dahl and Kalinowski, 2011; Uhler and Shivashankar, 2017). Interestingly, a down-regulation of Lamin B1 is necessary for somatic hypermutation of Germinal Center B cells, and has been correlated with B cell lymphoma aggressiveness (Klymenko et al., 2018) and chromatin decondensation (Camps et al., 2014).

The LINC complex extends from lamins under the inner nuclear membrane to cytoskeletal filaments in the cytoplasm. It consists of Sun proteins on the inner nuclear membrane and Nesprins on the outer nuclear membrane, that are bound via the KASH (Klarsicht, ANC1 and Syne Homology) domain of Nesprins in the nuclear envelope lumen. On the inner nuclear membrane, Sun proteins Sun1 and Sun2 (SUN: Sad1p/UNC (uncoordinated)-84) bind lamins, but also nuclear pore complexes or heterochromatin

(Leeuw, Gruenbaum, and Medalia, 2018). On the outer nuclear membrane, Nesprins extend in the cytoplasm to bind cytoskeletal filaments. Nesprin 1 and Nesprin 2 can bind F-actin, kinesin and dynein, while Nesprin 3 binds to plectin, that associates with intermediate filaments (Figure 1.15) (Kirby and Lammerding, 2018). Finally, Nesprin 4 is a kinesin-1 specific Nesprin found mainly in secretory epithelia, where its expression induces a separation of centrosome and Golgi apparatus from the nucleus (Figure 1.15) (Roux et al., 2009).

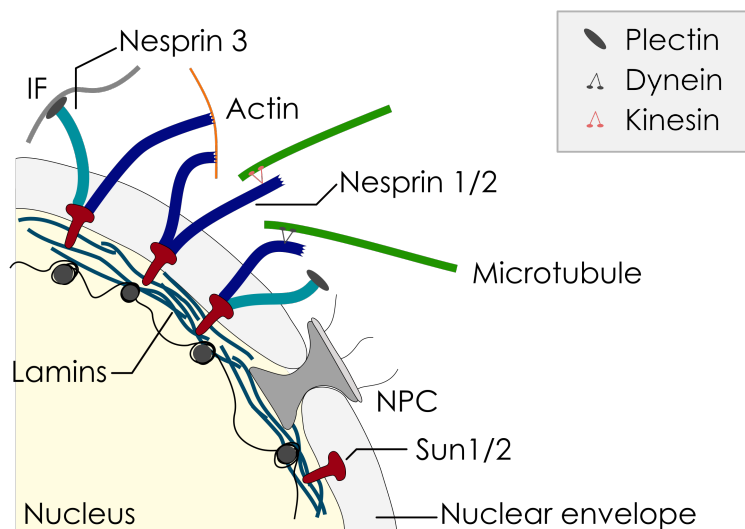


FIGURE 1.15: **Nucleus-cytoskeleton interactions: the LINC complex**

The nucleus and the cytoplasmic cytoskeleton are in constant interaction, ensuring mechanotransduction of external cues to the nucleus, nuclear positioning, controlling nuclear shape, and indirectly gene expression.

Nucleus positioning. In a non polarised cell, the nucleus is usually located at the center of the cell, tightly apposed to the centrosome through kinesin pulling (in *Dicystelium discoideum*, Tikhonenko et al., 2013), or through a centrosomal actin pool (in B lymphocytes, Obino et al., 2016). The physical separation of the centrosome and the nucleus is one of the events allowing the generation of a polarity axis. In that context, all three cytoskeletal networks have been implicated in nuclear movement in different cell types. While microtubules are responsible for nuclear movement in neuronal cells, actin controls nuclear re-positioning in fibroblasts (Fruleux and Hawkins, 2016) and at the T lymphocyte immune synapse (Fabrikant et al., 2013). Actin-dependent translocation of the nucleus can be achieved via Cdc42-triggered actin flows (Gomes, Jani, and Gundersen, 2005) or via actin-Nesprin2G-Sun2 cables (TAN lines) pulling on the nuclear envelope (Luxton et al., 2010). Vimentin can also be an actor of nuclear

movement, as shown in migrating astrocytes where actin-dependent vimentin polarisation is necessary to induce the rearward movement of the nucleus (Dupin, Sakamoto, and Etienne-Manneville, 2011). In some systems, nucleus polarisation involves rotation through dynein or actin flows (Fruleux and Hawkins, 2016; Kumar et al., 2014), sometimes in a LINC-dependent manner (Houben et al., 2009).

Nuclear Deformation. Deformation of the nucleus by cytoskeletal filaments has been described in many processes like polarisation, migration, or cell differentiation. Different amount of microtubules, actin or vimentin have even been shown to regulate the volume of the nucleus (Tariq et al., 2017; Keeling et al., 2017). The extent of filament-induced deformation depends not only on the density and organisation of filaments, but also on the stiffness of the nucleus set by the Lamin A/C content, the condensation state of chromatin and by chromatin anchoring to the nuclear lamina (Schreiner et al., 2015; Lammerding et al., 2006; Tariq et al., 2017). The balance between cytoskeletal filaments and nucleus stiffness is key to regulate nuclear shape and size, and ultimately gene expression and cell function.

Indeed, a recent study shows that microtubule-dependent deformation of the nucleus in hematopoietic stem cells regulate their differentiation into myeloid progenitors (Biedzinski et al., 2020). Nuclear deformation is also a regulator of gene expression in differentiated cells, as actin-dependent nuclear elongation has been described at the T cell immune synapse, and is necessary for the proper activation of the T lymphocyte and the expression of CD69 (Fabrikant et al., 2013; Gupta et al., 2012). Still, the impact of nuclear deformation and the pathways implicated remain very rarely elucidated.

1.4 The B cell immune synapse: a highly organised structure

Engagement of BCRs with cell surface-tethered antigens results in the formation of a very organised contact between the B cell and the antigen-bearing cell: the immune synapse. The immune synapse was initially described in T lymphocytes, but now serves as a general term for the structure formed between a lymphocyte and an antigen presenting cell. This structure serves as a platform for antigen affinity discrimination, receptor-mediated signaling and cell-cell communication through exocytosis and endocytosis events, and in the case of the B cell immune synapse, antigen extraction and internalisation (Monks et al., 1998).

The B cell immune synapse is the starting point of the adaptive immune response, making the regulation of immune synapse formation and function crucial to ensure appropriate B cell responses. Surprisingly, this key interaction is very short, with the B cell fully reorganising its cytoskeletal networks to form the immune synapse in \sim 5-10 minutes, and the interaction lasting around 20-30min. Two closely related events occur during this reorganisation: the formation of a concentric pattern in the plane of the synapse, and the polarisation of the B cell in the transversal plane.

1.4.1 Plane of the synapse: a concentric organisation

The structure of the B cell immune synapse has initially been described on antigen-coated glass substrates as a bulls-eye pattern, and while it has become clear that the organisation is not as stereotyped in the case of a cell-cell immune synapse, the original description of the concentric organisation of molecules remains a reference (Fleire, 2006).

On glass, the mature B cell immune synapse presents a concentric organisation of molecules: antigen-BCR complexes are gathered in an actin-poor central region, the central SupraMolecular Cluster (cSMAC), surrounded by a ring of actin and activated integrins (LFA-1, VLA-4) forming the peripheral SMAC (pSMAC). While integrin engagement is dispensable for B cell immune synapse formation, the engagement and recruitment of LFA-1 by ICAM-1 increases cell adhesion, signaling, and therefore lowers the threshold for antigen concentration and affinity (Carrasco et al., 2004). Large membrane proteins and potential negative regulators of BCR signaling (CD45 for example) are segregated even further, in the distal SMAC (dSMAC).

The formation of the B cell immune synapse is tightly linked with the crosstalk between BCR signaling and actin cytoskeleton remodeling. Indeed, at the resting state, BCRs are present at the surface of the B cell as single receptors or nanoclusters and maintained in a limited diffusion state by cortical actin and ERM proteins linking actin to the plasma membrane, preventing premature BCR clustering and activation (Treanor et al., 2010; Treanor et al., 2011). Defects in actin nucleation have been linked to abnormal B cell activation in diseases such as the Wiskott-Aldrich syndrome, and ERM upregulation has been linked to constitutive activation and proliferation in large B cell lymphoma (Li et al., 2019; Pore and Gupta, 2015). Overall, it appears that the dynamic regulation of actin, ERM and microtubules plays a crucial role in B cell function (Treanor et al., 2011).

Upon BCR engagement, transient dephosphorylation of ERM proteins and activation of cofilin by Rap induce local actin depolymerisation and increased BCR mobility (Freeman et al., 2011; Treanor et al., 2010). BCR nanoclusters merge into microclusters, recruit signaling molecules and increase signaling (Figure 1.16 **steps 1,2**) (Li et al., 2019; Sohn, Tolar, and Pierce, 2008).

The activation of Cdc42, Rac and Btk downstream of BCR signaling induces the activation of Arp^{2/3} (Freeman et al., 2011; Liu et al., 2011; Liu et al., 2013a; Le Roux et al., 2007; Sharma, Orłowski, and Song, 2009), leading to B cell spreading on the substrate with lamellipodial-like structures (Figure 1.6 **step 3**) (Bolger-Munro et al., 2019). Interestingly, the formation of these actin protrusions also requires Rap activation, which might be due to the ability of Rap to recruit Cdc42 and Rac or to the release of actin monomers during cofilin activation by Rap (Lin et al., 2008; Freeman et al., 2011; Arthur, Quilliam, and Cooper, 2004; Gérard et al., 2007). The extension of those protrusions allows the cell to scan a wide area, engage more BCRs and form more microclusters to sustain BCR signaling (Li et al., 2019). Microclusters are gradually transported towards the center to merge into clusters of growing size, which further increases signaling. The transport and merging of microclusters relies on branched actin, that traps and transports islets of BCRs in retracting protrusions, but also on dynein-mediated transport of BCR-antigen microclusters along microtubules (Figure 1.16 **step 4**) (Bolger-Munro et al., 2019; Schnyder et al., 2011; Liu et al., 2010).

Finally, the cell retracts its protrusions through differential regulation of Arp^{2/3} by Btk inhibition (Liu et al., 2011; Liu et al., 2013a), and forms a central cluster of BCRs, the cSMAC. Cell retraction and BCR concentration requires the inhibition of Btk, but also the activation of the actin-binding protein 1 (abp1) that has been shown to down-regulate BCR activation (Seeley-Fallen et al., 2014; Li et al., 2019; Rey-Suarez et al.,

2020). BCR signaling and BCR-antigen complex internalisation being mutually exclusive (Hou et al., 2006), this step also supports the internalisation of BCR-antigen complexes at the immune synapse (Onabajo et al., 2008). The extraction of antigen has recently been associated to actin patches found at the center of primary B cell immune synapse, and associated with clathrin and antigen patches (Figure 1.16 **step 5**) (Roper et al., 2019).

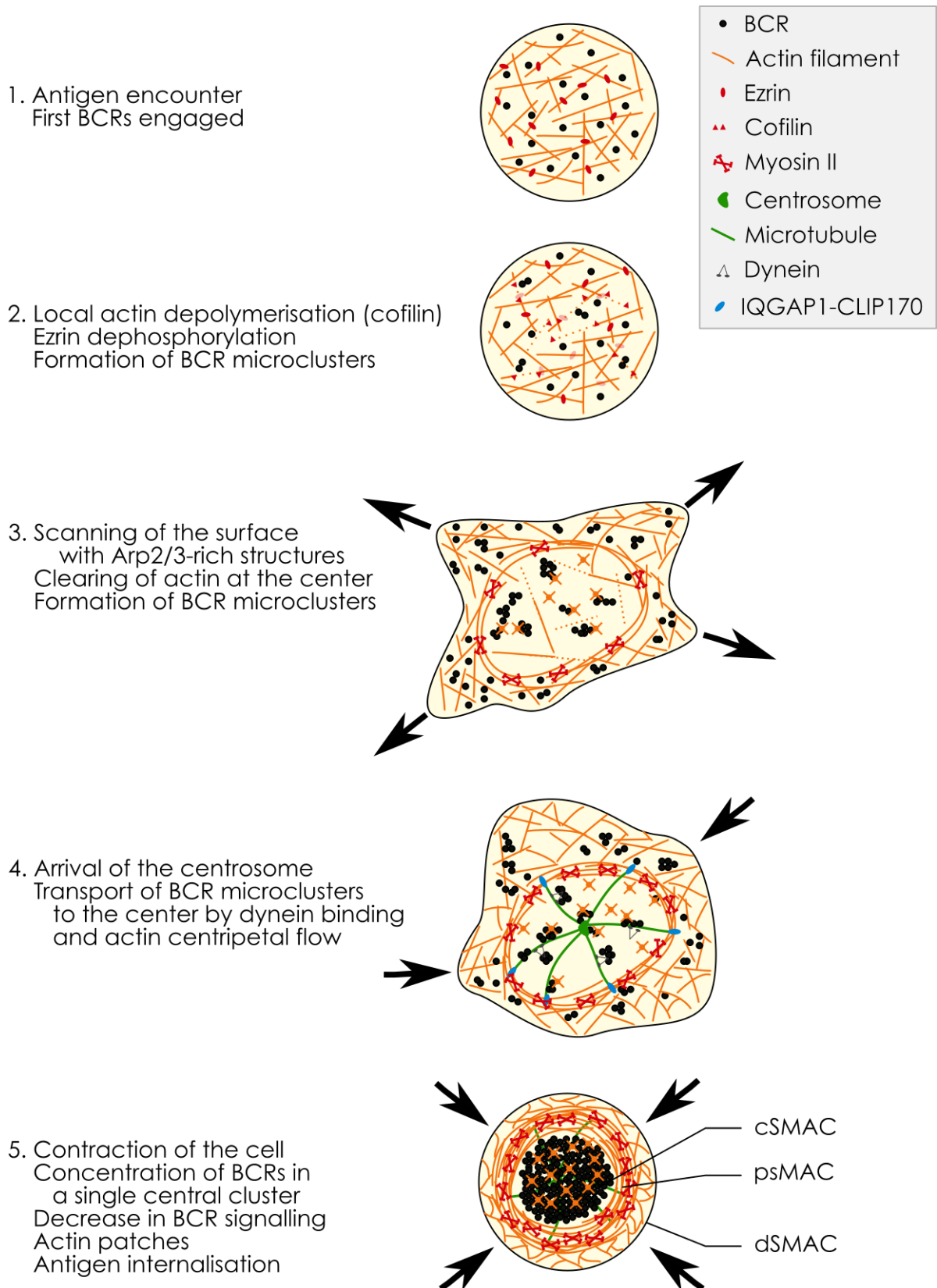


FIGURE 1.16: B cell immune synapse formation

The course of events at the B cell immune synapse is classically summarised in two drastic phases initially described on glass: spreading and contraction (Fleire, 2006). Since this first observation, many studies have tried to adapt the experimental system and approach physiological conditions by using primary B cells instead of cell lines, and by adapting substrate rigidity and ligand mobility. These studies have all highlighted that the structure of the synapse, the level of activation and the ability of B cells to extract the antigen strongly depends on the conditions of antigen presentation. Studies using mobile ligands show that these substrates induce less cell spreading, but fast and strong signaling associated to dense antigen clusters transported towards the center of the synapse (Ketchum et al., 2014).

The use of soft substrates or surrogate antigen presenting cells brings even more nuances to the classical spreading and contraction model. Indeed, B lymphocytes do not spread on the surface but rather scan the surface by extending and retracting lamellipodial structures. As a result, the typical bulls-eye pattern, with actomyosin arcs and an actin-dense periphery, is less defined (Bolger-Munro et al., 2019; Ketchum et al., 2014; Shaheen et al., 2017; Wan et al., 2013). The pathways involved in the stiffness-dependence of immune synapse formation and B cell activation are not clearly understood yet but seem to involve microtubules and, to a lesser extent, actin (Wan et al., 2013).

1.4.1.1 B cell antigen affinity discrimination and antigen extraction

Substrate and antigen-tethering properties impact not only the structure of the synapse, but also the pathway used by the B cell to extract antigen and its efficiency. Two mutually exclusive pathways exist for B lymphocytes to extract the antigen from the opposing surface: the mechanical pathway, that relies on mechanical pulling on the BCR-antigen link, or the proteolytic pathway, that relies on the release of proteases at the immune synapse to facilitate antigen extraction (Natkanski et al., 2013; Spillane and Tolar, 2016; Yuseff et al., 2011). Mechanical extraction has been observed mainly on soft substrates or for weakly tethered antigens. In the case of stiff substrates and strong antigen tethering, the mechanical pathway is inefficient, and only then will the proteolytic pathway go through (Spillane and Tolar, 2016).

Different environments and antigen extraction strategies can also impact the ability of B cells to test the affinity of its BCR for the antigen, and therefore its capacity to adapt the response accordingly. Indeed, the affinity of the BCR for the antigen modulates cell spreading, signaling and amount of calcium bursts, up to a certain saturation level (Batista and Neuberger, 1998; Liu et al., 2010). Different mechanisms have been

proposed to contribute to antigen affinity discrimination, the first being the activation-dependent spreading of the B cell, with high affinity antigen leading to more engaged BCRs, which in turn would induce more cell spreading and create a positive feedback loop (Fleire, 2006). More recently, results showing that a stronger BCR-antigen link leads to stronger pulling and activation suggested that mechanical pulling could also contribute to antigen affinity discrimination (Wan et al., 2015). Indeed, myosin II is very active during B cell activation, contraction and antigen extraction (Hoogeboom et al., 2018), and traction force microscopy experiments highlighted signaling- and antigen-dependent mechanical forces applied by B cells on the antigen-presenting substrate via myosin II and microcluster-microtubule binding (Wang et al., 2018). However, antigen affinity discrimination by mechanical pulling reportedly depends only slightly on myosin, and not at all on dynein (Wan et al., 2015), suggesting that the measured forces could simply correspond to the centripetal transport of BCR microclusters.

How B lymphocytes manage to discriminate antigen affinity efficiently *in vivo* is still difficult to understand, as it can be tethered on the surface of different types of cells, with variable mechanical and antigen-tethering properties. The nature of the antigen presenting cell would then impact affinity discrimination and antigen extraction by B cells. For example, soft substrates or weakly tethered antigen lead to fast and easy antigen extraction, but also to poor antigen affinity discrimination (Spillane and Tolar, 2016). Substrate topology could also play a role, as uneven surfaces generate actin patterns at the synapse, and in turn impact B cell signaling and calcium influx during B cell activation (Ketchum et al., 2018).

Given the diversity in cell mechanical, membrane and tethering properties and their impact on B cell activation, the modulation of antigen-presenting cell properties and lymph node structure during inflammation (Astarita et al., 2015; Bufi et al., 2015) could be a way to modulate the adaptive immune response *in vivo*.

Once internalised, the antigen is processed and antigenic peptides are loaded onto MHC II molecules for presentation to T lymphocytes. These last stages also rely on signaling-dependent actin remodeling and myosin II (Le Roux et al., 2007), putting the cytoskeleton at the heart of B cell activation.

1.4.2 Transversal plane: polarisation of the B lymphocyte

The engagement of BCRs not only induces the formation of the immune synapse but also results in a full reorganisation of the B lymphocyte with the polarisation of organelles, cytokines and cytoskeletal networks.

In the polarised state, F-actin, vimentin and microtubules are strongly enriched on the immune synapse side (Tsui et al., 2018), and the centrosome is positioned at the center of the contact area, surrounded by MHC II⁺ lysosomes (Reversat et al., 2015; Yuseff et al., 2011). This polarised reorganisation relies on the highly conserved PAR polarity complex proteins, and their related GTPases Cdc42 and Rac, activated downstream of BCR signaling (Figure 1.6) (Yuseff et al., 2011).

The activation of Cdc42 and the resulting polarisation are essential to allow efficient signaling, antigen extraction and ultimately presentation to Helper T cells (Yuseff et al., 2011; Yuseff and Lennon-Dumenil, 2015). Local activation of Cdc42 triggers the activation of aPKC- ζ and the recruitment of dynein by Par3, both necessary for the polarisation of the centrosome (Yuseff et al., 2013; Reversat et al., 2015). Interestingly, centrosome polarisation requires the remodelling of different pools of actin. The activity of cofilin and Rap1 at the B cell immune synapse is necessary for centrosome polarisation and docking, potentially due to the linking of microtubules to the peripheral actin ring through Rap1-dependent IQGAP1/CLIP170 that would pull on microtubule, or through dynein recruitment by IQGAP1 that would amplify dynein-mediated centrosome positioning (Wang et al., 2017). At the centrosome, degradation of the centrosomal pool of actin linking the centrosome to the nucleus at steady state is needed for centrosome polarisation and formation of the centrosome-nucleus polarity axis (Obino et al., 2016). Upon B cell activation, centrosomal actin is ubiquitinated and degraded by the proteasome (Ibañez-Vega et al., 2019), while a cortactin homolog (pHS1) is recruited to the immune synapse and contributes to depleting the centrosomal actin pool by recruiting actin monomers to induce local filament assembly (Obino et al., 2016). This suggests a balance between actin-dependent centrosome detachment from the nucleus and actin remodeling at the immune synapse, both necessary for proper cell polarisation.

Actin remodeling can also impact centrosome polarisation by directly affecting microtubules, as many co-regulations have been described in the previous section. Upon B cell activation, the down-regulation of centrosomal actin results in an increase in total cell tubulin (Inoue et al., 2019), and microtubule stabilisation (Sáez et al., 2019). In T lymphocytes, microtubule increased growth rate, resulting from the phosphorylation

of stathmin, as well as microtubule stabilisation are necessary for centrosome polarisation (Andrés-Delgado et al., 2012; Filbert et al., 2012). An actomyosin-microtubule collaborative mechanism has also been proposed in the T cell immune synapse, where myosin II is polarised at the back of the cell in a PKC- θ -dependent manner and pushes the centrosome towards the cell front, while dynein pulls from the front (Liu et al., 2013b). However, no such mechanism for centrosome polarisation has yet been shown in B lymphocytes.

Centrosome polarisation implies the reorientation of the whole microtubule network, and with it the polarisation of the main intracellular transportation media. Microtubules are responsible for organising and maintaining polarisation by anchoring and transporting organelles and cytokines (Ueda et al., 2015). Most strikingly, in the case of proteolytic extraction, lysosomes are transported along microtubules and cluster around the centrosome to fuse with the cell membrane and release proteases at the immune synapse (Spillane and Tolar, 2016; Yuseff et al., 2011). The secretion of lysosomes is then regulated by additional factors, like the relocalisation of Vamp7 from the Golgi apparatus to lysosomes (Obino et al., 2017) and the recruitment of the exocyst complex at the immune synapse in a microtubule stabilisation- and GEF-H1-dependent manner (Sáez et al., 2019). Actin patterning also plays an important role in the ability of the cell to perform exo- and endo-cytosis at the immune synapse, as actin clearing (recovery) at the center of the synapse has been shown to be an on (off) signal for the release of cytotoxic granules at the cytotoxic immune synapse (Ritter et al., 2017; Ritter et al., 2015).

While the individual roles of actin and microtubule organisation in B cell immune synapse functionality have been studied, their interplay during this process remains to be investigated. In Chapter 3, I will investigate the role of these networks and their reciprocal regulation in immune synapse formation and polarity.

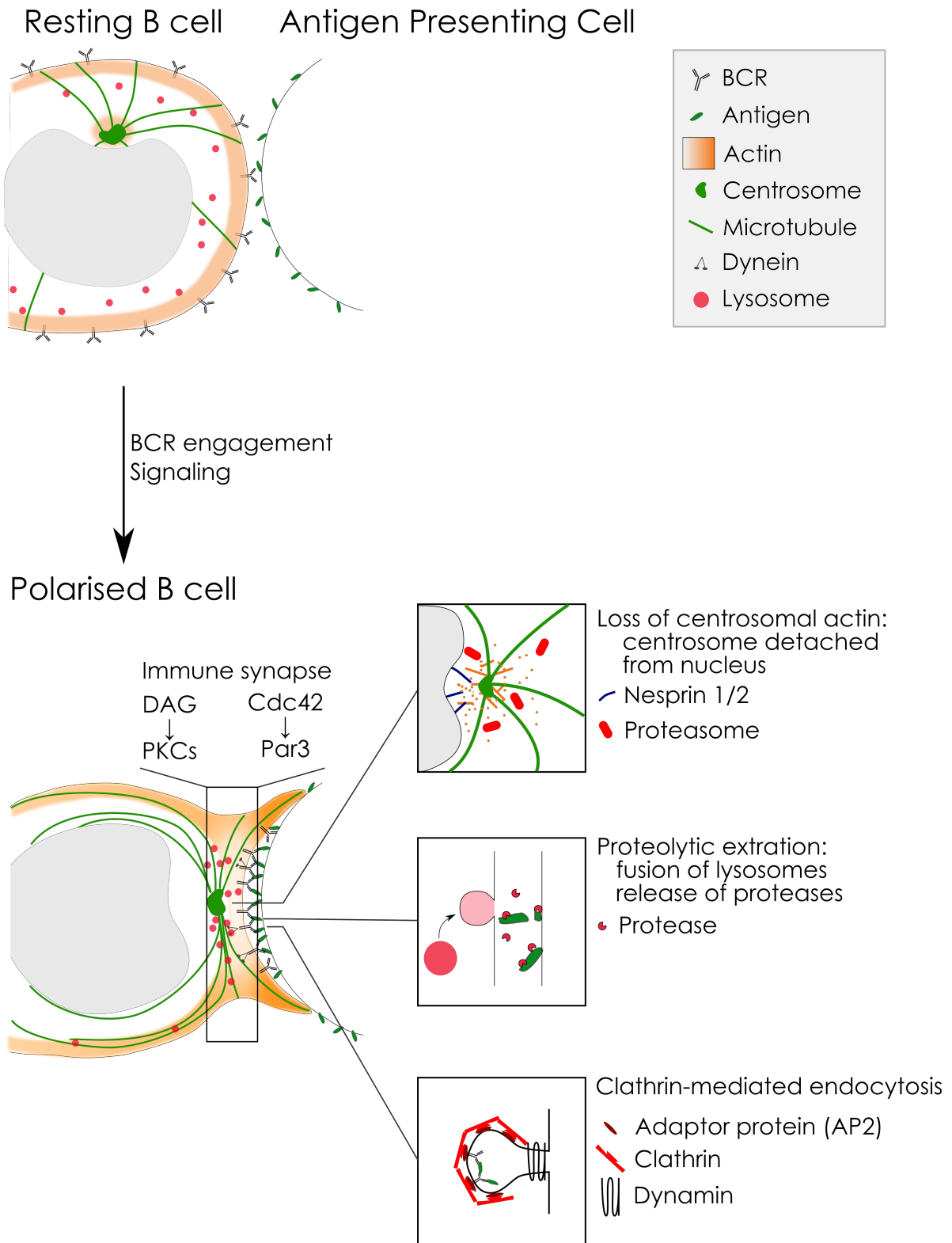


FIGURE 1.17: B cell polarisation at the immune synapse

1.5 Model systems of the immune synapse

1.5.1 Antigen presentation substrates

In the past decade, the observation that the properties of the antigen-presenting substrate can considerably impact synapse structure, activation, and pathways and efficiency of antigen extraction has stressed the need for new substrates recapitulating the properties of real antigen presenting cells. Researchers have now started exploring various types of substrates presenting different properties: planar or spherical, soft or stiff, with immobile or mobile ligand (Figure 1.18).

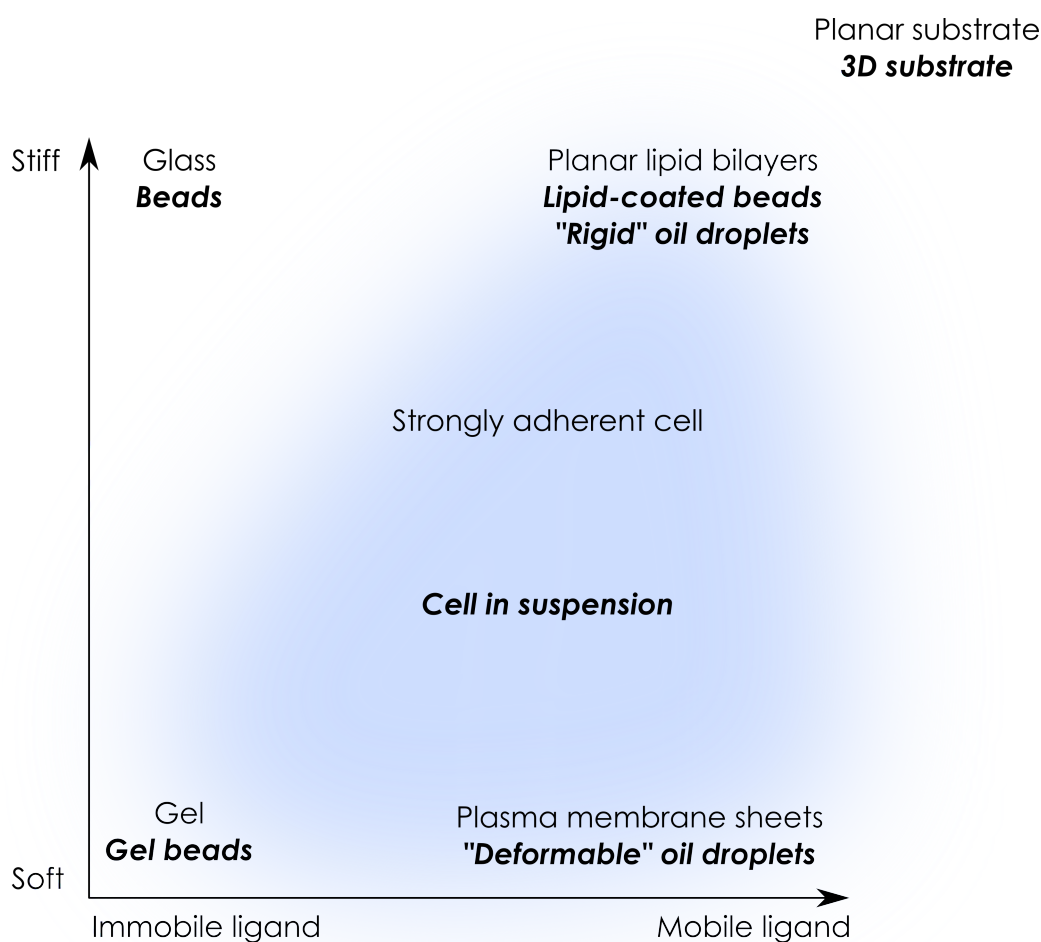


FIGURE 1.18: Model substrates for antigen presentation. Blue area: explored settings to approach physiological conditions.

To allow ligand mobility, and observe the striking pattern of antigen accumulation at the center of the immune synapse, antigens and adhesion molecules can be tethered to a lipid layer. In 2D, this is achieved by using either a fully synthetic lipid bilayer

(planar lipid bilayer) bound to glass, or fragments of plasma membrane of adherent cells (plasma membrane sheets). These two different approaches provide substrates with comparable ligand mobility, but different stiffnesses. Indeed, the space between the glass support and plasma membrane sheets is higher than for planar lipid bilayers, making plasma membrane sheets appear softer to cells seeded on top (Natkanski et al., 2013).

Non-planar substrates with mobile ligands can be obtained by using lipid-coated beads (Barral et al., 2008; Roman-Garcia et al., 2018) or oil droplets coated with phospholipids (Montel, Pinon, and Fattaccioli, 2019). Oil droplets present a real interest, as size, ligand mobility and surface tension can be tuned by changing settings on microfluidic production systems, phospholipid nature and density, surface and oil composition.

Solutions have also been explored to obtain substrates of lower rigidity, while keeping the ligand immobile. Rigidities ranging from hundreds of Pa (using polyacrylamide hydrogels) to tens of kPa (using PDMS) have been reached using different substrates and preparations (Teo et al., 2020; Bergert et al., 2016), allowing experimenters to obtain substrates with stiffnesses comparable to that of a macrophage (Bufi et al., 2015).

Finally, surrogate antigen presenting cells have been used to try to approach physiological conditions (Bolger-Munro et al., 2019). Still, the type of cell used, whether it is strongly adherent and spread, weakly adherent or in suspension changes its surface properties and can therefore impact the formation of the immune synapse.

1.5.2 Imaging the immune synapse

The view experimenters have of the immune synapse not only depends on what substrate is used, but also how it is looked at. Imaging provides many solutions to study proteins and organelles both in live and at fixed time points, but imaging under the right angle at the right time can prove challenging when one is looking at a fast event like immune synapse formation. Many technologies have been developed to study this type of cell-cell contacts under different angles (Figure 1.19).

The first strategies to image the immune synapse, in the plane of the synapse or

in the transversal plane to image polarisation, are straightforward. Imaging the formation of the bulls-eye structure on planar substrates can be achieved by letting the cells settle on the substrate, and imaging the evolution of the structure from the time of contact. This approach was compatible with substrates like glass, gels, planar lipid bilayers, plasma membrane sheets or even adherent surrogate antigen presenting cells that offer large flat membrane areas.

Simple approaches also exist to study the polarisation of B lymphocytes, by mixing B lymphocytes with beads or surrogate antigen presenting cells to create doublets, and seeding them on glass before imaging. However, this approach does not give access to the initial time of contact and is therefore not appropriate for fine dynamics. In addition, the formation and the angle of the doublet is not controlled and there can be many clumps of cells or out-of-plane synapses, difficult to image in a classical microscopy setting.

Technologies have been developed to allow the use of complex non planar substrates (non adherent surrogate antigen presenting cells, beads, droplets) while controlling the angle of imaging and the time of B lymphocyte-antigen encounter. The first big step forward to dynamically image immune synapse formation with these complex substrates was micro-manipulation using optical tweezers or micropipettes. With these tools, the experimenter can control the position of the B lymphocyte and/or the presenting object, and therefore control when and where they enter in contact. This allowed high resolution imaging of the NK cell cytotoxic synapse plane for example (Oddos et al., 2008), and the study of morphology and dynamics of the T cell immune synapse (Husson et al., 2011). While micro-manipulation is extremely precise, offers perfect doublet formation with full control of time and angle of contact for the experimenter, it is very time-consuming. Indeed, objects have to be captured using the tweezers or the micropipette and displaced until contact by the experimenter, one synapse at a time.

The recent advent of microfabrication and microfluidics led to new methods for high-throughput imaging of immune synapses. Indeed, microfluidics allow not only the production of substrates like droplets, but also the control of positioning of small objects. To image the plane of the immune synapse between two 3D objects, different systems of traps have been developed, all based on the successive trapping in a pit of the lymphocyte and the antigen presenting cell/droplet/beads (Vu et al., 2017). Objects are deposited or flown on an array of pits, with the number of objects by pits following a Poisson distribution. The creation of doublets is not as tightly controlled as in micro-manipulation, but this is compensated by multiplexing of this experiment

over an array of pits.

Microfluidic solutions have also been developed to image the polarisation of lymphocytes in real time, in a multiplexed manner. Again, several variants of arrays of microfluidic traps have been proposed, of different complexities. They all rely on the trapping of a first object, the antigen-presenting substrate for example, followed by the addition of the lymphocyte (Skelley et al., 2009). Increasing complexities of trap design and loading strategies can improve trapping and pairing efficiency, or even allow long-term culture and recovery of doublets (Dura et al., 2015; Dura et al., 2016).

Immune synapse imaging
Cell polarisation imaging

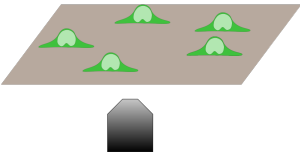

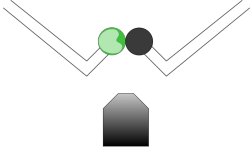
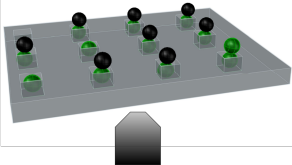
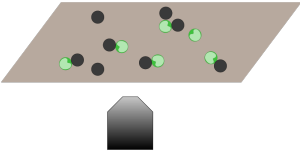
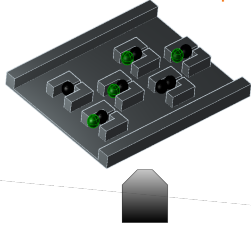
| "Tool-free" | Micromanipulation | Microfluidics |
|---|---|---|
| <p>Seeding cells Glass, gel, PLB, PMS, adherent surrogate APC</p>  <p>+: Easy, many cells, dynamic from t_0 -: Only planar substrates</p> | <p>Optical tweezers, Micropipettes Cells, beads, droplets</p>   | <p>Array of pits Cells, beads, droplets</p>  <p>+: Multiplexed, precise angle, use of 3D substrates -: variable pairing efficiency</p> |
| <p>Mixing cell-substrate Cells, beads, droplets</p>  <p>+: Easy, fast -: variable pairing, variable angle, not from t_0</p> | <p>+: Precise angle, perfect pairing, control of t_0, use of 3D substrates -: time-consuming, synapse by synapse</p> | <p>Array of traps Cells, beads, droplets</p>  <p>+: Multiplexed, precise angle, from t_0 -: variable pairing efficiency,</p> |

FIGURE 1.19: Systems to image B lymphocyte-antigen encounter

1.5.3 Measuring forces at the immune synapse

Cell-cell contacts are sites of tension where cells can apply forces to adhere or communicate. These forces are very important in the case of immune synapses, because they can be linked with cell activation, antigen affinity discrimination and antigen extraction in the case of B lymphocytes.

Many tools described above have been adapted to allow the measurement of forces applied by the B lymphocyte on the substrate, from the cell scale down to the single molecule scale (Figure 1.20).

At a global scale, normal forces applied by the cell on an antigen-presenting substrate can be measured using micropipette or biomembrane force probes. The cell is held by a micropipette and put in contact with an antigen-coated bead. The bead is attached either to a flexible micropipette (Sawicka et al., 2017) (a deformable red blood cell (Gourier et al., 2008)), and the deflection of the micropipette (the deformation of the red blood cell) is a measurement of the normal force applied by the cell on the bead. These methods give very precise measurements of the global normal forces, and allow imaging of cell morphology, calcium influx and polarisation, but cannot be linked to local forces or antigen extraction.

Traction force microscopy using deformable gels or micropillars allows the measurement of tangential forces applied by the cell in the plane of contact (Tan et al., 2003; Hui et al., 2015; Wang et al., 2018). These methods rely on the deformation of the substrate by the cell, measured by tracking either fluorescent beads embedded near the surface of the gel or the tips of micropillars. Traction Force Microscopy gives access to the spatial patterning of forces, which can be combined with imaging of cellular components in the synapse plane and allows studies on the correspondence between local forces and sub-cellular structures, like sites of internalisation. However, the difficulty of traction force microscopy lies in the manufacturing of substrates soft enough to be deformed by the cells, and with a density of markers that allows local force measurements in the cell, which is a challenge in the case of B lymphocytes.

Finally, some techniques allow to measure forces applied on a single molecule, in this case an antigen. Single molecule force spectroscopy approaches are based on the immobilisation of a ligand on a small bead, that is held by optical tweezers, magnetic tweezers or an AFM (Atomic Force Microscopy) cantilever (Neuman and Nagy, 2008; Natkanski et al., 2013). The ligand is put in contact with the cell, and the deflection of the cantilever or the movement of the bead is a measurement of the interaction forces, and can also give a measurement of the pulling force of the cell.

DNA-based tools have also been developed to investigate more precisely antigen extraction by B lymphocytes and the forces associated to this event. DNA force sensors consist in two strands of DNA or a DNA hairpin with sequences designed to separate at a given force, and are bound to a solid substrate on one side, and to the antigen on the other. Sensors are mainly based on FRET or quenching effects, and give a binary information: open or closed. Some DNA sensors have been designed to act as tension gauge tethers that break and become fluorescent above a certain force threshold, in the scale of tens of picoNewtons (Wang and Ha, 2013; Wan et al., 2015), but sensors have also been designed to distinguish mechanical from proteolytic extraction of antigen by B lymphocytes (Spillane and Tolar, 2016).

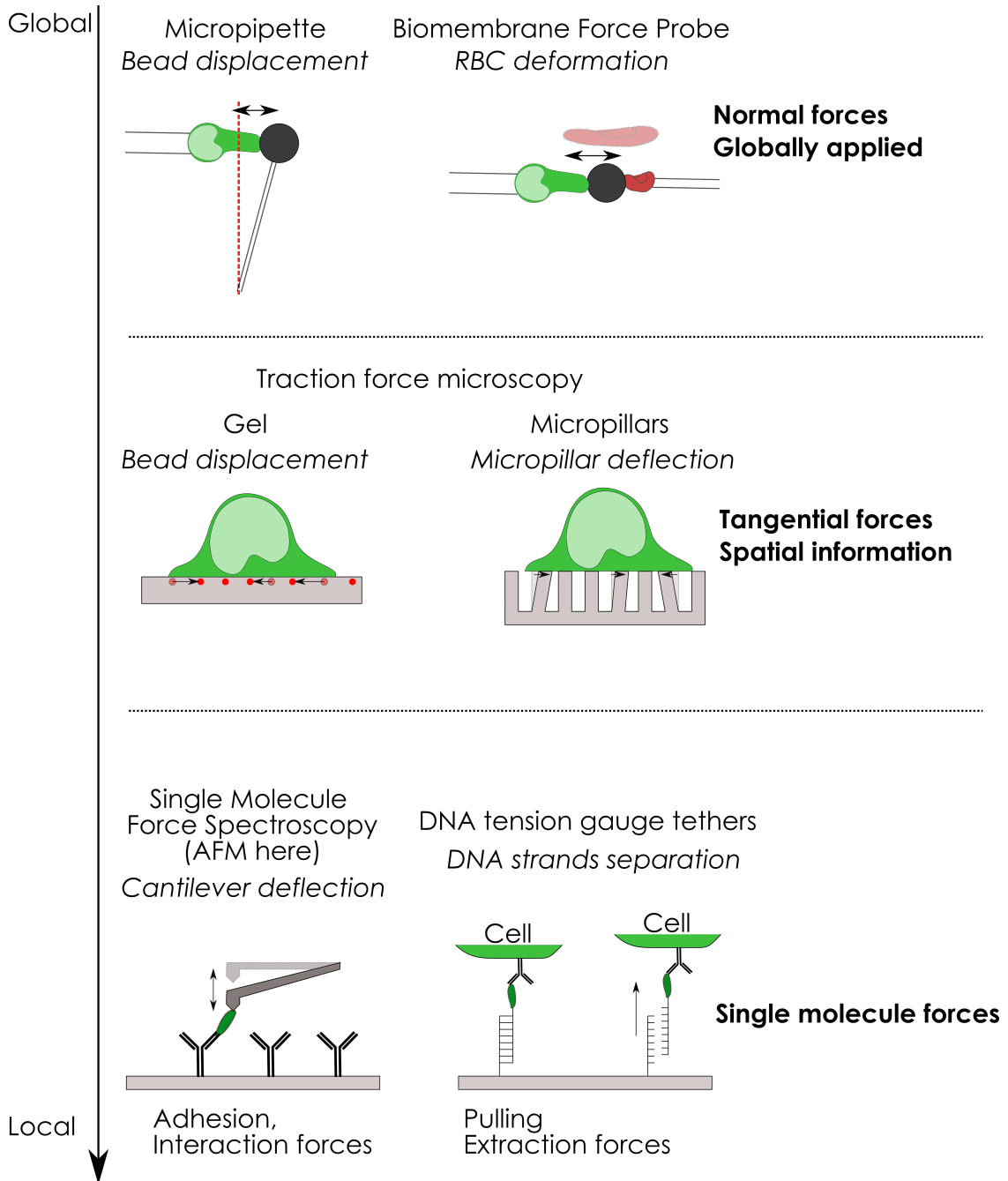


FIGURE 1.20: Measuring forces at the immune synapse. Tool, *readout*

1.6 Objectives and outline of the thesis

Despite the progresses made in the understanding of the link between structure and function at the B lymphocyte immune synapse, the current picture is often based on static descriptions of the final state. My PhD work attempts to fill this gap by looking at the spatiotemporal dynamics of cellular components and force generation downstream of BCR engagement, focusing in particular on the respective roles of the actin and microtubule networks.

This PhD thesis is organised as follows:

- In Chapter 1, I introduce B cell biology notions, as well as the existing tools to investigate the B cell immune synapse and polarity.
- In Chapter 2, I investigate the role of actomyosin structures in force generation and antigen extraction at the immune synapse.
- In Chapter 3, I study the coordination of different molecular and cellular events during immune synapse formation and cell polarisation, focusing on the roles of actin and microtubules.
- In Chapter 4, I discuss the results obtained in Chapter 2 and Chapter 3.
- In Chapter 5, I describe the materials and methods used in both Chapter 2 and Chapter 3.

The work performed during my PhD thesis led to the publication of two articles based on Chapter 2 (Kumari et al., 2019; Kumari et al., 2020), as well as three publications from scientific collaborations (Inoue et al., 2019; Merino-Cortés et al., 2020; Laplaud et al., 2021). These articles are attached in the Appendices.

Chapter 2

Actomyosin-driven force patterning controls endocytosis at the immune synapse

2.1 Introduction

The extraction and internalisation of antigen by B lymphocytes is a key step in the initiation of B cell activation, and therefore of the humoral adaptive immune response. As described in Chapter 1, the extraction of antigen from the antigen-bearing surface can be achieved through either proteolytic or mechanical pathways. In the case of mechanical extraction, two models had been proposed: (1) a global model based on the observation that B lymphocytes spread then contract on antigen-coated substrates, which could allow the transport of BCR-Antigen complexes towards the center of the immune synapse and their extraction and a (2) local model, based on Atomic Force Microscopy and DNA force sensors measurements showing that B cells could extract and internalise antigens by direct pulling on it through the BCR (Fleire, 2006; Natkaniski et al., 2013). In this study, we aimed at bridging these two scales by investigating the spatio-temporal distribution of forces exerted by B lymphocytes during antigen extraction at the immune synapse, and their regulation by the actomyosin cytoskeleton.

This chapter is a joined effort between a former PhD student from the lab, Anita Kumari, and myself. I will first summarize the main results obtained prior to my involvement, and then describe the results I obtained to complete this project.

The spatio-temporal distribution of forces applied by a B lymphocyte at the immune synapse was studied by using antigen-coated polyacrylamide (PAA) gels to perform Traction Force Microscopy (Figure 2.1A). In order to approach physiologically-relevant conditions for antigen presentation, the rigidity of the gel was set to 500Pa, the

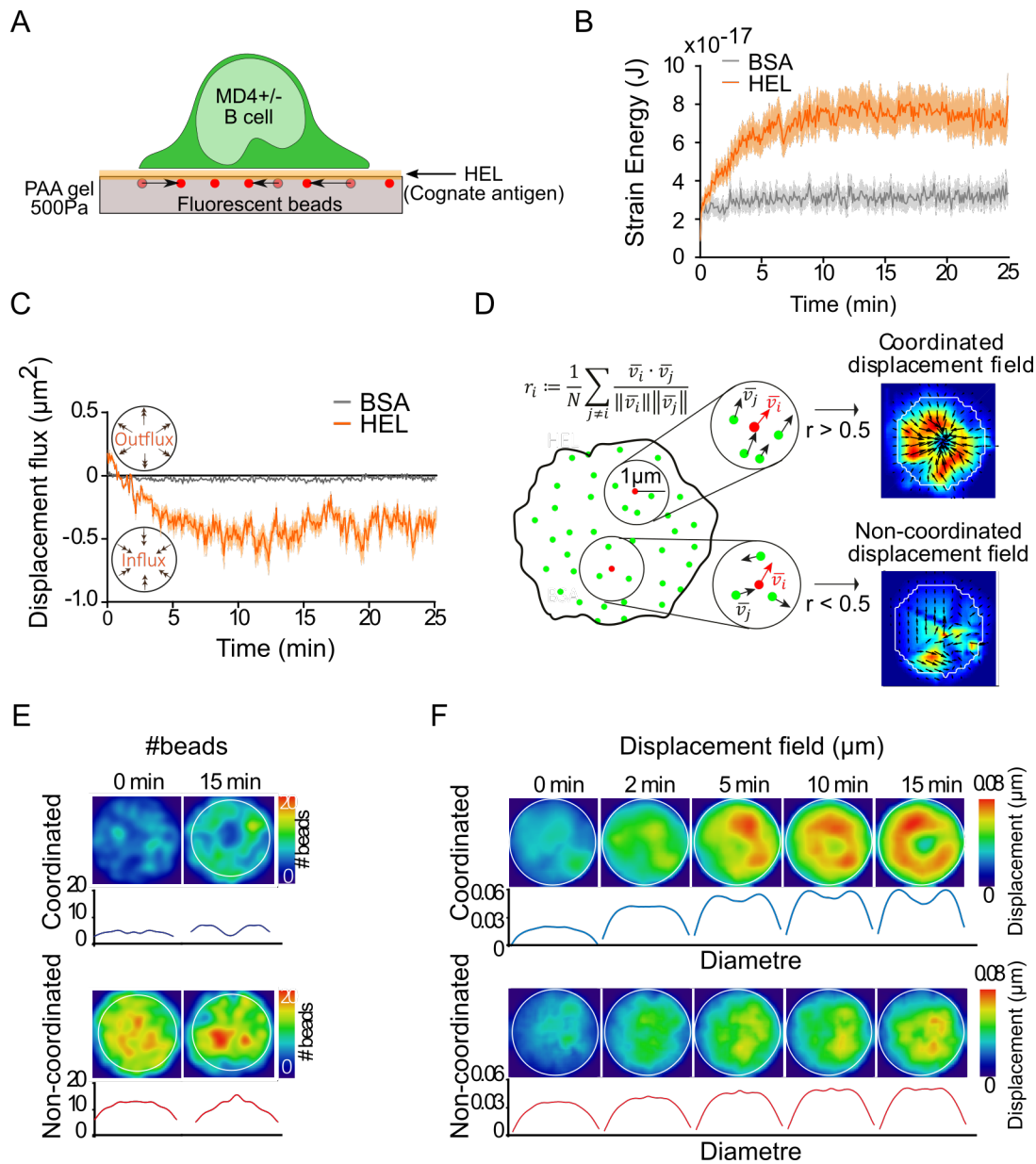


FIGURE 2.1: B lymphocytes generate antigen-specific forces at the immune synapse (A) Cartoon showing the principle of the experimental setup. Fluorescent beads serve as fiducial markers to measure the forces applied by the cell. (B) Average strain energy in time for HEL- or BSA-coated gels (Mean±SEM, 5 independent experiments, 5 mice, HEL N=65, BSA N=35). (C) Displacement flux reporting the direction of bead displacement over time for HEL- or BSA-coated gels (Mean±SEM, 5 independent experiments, 5 mice, HEL N=65, BSA N=35). (D) Schematic representation of the method used to distinguish beads exhibiting coordinated or non coordinated displacements. (E) Map of mean bead distribution in coordinated and non-coordinated pool (N=100 cells). Below: radial profile of the density map (obtained by resizing all cells and interpolating each bead with a Gaussian kernel) (F) Mean displacement field map (obtained by resizing all cells and averaging for a time point the individuals coordinated and non-coordinated displacement maps). Figure adapted from Kumari et al., 2019.

same order of magnitude as macrophages or dendritic cells (Bufi et al., 2015), which can present antigen to B cells in lymph nodes. Using primary naive B cells of MD4^{+/-} mice expressing a Hen Egg Lysozyme (HEL)-specific BCR and PAA gels coated with HEL, it was established that B cells apply antigen-specific forces on the substrate (Figure 2.1B), with a major component of centripetal forces as measured by the direction of movement of the beads with regards to the cell border (Figure 2.1C). Two different types of bead movement were observed when analysing trajectories: beads that moved in the same direction as neighbouring beads - designated as coordinated, and consistent with the measurement of tangential forces on the gel, and beads that did not move in the same direction as neighbouring beads - designated as non-coordinated, and that do not correspond to classical movements expected in the case of tangential forces (Figure 2.1D). Mapping of the density and displacement of beads from each population highlighted a spatial separation: coordinated movements, and therefore tangential centripetal forces, are localised at the periphery of the immune synapse, while non-coordinated movements are concentrated at the center of the immune synapse (Figure 2.1E,F).

The role of actomyosin in this system was first assessed by using conditional knockout mice lacking myosin IIA in B lymphocytes (Myosin II^{Flox/Flox} - CD21-Cre^{+/-}), as well as the myosin II inhibitor para-nitroBlebbistatin (70 μ M). This revealed that myosin II activity is essential for the generation of forces and the extraction of antigen from the gel (Figure 2.2A,B). In addition, inhibition of myosin II activity led to the loss of actin patches observed at the center of the cell (Figure 2.2C), and that resembled closely the pattern of extracted antigen (Figure 2.2D). This similarity, as well as the fact that patches of actin and antigen appear simultaneously (Figure 2.2E), suggests that actin patches could be hotspots for antigen extraction. This raised the question of the nature of these actin patches, and whether they could be 3D protrusive structures responsible for the non-coordinated bead movements at the center of the cell, as suggested by the presence of actin-rich protrusions in the gel in electron microscopy images (Figure 2.2F).

My work focused on defining the nature of these actin patches, and their dependence on antigen stimulation and myosin II contractility, as requested by the article referees. The published version of this work can be found in Appendix A.

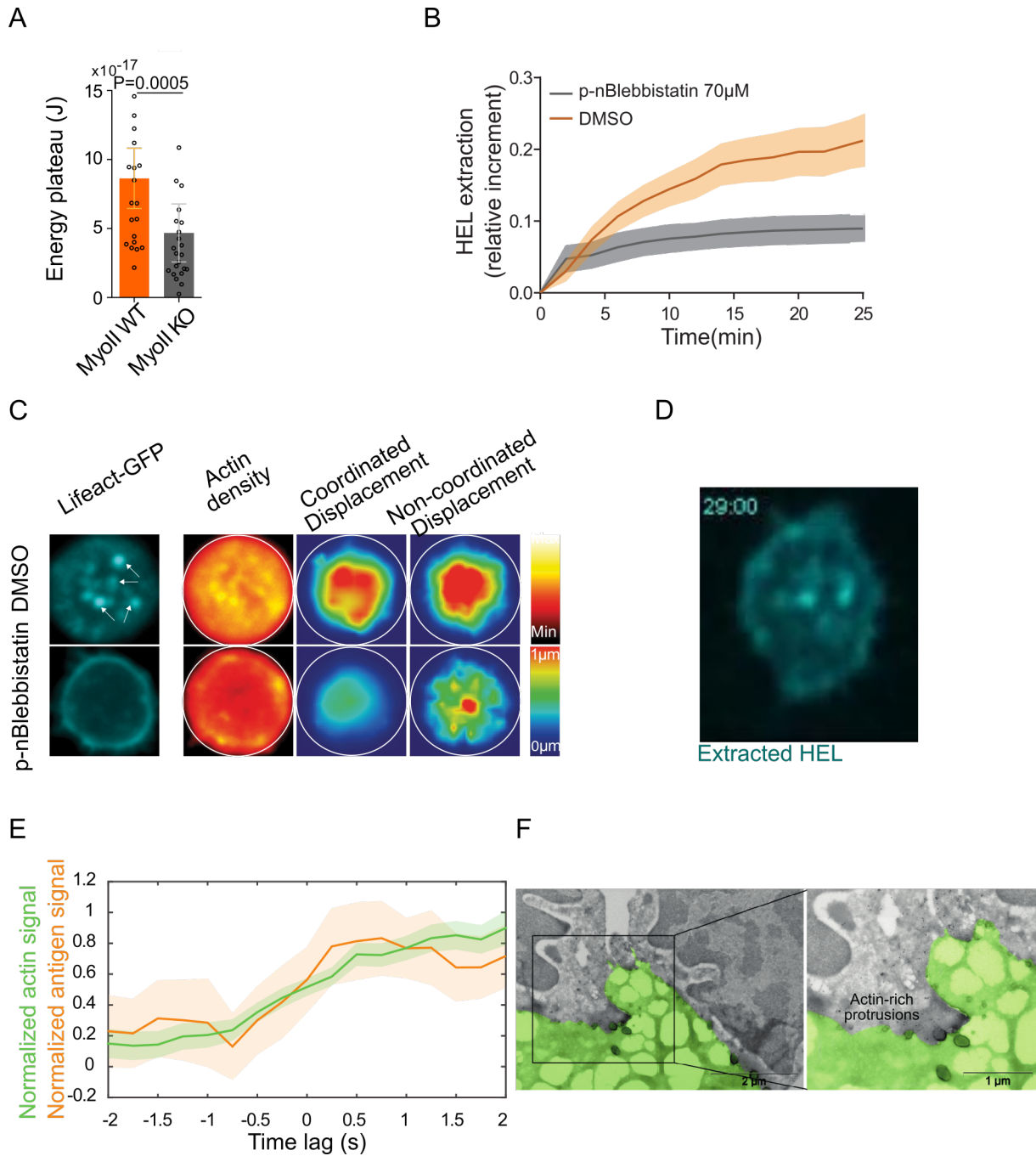


FIGURE 2.2: Myosin II is essential for force generation, actin patch formation and antigen extraction in B cells (A) Plateau of strain energy for Myosin II WT/WT and KO/KO cells (Median \pm IQR. WT/WT N=22, KO/KO N=23, 4 mice, 4 independent experiments). Statistical analysis: Mann-Whitney test. (B) Antigen extraction over time in control and p-nBlebbistatin treated cells (Mean \pm SEM, DMSO N=15, p-nBlebb N=9). (C) Left: single cell showing F-actin patches at the center of the cell, and no patches in a p-nBlebbistatin treated cell. Right: Maps of mean actin distribution and mean density of coordinated or non-coordinated displacements in DMSO or p-nBlebbistatin treated cells (N=12 cells). (D) Image of HEL extracted from the PAA gel at 29min after cell-antigen contact. Fluorescence of the fluorescently-labelled HEL is quenched by the gel, and only visible upon detachment. (E) Quantification of the signal of extracted antigen and actin over a $1\mu m \times 1\mu m$ square. Signals in both channels appear simultaneously (Mean \pm SEM, N=21, 6 cells). (F) Electron microscopy image showing actin (immunolabeling with gold beads) enriched in protrusions extending in the PAA gel (coloured in green). Scale bar 0.2 μm . Figure adapted from Kumari et al., 2019.

2.2 Results

2.2.1 Actin protrusions generate non-planar forces at the immune synapse

We investigated the nature of the non-coordinated movement of beads, focusing on their 3D movement to explore the hypothesis that these could be related to actin protrusions. The quantification of z displacements of beads (defined as the standard deviations of their z position over 60s) and the mapping of this value over a normalised cell revealed that beads located at the center of the cell ($2/3$ of cell diameter) displayed significantly higher z displacements than beads located at the periphery of the cell or outside the cell (Figure 2.3A,B). *This result strongly suggests that non-coordinated displacements are indeed linked with local 3D movement of the cell, namely actin protrusions or invaginations.*

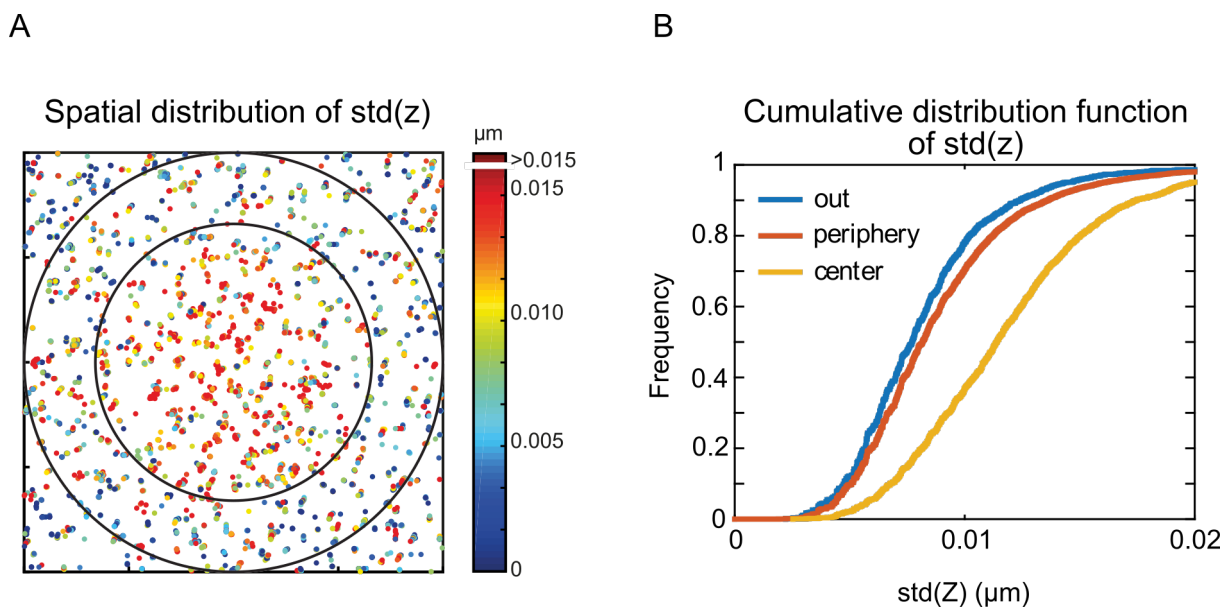


FIGURE 2.3: B lymphocytes exert forces orthogonal to the substrate at the center of the immune synapse. (A) Spatial distribution of bead displacement in the z direction: the standard deviation of the z position of each bead over 10 frames is colour-coded and projected on a normalized cell. the inner circle ($2/3$ of cell diameter) represents the center of the synapse (8422 points, superposition of 14 cells, one representative experiment). (B) Cumulative distribution of the $\text{std}(z)$ colour-coded in panel (A). The z displacement in the central area shows significantly higher displacements in z ($P < 0.0001$ for all comparison, Kolmogorov–Smirnov test). Figure adapted from Kumari et al., 2019.

2.2.2 Actin patches are antigen-dependent dynamic structures that resemble invadosome-like protrusions

The presence of actin patches at immunological synapses has been described in B cells and linked with BCR signaling (Roper et al., 2019; Kwak et al., 2018). We investigated the nature of the actin patches observed in our system by confirming their 3D nature through live imaging of LifeAct-GFP cells presented laterally with small pieces of gel (with Anita Kumari, Figure 2.4A), and evaluating their association with different proteins using immunofluorescence. The association of actin patches with antigen extraction prompted us to evaluate their colocalisation with clathrin. Clathrin associated only partially with actin patches (Figure 2.4B), suggesting that actin patches might be preferential sites for clathrin-mediated endocytosis, but not exclusively dedicated to this purpose. However, actin patches showed a strong and specific enrichment in phospho-Cortactin (Figure 2.4C), a hallmark of invadosome-like protrusions described in other cell types including T cells (Sage et al., 2012; Di Martino et al., 2016). Podosome hallmarks (vinculin, phospho-Paxillin) were not found to colocalise with actin patches (Figure 2.4D,E) (Carman, 2009; Linder, 2009).

In the case of T cells, invadosome-like protrusions (ILPs) have been shown to support antigen recognition, which in turn stabilized and promoted ILPs (Sage et al., 2012). We investigated the impact of antigen recognition on the actin patches of B lymphocytes by tracking actin patches on BSA- or HEL-coated PAA gels. We found that more patches were formed in the presence of antigen (Figure 2.5A,B). Moreover, these patches were concentrated at the center of the cell, as opposed to the patches scattered over the surface observed on BSA-coated gels (Figure 2.5C). We further found that patches had a significantly longer lifetime in the presence of antigen (Figure 2.5D).

Taken together, these results suggest that B lymphocytes form actin patches similar to invadosome-like protrusions to scan the opposing surface for antigen. In the presence of antigen, these protrusions are stabilised and form a denser array at the center of the cell, where they are preferential sites for antigen extraction and clathrin-mediated endocytosis.

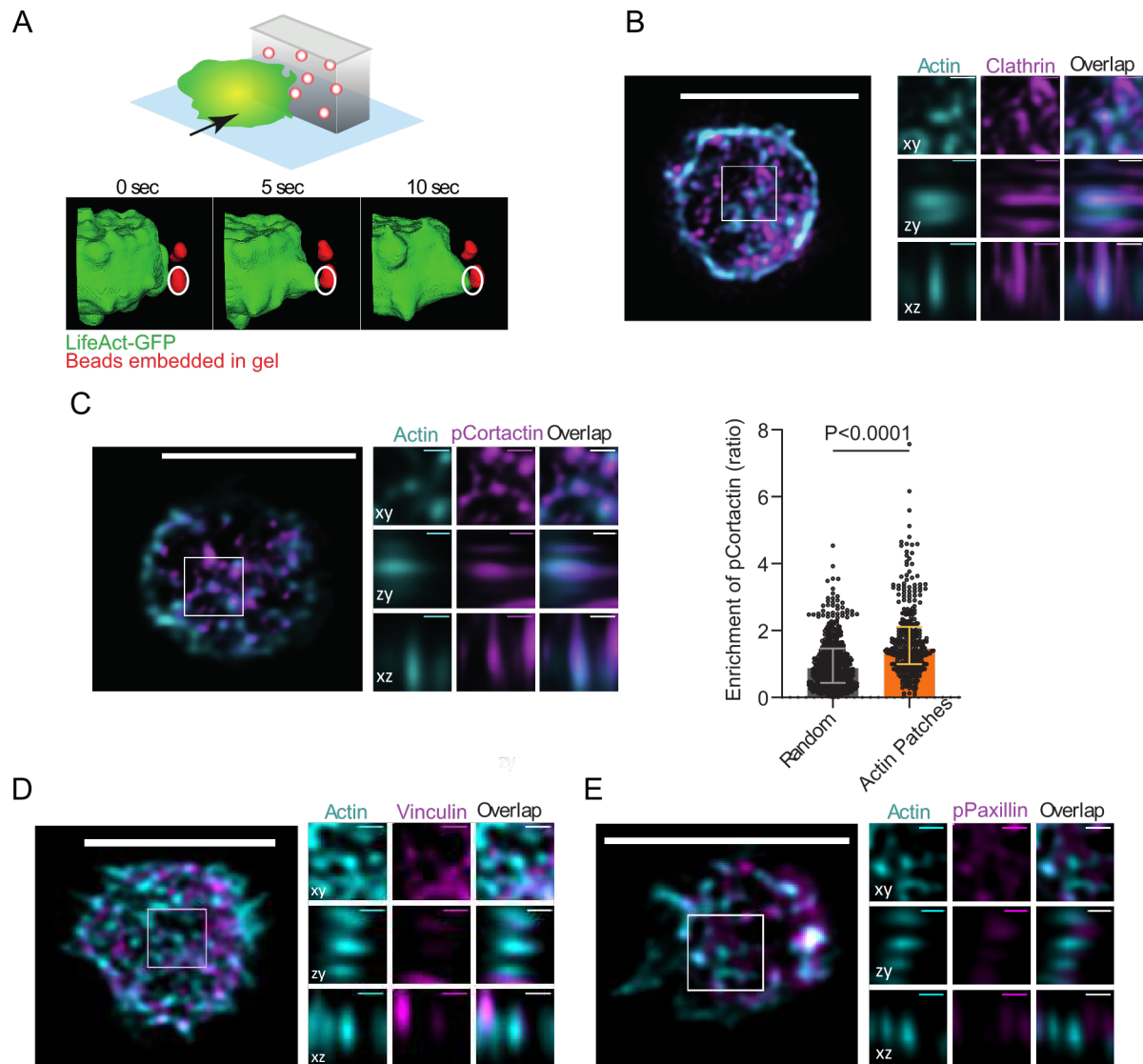


FIGURE 2.4: Actin patches are similar to invadosome-like protrusions. (A) 3D reconstruction of protrusions associated with bead movement (red) on antigen-coated gel pieces presented laterally to B cell (green). (B) Immunofluorescence of actin (cyan) and clathrin (magenta), zoomed orthogonal projections (Scale bar $5\mu\text{m}$, zoom $0.5\mu\text{m}$); showing partial colocalisation (not quantified). (C) Immunofluorescence of actin (cyan) and phospho-Cortactin (magenta), zoomed orthogonal projections (Scale bar $5\mu\text{m}$, zoom $0.5\mu\text{m}$); showing colocalisation. quantification on the right as ratio of pCortactin signal in the vicinity of actin hotspots (control: in the vicinity of random spots) over average pCortactin signal in the cell (Median \pm IQR, $N=26$ cells, 2 independent experiments, 2 mice, Statistical analysis: Mann-Whitney test). (D) Immunofluorescence of actin (cyan) and vinculin (magenta), zoomed orthogonal projections (Scale bar $5\mu\text{m}$, zoom $0.5\mu\text{m}$); showing no colocalisation (E) Immunofluorescence of actin (cyan) and phospho-Paxillin (magenta), zoomed orthogonal projections (Scale bar $5\mu\text{m}$, zoom $0.5\mu\text{m}$); showing no colocalisation. Figure adapted from Kumari et al., 2019.

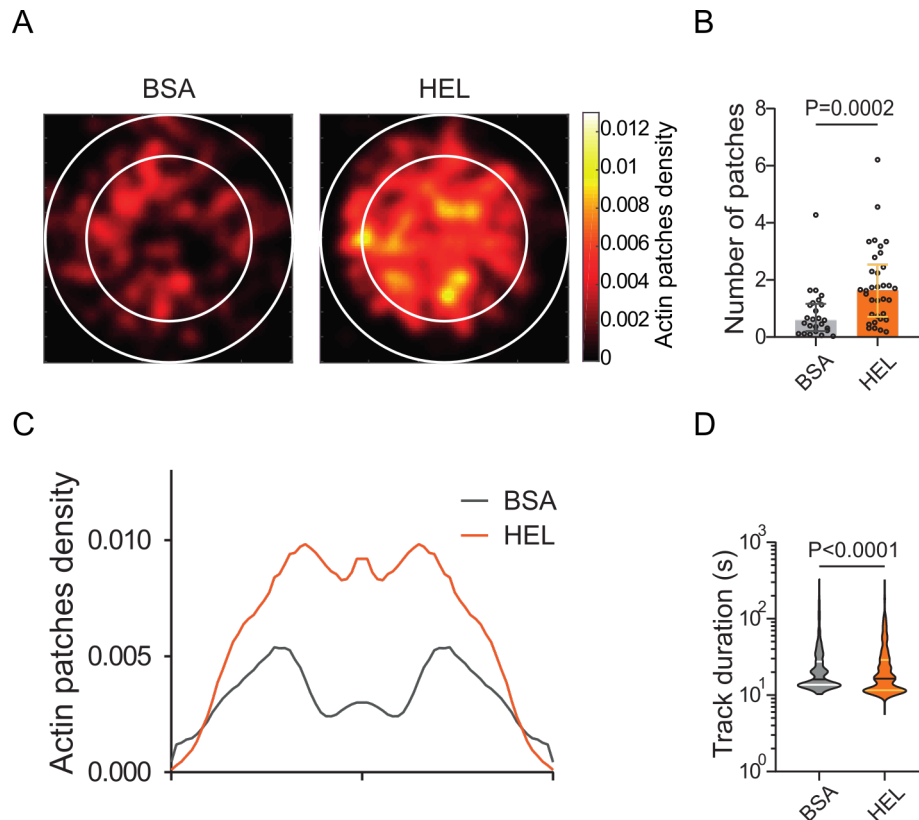


FIGURE 2.5: Actin patches are promoted and stabilized in the presence of antigen. (A) Average distribution of actin patches, mapping the integrated density as number of patches/cell/5min (obtained by tracking of patches and convolution of the tracks with a Gaussian kernel). The distribution on HEL-coated gels is different from the one on BSA-coated gels, regarding (B) the number of actin patches (Mann–Withney test, Median±IQR) and (C) their radial distribution (BSA N=25 cells, HEL N=34 cells, 3 mice). (D) Effective diffusion coefficient of actin patches (Median±IQR, HEL N=301 trajectories 34 cells, BSA N=84 trajectories 25 cells, Mann–Whitney test). Figure adapted from Kumari et al., 2019.

2.2.3 Actin patches stability, force generation and antigen extraction are modulated by actomyosin contractility

We next investigated the regulatory role of myosin II activity in actin patch formation, force generation and antigen extraction. Having established that myosin II inhibition abolishes all these processes (Figure 2.2), we sought to assess the impact of increased myosin II activity using MLSA1, an agonist of the lysosomal calcium channel TRPML1, which locally enhances myosin II flows and activity in dendritic cells (Bretou et al., 2017). We found that MLSA1-treated B cells display enhanced contractile energy, with both coordinated and non-coordinated displacements being increased (Figure 2.6A,B). Surprisingly, this did not correspond to an increase in the number of actin patches, nor in a change in their distribution (Figure 2.6C,D,E). However, MLSA1 treatment resulted in a strong decrease in the diffusion coefficient of actin patches (Figure 2.6F), indicating that it had a stabilizing effect. Consistent with this result, MLSA1-treated cells were able to extract more antigen, and faster, than untreated cells (Figure 2.6G).

Therefore, myosin II inhibition abolishes force generation, actin patch formation and antigen extraction, while increased myosin II activity enhances all of those events. This suggests that these three processes might be functionally linked, and regulated by the activity of this motor protein.

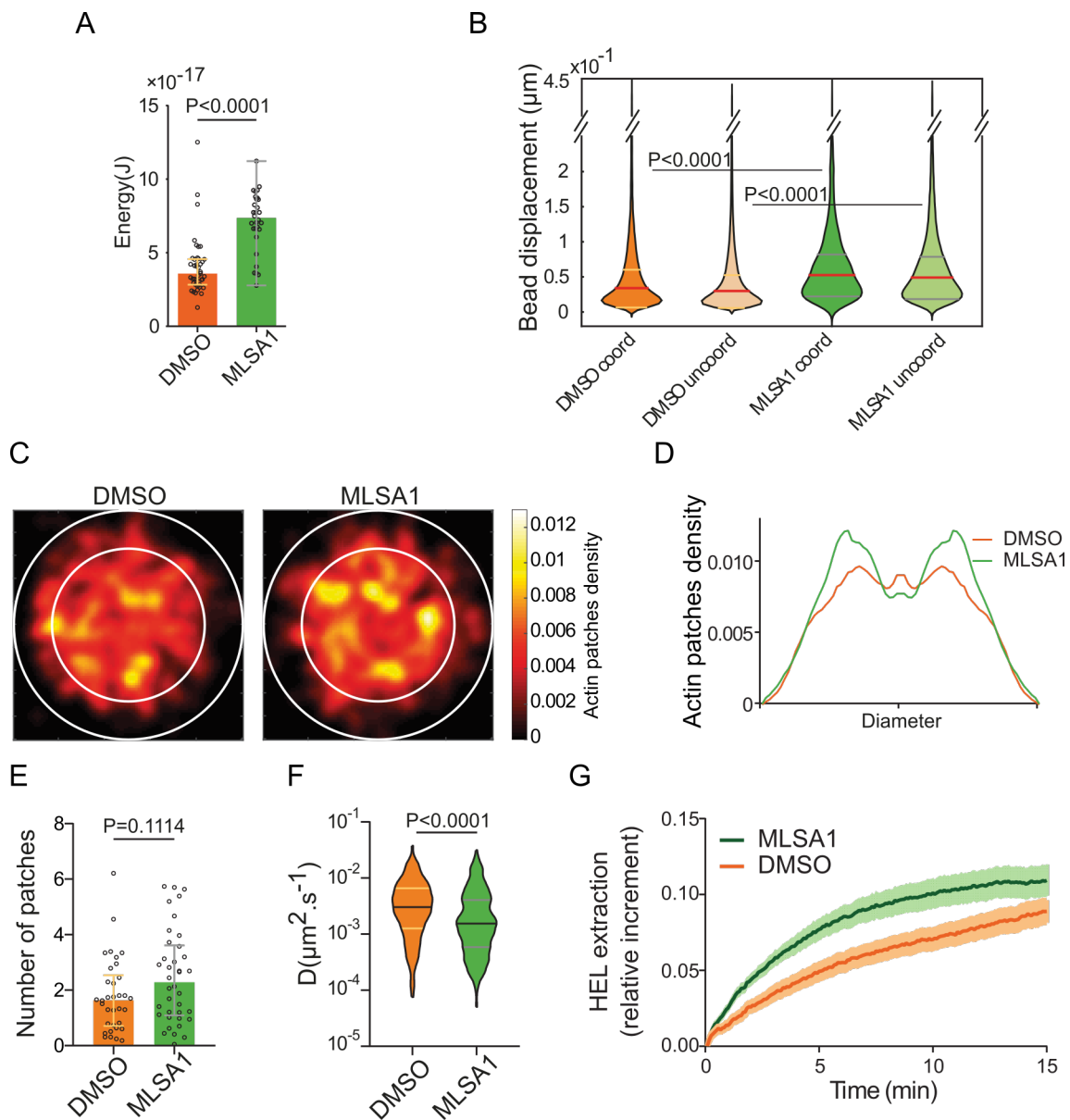


FIGURE 2.6: Actomyosin contractility regulates forces, actin patches and antigen extraction. (A) Plateau of strain energy for untreated (DMSO) or MLSA1-treated cells (Median \pm IQR, DMSO N=41, MLSA1 N=30, 3 independent experiments, 3 mice, statistical analysis: Mann-Whitney test). (B) Bead displacement for coordinated and non-coordinated beads, for untreated (DMSO) and MLSA1-treated cells (Median \pm IQR, DMSO N=41, MLSA1 N=30, 3 independent experiments, 3 mice, statistical analysis: Mann-Whitney test, total of >4400 beads). (C) Average distribution of actin patches, mapping the integrated density as number of patches/cell/5min (obtained by tracking of patches and convolution of the tracks with a Gaussian kernel). The distribution in MLSA1-treated cells does not differ strongly from the control cells regarding (D) the radial distribution or (E) the number of actin patches, although they exhibit a slight increase. (Median \pm IQR, DMSO N=34, MLSA1 N=38, 3 independent experiments, 3 mice, Mann-Whitney test). (F) Effective diffusion coefficient of actin patches (Median \pm IQR, DMSO N=301 trajectories, MLSA1 N=492 trajectories, Mann-Whitney test). (G) Antigen extraction over time in control and MLSA1-treated cells (Mean \pm SEM, DMSO N=55, MLSA1 N=53, 3 independent experiments, 3 mice). Figure adapted from Kumari et al., 2019.

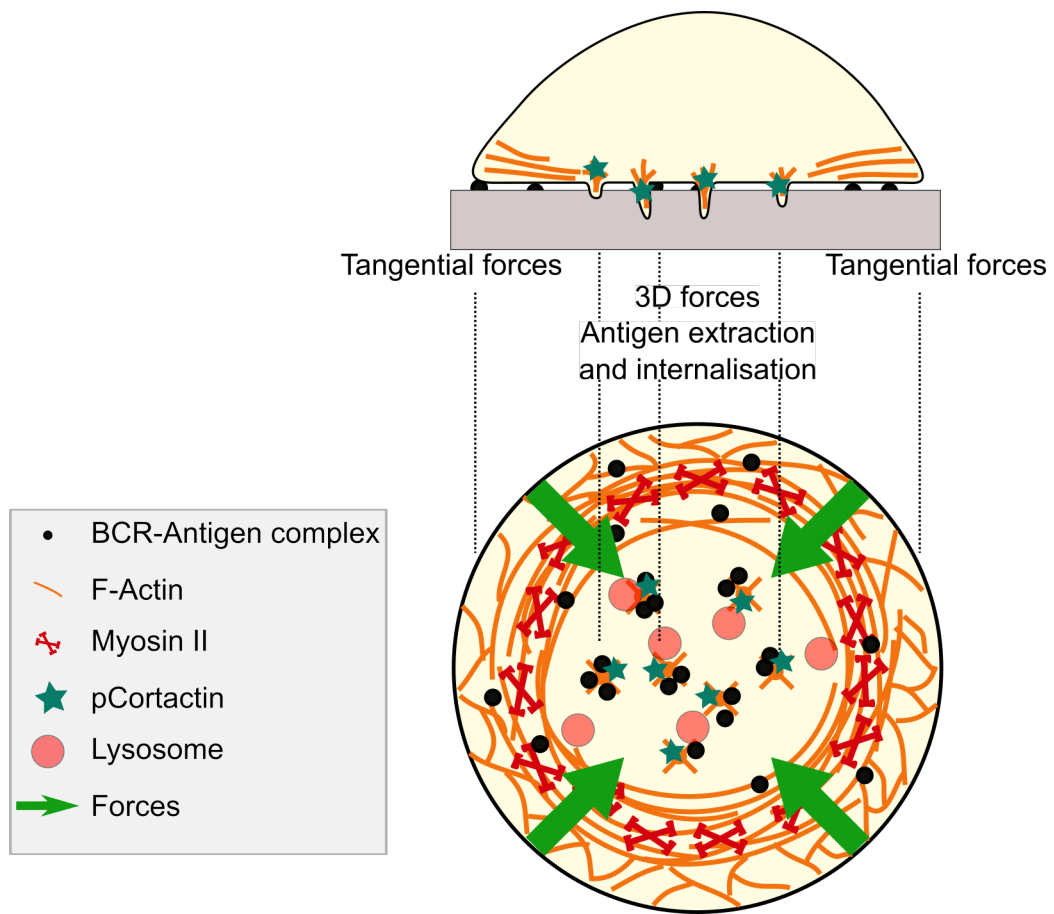


FIGURE 2.7: Actomyosin-driven force patterning controls endocytosis at the immune synapse.

2.3 Conclusion

In this work, we studied the spatio-temporal distribution of forces at the immune synapse of primary B lymphocytes, and its link with actomyosin activity and sub-cellular structures. We found that B lymphocytes apply forces at different scales, with global centripetal forces observed at the periphery of the cell, and local 3D forces measured at the center of the cell. These local 3D forces were associated with actin-rich protrusions, similar to invadosome-like protrusions, that are hotspots for antigen extraction and internalisation. Force generation, actin protrusion formation and antigen internalisation seem to be functionally linked, as all these processes are dependent on myosin II activity, being abrogated upon myosin II inhibition and increased upon myosin II activation by release of lysosomal calcium stores. These results led us to propose a model where peripheral centripetal forces facilitate the accumulation and building up of the endocytic machinery at the center of the immune synapse, where actin protrusions form in response to BCR engagement and facilitate the extraction and internalisation of antigen (Figure 2.7).

This work was published in Nature Communications in 2019 (Kumari, A., Pineau, J.*, Sáez, P.J., Maurin, M., Lankar, D., San Roman, M., Hennig, K., Boura, V.F., Voituriez, R., Karlsson, M. C.I., Balland, M., Lennon Duménil, A-M. & Pierobon, P., Actomyosin-driven force patterning controls endocytosis at the immune synapse. Nat Commun 10, 2870 (2019). <https://doi.org/10.1038/s41467-019-10751-7>, see Kumari et al., 2019) and as a protocol in JoVE in 2020 (Kumari, A., Pineau, J., Lennon-Duménil, A-M., Balland, M., Pierobon, P., Traction Force Microscopy to Study B Lymphocyte Activation. J. Vis. Exp. (161), e60947, doi:10.3791/60947 (2020), see Kumari et al., 2020), attached in Appendix A and B.*

Chapter 3

Dynamics of immune synapse formation in B lymphocytes

Immune synapse formation is a key step for B cell activation and onset of humoral immune responses. This calls for a better understanding of this complex cellular process. The key role played by the cytoskeleton in the formation and function of the immune synapse has become increasingly clear, with crucial roles for actin and microtubule filaments and/or associated motors in antigen extraction and in the exocytic and endocytic events that allow optimal cell-cell communication at the synapse. In this Chapter, we aim at understanding how the different events involved in synapse formation are coordinated by the actin and microtubule networks in space and time.

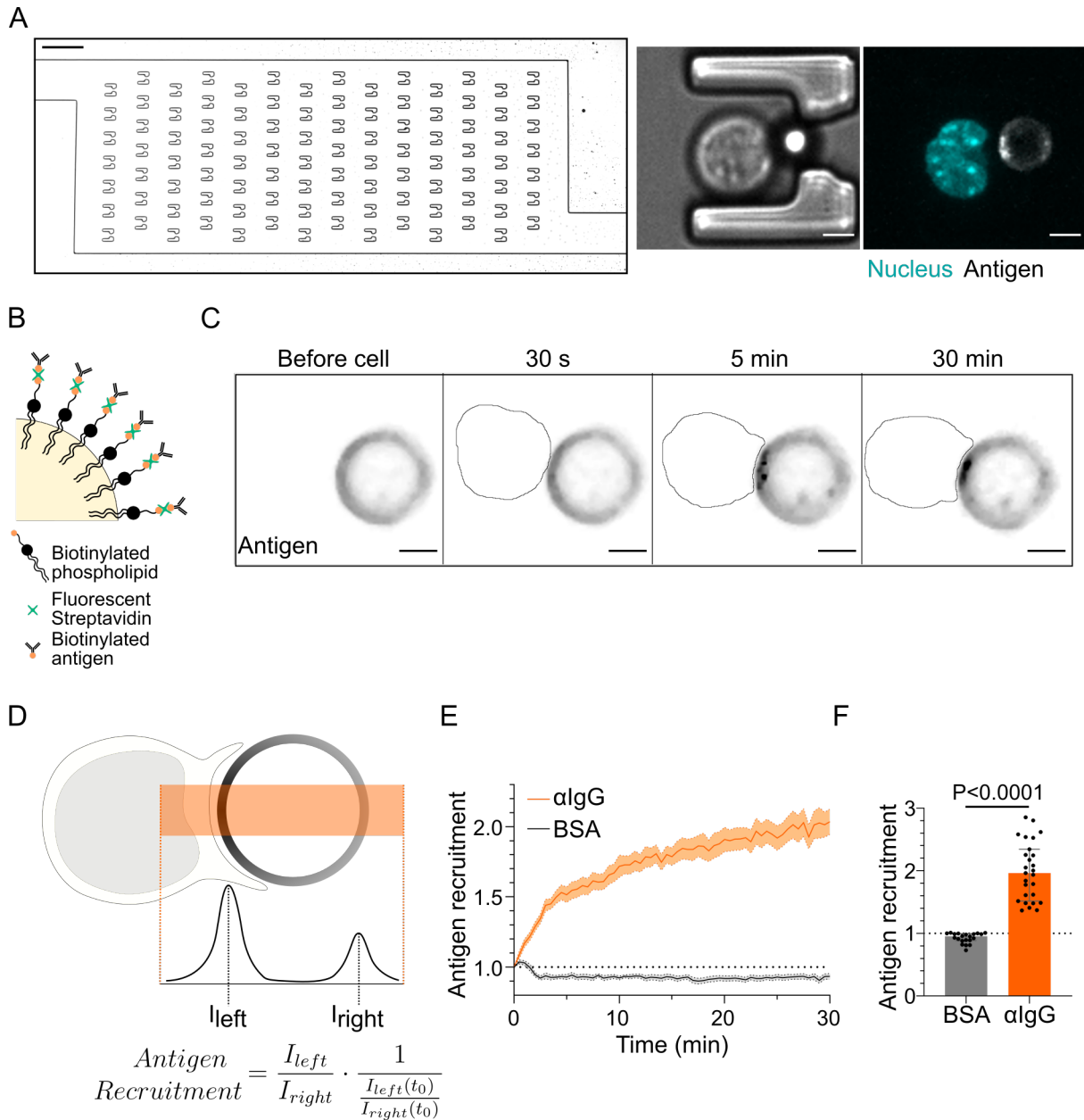


FIGURE 3.1: Microfluidic system to study dynamics of B lymphocyte polarisation and immune synapse formation (A) Transmission image of a chamber of the microfluidic chip containing the traps. Scale bar=100 μ m. Inset: Cell-droplet doublet in a microfluidic trap. Bright field image and fluorescence image (Nucleus: cyan, Antigen: grey). Scale bar=5 μ m. (B) Schematic representation of the surface of an oil droplet used for antigen presentation (C) Time-lapse images of antigen recruitment on an F(ab')₂ α IgG-coated droplet (acting as an antigen). Outline of the cell is drawn. Scale bar=5 μ m. (D) Schematic representation of the quantification of antigen recruitment at the immune synapse. (E) Quantification over time of recruitment on BSA-coated (negative control) or α IgG-coated droplets at the immune synapse (Mean \pm SEM, BSA N=21, α IgG N=27, 2 independent experiments) (F) Plateau of Antigen recruitment (average value 25-30min) on BSA- or α IgG-coated droplets (Median \pm IQR, BSA N=21, α IgG N=27, 2 independent experiments, Mann-Whitney test).

3.1 A microfluidic system for the systematic study of immune synapse formation

We developed, together with the team of Jacques Fattaccioli (Chemistry Department, ENS), a microfluidic tool that allows visualising the formation of the B cell immune synapse in a multiplexed manner, using an antigen-coated droplet as a surrogate antigen presenting cell. This tool is a modification of a system described in Dura et al., 2015, and is based on an array of traps where oil droplets and B cells can be sequentially captured (Figure 3.1A). The system is imaged from the time of cell injection, in order to follow synapse formation from the instant of contact with the droplet. Oil droplets provide reproducible 3D substrates for antigen presentation and allow mobility of the ligand to approach physiological conditions. Here, we used soybean oil droplets coated with biotinylated phospholipids, allowing us to functionalise the droplets with streptavidin plus biotinylated BCR ligands (Figure 3.1B). They behave like a stiff substrate (Surface tension $10\text{mN}\cdot\text{m}^{-1}$, equivalent to a Laplace pressure of 4kPa for a droplet of radius $5\mu\text{m}$, Berek et al., 2015), but with 1-2 orders of magnitude higher ligand diffusion at the surface ($1\mu\text{m}^2\cdot\text{s}^{-1}$) (Bourouina et al., 2011; Dustin et al., 1996; Zhu et al., 2007).

As an experimental model, we used the mouse IgG⁺ B lymphoma cell line IIA1.6 (A20-derived), and functionalised the droplets with biotinylated F(ab')₂ Goat anti-Mouse IgG. F(ab')₂ anti-IgG has been shown to be able to activate B lymphocytes and induce immune synapse formation and polarisation on both solid (bead, glass) and fluid (planar bilayers) substrates (Ketchum et al., 2014; Yuseff et al., 2011). By combining a normalised substrate for antigen presentation and parallelised observation of cell-antigen encounter, under a controlled angle of imaging and time of encounter, this system allows an unprecedented systematic study of the dynamics of immune synapse formation.

We imaged in 3D+time the formation of immune synapses by following antigen accumulation at the cell-droplet contact using fluorescent streptavidin. We were able to observe and quantify antigen accumulation on the droplet (Figure 3.1C,D). Using droplets coated with either BSA (negative control) or F(ab')₂ α IgG, we found that antigen recruitment was specifically triggered by BCR engagement (Figure 3.1E,F).

Based on these results, we are confident that this system can be used to specifically activate B cells and study how the cell cytoskeleton allows coordination of the various molecular events associated to immune synapse formation.

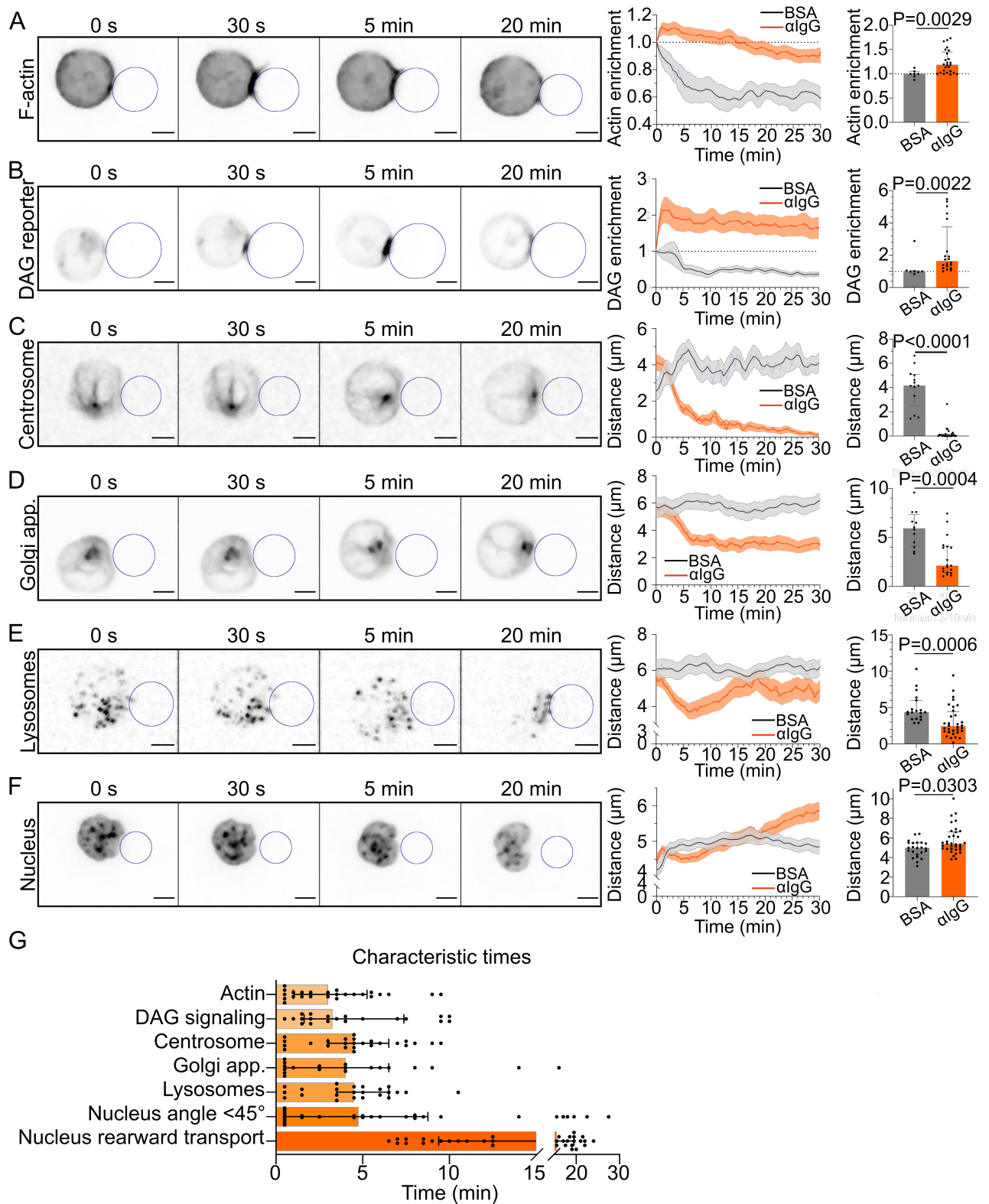


FIGURE 3.2: (Figure on previous page) **Timescales of B lymphocyte polarisation** (A) Time lapse images of F-actin in a cell in contact with a droplet (outlined in blue). Scale bar 5 μ m. Enrichment in time of F-actin near the droplet for BSA- or α IgG-coated droplets (Mean \pm SEM). Maximum enrichment (0-10min), (Median \pm IQR, BSA N=7, α IgG N=26, 2 independent experiments, Mann-Whitney test). (B) Time lapse images of DAG reporter in a cell in contact with a droplet (outlined in blue). Scale bar 5 μ m. Enrichment in time of DAG reporter (Mean \pm SEM). Maximum enrichment (0-10min), (Median \pm IQR, BSA N=7, α IgG N=20, 2 independent experiments, Mann-Whitney test). (C) Time lapse images of the centrosome in a cell in contact with a droplet (outlined in blue). Scale bar 5 μ m. Distance over time between the centrosome and droplet surface for BSA- or α IgG-coated droplets (Mean \pm SEM). Average plateau distance (25-30min), (Median \pm IQR, BSA N=13, α IgG N=25, 2 independent experiments, Mann-Whitney test). (D) Time lapse images of the Golgi body in a cell in contact with a droplet (outlined in blue). Scale bar 5 μ m. Distance over time between the Golgi body and droplet surface for BSA- or α IgG-coated droplets (Mean \pm SEM). Average plateau distance (25-30min), (Median \pm IQR, BSA N=12, α IgG N=19, 2 independent experiments, Mann-Whitney test). (E) Time lapse images of lysosomes in a cell in contact with a droplet (outlined in blue). Scale bar 5 μ m. Average distance over time between lysosomes and droplet surface for BSA- or α IgG-coated droplets (Mean \pm SEM). Minimum distance (3-10min), (Median \pm IQR, BSA N=19, α IgG N=32, 2 independent experiments, Mann-Whitney test). (F) Time lapse images of the nucleus (Hoechst) in a cell in contact with a droplet (outlined in blue). Scale bar 5 μ m. Nucleus-droplet distance in time (Mean \pm SEM). Average distance in the final state (25-30 min), (Median \pm IQR, BSA N=23, α IgG N=34, 2 independent experiments, Mann-Whitney test). (G) Characteristic times of polarisation events, extracted from the data of (A)-(F) and Figure 3.3.

3.2 Characteristic timescales at the B lymphocyte immune synapse

We first sought to establish the sequence of events leading to the redistribution of the distinct cellular organelles and components upon formation of the B cell synapse. Key actors of the immune synapse architecture and function were studied: production of DAG (DiAcylGlycerol) by PLC γ 2 to monitor signaling, F-actin organisation, centrosome and Golgi apparatus polarisation, lysosomes distribution, and nucleus positioning. We took volumetric images every 30 seconds of both the antigen on the droplet and these different molecular species/organelles, using droplets functionalised with either BSA or F(ab') $_2$ α IgG. For each element, a characteristic timescale of polarisation was extracted.

F-actin and DAG signaling peak in the first instants of immune synapse formation.

We followed the accumulation of F-actin at the immune synapse and quantified the enrichment of F-tractin-tdTomato at the cell-droplet interface over time. We observed that actin quickly polymerised in the vicinity of the immune synapse in the presence

of BCR ligand in the first instants (Figure 3.2A). Formation of the stereotypical actin pattern, with actin protrusions at the periphery and an actin-cleared area at the center, was observed. The peak of actin polymerisation occurred ~ 3 minutes after BCR engagement, which was concomitant with DAG production, which peaked after ~ 3.25 minutes of cell-droplet interaction (Figure 3.2B,G) (measured using C1 δ -GFP, the C1 domain of PKC δ is a DAG-binding domain and acts as a DAG reporter, from Botelho et al., 2000).

The centrosome polarises towards the immune synapse, followed by the Golgi apparatus and lysosomes.

We then analysed the trajectories of the centrosome (imaged using low concentrations of SirTubulin, a microtubule live marker) and the Golgi apparatus (Rab6-mCherry) (Figure 3.2 C,D). They displayed similar behaviors and polarised in the presence of BCR ligand around the first 4.5 minutes for the centrosome (reaching $< 2\mu\text{m}$), and 4 minutes for the Golgi apparatus (reaching $< 4\mu\text{m}$), in agreement with these organelles being physically associated (Figure 3.2G) (Stinchcombe and Griffiths, 2014). Lysosomes (visualised with LysoTracker, a marker of acidic compartments) are known to associate to microtubules for intracellular transport. However, they displayed a slightly different polarisation dynamic than the centrosome and Golgi apparatus. Indeed, the distance between lysosomes and the antigen-coated droplet decreased during the first 3-10 minutes, reaching $< 3\mu\text{m}$ in approximately 4.5 minutes, indicating that they reorient towards the immune synapse. However, this distance then increased, which is likely to be due to lysosome fusion with the cell membrane, these vesicles being exocytosed at the immune synapse (Figure 3.2E,G) (Yuseff et al., 2011).

The nucleus undergoes a rotation followed by rearward transport.

Finally, we monitored the movement of the nucleus (Hoechst staining) upon immune synapse formation. We observed that in the late time points, the nucleus was transported to the rear of the cell (Figure 3.2F), consistent with our previous finding showing that the nucleus and centrosome separate upon immune synapse formation (Obino et al., 2016). Interestingly, closer observation revealed a biphasic movement of the nucleus: it first undergoes a rotation, that starts at the time of contact between the cell and the droplet, and ends when the stereotypical nucleus invagination of lymphocytes faces the immune synapse (median time to reach $\theta_N < 45^\circ$: 4.75 minutes)(Figure 3.3A,B). This rotation is followed by a global nucleus translocation towards the cell rear, starting after 15 minutes of synapse formation (time of last local minima of nucleus-droplet distance) (Figure 3.3C,D). Nuclear deformations were also

observed during rotation and translocation, resulting in the flattening of the nucleus invagination over time (Figure 3.3E), in agreement with a recent publication (Ulloa et al., 2021). Invagination flattening might result from centrosomal actin depletion and nucleus-centrosome detachment during synapse formation (Obino et al., 2016).

The typical timescales extracted from single kinetic curves are summarised in Figure 3.2G. This analysis suggests that two main time scales operate during B lymphocyte polarisation. Within the first 4 minutes, events are mainly related to the formation of the immune synapse and the contact side: in phase 1, BCR engagement triggers a strong polarised F-actin polymerisation, which is quickly followed by a peak in DAG signaling. In phase 2, organelles are rearranged along the cell-droplet axis with the relocalisation of the centrosome, the Golgi apparatus, and lysosomes towards the immune synapse, to end with the rearward transport of the nucleus.

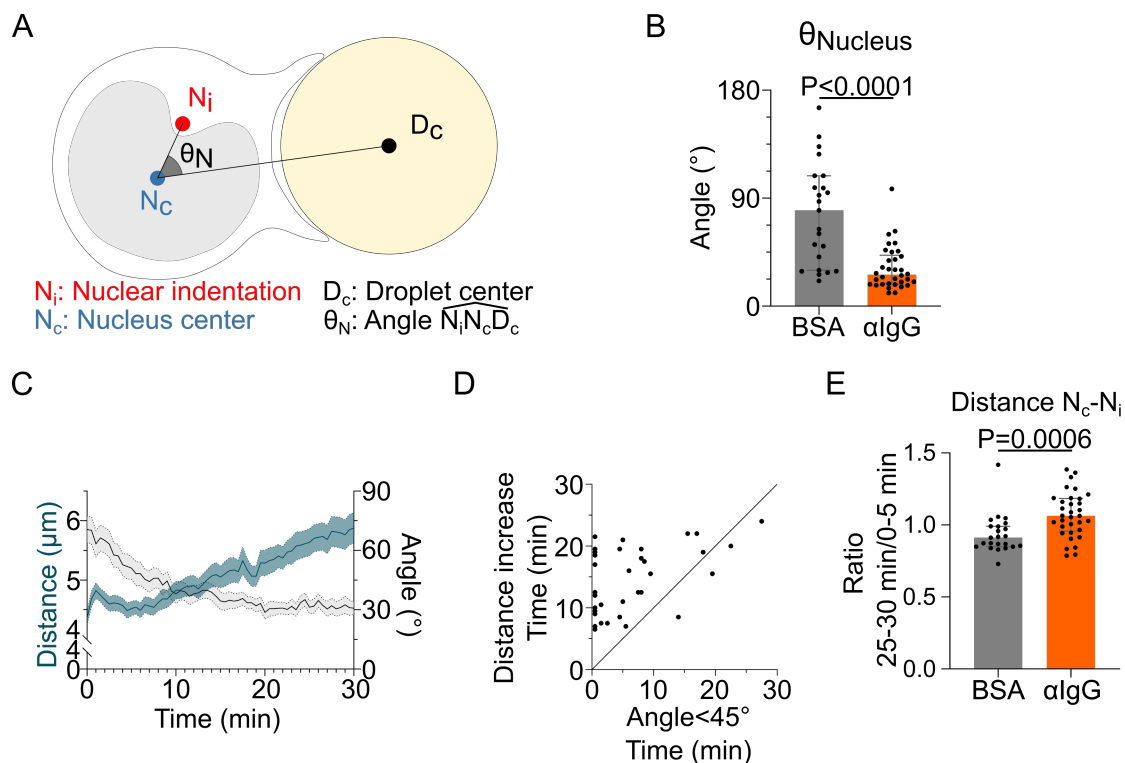


FIGURE 3.3: The nucleus undergoes a rotation followed by rearward transport. (A) Schematic defining the angle measured to assess nucleus orientation (Analysis was done in 3D). The indentation was detected based on local curvature. (B) Average angle θ_N in the final state (25-30 min) (Median \pm IQR, BSA N=23, α IgG N=34, 2 independent experiments, Mann-Whitney test). (C) Overlay of nucleus-droplet distance and θ_N over time for cells in contact with α IgG-coated droplets and (D) time for which the cell reaches $\theta_N < 45^\circ$ (invagination oriented towards the immune synapse), and time of last local minima of nucleus-droplet distance (time after which the nucleus is only transported to the rear) (N=34, 2 independent experiments). Line at Y=X. (E) Ratio between the $N_c N_i$ distance at the final state (25-30 min) and the initial state (0-5 min), to estimate cell deformation regarding the invagination (Median \pm IQR, BSA N=23, α IgG N=34, 2 independent experiments, Mann-Whitney test).

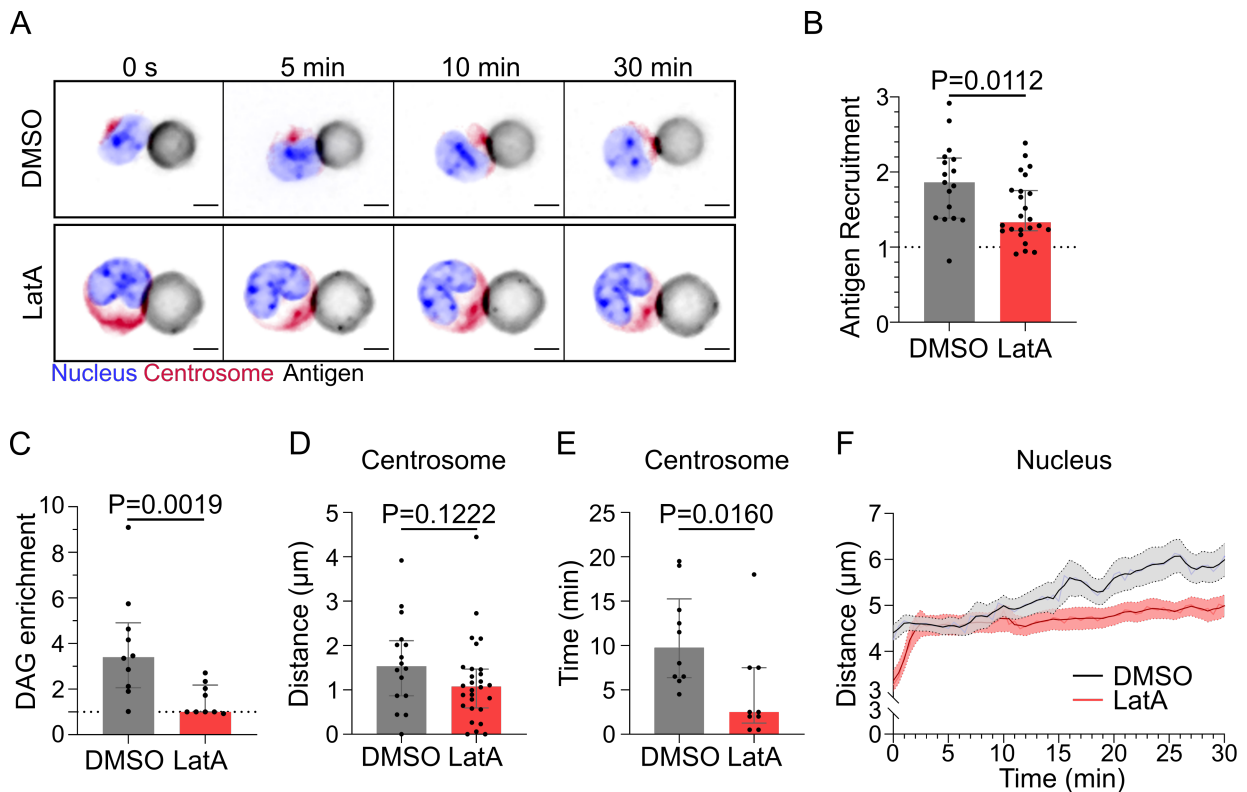


FIGURE 3.4: F-actin is essential for antigen recruitment and signaling amplification, but not for the establishment of the polarity axis (A) Time lapse images of untreated (DMSO) or LatA-treated cells, centrosome (SirTubulin) in red, nucleus (Hoechst) in blue, antigen in grey. Scale bar $5\mu\text{m}$. (B) Plateau of antigen recruitment (average values 25-30 min). Line at Antigen recruitment=1, representing a uniform fluorescence on the droplet (Median \pm IQR, DMSO N=17, LatA N=24, 2 independent experiments, Mann-Whitney test). (C) Maximum DAG enrichment (in 0-10 min) (Median \pm IQR, DMSO N=10, LatA N=9, 2 independent experiments, Mann-Whitney test). (D) Average centrosome-droplet distance (25-30 min) (Median \pm IQR, DMSO N=16, LatA N=28, 2 independent experiments, Mann-Whitney test) (E) Time of centrosome polarisation (t hreshold distance $<2\mu\text{m}$) (Median \pm IQR, DMSO N=10, LatA N=9, 2 independent experiments, Mann-Whitney test). (F) Nucleus-droplet distance over time (Mean \pm SEM, DMSO N=17, LatA N=32, 2 independent experiments).

3.3 Cytoskeletal networks and synapse formation

How do these distinct polarisation events relate to each other? Are they coordinated or do they occur independently? The apparent temporal separation between the first phase of synapse formation, related to signaling and actin polymerisation at the cell-droplet interface, and the second phase, related to the formation of a global polarisation axis with the reorientation of the centrosome and microtubule-associated organelles, prompted us to analyse whether the actin and microtubule networks could play a role in coordinating these two sets of events.

3.3.1 The actin cytoskeleton is necessary for antigen clustering and signaling at the immune synapse

To assess the role of the actin cytoskeleton in the two phases of immune synapse formation, we inhibited actin polymerisation using Latrunculin A. Depolymerisation of F-actin almost completely prevented the recruitment of antigen at the immune synapse (Figure 3.4A,B), as expected given the central role of F-actin in the formation of BCR-antigen microclusters (Liu et al., 2011; Bolger-Munro et al., 2019). The slight clustering observed in Latrunculin A-treated cells could be explained by free diffusion of $F(ab')_2 \alpha IgG$ at the droplet surface, which would be captured by BCRs. Importantly, depolymerisation of F-actin led to a drastic decrease in DAG signaling (Figure 3.4C), confirming the central role of F-actin in early signaling at the immune synapse.

Myosin II is essential for mechanical extraction of antigen as well as for antigen processing (Hoogeboom et al., 2018; Kumari et al., 2019; Vascotto et al., 2007). We thus investigated its impact on the dynamics of immune synapse formation. We chose to either inhibit myosin II activity using para-nitroBlebbistatin or increase its activity using MLSA1, an agonist of the lysosomal calcium channel TRPML1 that stimulates actomyosin contractility in dendritic cells and B cells (Bretou et al., 2017; Kumari et al., 2019). These treatments had little effect on F-actin enrichment, antigen recruitment or DAG signaling (Figure 3.5A-E). Myosin II inhibition only resulted in a minor effect on actin first polymerisation peak at the synapse and on its sustained enrichment over time, as well as a slight decrease in antigen recruitment (Figure 3.5A,B,E). In contrast, while DAG accumulation at the immune synapse was slightly increased during the initial peak in Blebbistatin-treated cells, it remained unchanged once synapse formation completed (Figure 3.5C,D). These results suggest the existence of an optimal spatiotemporal regulation of myosin II activity at the immune synapse,

even though the role played by the motor protein was rather marginal.

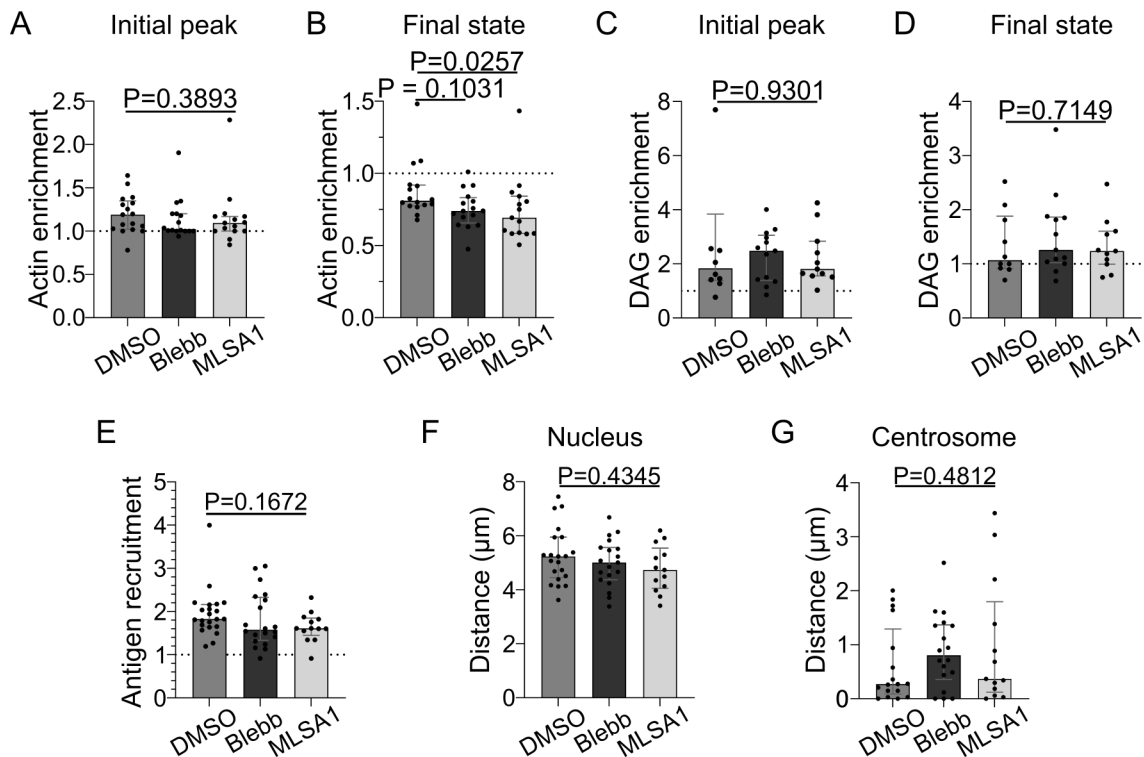


FIGURE 3.5: Myosin II activity does not have a significant impact on immune synapse formation and B cell polarisation. (A) Maximum enrichment of F-actin (in 0-20 min) and (B) average enrichment in the final state (25-30 min) (Median \pm IQR, DMSO N=16, p-nBlebb 20 μM N=16, MLSA1 1 μM N=15, 3 independent experiments, Kruskal-Wallis test, and if significant difference, multiple comparisons to DMSO). (C) Maximum (in 0-20 min) and (D) average final (25-30 min) DAG reporter enrichment (Median \pm IQR, DMSO N=10, p-nBlebb 20 μM N=13, MLSA1 1 μM N=11, 2 independent experiments, Kruskal-Wallis test). (E) Plateau of antigen recruitment (average 25-30 min) (Median \pm IQR, DMSO N=22, p-nBlebb 20 μM N=20, MLSA1 1 μM N=13, 2 independent experiments, Kruskal-Wallis test). (F) Average nucleus-droplet distance at the final state (25-30 min)(Median \pm IQR, DMSO N=21, p-nBlebb N=19, MLSA1 N=13, 2 independent experiments, Kruskal-Wallis test). (G) Average centrosome-droplet distance at the final state (25-30 min)(Median \pm IQR, DMSO N=17, p-nBlebb N=18, MLSA1 N=13, 2 independent experiments, Kruskal-Wallis test).

3.3.2 The actin cytoskeleton does not impact later events of synapse formation

Noticeably, imaging of centrosome and nucleus polarisation in Latrunculin A-treated cells revealed that actin polymerisation is dispensable for these phase 2 events of synapse formation (Figure 3.4A,D,F). These results show that actin-dependent signaling events such as BCR-antigen microcluster formation are not required for the progress of Phase 2. Of note, we observed that the F-actin cytoskeleton even slows down the formation of the centrosome-nucleus axis, with the centrosome reaching the droplet faster, and the nucleus being transported towards the cell rear earlier and faster in Latrunculin A-treated cells (Figure 3.4E,F). This is consistent with previous work from the lab showing that the centrosome of B lymphocytes is tethered to the nucleus through a pool of actin nucleated at the centrosome, which is depleted after a few minutes of BCR signaling to allow centrosome docking at the immune synapse (Obino et al., 2016; Ibañez-Vega et al., 2019). Consistently, we observed that in Latrunculin-A-treated cells, the centrosome is separated from the nucleus earlier (visible on Figure 3.4A). These results highlight that centrosomal actin clearing is a time-limiting step for centrosome and nucleus polarisation (Obino et al., 2016). Of note, Latrunculin A treatment also led to a slight increase in cell volume, more pronounced nucleus indentation and stronger SiRTubulin staining (as visible on Figure 3.4A), the latter being due to an increase in total density of microtubules after the depletion of centrosomal actin (Inoue et al., 2019). As Latrunculin A, neither p-nBlebbistatin nor MLSA1 altered centrosome polarisation and nucleus retrograde transport (Figure 3.5F,G).

We conclude that although the F-actin cytoskeleton is strictly required for the phase 1 events of synapse formation, such as antigen clustering and DAG signaling, it is dispensable for the phase 2 events leading to the establishment of the centrosome-nucleus polarity axis. Only a rather minor role was observed for myosin II-dependent contractility in both phases of immune synapse formation.

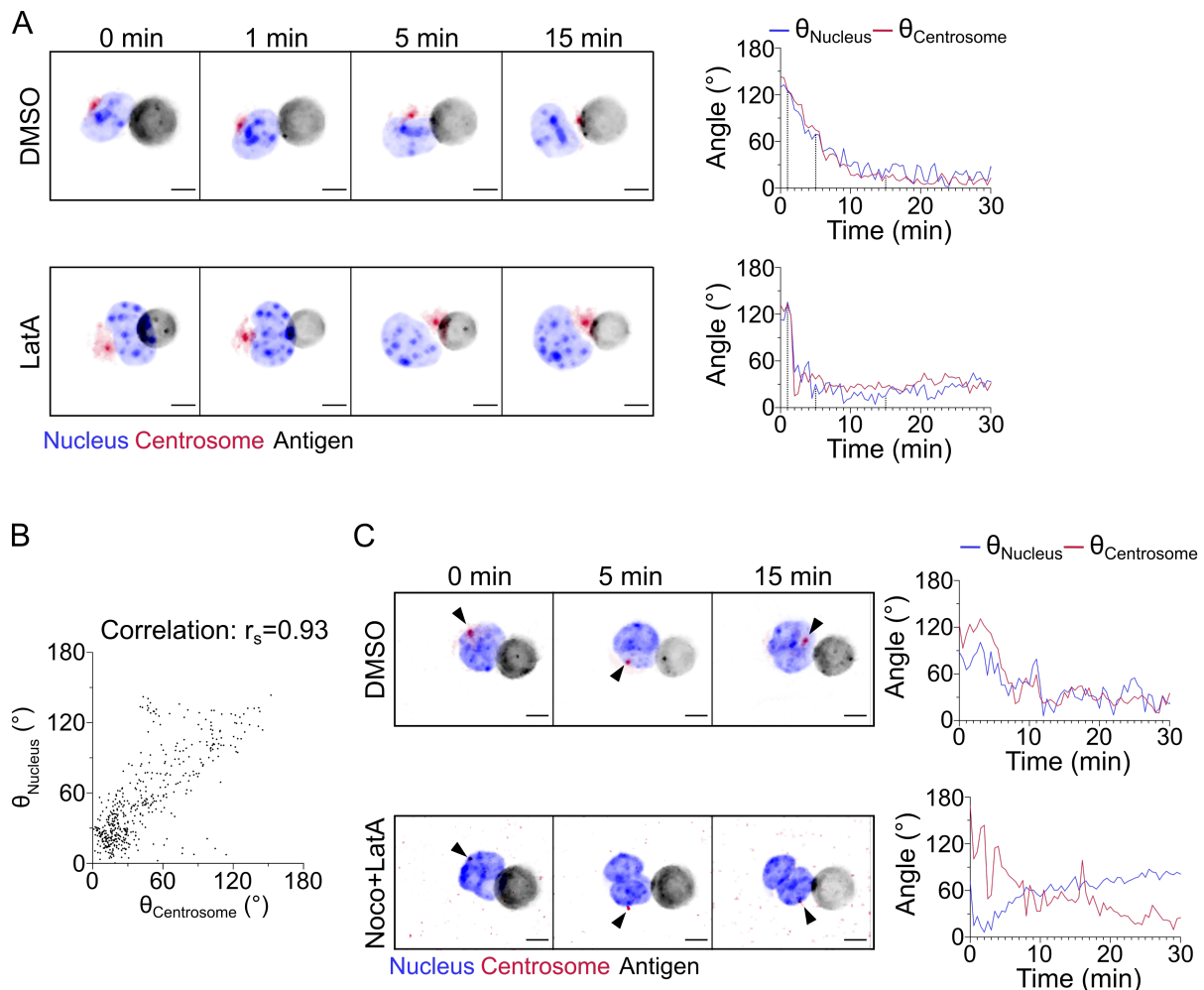


FIGURE 3.6: Centrosome and nucleus reorientation are correlated, and actin-independent. (A) Time lapse images of untreated (DMSO) or LatA-treated cells, centrosome in red, nucleus in blue, antigen in grey. Scale bar 5 μm . Right: Angle between the cell-droplet axis and the cell-nucleus invagination (blue) or cell-centrosome (red) axis in time. (B) Nucleus orientation and centrosome orientation (defined as in (A)) during the first 15 min, for DMSO-treated cells (N=16 cells, 1 image every 30s, 2 independent experiments). Nonparametric Spearman correlation between nucleus-centrosome pairs of data, average correlation 0.93, Confidence interval: 0.8562 to 0.9668). (C) Time lapse images of untreated (DMSO) or Noco+LatA-treated cells, centrosome (Centrin-GFP) in red, nucleus in blue, antigen in grey. Scale bar 5 μm . Black arrowheads indicate the centrosome. Right: Angle between the cell-droplet axis and the cell-nucleus invagination (blue) or cell-centrosome (red) axis in time. Correlation between θ_N and θ_C : DMSO $r_s = 0.824$, C.I: 0.6568 to 0.9138, 6 cells over 31 time points. Noco+LatA $r_s = -0.826$, C.I: -0.5885 to 0.08705, 6 cells over 31 time points. 2 independent experiments. Nonparametric Spearman correlation.

3.3.3 Microtubules are essential for the formation of the centrosome-nucleus polarity axis

We observed that the centrosome faces the nuclear invagination throughout the entire process of synapse formation (Figure 3.4A), suggesting that these two organelles move together, likely involving the microtubule network. Decomposing the centrosome movement in polar coordinates to separate its rotation (by measuring the angle between the cell-droplet axis and the cell-centrosome axis) from its displacement along the cell radius revealed strong similarities between centrosome orientation ($\theta_{\text{Centrosome}}$) and nuclear indentation orientation (θ_{Nucleus}) in time (Figure 3.6A). This observation suggests that centrosome and nucleus positioning are intimately linked. Accordingly, we found that during cell polarisation, centrosome and nucleus reorientation correlated very strongly (Figure 3.6B). Of note, this was unaffected by the depolymerisation of the F-actin network, again stressing the lack of requirement for these filaments in the phase 2 events of synapse formation (Figure 3.6A). However, F-actin and microtubule depolymerisation with Nocodazole deeply compromised this correlation, as well as nucleus invagination reorientation towards the immune synapse (Figure 3.6C). As expected from these results, we found that the centrosome (visualised here using eGFP-Cent1) was not able to polarise to the immune synapse in the absence of microtubules (Figure 3.7H).

These results indicate that the centrosome and the nucleus reorient together to the immune synapse, in a microtubule-dependent and actin-independent manner.

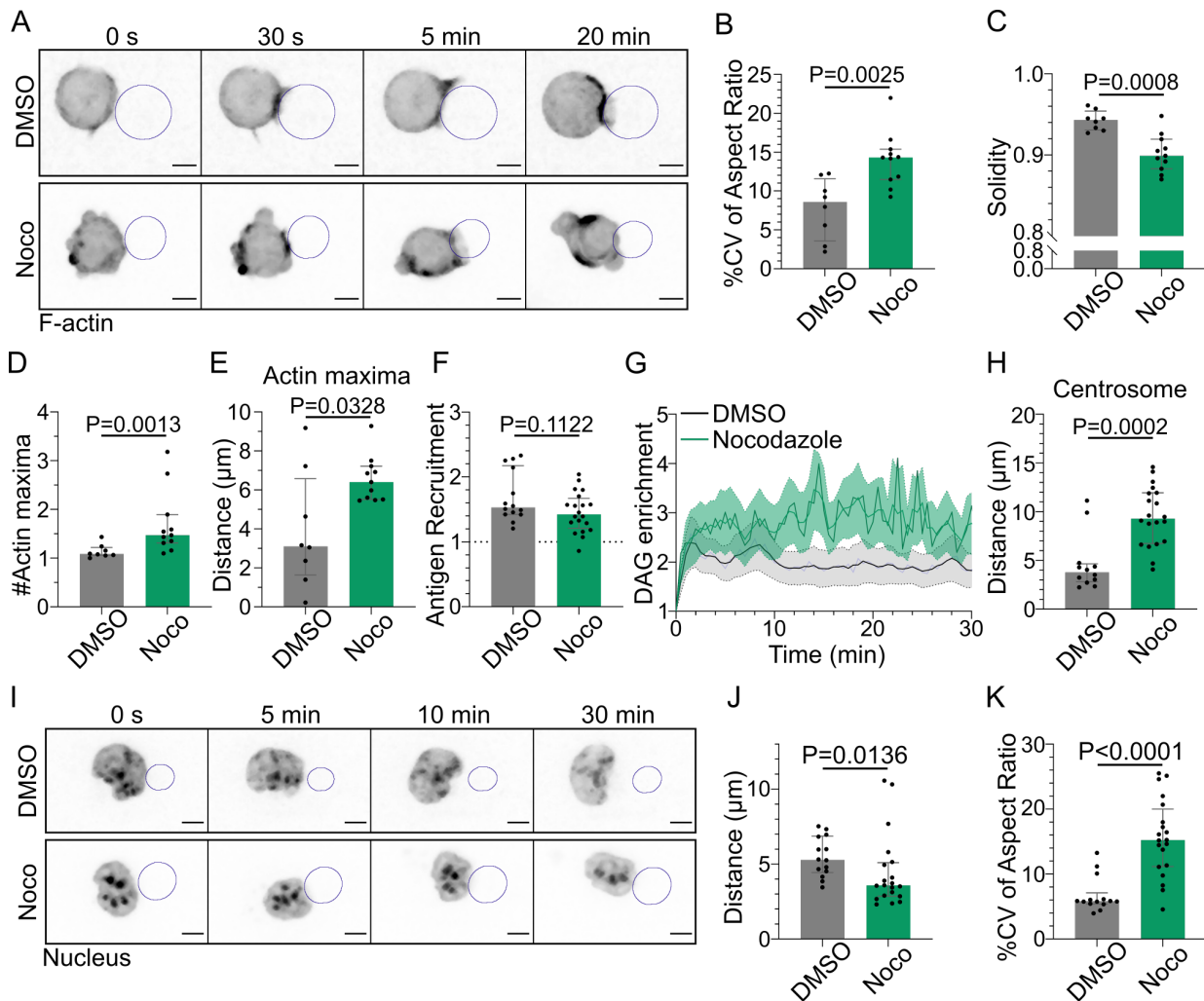


FIGURE 3.7: Microtubule disruption leads to intense cell and nucleus deformation, and impairs the establishment and maintenance of a polarised organisation. (A) Time lapse images of F-actin in DMSO- or Nocodazole-treated cells, droplet outlined in blue. Scale bar 5 μ m. (B) %Coefficient of Variation of 2D aspect ratio of individual cells over time and (C) Median 2D solidity of individual cells (Median \pm IQR, DMSO N=8, Noco N=11, 2 independent experiments, Mann-Whitney test). (D) Average number of F-actin maxima detected per cell over time and (E) Average distance of maxima to the droplet surface (Median \pm IQR, DMSO N=8, Noco N=11, 2 independent experiments, Mann-Whitney test). (F) Plateau of antigen recruitment on the droplet (average values 25-30 min) (Median \pm IQR, DMSO N=14, Noco N=20, 2 independent experiments, Mann-Whitney test). (G) DAG enrichment over time (Mean \pm SEM, DMSO N=13, Noco N=10, 2 independent experiments). (H) Average centrosome-droplet distance (25-30 min) (Median \pm IQR, DMSO N=12, Noco N=20, 2 independent experiments, Mann-Whitney test). (I) Time lapse images of the nucleus, droplet outlined in blue. Scale bar 5 μ m. (J) Average Nucleus-droplet distance (25-30 min) and (K) %Coefficient of Variation of 2D aspect ratio of individual nuclei over time (Median \pm IQR, DMSO N=14, Noco N=20, 2 independent experiments, Mann-Whitney test).

3.3.4 Microtubules restrict actin nucleation to the immune synapse and prevent polarity loss

So far, our results show that the distinct events leading to synapse formation can be segregated into two groups. Early (phase 1) events (antigen recruitment, actin polymerisation and DAG signaling) rely on F-actin, which is dispensable for late (phase 2) events (formation of the centrosome-nucleus polarity axis and centrosome/organelle reorientation towards the immune synapse) that are driven by the microtubule network. Strikingly, we found that microtubules are not only needed for late phase 2 events of lymphocyte polarisation, but further control early phase 1 events. Indeed, F-actin patterning was drastically compromised in Nocodazole-treated cells (Figure 3.7A), that exhibited actin-dense and actin-depleted areas located not only at the immune synapse, but at multiple locations in the cell cortex (Figure 3.7D,E). This was accompanied by a lack of down-regulation of DAG production in Nocodazole-treated cells (Figure 3.7G), indicative of a sustained BCR signaling. Antigen clustering was only slightly reduced (Figure 3.7F). In addition, cells underwent dynamic cell deformation as well as cell blebbing, quantified respectively by variations in aspect ratio and cell solidity ($\text{Solidity} = \frac{\text{Area}}{\text{convexarea}}$) (Figure 3.7A-C). Finally, the nucleus was not able to polarise, and was strongly and dynamically deformed, likely by the actin cortex, losing its polarisation and characteristic shape (Figure 3.7I-K). Noticeably, we did not observe any cell or nucleus deformation in the cells treated with Nocodazole and Latrunculin A (Figure 3.6C), thus confirming the fact that the intense deformation upon microtubule disruption is a result of abnormal actomyosin regulation.

These results indicate that microtubule network disruption impairs not only late events (formation of the polarisation axis, nucleus positioning), but also actin patterning and global cell shape. They further suggest that early and late events of immune synapse formation are tightly coordinated.

Constitutive activation of RhoA recapitulates intense actin polymerisation outside of the immune synapse and cell deformation.

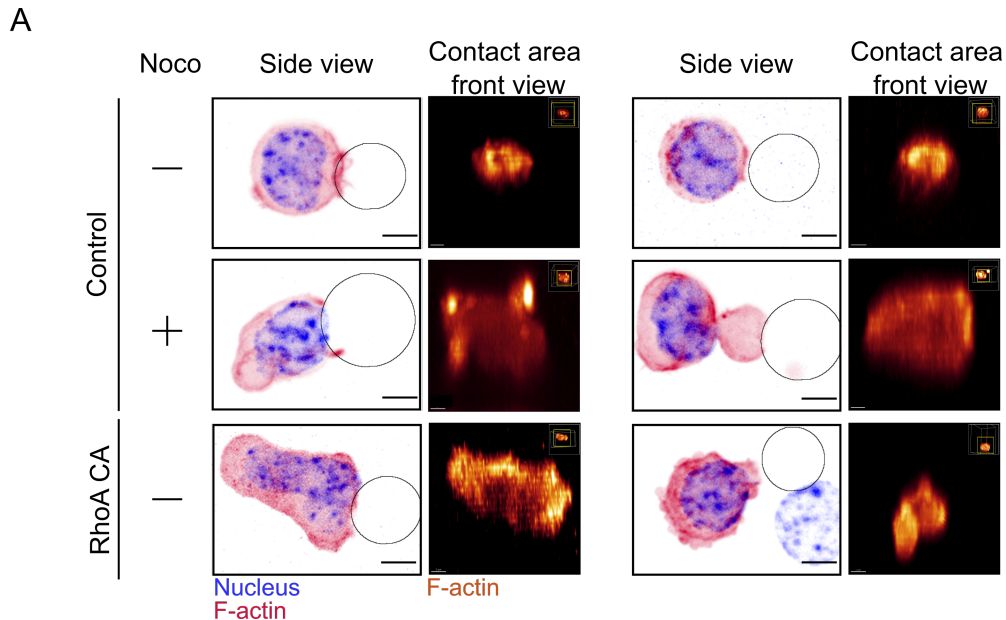


FIGURE 3.8: **Controlled RhoA activation regulates actin patterning and polarisation.** (A) Preliminary experiment, to be repeated: Illustration of control cells and cells overexpressing RhoA L63 (RhoA CA) and F-tractin-tdTomato, after 40 minutes of immune synapse formation. Side view for visualisation of polarisation (Scale bar 5 μ m), and 3D reconstruction of F-actin to visualise the cell-droplet contact (Scale bar 2 μ m).

Microtubule depolymerisation by Nocodazole leads to the release and activation of GEF-H1, a microtubule-bound RhoA-specific GEF. This has two consequences: (1) activation of the kinase ROCK, leading to myosin II-dependent contractility and (2) initiation of mDia1-dependent nucleation of actin filaments (Chang et al., 2008; Suarez and Kovar, 2016). To assess whether activation of RhoA is responsible for the phenotype observed in Nocodazole-treated cells, we expressed RhoA L63, a constitutively active form of this small GTPase (RhoA CA) (Nobes and Hall, 1999). RhoA CA-overexpressing cells displayed characteristics similar to Nocodazole-treated cells: abnormal F-actin patterning, cell deformation and blebbing, and impaired nucleus polarisation (Figure 3.8A).

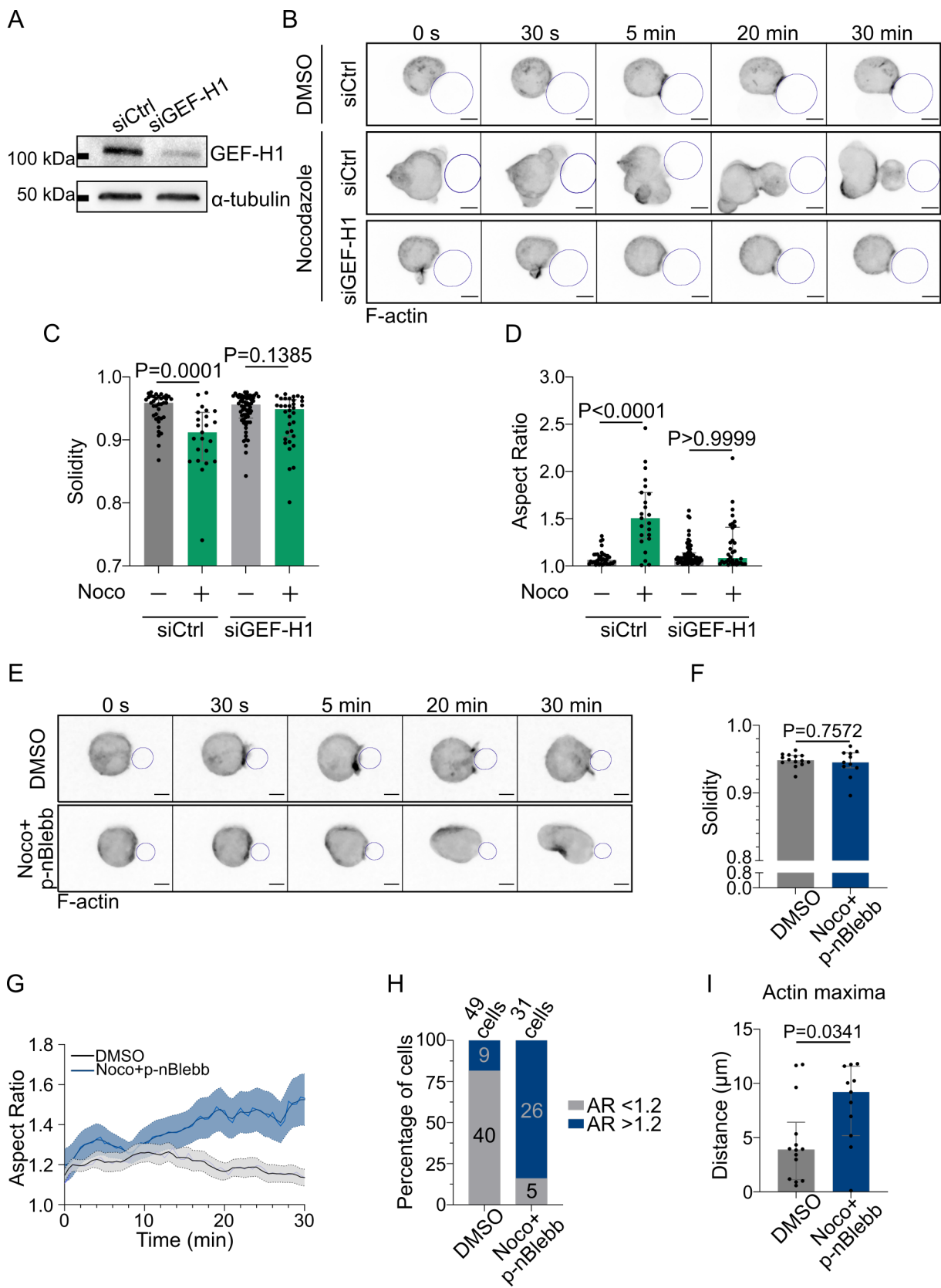


FIGURE 3.9: (Figure on previous page) **GEF-H1 is responsible for cell shape and actin patterning defects upon microtubule depletion, independently of myosin II.** (A) Western blot quantification of the efficiency of GEF-H1 silencing. α -tubulin was used as a loading control. The blot presented is representative of 2 independent experiments. (B) Time lapse images of F-actin in cells transfected with siCtrl or siGEF-H1, and treated with DMSO (control) or Nocodazole. Scale bar 5 μ m. (C) Solidity in 2D and (D) Aspect ratio of cells after 40min of immune synapse formation (siCtrl DMSO N=38, siCtrl Noco N=23, siGEF-H1 DMSO N=65, siGEF-H1 Noco N=34, 2 independent experiments, Kruskal-Wallis test with multiple comparisons between DMSO and Noco). (E) Time lapse images of F-actin, droplet outlined in blue. Scale bar 5 μ m. (F) Median 2D solidity of individual cells over time (Median \pm IQR, DMSO N=14, Noco+p-nBlebb N=11, 3 independent experiments, Mann-Whitney test). (G) Aspect ratio of cells in time (Mean \pm SEM, DMSO N=14, Noco+p-nBlebb N=11, 3 independent experiments). (H) Percentage of cells with Aspect Ratio >1.2 or <1.2 after 40min of synapse formation. (I) Average distance of F-actin maxima to the droplet over 30min of synapse formation (Median \pm IQR, DMSO N=14, Noco+p-nBlebb N=11, 3 independent experiments, Mann-Whitney test)

GEF-H1 is responsible for cell shape and actin patterning defects upon microtubule depletion, independently of myosin II.

The observation that constitutive activation of RhoA leads to abnormal cell shape and actin patterning, which is similar to the phenotype of Nocodazole-treated cells, suggests that this phenotype might indeed result from the activation of the RhoA-specific GEF-H1. To test this hypothesis, we silenced GEF-H1 expression using siRNA (Figure 3.9A). F-actin dynamics and cell shape of these cells were then compared to the ones of DMSO- or Nocodazole-treated cells. We observed that GEF-H1-silenced cells treated with Nocodazole did not display actin-dense regions outside the cell-droplet contact (Figure 3.9B) or blebbs, and maintained a round shape similar to the one of control cells (Figure 3.9B-D). These results therefore suggest that microtubules maintain actin polarisation and cell shape during the phase I of synapse formation by limiting the activation of RhoA-GEF-H1 axis.

Microtubules restrict actin nucleation to the immune synapse

Our results show that when microtubules are depolymerised, GEF-H1 is released, leading to RhoA activation and preventing the polarisation of the actin cytoskeleton at the immune synapse as well as proper cell shape maintenance. We thus next sought to assess the 3D organisation of F-actin, both at the immune synapse and across the cell cortex. For this, we performed 3D SIM imaging of cells fixed after 15-20min of contact with α IgG-coated droplets. We found that the concentric organisation of actin at the immune synapse was conserved upon microtubule depletion, confirming that it did not prevent immune synapse formation (Figure 3.10). However, while the cortex of untreated cells or GEF-H1-silenced Nocodazole-treated cells was relatively uniform

and displayed microvilli-like structures, the cortex of Nocodazole treated cells was very heterogeneous, with actin dense regions, and actin depleted regions, as well as structures similar to small actin bundles in the cortex (Figure 3.10).

These results highlight that microtubules are instrumental to maintain actin polarisation as well as the shape of the cell.

GEF-H1 controls the localised nucleation of F-actin in a myosin II-independent manner

GEF-H1-dependent activation of RhoA can regulate actin patterning either through its impact on myosin II activity, and/or through its promotion of formin-mediated actin polymerisation. We assessed the contribution of myosin II activation in the phenotype of Nocodazole-treated cells by combining Nocodazole with the myosin II inhibitor para-nitroBlebbistatin. We observed that cells treated with Nocodazole+p-nBlebbistatin still displayed actin-rich areas outside of the immune synapse (Figure 3.9E,I). While this abnormal actin polymerisation did not induce cell blebbing (Figure 3.9E,F), it still resulted in cell deformation over time, characterised here by cell elongation in the cell-droplet axis (Figure 3.9G,H). Therefore, myosin II contractility is not responsible for the unpolarised phenotype of the F-actin network observed in nocodazole-treated cells.

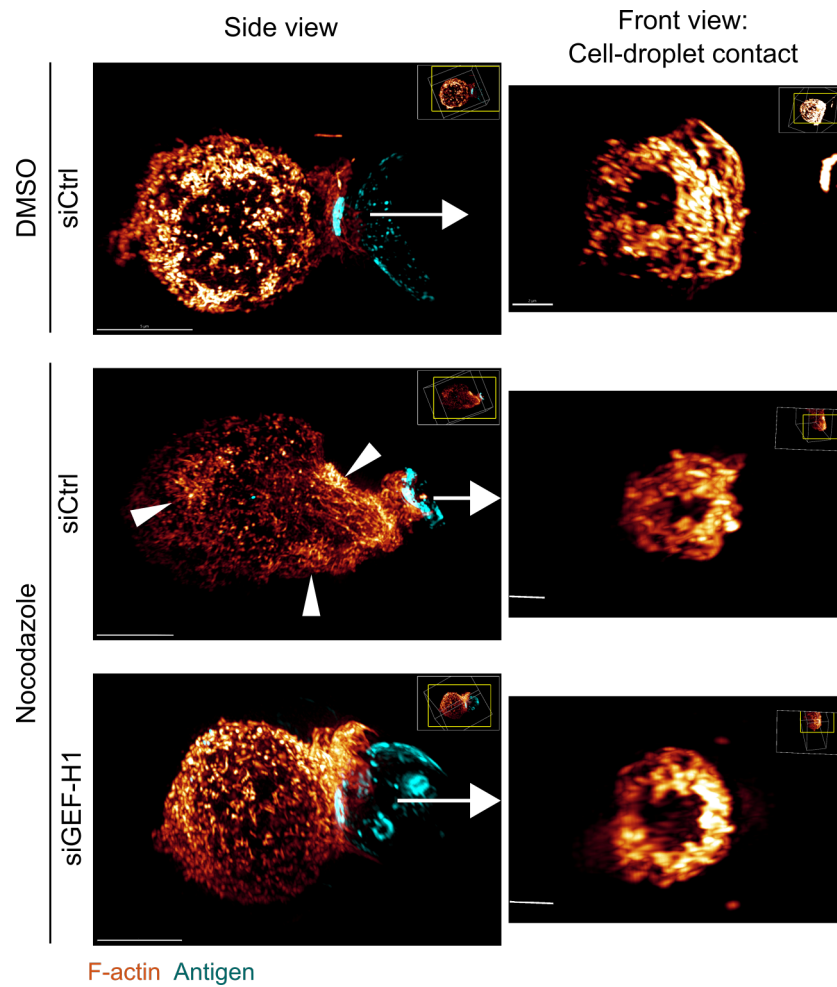


FIGURE 3.10: **Microtubules control the polarised enrichment in F-actin via GEF-H1.** Examples of 3D SIM immunofluorescence imaging of F-actin and antigen on the droplet after 15-20 minutes of immune synapse formation. White arrowheads: sites of actin enrichment outside of the immune synapse. Side view: Scale bar 5 μm . Front view: Scale bar 2 μm .

3.4 Conclusion

In this work, we used a custom microfluidic system to study the role of the actin and microtubule networks in the B lymphocyte immune synapse formation.

We characterised the polarisation dynamics of major actors of the immune synapse, and determined that this process took place in two phases. During Phase 1 (in the first 4 minutes), F-actin is strongly polymerised at the site of contact, leading to antigen accumulation and production of DAG as a result of BCR signaling. During Phase 2, the centrosome is reoriented towards the immune synapse, together with the Golgi apparatus and lysosomes. Meanwhile, the nucleus reorients until its invagination faces the immune synapse, and then transported to the rear of the cell.

We found that while F-actin polymerisation is only necessary for Phase 1 events, microtubules are responsible both for the establishment of the polarity axis during Phase 2, rotating and transporting simultaneously the centrosome and the nucleus, and for restricting actin nucleation to the immune synapse. We showed that this restriction is due to the spatial control of GEF-H1 release and activation, and therefore of RhoA activity. Indeed, global activation of RhoA induced actin polymerisation outside of the immune synapse area in a GEF-H1 dependent manner, but independently of myosin II activity (Figure 3.11).

These results show that the early and late events of synapse formation are not independent but rather coupled through the GEF-H1-mediated interaction between the microtubule and actin cytoskeleton.

This work is on-going and will soon be submitted for publication in a peer-reviewed journal.

Microtubules

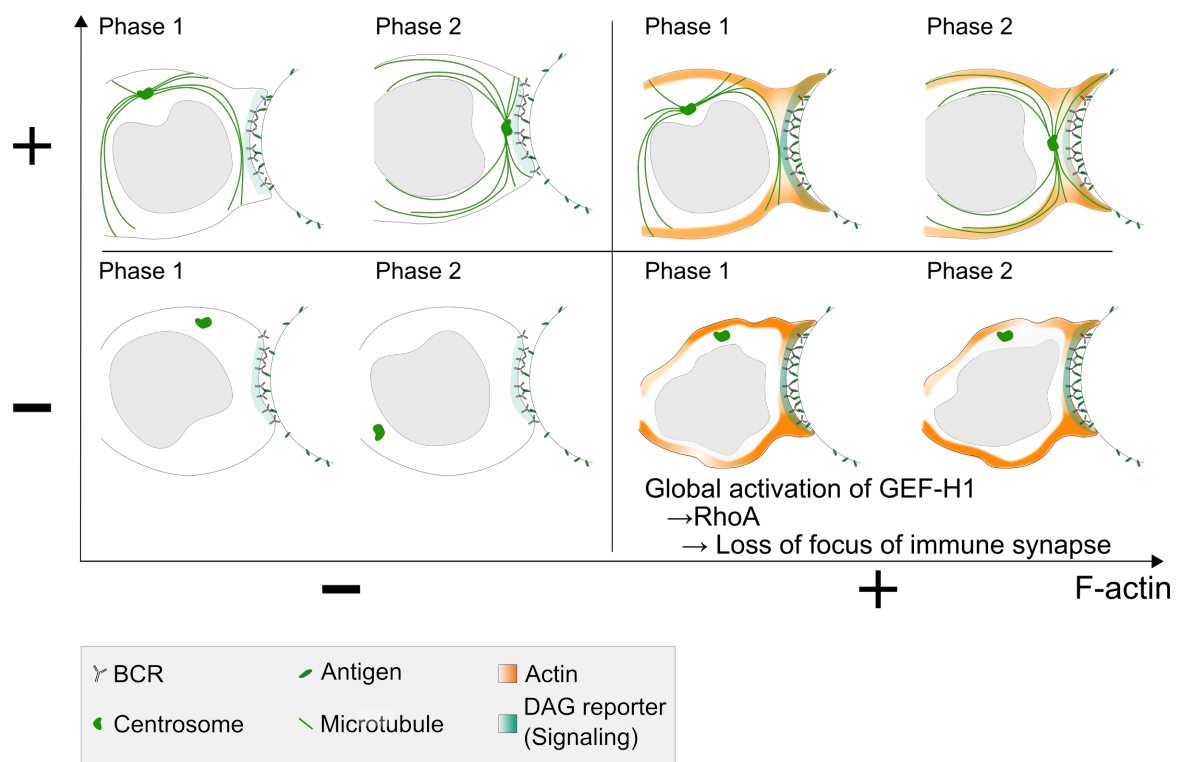


FIGURE 3.11: Immune synapse formation has two phases, with different dependencies on actin and microtubules.

Chapter 4

Discussion

While the existence of immune synapses was first suggested by Norcross, 1984, and described in CD4⁺ T cells in Monks et al., 1998 and Dustin et al., 1998, the cell biology aspect of lymphocyte activation remained largely overlooked in B cells for a long time. The discovery that B lymphocytes could acquire antigens from the surface of other immune cells in lymph nodes, and therefore establish immune synapses, gave a new impulse to this research field (Carrasco and Batista, 2007; Junt et al., 2007; Fleire, 2006). One distinguishing factor of the B lymphocyte immune synapse is that it serves as a platform for antigen extraction and internalisation. This process is key for the further activation of B lymphocytes and can occur either through mechanical pulling on the antigen, or through cell polarisation and protease secretion to facilitate antigen degradation and uptake.

In this work, we focused on two aspects of antigen extraction: force generation at the immune synapse for mechanical extraction, and the relationship between the establishment of polarity and immune synapse formation, with particular attention to the cell cytoskeleton.

In this last part, I would like to discuss the results presented in Chapter 2 and 3 along three different axis: (1) the role of actomyosin contractions at the immune synapse, (2) the importance of actin-microtubule interactions in immune synapse formation, and (3) the implications for primary B cells and physiological conditions.

4.1 Role of actomyosin contractions and structures at the immune synapse

In Chapter 2, we showed that forces are patterned at the immune synapse of B lymphocytes, with the build-up of a contractile concentric ring upon BCR engagement, consistent with findings from other teams (Wang et al., 2018), as well as localised forces found at the centre of the immune synapse. We propose that force patterning emerges from the segregation of molecular components at the cell-antigen interface due to actomyosin-dependent pulsatile contractions. This process differs from the one previously described in B lymphocytes interacting with antigen-coated lipid bilayers, in which the transport of molecules requires centripetal actin flows (Fleire, 2006; Liu et al., 2012; Murugesan et al., 2016), which we did not detect in B cells interacting with antigen-coated gels. This difference could stem from the fact that (1) on gels, antigens and cells are anchored to the substrate and allow force transmission, and/or (2) lipid bilayers and glass are several orders of magnitude stiffer than the PAA gels used in this study.

We observed protrusive actin patches at the centre of the synapse, similar to invadosome-like protrusions, where antigen extraction occurs. This is consistent with *in vitro* studies showing that when an actomyosin active gel is coupled to the cell membrane, it can indeed form actin patches as long as a sufficient number of contractile elements are present (Chaudhuri et al., 2011; Gowrishankar et al., 2012; Laplaud et al., 2021). It is therefore likely that shear coordinated forces generated by myosin II-dependent pulsatile contractions at the synapse periphery do not directly contribute to antigen extraction but rather help the cell to build stable protrusive actin structures where extraction occurs. Of note, we and the teams of Olivia du Roure and Matthieu Piel have recently shown that, in dendritic cells, cortex thickness and instabilities are mostly regulated by myosin II activity, as compared to the contribution of actin nucleators (Laplaud et al., 2021, see Appendix C.3). Indeed, myosin II inhibition led not only to a decrease in cortex thickness, but also to a 2-fold decrease in cortex thickness fluctuation amplitude and in actin protrusion frequencies (Laplaud et al., 2021).

We propose that the protrusive actin structures described in B lymphocytes correspond to protrusions emerging from actomyosin contractility in the cortex.

In this context, the increased number of actin patches observed in the presence of antigen could result from increased actomyosin contractility upon BCR engagement. Conversely, their loss upon myosin II inhibition reflects the strong myosin II-dependent cortex fluctuations described in dendritic cells. Hence, it appears that both global contractility and local force generation are involved in antigen extraction,

reconciling the two existing models. Alternatively, the actomyosin peripheral ring might also act as a mechanical damper by sealing the synapse area and isolating its centre from external mechanical noise, for example, owing to lymph node/vessel contractions or cell movements/proliferation. This could improve antigen affinity mechanical discrimination by the BCR (Natkanski et al., 2013).

We showed that protrusive actin patches are stabilised in the presence of BCR-specific antigens. This suggests that B lymphocytes might scan their environment using unstable actin protrusions which would be stabilised upon antigen binding, similar to the process described in T cells (Cai et al., 2017). We observed that actin rich protrusions often associated with sites of antigen extraction, and sometimes with clathrin patches. This points to actin patches being preferential sites for antigen internalisation, as has been described for both clathrin-mediated endocytosis and clathrin-independent IL2 receptor endocytosis (Shevchuk et al., 2012; Basquin et al., 2015). Interestingly, similar actin-rich pod-like structures have recently been described in human Light Zone B cells plated on activating plasma membrane sheets, where they are sites of antigen internalisation (Kwak et al., 2018). Although we cannot, at this stage, be certain of the correspondence between these actin pods and the protrusive structures we describe, our study provides a possible mechanism for their emergence.

We demonstrated that the release of lysosomal calcium stores enhances myosin II-driven peripheral forces, but also actin patch formation and antigen extraction. This further supports the hypothesis that cortical actomyosin contractility could regulate the formation and stability of protrusive actin structures. We do not exclude that calcium release might also promote the activity of other myosin motors such as class I myosins, which are typically required for clathrin-mediated endocytosis (Kaksonen, Toret, and Drubin, 2006; Pedersen and Drubin, 2019; Cheng, Grassart, and Drubin, 2012). This would help to couple global myosin II contractions at the cell periphery with local endocytosis at actin patches. Indeed, while the stall force of a single myosin motor is $<2\text{pN}$ (McIntosh and Ostap, 2016), the minimal force required to activate a BCR is 16pN (measured by DNA tension sensors in Wan et al., 2015), indicating the need for at least eight myosin motors to activate a single receptor. Moreover, even higher forces have been reported at sites of antigen extraction, with 56pN rupture forces being measured by Wan et al., 2015, and biotin-streptavidin bond ruptures being reported by Natkanski et al., 2013 (requiring 160pN , or 80 myosin II motors). Temporal coordination of motor activity has been shown to allow a single contractile element to apply forces of up to 1nN (Lohner et al., 2019). Ca^{2+} oscillations triggered upon BCR engagement (Ketchum et al., 2018) might contribute to the synchronisation

of myosin II motor activity, and the release of lysosomal calcium stores upon MLSA1 treatment would amplify this phenomenon. While lysosome polarisation has been shown to be not as pronounced during mechanical antigen extraction as during proteolytic antigen extraction, descriptions from Spillane and Tolar, 2016 still find around 90% of lysosomes to be in the synapse area rather than in the total cell volume. This proximity of lysosomes to the immune synapse area could support mechanical extraction of surface antigen by facilitating local calcium release.

Spatio-temporal force patterning was first highlighted in the context of tissues (Heisenberg and Bellaïche, 2013), cell adhesion to a substrate (Heisenberg and Bellaïche, 2013; Shiu et al., 2018), and cell motility (Trepate et al., 2009). Our study shows that it might be a more general and basic feature of cell–cell interfaces where the engagement of surface receptors leads to both juxtacrine signaling and ligand endocytosis. We found that myosin II intervenes in this process as a global master organiser of forces and actin organisation, and thus as an indirect but key actor of endocytosis, which is essential for adaptive immunity. We anticipate that this study could set the ground for future work aimed at exploring force patterning in additional cell-to-cell communication models.

4.2 Control of immune synapse formation by actin and microtubule interactions

The importance of interactions and co-regulations between cytoskeletal networks in cell polarity has become increasingly clear in the past few years (Dogterom and Koenderink, 2019). In the context of the B lymphocyte immune synapse, we believe that both actin and microtubule networks could contribute to the robustness of immune synapse formation, antigen extraction and internalisation. A few years ago, Spillane and Tolar, 2016 described that B lymphocytes first attempt to extract the antigen mechanically, and only proceed to lysosome polarisation for proteolytic extraction of the antigen upon failure of mechanical extraction. In this context, actomyosin was described to be at the core of the mechanical pathway (Natkanski et al., 2013; Kumari et al., 2019), while the proteolytic pathway relies heavily on the microtubule network for lysosome transport towards the immune synapse (Sáez et al., 2019; Yuseff et al., 2011). However, the importance of microtubules in the mechanical pathway, and of actomyosin in the proteolytic pathway, is not clear.

We showed that, in our system, F-actin is only necessary for the early events of immune synapse formation (Phase 1: F-actin polymerisation, antigen gathering, BCR signaling amplification), while microtubules control late events (Phase 2: reorganisation of organelles along a polarity axis) and restrict F-actin polymerisation to the immune synapse.

We propose that Phase 1 could correspond to an attempt at mechanical extraction of the antigen, and Phase 2 to the reorganisation of intracellular components for proteolytic extraction (Figure 4.1).

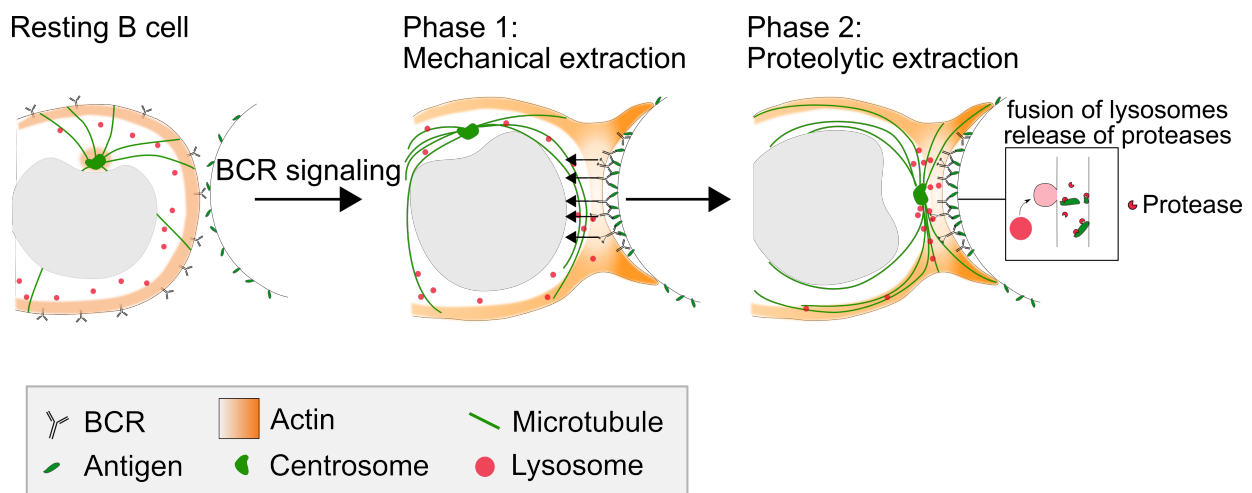


FIGURE 4.1: Phase 1 corresponds to an attempt at mechanical extraction of the antigen, and Phase 2 to the reorganisation of intracellular components for proteolytic extraction.

In this context, Phase 2 events such as the reorientation of the microtubule network would not be necessary for mechanical extraction of the antigen, consistent with the absence of lysosome polarisation in that pathway (Spillane and Tolar, 2016). Interestingly, centrosome reorientation starts from the instant of contact with the antigen, suggesting that this process would occur by default, from the start of BCR signaling, and could be stopped upon antigen internalisation through the mechanical pathway, as described by Spillane and Tolar, 2016. This hypothesis is reinforced by the fact that centrosome polarisation is maintained upon F-actin depolymerisation, when BCR signaling is very low and only due to residual BCR-antigen interaction at the cell-droplet contact. These observations point to centrosome polarisation being triggered by a low threshold of lymphocyte receptor signaling, similar to what was described in Cytotoxic T cells by Jenkins et al., 2009, where centrosome polarisation occurs in response to low-avidity interactions, while killing efficiency relied on a higher threshold set for granule polarisation and secretion. In the case of B lymphocytes, centrosome polarisation in the absence of proper F-actin polymerisation could be a way to keep the mechanical and the proteolytic pathways independent. Indeed, if the B cell fails to extract antigen mechanically due to defects in actin polymerisation at the immune synapse, it is still able to reorient the centrosome, and possibly carry out proteolytic extraction. However, we do not know whether B lymphocytes are able to polarise lysosomes and secrete proteases in the absence of F-actin, or whether these steps require stronger receptor signaling as in Cytotoxic T cells (Jenkins et al., 2009). Moreover, the polarisation state of the microtubule network, and its role in mechanical extraction remains to be described to fully assess the independency of the two pathways of antigen extraction.

In Phase 2, the centrosome reorients and transports materials necessary for proteolytic extraction of the antigen. It has been shown recently that microtubules are acetylated in the vicinity of the centrosome upon immune synapse formation, resulting in the localised release and activation of GEF-H1 at the immune synapse (Sáez et al., 2019; Seetharaman et al., 2021). In our system, disruption of microtubules induced the activation of RhoA throughout the cell via GEF-H1 release, leading to areas of strong actin polymerisation outside of the immune synapse.

We propose that the reorientation of the microtubule network and the local activation of mDia1 by RhoA-GEF-H1 promotes actin polymerisation at the immune synapse, while leaving mDia1 in its autoinhibited state in the rest of the cell (Figure 4.2).

One possible interpretation of this polarisation mechanism is the LEGI (Local Excitation Global Inhibition) model (Parent and Devreotes, 1999). In this model, classically used in *D.discoideum* amoeba, symmetry breaking arises from local positive feedback

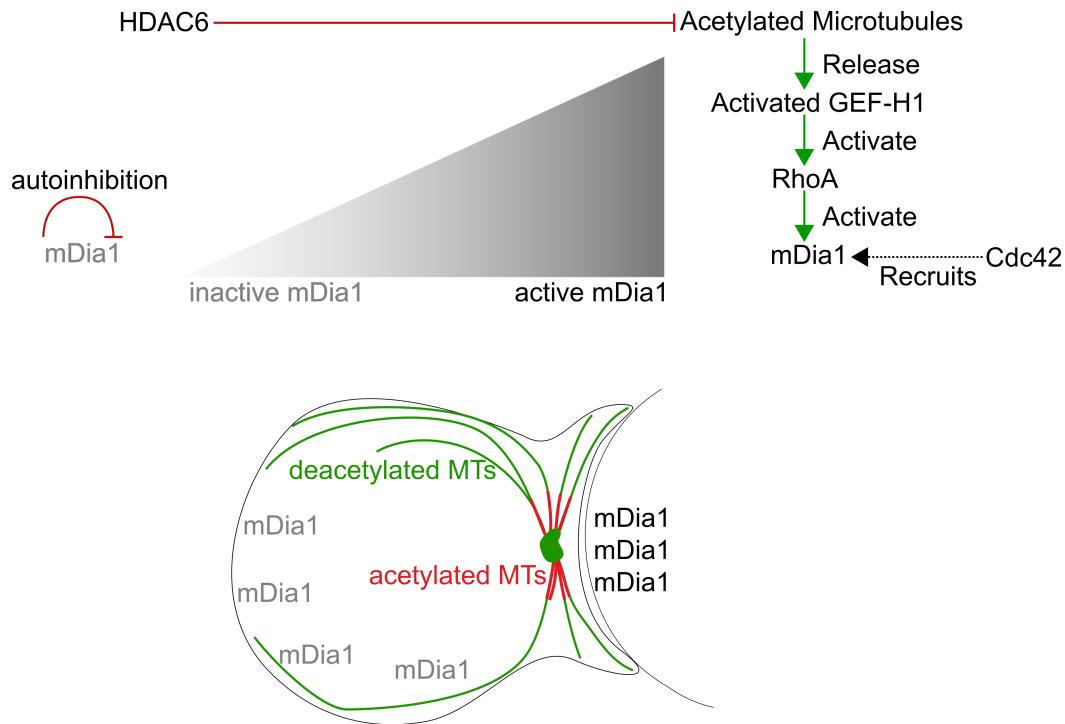


FIGURE 4.2: **Model for the polarised activation of mDia1.**

(typically PIP_3 , promoting F-actin polymerisation) combined with a globally active diffusible inhibitory signal (typically PTEN, a PIP_3 phosphatase, hence polarity) (Janetopoulos et al., 2004; Devreotes and Janetopoulos, 2003). In our case, local excitation could emerge from BCR signaling, resulting in Cdc42 activation and mDia1 recruitment (Etienne-Manneville, 2004), as well as the local recruitment and activation of GEF-H1 at the immune synapse and subsequent release of mDia1 auto-inhibition (Sáez et al., 2019; Suarez and Kovar, 2016). Meanwhile, the global inhibition signal would correspond to the return of mDia1 to its basal auto-inhibited state (Li and Higgs, 2003), and possibly to the deacetylation of microtubules by HDAC6, whose role in immune synapse organisation has already been highlighted in CD4^+ and CD8^+ T cells (Núñez-Andrade et al., 2016; Serrador et al., 2004).

In addition, GEF-H1 is necessary for the assembly of the exocyst complex at the immune synapse, and therefore for protease secretion (Sáez et al., 2019). *In this context, we propose that the localised release and activation of GEF-H1 by microtubules at the immune synapse allows for the concentration of resources, promoting F-actin polymerisation and optimising proteolytic extraction at one site.* Polarisation of the centrosome and reorientation of the microtubule network would thus ensure the formation of a unique immune synapse during proteolytic extraction, raising the question of whether, in the absence of microtubules or during mechanical extraction, multiple synapses could form. We were able to observe multiple fully formed immune synapses on Nocodazole-treated

cells (Figure 4.3), but whether or not this is specific to the non-localised activation of RhoA, and whether this could occur in the case of mechanical extraction remain to be explored.

In the case of mechanical extraction, the formation of multiple synapses, for example with several subcapsular macrophages having captured antigen from the afferent lymph flow, could allow B lymphocytes to scan more surfaces for antigen, and accelerate antigen uptake.

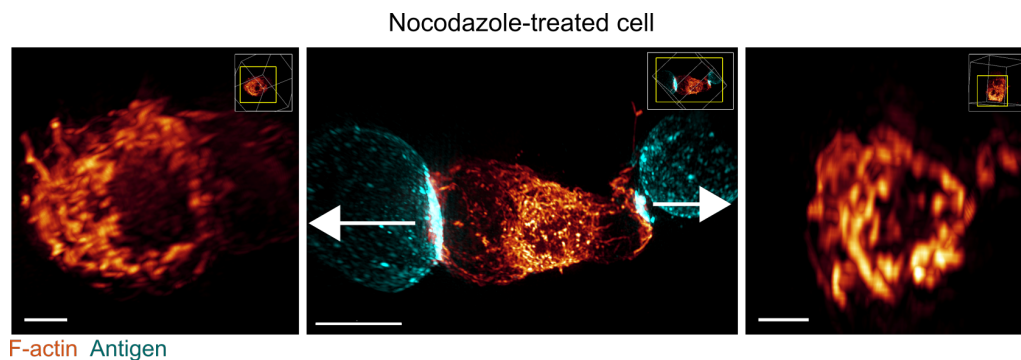


FIGURE 4.3: Nocodazole-treated cells can form multiple immune synapses Example of 3D SIM immunofluorescence imaging of F-actin and antigen on the droplet in a Nocodazole-treated cell, after 15-20 minutes of immune synapse formation. Global view: Cell forming contacts with 2 droplets, Scale bar 5 μ m. Insets: views of the cell-droplet contacts/immune synapses, Scale bar 2 μ m.

Ultimately, we propose that this mechanism allows B lymphocytes to optimise the specific extraction of high-affinity antigens. While mechanical extraction relies on direct pulling on the BCR-antigen link and is therefore limited to antigens with a strong interaction with the BCR, secreted proteases would affect any protein in the vicinity of the release area. If not focused on a dense cluster of high-affinity antigens, the release of proteases could increase the uptake of low-affinity antigens. In addition, the release of proteases in several locations, or in an open environment (as opposed to the tight synaptic cleft) could result in a lower local concentration of proteases, and therefore lower efficiency of antigen uptake. Thus, these results further suggest a role for the contractile actomyosin ring in immune synapse isolation, optimising antigen affinity discrimination and specific uptake of high-affinity antigens.

In the future, monitoring of immune synapse formation and B lymphocyte polarisation during both mechanical and proteolytic extraction, for example by using antigens tethered through DNA force sensors of increasing rupture forces (Spillane and Tolar, 2016; Wan et al., 2015) or tuning droplet surface tension, could help to decipher the processes necessary for each pathway. Furthermore, combination of this system with

antigens of different affinities could shed light on the importance of the different phases of immune synapse formation, and of the different pathways of antigen extraction in the specific uptake of high-affinity antigens.

4.3 Implications in primary cells and physiological conditions

While cell lines are very versatile and easy models to study lymphocytes, it is well known that their properties do not always recapitulate those of primary lymphocytes. For example, many differences between actin structures at the immune synapse of CD4⁺ T cells of primary murine/human T cells or immortalised Jurkat T cells have been highlighted recently by Colin-York et al., 2020. In the lab, we noticed a strong difference in traction forces between primary murine B lymphocytes and immortalised IIA1.6 cells or A20 B cells, with cell lines applying considerably less forces on the substrate (measure of bead movement close to noise, data not shown). These observations, in addition to the fact that IIA1.6 cells are IgG⁺ while naive B cells are IgM⁺, prompted us to explore whether the characterisation of immune synapse formation made in IIA1.6 cells would match observations in primary murine B cells. Of note, very few studies looking at B lymphocyte polarisation have been conducted with primary B cells. This is mostly due to their small size (half that of the cell line), short lifespan without activation after extraction from the spleen (~1 day), and limited possibilities of transfection, making both their imaging and the study of molecular mechanisms difficult. Here, I will present original data obtained during my PhD using murine primary B lymphocytes.

To study immune synapse formation in primary cells, we adapted our microfluidic system to the small size of primary B lymphocytes (~6-7µm diameter). Indeed, a cell of this dimension could easily pass through the hole at the back of the traps of the original design and slip above/below droplets due to the height of the chips (~16µm). We therefore designed smaller traps, with smaller holes, and manufactured chips of only ~9µm height, which is a technical challenge in microfabrication (Figure 4.4A).

We established that primary B lymphocytes were able to form an immune synapse with F(ab')₂ αIgM-coated droplets, specifically recruiting antigen and enriching the synaptic area in both F-actin and myosin II (Figure 4.4B-D). Interestingly, we noticed that a little over 50% of cells formed small actomyosin-rich punches at the cell-droplet interface, extending a protrusion perpendicular to the droplet surface (Figure 4.5A,D). However, imaging of the centrosome of primary B lymphocytes during immune synapse formation revealed a behaviour that differed strongly from the one observed in cell lines, with no stable centrosome polarisation or docking (Figure 4.4E,F).

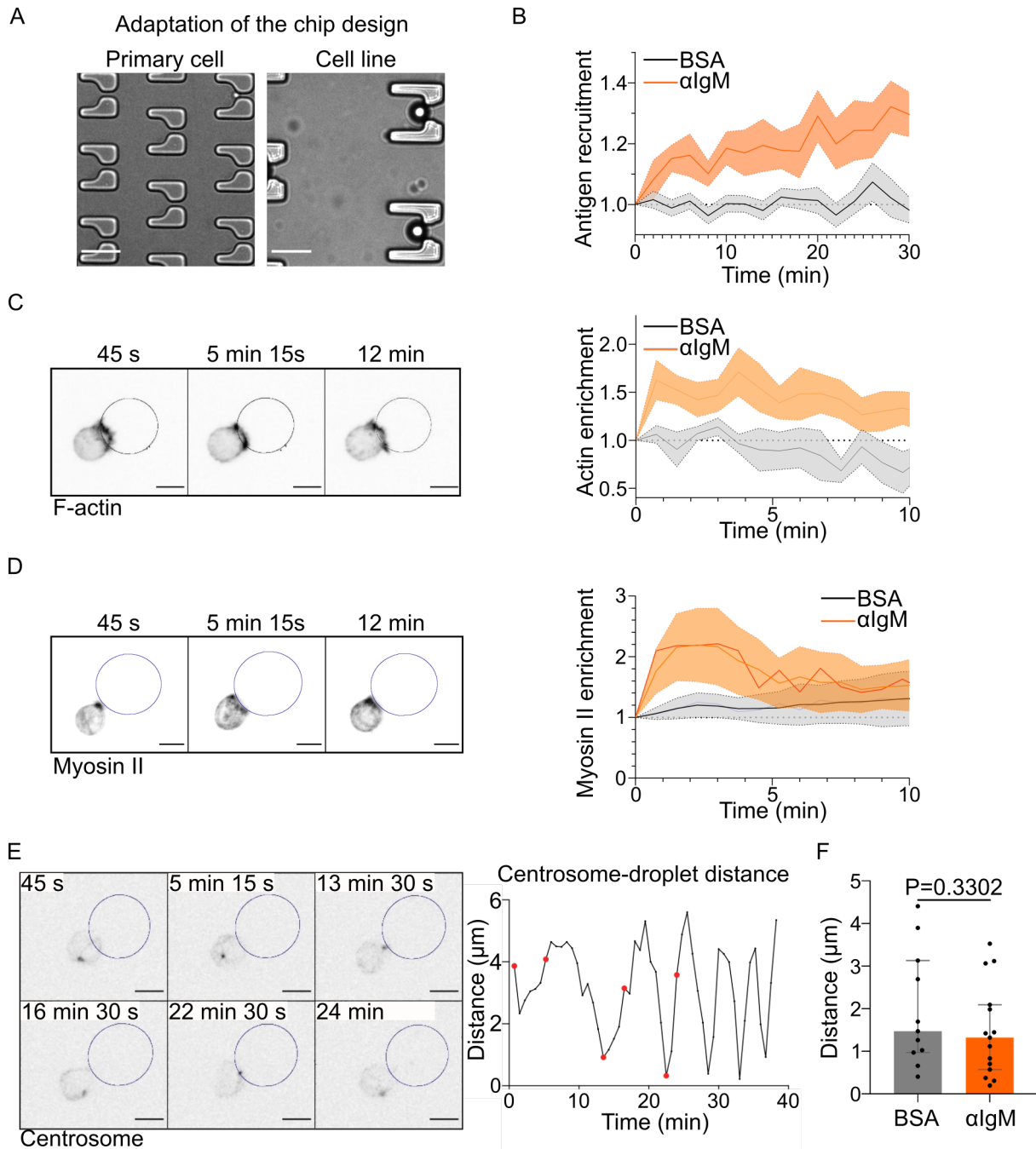


FIGURE 4.4: Primary B lymphocytes complete Phase 1, but not Phase 2 of immune synapse formation. (A) Bright field image of microfluidic traps adapted for primary B lymphocytes, and the original traps for cell lines. Scale bar $20\mu\text{m}$. (B) Preliminary experiment: antigen recruitment in time for BSA- (negative control) or α IgM-coated droplets (Mean \pm SEM, BSA N=12, α IgM N=12, 1 experiment). (C) Time lapse images of F-Actin (LifeAct-GFP) in a cell in contact with a α IgM-coated droplet. Outline of the droplet. Scale bar $5\mu\text{m}$. Right: Actin enrichment near the droplet in time for BSA- (negative control) or α IgM-coated droplets (Mean \pm SEM, BSA N=3, α IgM N=18, 2 independent experiments). (D) Time lapse images of Myosin II (Myosin II-GFP). Right: Myosin II enrichment near the droplet in time for BSA- (negative control) or α IgM-coated droplets (Mean \pm SEM, BSA N=7, α IgM N=12, 2 independent experiments). (E) Time lapse images of the centrosome (SirTubulin). Outline of the droplet. Right: Centrosome-droplet distance for the cell, points corresponding to the timelapse highlighted in red. (F) Average Centrosome-droplet distance (10-20 min of synapse formation) (Media \pm IQR, BSA N=11, α IgM N=15, 1 representative experiment, Mann-Whitney test).

We first hypothesised that this phenomenon could be due to insufficient B cell activation by F(ab')₂ α IgM in this system, leading to an unstable synapse, similar to the kinapse described in CD8⁺ T cells (Moreau et al., 2012; Moreau et al., 2015; Mayya et al., 2018). We therefore explored experimental conditions to increase BCR signaling. First, we repeated this experiment using naive B cells extracted from MD4⁺/⁻ mice (expressing a HEL-specific BCR as in Traction Force Microscopy experiments), paired with HEL-coated droplets. However, this did not induce stable polarisation of the centrosome towards HEL-coated droplets compared to BSA-coated droplets (data not shown). We then proceeded to combine BCR ligand with ICAM-1 on the droplet, as LFA-1 engagement by ICAM-1 has been described to lower the threshold for B cell activation and facilitate immune synapse formation (Carrasco et al., 2004). Surprisingly, we still did not observe stable centrosome polarisation, and instead noticed that cells formed longer punches at the immune synapse (Figure 4.5B), reminiscent of those observed in Nocodazole or Nocodazole+p-nBlebbistatin-treated cell lines. Of note, we also observed actomyosin-dense punches in Nocodazole-treated primary cells (Figure 4.5C). We established, as part of a collaboration with the team of Yolanda Carrasco, that LFA-1 engagement by ICAM-1 increases traction forces at the B cell immune synapse (Merino-Cortés et al., 2020, see Appendix C.2). Together with the phenotype observed in Nocodazole treated cells, these results suggest a role for actomyosin contractility in the formation of actomyosin-rich punches at the immune synapse, and the absence of centrosome polarisation.

The low traction forces exerted by B lymphoma cell lines as compared to primary B cells suggest that primary B cells could be more contractile than their immortalised counterpart. We propose that the high contractility of primary B lymphocytes could make them more apt at performing mechanical extraction of the antigen, therefore limiting the need for centrosome polarisation. In the presence of ICAM-1, enhanced actomyosin contractility would lead to microtubule instability, global release and activation GEF-H1, and increase in RhoA activity, thus creating a positive feedback loop of actomyosin contractility (Merino-Cortés et al., 2020; Colin et al., 2018; Chang et al., 2008).

Previous studies have described polarisation of the centrosome of primary B lymphocytes upon antigen encounter on polystyrene beads (Yuseff et al., 2011; Wang et al., 2017), although it appeared less stable and direct than in B lymphoma cell lines. However, none have described the formation of actomyosin-rich punches at the B cell immune synapse, while this phenomenon has been studied in the case of CD4⁺ T cells (Husson et al., 2011; Sawicka et al., 2017). The strikingly divergence between

phenotypes observed on antigen-coated beads or on antigen-coated lipid droplets stresses the importance of substrate properties for the study of immune synapse formation. Here, the differences could be explained by two separate phenomena. (1) Antigen-coated beads allow force transmission to the substrate through anchored antigens, while the high ligand mobility on oil droplets deprives B lymphocytes of anchorage. Without force transmission to the substrate, and due to high actomyosin contractility, primary B lymphocytes could collapse the actin-rich protrusions that scan the antigen-coated surface into an actomyosin-rich punch, thus preventing centrosome polarisation by hindering microtubule access to the immune synapse (Colin et al., 2018; Reymann et al., 2012). (2) Polystyrene beads appear much stiffer than oil droplets, with polystyrene having a Young's modulus of $\sim 3200\text{-}3400\text{MPa}$ (Brandrup, Immergut, and Grulke, 1975), while the surface tension of the soybean oil droplets used in this study corresponds to a Laplace pressure of 4kPa for a droplet of $5\mu\text{m}$ diameter. Oil droplets could appear "soft" enough to the B lymphocytes and allow mechanical extraction of the antigen to occur.

We believe that the use of primary B lymphocytes for the study of polarisation at the immune synapse could allow further exploration of the balance between mechanical and proteolytic extraction and its link with cell polarity, in a dynamic manner. Adaptation of this system to primary B lymphocytes also paves the way to its application to the study of the dynamics of immune synapse formation and polarisation in T lymphocytes or NK cells.

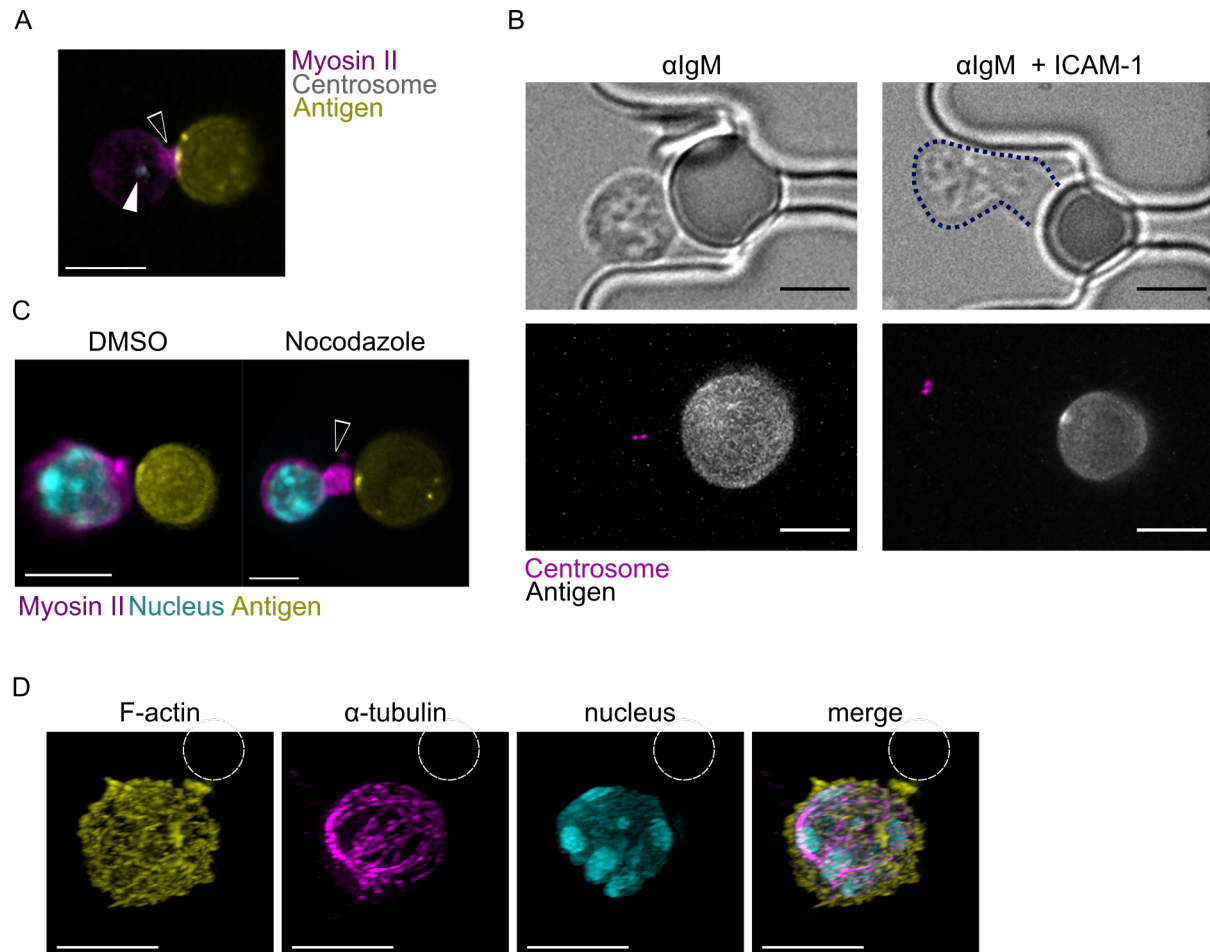


FIGURE 4.5: Primary B lymphocytes form actomyosin-rich punches at the immune synapse, promoted by actomyosin contractility (A) Example of a myosin II-GFP primary B lymphocyte forming a punch at the contact with an α IgM-coated droplet after 20min of contact. Scale bar 5 μ m. Centrosome (SirTubulin) in grey, myosin II in magenta, α IgM in yellow. White full arrowhead points to the centrosome, empty arrowhead points to the punch. (B) Example of a Centrin-GFP primary B lymphocyte forming a punch at the contact with an α IgM- or α IgM+ICAM-1-coated droplet after 20min of contact. Scale bar 5 μ m. Centrin in magenta, α IgM/ α IgM+ICAM-1 in yellow. (C) Example of a Nocodazole-treated myosin II-GFP primary B lymphocyte forming a punch at the contact with an α IgM-coated droplet after 20min of contact. Scale bar 5 μ m. Nucleus (Hoechst) in cyan, myosin II in magenta, α IgM in yellow, empty arrowhead points to the punch. (D) 3D SIM imaging of a primary B cell in contact with an α IgM-coated droplet. F-actin (Phalloidin) in yellow, α -tubulin (Rat anti- α -tubulin) in magenta, nucleus (Hoechst) in cyan. Outline of the droplet in white. Scale bar 5 μ m.

4.4 Concluding remarks and perspectives

In this work, we studied different aspects of the cytoskeletal regulation of immune synapse formation, in the case of mechanical extraction and proteolytic extraction. First, we established that **B lymphocytes pattern forces at the immune synapse in a myosin II-dependent manner, and that actomyosin contractility regulates the formation and stability of actin protrusive structures at the centre of synapse, and the extraction and internalisation of antigen at these sites.** Next, we conducted a systematic study of the dynamics of immune synapse formation and established that this process comprises two phases. The first phase consists in F-actin polymerisation at the immune synapse, antigen gathering and BCR signaling amplification, and is followed by a second phase during which a cell polarity axis is formed, with the docking of the centrosome and the Golgi apparatus at the immune synapse, lysosome polarisation and nucleus rearward transport. **We established that while F-actin is only necessary for Phase 1 events, microtubules not only support the establishment of the nucleus-centrosome polarity axis, but also restrict F-actin polymerisation to the immune synapse. This regulation is achieved through the spatiotemporal control of GEF-H1 release and activation, and therefore of RhoA activation, independently of myosin II activity.** Disruption of this regulation, through microtubule depolymerisation for example, does not impair the structure of the immune synapse, but affects the state of the whole cortex and could lead to the formation of multiple synapses, or to decreased efficiency of the immune synapse due to scattering of resources between several sites.

This work highlights the importance and robustness of the formation of the stereotypical actin pattern at the immune synapse. In the case of mechanical extraction, the contractile ring could promote the formation of actin protrusive structures by regulating cortex or membrane tension, and mechanically isolate the centre of the synapse to facilitate antigen affinity discrimination by mechanical pulling. In the case of proteolytic extraction, our data suggest that microtubule properties and centrosome reorientation ensure the unicity of the immune synapse by transporting intracellular components such as vesicles, but also preventing the polymerisation of F-actin outside of the immune synapse. In this context, microtubule support the formation of a unique immune synapse, as well as the assembly of the exocyst complex, by the local release and activation of GEF-H1. The actomyosin ring provides a scaffold to isolate the synaptic cleft from the environment and concentrate proteases to an antigen-enriched area.

Despite having been studied for over 60 years, some aspects of B lymphocyte function, namely the cellular biology mechanisms regulating their activation and the onset of the humoral immune response, remain poorly understood. How do B lymphocytes discriminate antigen affinity *in vivo*, in a crowded environment, surrounded by potential ligands, pushed by migrating cells? How do B lymphocytes terminate an immune synapse and detach? What aspects of cell polarisation are conserved in the case of mechanical extraction? Which one of the antigen extraction pathways is more common *in vivo*, and does it differ depending on the context (inflammation state, antigen type)? What is the role of nuclear deformation during B lymphocyte activation, does it have an impact on gene expression, similar to what was described in T cells (Gupta et al., 2012)?

These results stress the need for new systems to study B cell immune synapse formation, facilitating the comparison of cellular processes during mechanical or proteolytic extraction, and complexifying the experimental environment to recapitulate some aspects of *in vivo* conditions for antigen encounter by B lymphocytes. In the past 15 years, moving from the study of B cell immune synapses on glass to their study on fluid substrates, soft substrates or 3D substrates has greatly contributed to understanding the mechanisms of immune synapse formation, antigen affinity discrimination and extraction. I believe that the use of oil droplets as antigen presenting substrates could allow the diversification of substrate properties in a controlled manner, modifying one physico-chemical feature (surface tension, size, coating, diffusion) at a time. Complexification could also come from modifying the 3D environment, for example, recapitulating 3D crowding in densely packed lymph nodes, its variation upon clonal expansion, or the viscosity of the lymphatic fluid that constitutes the environment in which B lymphocytes live. I am confident that the development of new systems to study the immune synapse will unravel new functions for some of the previously described structures.

I end this PhD with more questions than I could possibly answer, and the hope that my work could provide the B cell biology community with new approaches to answer many of them. I have the intuition that this field still has many exciting discoveries to be made, and am impatient to discover the next surprises that the long-known B cells still have for us.

Chapter 5

Materials and Methods

5.1 For Chapter 2

5.1.1 Cells and cell culture

CLICK medium: RPMI 1640 – GlutaMax-I + 10% fetal calf serum, 1% penicillin–streptomycin, 0.1% β mercaptoethanol, and 2% sodium pyruvate). Fetal calf serum was decomplexed for 40min at 56°C. All cell culture products were purchased from GIBCO/Life Technologies.

Murine primary B lymphocytes were extracted from the spleen of 8 to 12 weeks-old male of female mice using the B cell purification kit (Miltenyi 130-090-862). Primary B lymphocytes were kept in CLICK medium supplemented with 25mM HEPES (15630080, Gibco) and 1X NEAA (11140050, Gibco) throughout the experiment. The C57BL/B6J mouse line as well as transgenic MD4 and LifeAct-GFP mouse lines (described elsewhere, (Riedl et al., 2008; Goodnow et al., 1988)) allowed us to obtain all combinations necessary. Animals were bred and cared for according to the European and French national regulations for the protection of vertebrate animals used for experimental and other scientific purposes (Directive 2010/63; French Decree 2013-118).

5.1.2 Reagents

For Polyacrylamide gel preparation and related experiments 40% Acrylamide Solution (Biorad 1610140), 2% Bis Solution (Biorad 161-0142), 3-aminopropyltrimethoxysilane (APTMS) (Sigma-Aldrich 281778), Ammonium Persulfate (APS) (Sigma-Aldrich A3678), TEMED (Euromedex 50406-B), Sigmacote (Sigma-Aldrich SL2), Fluosphere: carboxylate-modified, 0.2 μ m, dark red (Molecular Probes F8807), Sulfo-SANPAH (Thermofisher 22589), Alexa555 microscale protein labeling kit (Molecular Probes A30007).

Antibodies and reagents Fluoromount-G (Southern Biotech, 0100-01), Mouse Fc Block (BD Pharmingen, 553142), Rabbit anti-phospho-Cortactin (pTyr466) (Sigma-Aldrich, SAB4504373, 1:200), rabbit anti Clathrin (Cell Signalling, 4796, 1:50), Mouse anti Vinculin (Sigma, V9264, 1:200), Rabbit anti phospho-Paxillin (Cell Signalling, 2541, 1:50), Alexa Fluor 488 Phalloidin (Invitrogen, A12379 1:200), Alexa Fluor 405 Goat anti-Rabbit IgG (H+L) (Thermofisher, A31556, 1:200), Alexa Fluor 546 Goat anti-Mouse IgG1 (Thermofisher, A-21123, 1:200), Formaldehyde 16% in aqueous solution (Euromedex, 15710), BSA (Euromedex, 04-100-812-C), PBS (Gibco, 10010002), Triton X-100 (Sigma-Aldrich, T8787), Glycine (Invitrogen, 15527013), Hen Egg Lysozyme (Sigma-Aldrich L6876).

Drugs MLSA1 (Tocris, 4746, incubated at 10 μ M for 1h in media before experiment).

5.1.3 Experimental protocols

Preparation of Traction Force Microscopy gels Polyacrylamide (PAA) gels of 500Pa were prepared less than a week before the experiment. The protocol for this experiment has been described in the video protocol article we published (see Appendix B). Fluorodish (World Precision instruments FD35) were used as a support for live imaging experiments, and 18mm coverslips were used as a support for immunofluorescence on gel. The support is activated using UV light for 2min, covered with approximately 200 μ L APTMS for 5min to support covalent binding of the gel, then thoroughly washed with MilliQ water and dried. The coverslip used to flatten the gel (18mm for Fluorodish gel, 12mm for 18mm coverslip gel) is rendered hydrophobic by 3min immersion in Sigmacote, then washed thoroughly using MilliQ water and dried. The 500Pa PAA gel is prepared from 167 μ L of gel premix (75 μ L 40% acrylamide + 30 μ L 2% bisacrylamide + 895 μ L PBS, can be kept for up to a month at 4°C). For traction force microscopy, 1% beads are added to the solution, that is then vortex and sonicated for 5min and protected from light. Polymerisation of the gel is initiated by addition of 1% APS and 0.2% TEMED, followed by homogenisation. Quickly, 9 μ L of this solution is deposited at the center of the fluorodish (7 μ L for 18mm coverslips) and flattened using the second coverslip, until liquid get out from the side. The fluorodish is then flipped and tapped on the bench, and the gel is left to polymerize at room temperature in a humid chamber for 1h. After polymerization, PBS is added onto the gel to facilitate detachment of the sigmacote-treated coverslip. Gels are then kept in PBS at 4°C until functionalisation.

The evening before experiment, gels are functionalised with the ligand (HEL or BSA). Gels are covered with 150 μ L Sulfo-Sanpah solution (0.5mg/mL in 10mM HEPES buffer, stored up to a week at 4°C protected from light) at RT, and UV-treated for 2min,

followed by washing with PBS, and repetition of the previous steps. Gels are then covered with 250 μ L of a 100 μ g/mL solution of HEL (or BSA), and incubated overnight in a humid chamber at 4°C. Before the experiment, gels are washed with PBS, then covered with media (or media+drug), and kept at RT until imaging.

Antigen extraction from PAA gel Gels were prepared without fluorescent beads to avoid cross talk, and functionalised with HEL freshly conjugated to Alexa 555. HEL-Alexa555 fluorescence is quenched when attached to the gel, and appear upon detachment from the gel (Kumari et al., 2019). Movies were acquired with low frame rate and illumination to avoid photo bleaching. Antigen extraction is quantified by measuring the intensity in the cell area for each frame $I(t)$, and taking into account the initial intensity : $\frac{I(t)-I(t=0)}{I(t=0)}$.

Immunofluorescence on PAA gels B lymphocytes were plated for 30min in an incubator, on 500Pa PAA gels prepared on 18mm coverslips. Samples were fixed for 15min at RT using 4% PFA in PBS, washed 3x with PBS, then permeabilised by 5min incubation with 0.1% Triton, that was washed 3x with PBS. Samples were blocked by 30min incubation at RT in CLSM Buffer (PBS, 20mM Glycine, 3%BSA), washed 3x with PBS, then blocked using Fc Block (1/100) for 10min at RT, and washed again 3x with PBS. Samples were then incubated overnight at 4°C with primary antibodies diluted in CLSM Buffer. The next day, samples were washed 3x with PBS, then incubated with secondary antibodies for 1h at RT in PBS. After washing 3x with PBS, the samples were mounted using Fluoromount-G in a way that allows imaging the cells directly without going through the gel to improve image quality. Imaging was done using a laser scanning microscope (Leica SP8) equipped with a 60x, NA 1.3 oil immersion objective. Deconvolution was performed on the images using the Huygens software. The enrichment of p-Cortactin at actin patches was quantified using a custom made ImageJ macro, and defined as the average intensity of p-Cortactin in a disk around an actin patch (versus around a random point in the cell), divided by the average intensity of p-Cortactin in the cell.

Traction Force microscopy imaging Live imaging was performed on an inverted spinning disk confocal microscope (Eclipse Ti Nikon/Roper spinning head) equipped with a 60x, NA 1.4 oil immersion objective and CoolSNAP HQ2 camera (pixel size 6.4 μ m) with MetaMorph software (Molecular Device, France). Fluorodishes containing gels were set up on the microscope, with the focus made on the fluorescent beads plane. Right before the beginning of the acquisition, 1.10^5 B lymphocytes were added

to the plate, and the system was kept at 37°C with 5% CO₂. Images were taken every 5s, during at least 15min.

Image analysis for Traction Force Microscopy The traction force algorithm was designed on Matlab. It was based on the algorithm used by Butler et al., 2002, taking into account the modifications by Mandal et al., 2014. The substrate was assumed to be a linear elastic half space, and force reconstruction was performed using Fourier Transform Traction Cytometry with Tikhonov regularisation (regularisation parameter was set to $5 \cdot 10^{-19}$). MTT algorithm was used to measure the position of the beads in the reference and deformed image (Sergé et al., 2008). Calculation of stress fields from the displacement is performed in Fourier space, then inverted back to real space, resulting in a final stress field on a grid with 0.432µm spacing (4 pixels).

Quality of the analysis was evaluated by computing the non-equilibrated forces, i.e. the ratio of the sum of forces vectors (that should be zero, as the cell is not moving) and the sum of magnitude of the forces. We set the upper limit at 0.15, with lower values corresponding to better analysis quality. Energy and fluxes were computed inside the mask of the cell (extracted using an imageJ macro, and increased by 10% to avoid loss of information and border effects). Total strain energy was defined as the sum over the mask of the scalar product force by displacement, and fluxes were calculated by standard vector analysis, and corresponds to the integral over the cell area of the divergence of the 2D field (displacement).

Imaging of actin patches on the PAA gels Live imaging was performed on an inverted spinning disk confocal microscope (Eclipse Ti Nikon/Roper spinning head) equipped with a 40x Water immersion objective NA 1.4 and CoolSNAP HQ2 camera (pixel size 6.4µm) with MetaMorph software (Molecular Device, France). B lymphocytes extracted from MD4 Lifeact-GFP mice were settled on 500Pa HEL-coated PAA gels, without fluorescent beads, and kept at 37°C with 5% CO₂. Cells were imaged for 6min with a frame rate of 1 image every 6s, doing stacks of 10 images with $\delta z = 0.4\mu\text{m}$. The data was corrected for bleaching and projected in z before cropping the cells. Tracking of the patches (excluding the ones on the cortex) was performed using ImageJ (Trackmate Tinevez et al., 2017). Tracks of length n ($n > 3$) were then analyzed using Matlab to obtain the diffusion coefficient D, by doing a linear fit without offset of the first $\max(10, n)$ points of the mean square displacement. The duration and the localization relative to the center of the synapse were also extracted. Density maps were then computed using a Gaussian kernel.

Imaging of Z movement of beads in PAA gels Primary B lymphocytes extracted from the spleen of MD4 mice were settled onto a 500Pa HEL-coated PAA gel containing fluorescent beads. Cells were allowed to settle for 10min, then imaged using an inverted spinning disk confocal microscope (Eclipse Ti Nikon/Roper spinning head) equipped with a 40x Water immersion objective NA 1.4 and CoolSNAP HQ2 camera (pixel size 6.4 μm) with MetaMorph software (Molecular Device, France). The beads were imaged every 6s for 60 to 360s, taking stacks of 16 images with $\delta z=0.2\mu\text{m}$. Beads were tracked by 3D single particle tracking using ImageJ (Trackmate Tinevez et al., 2017), and the trajectories obtained were analysed using Matlab. To be able to exploit movies of different duration, trajectories were divided in sub-trajectories of 10 frames and the standard deviation of the z position was computed on the sub-trajectories. A mask of the cell was manually drawn using the transmission image, and allowed the determination of the center and radius of the cell to compute a normalized position of the trajectory in an average immune synapse. The central region of the immune synapse was considered to be within a radius $r = \frac{2}{3} * \text{CellRadius}$.

5.2 For Chapter 3

5.2.1 Cells and cell culture

CLICK medium: RPMI 1640 – GlutaMax-I + 10% fetal calf serum, 1% penicillin–streptomycin, 0.1% β mercaptoethanol, and 2% sodium pyruvate). Fetal calf serum was decomplexed for 40min at 56°C. All cell culture products were purchased from GIBCO/Life Technologies.

The mouse IgG⁺ B lymphoma cell line IIA1.6 (derived from the A20 cell line [ATCC #: TIB-208]) was cultured as previously reported (Yuseff et al., 2011) in CLICK Medium. All experiments were conducted in CLICK + 25mM HEPES (15630080, Gibco).

5.2.2 Reagents

For droplet preparation fabrication and functionalisation DSPE-PEG(2000) Biotin in chloroform (Avanti Lipids, Coger 880129C-10mg), Soybean oil (Sigma-Aldrich, CAS no. 8001-22-7), Pluronic F68 (Sigma-Aldrich, CAS no. 9003-11-6), Sodium Alginate (Sigma-Aldrich, CAS no. 9005-38-3), Tween 20 (Sigma Aldrich, CAS 9005-64-5), $\text{Na}_2\text{HPO}_4 \cdot 7\text{H}_2\text{O}$ (Sodium phosphate dibasic heptahydrate, M=268g/mol, CAS

7782-85-6, Merck), $\text{NaH}_2\text{PO}_4 \cdot \text{H}_2\text{O}$ (Sodium phosphate monobasic monohydrate $M = 138\text{g/mol}$, CAS 10049-21-5, Carlo Erba), Streptavidin Alexa Fluor 488 (ThermoFisher, S11223), Streptavidin Alexa Fluor 546 (ThermoFisher S11225), Streptavidin Alexa Fluor 647 (ThermoFisher S32357), biotin-SP-conjugated AffiniPure F(ab')₂ Fragment Gt anti Ms IgG (Jackson ImmunoResearch 115-066-072), Biotin labeled bovine albumin (Sigma-Aldrich A8549-10MG).

For microfluidic chips PDMS-RTV 615 (Neyco RTV6115), Polyvinylpyrrolidone K 90 (Sigma 81440, called PVP), Medical tubing, Tygon® ND 100-80 (Saint-Gobain), Stainless Steel Plastic Hub Dispensing Needles 23 GA (Kahnetics KDS2312P), Fluorodish (World Precision instruments FD35).

Dyes and plasmids for live cell imaging Hoechst 33342 (ThermoFisher, R37605) kept in solution, LysoTracker Deep Red (ThermoFisher, L12492) 50nM in incubator for 45min then wash, SirTubulin kit (Spirochrome AG, Tebu-bio SC002) 100nM SiRTubulin+10 μM verapamil >6h, eGFP-Centrin1 plasmid used in Obino et al., 2016, F-tractin tdTomato obtained from the team of Patricia Bassereau (Institut Curie, Paris), Rab6-mCherry plasmid obtained from Stéphanie Miserey (Institut Curie, Paris), C1 δ -GFP plasmid obtained from Sergio Grinstein (Botelho et al., 2000). pRK5myc RhoA L63 was a gift from Alan Hall (Addgene plasmid 15900 ; <http://n2t.net/addgene:15900> ; RRID:Addgene_15900). Expression of Ftractin-tdTomato, Rab6-mCherry, C1 δ -GFP and RhoA L63 was achieved by electroporating 1.10^6 B lymphoma cells with 0.25 to 0.5 μg of plasmid using the 10 μL Neon Transfection system (ThermoFisher). Expression of eGFP-Centrin1 was achieved by electroporating 4.10^6 B lymphoma cells with 4 μg of plasmid using the Amaxa Cell Line Nucleofector Kit R (T-016 program, Lonza). Cells were cultured in CLICK medium for 5 to 16h before imaging.

For transfection with siRNA, IIA1.6 cells were transfected 60-70h before live experiment with 40pmol siRNA per 10^6 cells using the 10 μL Neon Transfection system (ThermoFisher) and ON-TARGETplus Control n=Non-Targeting Pool (Dharmacon, D-001810-10-05) or SMARTPool ON-TARGETplus Mouse Arhgef2 siRNA (Dharmacon, L-040120-00-0005).

Antibodies and reagents for immunofluorescence and Western Blot Formaldehyde 16% in aqueous solution (Euromedex, 15710), BSA (Euromedex, 04-100-812-C), PBS (Gibco, 10010002), Rabbit anti GEF-H1 (Abcam, ab155785, 1/1000 for WB), Rat anti α -tubulin (Biorad, MCA77G, 1/1000 for WB), Anti-Rabbit IgG, HRP-linked Antibody (Cell signaling, 7074, 1/5000 for WB), Anti-Rat IgG, HRP-linked Antibody

(Cell signaling, 7077, 1/10000 for WB), Alexa Fluor 546 Phalloidin (ThermoFisher, A22283, 1/200), DAPI (BD Bioscience, 564907, 1/1000), Saponin (Sigma, 8047-15-2), Fluoromount-G (Southern Biotech, 0100-01). for Western blots, B cells were lysed for 10min at 4°C in RIPA Lysis and Extraction Buffer (ThermoFisher, 89900) supplemented with protease inhibitor cocktail (Roche, 11697498001), then treated with benzonase (Sigma, E1014-5KU). Lysates were spinned for 15min at 4°C at maximum speed to remove debris, followed by heating of supernatants for 5min at 95°C with Laemmli sample buffer (Biorad, 1610747) and NuPAGE™ Sample reducing agent (Invitrogen, NP0004). Supernatants were loaded onto gels and transferred to PVDF membranes (Gels, and materials for gel migration and membrane transfer were purchased from Biorad). Membranes were blocked for 45min at RT with 5% BSA in TBS+0.05% Tween20, incubated overnight at 4°C with primary antibodies, then incubated 1h at RT with secondary antibodies. Membranes were revealed using Clarity™ Western ECL Substrate (Biorad, 1705060) and chemiluminescence was detected using a BioRad ChemiDoc MP imaging system. Western blot were quantified using ImageLab.

Drugs Latrunculin A (Abcam, ab144290, incubated at 2µM for 1h before experiment), para-nitroBlebbistatin (Optopharma, 1621326-32-6, incubated at 20µM for 1h before experiments), Nocodazole (Sigma, M1404, used 5µM), MLSA1 (Tocris, 4746, incubated at 1µM for 1h before experiment). For all experiments in microfluidic chips involving drugs, chips were filled with media+drug (or DMSO) at least 1h before experiment, and only media + drug was used at each step.

5.2.3 Experimental protocols

Droplet stock formulation DSPE-PEG(2000) Biotin is resuspended in chloroform at 10mg/mL solution. The oil phase is prepared by adding 150µL of DSPE-PEG(2000) Biotin solution to 30g of soybean oil, and leaving the oil phase at least 4h in a vacuum chamber to allow chloroform evaporation. The aqueous phase (15% Pluronic F68, stock 30%, + 1% Sodium alginate, stock 4% in H₂O) was prepared by pouring 2.5g of Sodium alginate in a beaker, completing to 5g with deionized water, then adding 5g of Pluronic F68 solution. The solution was gently stirred with a spatula, avoiding bubbles and removing them using the vacuum. The oil phase was slowly added to the aqueous phase, starting by 2-3 drops, gentle stirring until oil was unincorporated, then repeating. The oil phase incorporates more easily over time, and could be added faster towards the end, when a white emulsion was obtained. The emulsion was then sheared in a Couette cell (Mason and Bibette, 1996) at 150rpm to obtain smaller and

more homogeneous droplets. It was recovered as it gets out of the Couette cell, and had 25% aqueous phase containing 15% Pluronic F68. To wash and remove the smallest droplets, the droplet emulsion was put in a separating funnel for 24h at 1% Pluronic F68, 5% oil phase. This operation was repeated at least 2 times. The final emulsion was stored in glass vials at 12°C.

Droplet functionalisation Droplets were functionalised on the day of experiment. This process was performed in low binding eppendorfs (Axygen Microtubes Maxy-Clear Snaplock, 0.60 ml, Axxygen MCT-060-L-C), and using PB + Tween20 buffer (Tween 20 at 0.2%v/v in PB Buffer pH=7, 20mM). A small volume of droplet emulsion (here for 2µL) was diluted 100 times in PB+Tween20 buffer, and washed 3 times in this buffer. Washes were performed by centrifugating the solution for 30s at 3000rpm in a minifuge, waiting 30s and then removing 170µL of the supernatant using a gel tip, and adding again 170µL of PB+Tween20. At the last wash, a solution of 170µL + 2.5µL of fluorescent streptavidin solution (1mg/mL) was added to the droplet solution, and after homogenisation by pipetting, this solution was left on a rotating wheel for 15min, protected from light. Droplets were then washed 3 times, and at the last wash a solution of 170µL PB+Tween20 + 5µL of Biotin Goat F(ab')₂ anti-Mouse IgG (1mg/mL) (or other biotinylated protein in the same proportion) was added and left to incubate for >30 min on a rotating wheel, protected from light. Droplets were finally washed three times before use, with PB+Tween20. For experiments using drug treatments, droplets were resuspended in culture media + drug before the experiment.

Microfluidic chip fabrication Microfluidic chips for the IIA1.6 cell line were made using an original design from the team of Jacques Fattaccioli (ENS Paris, IPGG) (Mesdjian, 2017). The PDMS was mixed 1:10, poured in the moulds, left in the vacuum chamber to remove air bubbles and cooked. The PDMS piece with the chamber and traps embedded was cut, and 0.5mm diameter holes were made at the entry/exit sites. The PDMS chip and a Fluorodish were then activated in a plasma cleaner (PDC-32G Harrick) for 1min and bonded to each other for 1h at 60°C. Bonded chips were activated in the plasma cleaner for 1min to reduce hydrophobicity, and filled gently with a 0.2%w/v PVP K90 solution in MilliQ water using a syringe, until some solution exited. Microfluidic chips were then kept at 4°C in the 0.2%w/v PVP K90-filled fluorodish to prevent drying, for up to a week before the experiment. PVP K90 deposits at the surface of the PDMS and makes it more hydrophilic on the long term. Microfluidic chips were put at room temperature on the morning of the experiment, and then kept in an incubator before imaging. For experiments using drug treatments, microfluidic chips

were injected with culture media + drug in the morning, and left to incubate to ensure stable drug concentration during the experiment.

Live imaging of polarisation of IIA1.6 cells in microfluidic chips Live imaging of polarisation was performed using an inverted spinning disk confocal microscope (Eclipse Ti Nikon/Roper spinning head) equipped with a Nikon 40x, NA 1.3, Plan Fluor oil immersion objective, a CMOS BSI photometrics camera (pixel size 6.5 μ m), and controlled with the Metamorph software (Molecular Device, France). Stacks of 21 images ($\delta z=0.7\mu$ m) were taken every 30s during 40min, with a binning of 2. Auto Focus was implemented in Metamorph using the Bright Field image, then applied to fluorescent channels with a z-offset at each time point. On the day of the experiment, droplets were functionalised and cells were resuspended at $1.5 \cdot 10^6$ cells/mL in CLICK+25mM HEPES. Microfluidic chips, cells and media were kept in an incubator at 37°C with 5% CO₂ until imaging.

Droplets were injected in the microfluidic chip using a Fluigent MFCSTM-EZ pressure controller, until enough traps contain one droplet. The inlet was then changed to CLICK+25mM HEPES (or CLICK+25mM HEPES+drug) to rinse the PB+Tween20 buffer and remove any antigen in solution or droplet that could remain. After a few minutes, the inlet was changed to the cell suspension, keeping a minimum pressure to avoid cells encountering droplets before acquisition was launched. Stage positions were selected and the acquisition was launched. After one time point (to have an image of droplets without cells, and ensure to have the first time of contact), the inlet pressure was increased to inject cells and create doublets. After 2-5min, the injection pressure was lowered to a minimum to limit cell arrival, and perturbation of the cell by strong flows.

Immunofluorescence with droplets To approach the non-adherent condition of the cells in the microfluidic chips, IIA1.6 cells were seeded for 15 minutes on glass coverslips (Marienfeld Superior Precision Cover Glasses, 12mm diameter) coated with 100 μ g/mL BSA, on which they should display limited spreading. Droplets were prepared as for live imaging, then resuspended in 13 times the initial volume of droplets stock of CLICK+HEPES. A small volume of this droplet solution was deposited onto parafilm for each coverslip, and the coverslip was then flipped onto the droplets and left for 5 minutes, so that droplets would float up to encounter the cells. Coverslips were then put in pre-heated CLICK+HEPES media in a 12 well plate, with the cells facing up, for 15 minutes. All manipulations and washes were performed very gently, using cut pipet tips to limit cell and droplet detachment. Samples were fixed for 12min

at RT using 4% PFA in PBS, then washed three times with PBS. After 30min of incubation with PBS/BSA/Saponin 1X/0.2%/0.05%, samples were incubated for 1h at RT with 1/200 Alexa Fluor 546 and 1/1000 DAPI in PBS/BSA/Saponin 1X/0.2%/0.05%, then washed three times with PBS. Samples were then mounted using Fluoromount-G and left at RT until dry.

Samples were imaged by 3D SIM, using a Delta Vision OMX v4 microscope, equipped with an Olympus 100X, NA 1.42, Plan Apo N, oil immersion objective, and EMCCD cameras. Image reconstruction was performed using the SoftWoRx image software, under Linux. 3D visualisation for figures were performed using the Imaris Viewer software.

5.2.4 Image analysis

Image analysis was performed on the Fiji software (Schindelin et al., 2012) using custom macros, unless stated otherwise. Single kinetic curves analysis were performed using Rstudio (RStudio, 2020). Graphs and statistical analysis were made using GraphPad PRISM version 9.2.0 for Windows, GraphPad Software, San Diego, California USA, www.graphpad.com.

For graphs of polarisation in time of BSA vs α IgG (Figure 3.2), a moving average filter of length 3 was applied on the mean and SEM before plotting. The non-smoothed mean curve is superimposed to the graphs.

Image analysis for cell polarisation in microfluidic chips: Cell-droplet doublets were cropped from original acquisitions, and were cut so that cells arrive at the second frame (marked as 0 s in figures).

Analysis of antigen recruitment on the droplet: Bleaching of the fluorescent streptavidin was corrected before analysis using Bleach Correction - Histogram Matching. Antigen recruitment was measured by computing the ratio between fluorescence intensity at the synapse and fluorescence intensity at the opposite side on three planes passing through the droplet and the cell, normalized by this value at the time of cell arrival (Figure 3.1D).

Analysis of F-tractin-tdTomato: Fluorescence was corrected using the Bleach Correction-simple ratio program. Using a custom Fiji macro, 3D masks of the droplet and the cell were generated. Enrichment of F-actin at the immune synapse was defined as the sum of intensity in the mask of the cell within a 2 μ m layer around the droplet

in 3D, divided by the sum of intensity in the mask of the cell. This measurement was normalised by its value at the first time point of encounter between the cell and the droplet, to compensate for potential heterogeneity of the initial state. Extraction of characteristic values (time of peak, maximum, plateau value relative to maximum) were extracted with R, on single kinetic curves smoothed using 3R Tukey smoothing (repeated smoothing until convergence) (Tukey, 1977). Time and value of maximum were computed in the first 10min of cell-droplet contact. Shape characteristics of the cell (aspect ratio, solidity) were measured on maximum z projections of cell masks.

Analysis of C1 δ -GFP DAG reporter: Fluorescence was corrected using the Bleach Correction-simple ratio program. Using a custom Fiji macro, masks of the droplet and the cell were generated. Enrichment of the C1 δ -GFP DAG reporter was defined as the sum of intensity in the mask of the cell, within a 1 μ m layer around the droplet. This measurement was normalised with its value at the first time point of encounter between the cell and the droplet, to account for variability of reporter expression between cells. Extraction of characteristic values (time of peak, maximum, plateau value relative to maximum) were extracted with R, on single kinetic curves smoothed using 3R Tukey smoothing (repeated smoothing until convergence) (Tukey, 1977). Time and value of maximum were computed in the first 10min of cell-droplet contact.

Analysis of the centrosome: The 3D movie was first interpolated to obtain isotropic voxels for the advanced analysis. Using a custom Fiji macro, a mask of the droplet was generated, and position of the centrosome (stained with SiRtubulin or eGFP-cent1) was detected, to measure the distance of the centrosome from the droplet surface. Characteristic times were extracted on single kinetic curves smoothed using 3R Tukey smoothing (repeated smoothing until convergence) (Tukey, 1977) using R, and defined as the first time for which the distance is below 2 μ m. For the comparison of characteristic times in DMSO vs LatA treatments, only cells with centrosome starting >3 μ m from the droplet were selected in order to be able to detect the process of polarisation. This threshold value was chosen looking at the distribution of plateau values for BSA- or α -IgG-coated droplets. Tracking of the cell for analysis of centrosome orientation was performed by first obtaining a mask of the cell, from either SirTubulin or eGFP-cent1 background cytoplasmic signal. This channel is used to create a mask of the cell on Fiji and find its center of mass. Briefly, the 3D stack is interpolated (to obtain an isotropic voxel), a background subtraction (based on a Gaussian filtered (radius=4) image of the field without cell, time=0) is applied. A Gaussian filter is applied on the resulting image (radius=2) to remove local noise and the cell is finally segmented using an automatic threshold (Huang). Advanced analysis of centrosome trajectories

was performed by using the 3D cell contour generated on Fiji, and then computing the distance of the centrosome from the center of the cell, and the angle formed with the cell-droplet axis on Matlab, to merge this data with advanced nucleus analysis data. The code for this advanced analysis was written by Paolo Pierobon.

Analysis of the Golgi Apparatus was performed on Icy Bioimage analysis software (De Chaumont et al., 2012). Briefly, a mask of the Golgi apparatus and the droplet was obtained, and the average distance of the Golgi apparatus to the surface of the droplets was computed using a 3D distance map from the droplet. Characteristic times were extracted on single kinetic curves smoothed using 3R Tukey smoothing (repeated smoothing until convergence) (Tukey, 1977) using R, and defined as the first time for which the distance is below $4\mu\text{m}$. This threshold value was chosen looking at the distribution of plateau values for BSA- or αIgG -coated droplets.

Analysis of the lysosomes was performed on Icy Bioimage analysis software (De Chaumont et al., 2012). Briefly, a mask of the lysosomes and the droplet was obtained, and the average distance of all the lysosomes to the surface of the droplets was computed using a 3D map of distances from the droplet. Characteristic times were extracted on single kinetic curves smoothed using 3R Tukey smoothing (repeated smoothing until convergence) (Tukey, 1977) using R, and defined as the first time for which the distance is below $3\mu\text{m}$. This threshold value was chosen looking at the distribution of plateau values for BSA- or αIgG -coated droplets.

Analysis of the Nucleus and detection of nuclear indentation was performed using a custom Fiji macro and the Matlab software. B cell nucleus is bean-shaped and exhibits a marked invagination where the centrosome sits at steady state. To automatically detect the invagination at each time point, we interpolated the confocal images of the nucleus to obtain an isotropic voxel, segmented the nucleus and found the interpolating surface (isosurface function in Matlab). We smoothed the surface to avoid voxelization and computed the mean curvature at each vertex with standard differential geometry methods. We defined the invagination as the point with the minimal mean curvature obtained on this surface. Ad hoc correction based on nearest neighbor tracking is applied when several local minima are found (in nuclear that exhibit several lobes), the selected minimum is the nearest to the one found in the previous frame. The orientation of the nucleus with respect to the $\text{Cell}_{\text{Center}} - \text{Droplet}_{\text{Center}}$ axis is quantified as the angle $N_{\text{indentation}} - \text{Cell}_{\text{Center}} - \text{Droplet}_{\text{Center}}$. The code for this advanced analysis was written by Paolo Pierobon.

Bibliography

- Adler, Lital N. et al. (Mar. 2017). "The Other Function: Class II-restricted antigen presentation by B cells". In: *Frontiers in Immunology* 8.MAR, p. 319. ISSN: 16643224. DOI: 10.3389/fimmu.2017.00319.
- Alberts, Bruce et al. (2008). *Molecular Biology of the Cell, 5th Edition*. ISBN: 9780815341109. DOI: 10.1017/CB09781107415324.004.
- Alushin, Gregory M et al. (2014). "High-Resolution microtubule structures reveal the structural transitions in $\alpha\beta$ -tubulin upon GTP hydrolysis". In: *Cell* 157.5, pp. 1117–1129. ISSN: 10974172. DOI: 10.1016/j.cell.2014.03.053. URL: <http://dx.doi.org/10.1016/j.cell.2014.03.053>.
- Andrés-Delgado, Laura et al. (Sept. 2012). "INF2 promotes the formation of detyrosinated microtubules necessary for centrosome reorientation in T cells". In: *Journal of Cell Biology* 198.6, pp. 1025–1037. ISSN: 00219525. DOI: 10.1083/jcb.201202137.
- Arthur, William T, Lawrence A Quilliam, and Jonathan A Cooper (2004). "Rap1 promotes cell spreading by localizing Rac guanine nucleotide exchange factors". In: *Journal of Cell Biology* 167.1, pp. 111–122. ISSN: 00219525. DOI: 10.1083/jcb.200404068. URL: <http://www.jcb.org/cgi/>.
- Astarita, Jillian L. et al. (Oct. 2015). "The CLEC-2-podoplanin axis controls the contractility of fibroblastic reticular cells and lymph node architecture". In: *Nature Immunology* 16.1, pp. 75–84. ISSN: 15292916. DOI: 10.1038/ni.3035. URL: <https://www-nature-com.proxy.insermbiblio.inist.fr/articles/ni.3035>.
- Barek, Kalthoum Ben M et al. (2015). "Adhesion et phagocytose de gouttes d'emulsions fonctionnalisées". PhD thesis.
- Barral, Patricia et al. (2008). "B cell receptor-mediated uptake of CD1d-restricted antigen augments antibody responses by recruiting invariant NKT cell help in vivo". In: *Proceedings of the National Academy of Sciences of the United States of America* 105.24, pp. 8345–8350. ISSN: 00278424. DOI: 10.1073/pnas.0802968105. URL: www.pnas.org/cgi/doi/10.1073/pnas.0802968105.
- Basquin, Cyril et al. (2015). "Membrane protrusion powers clathrin-independent endocytosis of interleukin-2 receptor". In: *The EMBO Journal* 34.16, pp. 2147–2161. ISSN: 0261-4189. DOI: 10.15252/embj.201490788.

- Batista, F D and M S Neuberger (June 1998). "Affinity dependence of the B cell response to antigen: a threshold, a ceiling, and the importance of off-rate." In: *Immunity* 8.6, pp. 751–9. ISSN: 1074-7613. DOI: 10.1016/S1074-7613(00)80580-4. URL: <http://www.ncbi.nlm.nih.gov/pubmed/9655489>.
- Batista, Facundo D. and Naomi E. Harwood (2009). "The who, how and where of antigen presentation to B cells". In: *Nature Reviews Immunology* 9.1, pp. 15–27. ISSN: 1474-1733. DOI: 10.1038/nri2454. URL: <http://www.nature.com/doi/10.1038/nri2454>.
- Batista, Facundo D, Dagmar Iber, and Michael S Neuberger (May 2001). "B cells acquire antigen from target cells after synapse formation". In: *Nature* 411.6836, pp. 489–494. ISSN: 0028-0836. URL: <http://dx.doi.org/10.1038/35078099>http://www.nature.com/nature/journal/v411/n6836/supinfo/411489a0_S1.html.
- Baum, Buzz and Patricia Kunda (2005). "Actin nucleation: Spire - Actin nucleator in a Class of its own". In: *Current Biology* 15.8. ISSN: 09609822. DOI: 10.1016/j.cub.2005.04.002.
- Bergert, Martin et al. (2016). "Confocal reference free traction force microscopy". In: *Nature Communications* 7. ISSN: 20411723. DOI: 10.1038/ncomms12814. URL: www.nature.com/naturecommunications.
- Biedzinski, Stefan et al. (Dec. 2020). "Microtubules control nuclear shape and gene expression during early stages of hematopoietic differentiation". In: *The EMBO Journal* 39.23, e103957. ISSN: 0261-4189. DOI: 10.15252/embj.2019103957. URL: <https://www.embopress.org/doi/full/10.15252/embj.2019103957><https://www.embopress.org/doi/abs/10.15252/embj.2019103957>.
- Bolger-Munro, Madison et al. (2019). "Arp2/3 complex-driven spatial patterning of the B cell receptor (BCR) enhances immune synapse formation, BCR signaling, and cell activation". In: *eLife*. DOI: 10.1101/490698. URL: <http://dx.doi.org/10.1101/490698>.
- Botelho, Roberto J. et al. (Dec. 2000). "Localized biphasic changes in phosphatidylinositol-4,5-bisphosphate at sites of phagocytosis". In: *Journal of Cell Biology* 151.7, pp. 1353–1367. ISSN: 00219525. DOI: 10.1083/jcb.151.7.1353. URL: [/pmc/articles/PMC2150667/](https://pmc/articles/PMC2150667/)[/pmc/articles/PMC2150667/?report=abstract](https://pmc/articles/PMC2150667/?report=abstract)<https://www.ncbi.nlm.nih.gov/pmc/articles/PMC2150667/>.
- Bourouina, Nadia et al. (2011). "Formation of specific receptor-ligand bonds between liquid interfaces". In: *Soft Matter* 7.19, pp. 9130–9139. ISSN: 1744683X. DOI: 10.1039/c1sm05659j.
- Brandrup, J., E.H. Immergut, and E.A. Grulke (1975). *Polymer Handbook, 2nd Edition*. New York: John Wiley & Sons, Ltd.

- Bretou, Marine et al. (Oct. 2017). "Lysosome signaling controls the migration of dendritic cells". In: *Science Immunology* 2.16, p. 9573. ISSN: 24709468. DOI: 10.1126/sciimmunol.aak9573. URL: <https://immunology.sciencemag.org/content/2/16/eaak9573><https://immunology.sciencemag.org/content/2/16/eaak9573.abstract>.
- Brinkley, William (1997). *Microtubules: A Brief Historical Perspective*. Tech. rep.
- Bufi, Nathalie et al. (May 2015). "Human primary immune cells exhibit distinct mechanical properties that are modified by inflammation". In: *Biophysical Journal* 108. ISSN: 15420086. DOI: 10.1016/j.bpj.2015.03.047.
- Burke, Thomas A. et al. (2014). "Homeostatic actin cytoskeleton networks are regulated by assembly factor competition for monomers". In: *Current Biology* 24.5, pp. 579–585. ISSN: 09609822. DOI: 10.1016/j.cub.2014.01.072. URL: <http://dx.doi.org/10.1016/j.cub.2014.01.072>.
- Burkhardt, Janis K. (Aug. 1998). "The role of microtubule-based motor proteins in maintaining the structure and function of the Golgi complex". In: *Biochimica et Biophysica Acta* 1404.1-2, pp. 113–126. ISSN: 01674889. DOI: 10.1016/S0167-4889(98)00052-4.
- Butler, James P. et al. (2002). "Traction fields, moments, and strain energy that cells exert on their surroundings". In: *American Journal of Physiology - Cell Physiology* 282.3 51-3, pp. 595–605. ISSN: 03636143. DOI: 10.1152/ajpcell.00270.2001. URL: <https://journals.physiology.org/doi/abs/10.1152/ajpcell.00270.2001>.
- Cai, En et al. (2017). "Visualizing dynamic microvillar search and stabilization during ligand detection by T cells". In: *Science* 356.6338. ISSN: 10959203. DOI: 10.1126/science.aal3118. URL: <http://science.sciencemag.org/>.
- Campellone, Kenneth G. and Matthew D. Welch (Apr. 2010). "A nucleator arms race: Cellular control of actin assembly". In: *Nature Reviews Molecular Cell Biology* 11.4, pp. 237–251. ISSN: 14710072. DOI: 10.1038/nrm2867.
- Camps, Jordi et al. (Aug. 2014). "Loss of lamin B1 results in prolongation of S phase and decondensation of chromosome territories". In: *FASEB Journal* 28.8, pp. 3423–3434. ISSN: 15306860. DOI: 10.1096/fj.14-250456. URL: <https://onlinelibrary.wiley.com/doi/abs/10.1096/fj.14-250456>.
- Carman, Christopher V (Sept. 2009). "Mechanisms for transcellular diapedesis: probing and pathfinding by 'invadosome-like protrusions'." In: *Journal of cell science* 122.Pt 17, pp. 3025–35. ISSN: 1477-9137. DOI: 10.1242/jcs.047522. URL: <http://www.ncbi.nlm.nih.gov/pubmed/19692589>.

- Carrasco, Yolanda R and Facundo D Batista (2007). "B Cells Acquire Particulate Antigen in a Macrophage-Rich Area at the Boundary between the Follicle and the Subcapsular Sinus of the Lymph Node". In: *Immunity* 27.1, pp. 160–171. ISSN: 10747613. DOI: 10.1016/j.immuni.2007.06.007.
- Carrasco, Yolanda R et al. (May 2004). "LFA-1/ICAM-1 interaction lowers the threshold of B cell activation by facilitating B cell adhesion and synapse formation." In: *Immunity* 20.5, pp. 589–99. ISSN: 1074-7613. DOI: 10.1016/S1074-7613(04)00105-0. URL: <http://www.ncbi.nlm.nih.gov/pubmed/15142527>.
- Chang, Yuan Chen et al. (May 2008). "GEF-H1 couples nocodazole-induced microtubule disassembly to cell contractility via RhoA". In: *Molecular Biology of the Cell* 19.5, pp. 2147–2153. ISSN: 10591524. DOI: 10.1091/mbc.E07-12-1269.
- Chaudhuri, Abhishek et al. (2011). "Spatiotemporal regulation of chemical reactions by active cytoskeletal remodeling". In: *Proceedings of the National Academy of Sciences of the United States of America* 108.36, pp. 14825–14830. ISSN: 00278424. DOI: 10.1073/pnas.1100007108. URL: www.pnas.org/lookup/suppl/.
- Cheng, Jackie, Alexandre Grassart, and David G. Drubin (2012). "Myosin 1E coordinates actin assembly and cargo trafficking during clathrin-mediated endocytosis". In: *Molecular Biology of the Cell* 23.15, pp. 2891–2904. ISSN: 10591524. DOI: 10.1091/mbc.E11-04-0383.
- Chesarone, Melissa A and Bruce L Goode (2009). "Actin nucleation and elongation factors: mechanisms and interplay". In: *Current Opinion in Cell Biology* 21.1, pp. 28–37. ISSN: 09550674. DOI: 10.1016/j.ceb.2008.12.001. URL: www.sciencedirect.com.
- Chhabra, Ekta Seth and Henry N Higgs (2007). *The many faces of actin: Matching assembly factors with cellular structures*. DOI: 10.1038/ncb1007-1110.
- Colin, Alexandra et al. (2018). "Actin-Network Architecture Regulates Microtubule Dynamics". In: *Current Biology* 28.16, pp. 2647–2656. ISSN: 09609822. DOI: 10.1016/j.cub.2018.06.028. URL: <https://doi.org/10.1016/j.cub.2018.06.028>.
- Colin-York, Huw et al. (2020). "Distinct actin cytoskeleton behaviour in primary and immortalised T-cells". In: *Journal of cell science* 133.5. ISSN: 14779137. DOI: 10.1242/jcs.232322.
- Cooper, Max D. (2015). "The early history of B cells". In: *Nature Reviews Immunology* 15.3, pp. 191–197. ISSN: 14741741. DOI: 10.1038/nri3801. URL: www.nature.com/reviews/immunol.
- Dahl, Kris Noel and Agnieszka Kalinowski (Mar. 2011). "Nucleoskeleton mechanics at a glance". In: *Journal of Cell Science* 124.5, pp. 675–678. ISSN: 00219533. DOI: 10.1242/jcs.069096.

- De Chaumont, Fabrice et al. (June 2012). "Icy: An open bioimage informatics platform for extended reproducible research". In: *Nature Methods* 9.7, pp. 690–696. ISSN: 15487091. DOI: 10.1038/nmeth.2075. URL: <https://www.nature.com/articles/nmeth.2075>.
- Devreotes, Peter and Chris Janetopoulos (June 2003). "Eukaryotic chemotaxis: Distinctions between directional sensing and polarization". In: *Journal of Biological Chemistry* 278.23, pp. 20445–20448. ISSN: 00219258. DOI: 10.1074/jbc.R300010200. URL: <http://www.jbc.org/article/S002192582073334X/fulltext><http://www.jbc.org/article/S002192582073334X/abstract>[https://www.jbc.org/article/S0021-9258\(20\)73334-X/abstract](https://www.jbc.org/article/S0021-9258(20)73334-X/abstract).
- Di Martino, Julie et al. (2016). "The microenvironment controls invadosome plasticity". In: *Journal of Cell Science*. DOI: 10.1242/jcs.182329. URL: <http://jcs.biologists.org/content/joces/early/2016/03/29/jcs.182329.full.pdf>.
- Dogterom, Marileen and Gijssje H Koenderink (2019). "Actin–microtubule crosstalk in cell biology". In: *Nature Reviews Molecular Cell Biology*. ISSN: 14710080. DOI: 10.1038/s41580-018-0067-1. URL: www.nature.com/nrm.
- Dupin, Isabelle, Yasuhisa Sakamoto, and Sandrine Etienne-Manneville (2011). "Cytoplasmic intermediate filaments mediate actin-driven positioning of the nucleus". In: *Journal of Cell Science* 124.6, pp. 865–872. ISSN: 00219533. DOI: 10.1242/jcs.076356.
- Dura, Burak et al. (2015). "Profiling lymphocyte interactions at the single-cell level by microfluidic cell pairing". In: *Nature Communications* 6.1, pp. 1–13. ISSN: 2041-1723. DOI: 10.1038/ncomms6940. URL: <http://www.ncbi.nlm.nih.gov/pubmed/25585172>.
- Dura, Burak et al. (2016). "Longitudinal multiparameter assay of lymphocyte interactions from onset by microfluidic cell pairing and culture". In: *Proceedings of the National Academy of Sciences of the United States of America*. ISSN: 10916490. DOI: 10.1073/pnas.1515364113.
- Dustin, Michael L et al. (1996). "Visualization of CD2 interaction with LFA-3 and determination of the two-Dimensional dissociation constant for adhesion receptors in a contact area". In: *Journal of Cell Biology* 132.3, pp. 465–474. ISSN: 00219525. DOI: 10.1083/jcb.132.3.465.
- Dustin, Michael L. et al. (1998). "A novel adaptor protein orchestrates receptor patterning and cytoskeletal polarity in T-cell contacts". In: *Cell* 94.5, pp. 667–677. ISSN: 00928674. DOI: 10.1016/S0092-8674(00)81608-6.
- Etienne-Manneville, Sandrine (2004). "Cdc42 - The centre of polarity". In: *Journal of Cell Science* 117.8, pp. 1291–1300. ISSN: 00219533. DOI: 10.1242/jcs.01115.

- Etienne-Manneville, Sandrine (2018). "Cytoplasmic Intermediate Filaments in Cell Biology". In: *Annual Review of Cell and Developmental Biology*. DOI: 10.1146/annurev-cellbio-100617. URL: <https://doi.org/10.1146/annurev-cellbio-100617->.
- Fabrikant, Gur et al. (Sept. 2013). "Model of T-Cell nuclear deformation by the cortical actin layer". In: *Biophysical Journal* 105.6, pp. 1316–1323. ISSN: 00063495. DOI: 10.1016/j.bpj.2013.07.024.
- Farina, Francesca et al. (2016). "The centrosome is an actin-organizing centre". In: *Nature Cell Biology* 18.1, pp. 65–75. ISSN: 14764679. DOI: 10.1038/ncb3285.
- Filbert, Erin L et al. (2012). "Stathmin Regulates Microtubule Dynamics and Microtubule Organizing Center Polarization in Activated T Cells". In: *The Journal of Immunology* 188.11, pp. 5421–5427. ISSN: 0022-1767. DOI: 10.4049/jimmunol.1200242. URL: <http://www.jimmunol.org/content/188/11/5421><http://www.jimmunol.org/content/188/11/5421.full#ref-list-1>.
- Fleire, S. J. (2006). "B Cell Ligand Discrimination Through a Spreading and Contraction Response". In: *Science* 312.5774, pp. 738–741. ISSN: 0036-8075. DOI: 10.1126/science.1123940. URL: <http://www.sciencemag.org/cgi/doi/10.1126/science.1123940>.
- Freeman, Spencer A et al. (2011). "Cofilin-Mediated F-Actin Severing Is Regulated by the Rap GTPase and Controls the Cytoskeletal Dynamics That Drive Lymphocyte Spreading and BCR Microcluster Formation". In: *The Journal of Immunology* 187.11, pp. 5887–5900. ISSN: 0022-1767. DOI: 10.4049/jimmunol.1102233. URL: <http://www.jimmunol.org/content/187/11/5887>.
- Fruleux, Antoine and Rhoda J. Hawkins (2016). "Physical role for the nucleus in cell migration". In: *Journal of Physics Condensed Matter* 28.36. ISSN: 1361648X. DOI: 10.1088/0953-8984/28/36/363002.
- Fukata, Masaki et al. (June 2002). "Rac1 and Cdc42 capture microtubules through IQ-GAP1 and CLIP-170". In: *Cell* 109.7, pp. 873–885. ISSN: 00928674. DOI: 10.1016/S0092-8674(02)00800-0.
- Gall, Joseph G (1966). "Microtubule fine structure." In: *The Journal of cell biology* 31.3, pp. 639–643. ISSN: 00219525. DOI: 10.1083/jcb.31.3.639.
- Gan, Zhuo et al. (2016). "Vimentin Intermediate Filaments Template Microtubule Networks to Enhance Persistence in Cell Polarity and Directed Migration". In: *Cell Systems* 3.3, pp. 252–263. ISSN: 24054720. DOI: 10.1016/j.cels.2016.08.007. URL: <http://dx.doi.org/10.1016/j.cels.2016.08.007>.
- Gérard, Audrey et al. (2007). "The Par polarity complex regulates Rap1- and chemokine-induced T cell polarization". In: *Journal of Cell Biology* 176.6, pp. 863–875. ISSN: 00219525. DOI: 10.1083/jcb.200608161.

- Gomes, Edgar R, Shantanu Jani, and Gregg G. Gundersen (2005). "Nuclear movement regulated by Cdc42, MRCK, myosin, and actin flow establishes MTOC polarization in migrating cells". In: *Cell* 121.3, pp. 451–463. ISSN: 00928674. DOI: 10.1016/j.cell.2005.02.022. URL: [http://www.cell.com/cell/pdf/S0092-8674\(05\)00188-1.pdf](http://www.cell.com/cell/pdf/S0092-8674(05)00188-1.pdf).
- Gomez, Timothy S et al. (2007). "Formins Regulate the Actin-Related Protein 2/3 Complex-Independent Polarization of the Centrosome to the Immunological Synapse". In: *Immunity* 26.2, pp. 177–190. ISSN: 10747613. DOI: 10.1016/j.immuni.2007.01.008. URL: <https://www.ncbi.nlm.nih.gov/pmc/articles/PMC2836258/pdf/nihms18854.pdf>.
- Goodnow, Christopher C. et al. (1988). "Altered immunoglobulin expression and functional silencing of self-reactive B lymphocytes in transgenic mice". In: *Nature* 334.6184, pp. 676–682. ISSN: 00280836. DOI: 10.1038/334676a0.
- Gourier, Christine et al. (2008). "A Nanospring Named Erythrocyte. The Biomembrane Force Probe". In: *Cellular and Molecular Bioengineering* 1.4, pp. 263–275. ISSN: 1865-5025. DOI: 10.1007/s12195-008-0030-x.
- Gowrishankar, Kripa et al. (2012). "Active remodeling of cortical actin regulates spatiotemporal organization of cell surface molecules". In: *Cell* 149.6, pp. 1353–1367. ISSN: 10974172. DOI: 10.1016/j.cell.2012.05.008. URL: <http://dx.doi.org/10.1016/j.cell.2012.05.008>.
- Grega-Larson, Nathan E., Scott W. Crawley, and Matthew J. Tyska (2016). "Impact of cordon-bleu expression on actin cytoskeleton architecture and dynamics". In: *Cytoskeleton* 73.11, pp. 670–679. ISSN: 19493592. DOI: 10.1002/cm.21317.
- Gupta, Soumya et al. (Dec. 2012). "Role of Actin Dependent Nuclear Deformation in Regulating Early Gene Expression". In: *PLoS ONE* 7.12. Ed. by Jon CD. Houtman, e53031. ISSN: 1932-6203. DOI: 10.1371/journal.pone.0053031. URL: <https://dx.plos.org/10.1371/journal.pone.0053031>.
- Heck, Jessica N. et al. (July 2012). "Microtubules regulate GEF-H1 in response to extracellular matrix stiffness". In: *Molecular Biology of the Cell* 23.13, pp. 2583–2592. ISSN: 10591524. DOI: 10.1091/mbc.E11-10-0876.
- Heisenberg, Carl-Philipp and Yohanns Bellaïche (May 2013). "Forces in Tissue Morphogenesis and Patterning". In: *Cell* 153.5, pp. 948–962. ISSN: 0092-8674. DOI: 10.1016/j.cell.2013.05.008. URL: <http://www.cell.com/article/S0092867413005734/fulltext><http://www.cell.com/article/S0092867413005734/abstract>[https://www.cell.com/cell/abstract/S0092-8674\(13\)00573-4](https://www.cell.com/cell/abstract/S0092-8674(13)00573-4).
- Henty-Ridilla, Jessica L. et al. (May 2016). "Accelerated actin filament polymerization from microtubule plus ends". In: *Science* 352.6288, pp. 1004–1009. ISSN: 10959203.

- DOI: 10.1126/science.aaf1709. URL: <https://science.sciencemag.org/content/352/6288/1004><https://science.sciencemag.org/content/352/6288/1004.abstract>.
- Hohmann, Tim and Faramarz Dehghani (2019). "The Cytoskeleton—A Complex Interacting Meshwork". In: *Cells* 8.4, p. 362. ISSN: 2073-4409. DOI: 10.3390/cells8040362.
- Hoogeboom, Robbert et al. (2018). "Myosin IIa Promotes Antibody Responses by Regulating B Cell Activation, Acquisition of Antigen, and Proliferation". In: *Cell Reports* 23.8, pp. 2342–2353. ISSN: 22111247. DOI: 10.1016/j.celrep.2018.04.087. URL: <https://doi.org/10.1016/j.celrep.2018.04.087>.
- Hou, Ping et al. (2006). "B cell antigen receptor signaling and internalization are mutually exclusive events". In: *PLoS Biology* 4.7, pp. 1147–1158. ISSN: 15457885. DOI: 10.1371/journal.pbio.0040200. URL: <https://journals.plos.org/plosbiology/article?id=10.1371/journal.pbio.0040200>.
- Houben, F. et al. (Feb. 2009). "Disturbed nuclear orientation and cellular migration in A-type lamin deficient cells". In: *Biochimica et Biophysica Acta* 1793.2, pp. 312–324. ISSN: 01674889. DOI: 10.1016/j.bbamcr.2008.10.003.
- Hui, King Lam and Arpita Upadhyaya (May 2017). "Dynamic microtubules regulate cellular contractility during T-cell activation." In: *Proceedings of the National Academy of Sciences of the United States of America* 114.21, E4175–E4183. ISSN: 1091-6490. DOI: 10.1073/pnas.1614291114. URL: www.pnas.org/cgi/doi/10.1073/pnas.1614291114<http://www.ncbi.nlm.nih.gov/pubmed/28490501><http://www.ncbi.nlm.nih.gov/pubmedcentral.nih.gov/articlerender.fcgi?artid=PMC5448208>.
- Hui, King Lam et al. (Feb. 2015). "Cytoskeletal forces during signaling activation in Jurkat T-cells". In: *Molecular Biology of the Cell* 26.4. Ed. by Yu-Li Wang, pp. 685–695. ISSN: 19394586. DOI: 10.1091/mbc.E14-03-0830. URL: <https://www.molbiolcell.org/doi/10.1091/mbc.E14-03-0830>.
- Husson, Julien et al. (May 2011). "Force generation upon T cell receptor engagement". In: *PLoS ONE* 6.5. Ed. by Javed N. Agrewala, e19680. ISSN: 19326203. DOI: 10.1371/journal.pone.0019680. URL: <http://dx.plos.org/10.1371/journal.pone.0019680>.
- Ibañez-Vega, Jorge et al. (Feb. 2019). "Proteasome dependent actin remodeling facilitates antigen extraction at the immune synapse of B cells". In: *Frontiers in Immunology* 10.FEB, p. 225. ISSN: 16643224. DOI: 10.3389/fimmu.2019.00225. URL: <https://www.frontiersin.org/article/10.3389/fimmu.2019.00225/full>.
- Iden, Sandra and John G. Collard (2008). "Crosstalk between small GTPases and polarity proteins in cell polarization". In: *Nature Reviews Molecular Cell Biology* 9.11,

- pp. 846–859. ISSN: 14710072. DOI: 10.1038/nrm2521. URL: www.nature.com/reviews/molcellbio.
- Illukkumbura, Rukshala, Tom Bland, and Nathan W Goehring (2019). “Patterning and polarization of cells by intracellular flows”. In: *Current Opinion in Cell Biology* 62, pp. 123–134. ISSN: 18790410. DOI: 10.1016/j.ceb.2019.10.005.
- Inoue, Daisuke et al. (2019). “Actin filaments regulate microtubule growth at the centrosome”. In: *EMBO Journal*. DOI: 10.15252/emboj.201899630. URL: <http://emboj.embopress.org.gate2.inist.fr/content/embojnl/38/11/e99630.full.pdf>.
- Ishikawa, H., R. Bischoff, and H. Holtzer (1968). “Mitosis and intermediate-sized filaments in developing skeletal muscle.” In: *The Journal of cell biology* 38.3, pp. 538–555. ISSN: 00219525. DOI: 10.1083/jcb.38.3.538.
- Jahed, Zeinab et al. (Sept. 2016). “The LINC and NPC relationship - it’s complicated!” In: *Journal of Cell Science* 129.17, pp. 3219–3229. ISSN: 14779137. DOI: 10.1242/jcs.184184.
- Janetopoulos, Chris et al. (2004). “Chemoattractant-induced phosphatidylinositol 3,4,5-trisphosphate accumulation is spatially amplified and adapts, independent of the actin cytoskeleton”. In: *Proceedings of the National Academy of Sciences of the United States of America* 101.24, pp. 8951–8956. ISSN: 00278424. DOI: 10.1073/pnas.0402152101. URL: www.pnas.org/cgi/doi/10.1073/pnas.0402152101.
- Jenkins, Misty R. et al. (2009). “The Strength of T Cell Receptor Signal Controls the Polarization of Cytotoxic Machinery to the Immunological Synapse”. In: *Immunity* 31.4, pp. 621–631. ISSN: 10747613. DOI: 10.1016/j.immuni.2009.08.024. URL: <http://dx.doi.org/10.1016/j.immuni.2009.08.024>.
- Jiu, Yaming et al. (2017). “Vimentin intermediate filaments control actin stress fiber assembly through GEF-H1 and RhoA”. In: *Journal of Cell Science* 130.5, pp. 892–902. ISSN: 14779137. DOI: 10.1242/jcs.196881.
- Jourdain, Line et al. (1997). “Stathmin: A tubulin-sequestering protein which forms a ternary T2S complex with two tubulin molecules”. In: *Biochemistry*, pp. 10817–10821. ISSN: 00062960. DOI: 10.1021/bi971491b. URL: <https://pubs.acs.org/sharingguidelines>.
- Junt, Tobias et al. (2007). “Subcapsular sinus macrophages in lymph nodes clear lymph-borne viruses and present them to antiviral B cells”. In: *Nature* 450.7166, pp. 110–114. ISSN: 0028-0836. DOI: 10.1038/nature06287. URL: <http://www.nature.com/doi/10.1038/nature06287>.
- Kaksonen, Marko, Christopher P. Toret, and David G. Drubin (2006). “Harnessing actin dynamics for clathrin-mediated endocytosis”. In: *Nature Reviews Molecular Cell Biology* 7.6, pp. 404–414. ISSN: 14710072. DOI: 10.1038/nrm1940. URL: www.nature.com/reviews/molcellbio.

- Keeling, Michael C. et al. (Dec. 2017). "Actomyosin and vimentin cytoskeletal networks regulate nuclear shape, mechanics and chromatin organization". In: *Scientific Reports* 7.1, pp. 1–14. ISSN: 20452322. DOI: 10.1038/s41598-017-05467-x.
- Kemphues, Kenneth J et al. (1988). "Identification of genes required for cytoplasmic localization in early *C. elegans* embryos". In: *Cell* 52, pp. 311–320. ISSN: 00928674. DOI: 10.1016/S0092-8674(88)80024-2.
- Ketchum, Christina et al. (2014). "Ligand Mobility Regulates B Cell Receptor Clustering and Signaling Activation". In: *Biophysical Journal* 106, pp. 26–36. DOI: 10.1016/j.bpj.2013.10.043. URL: <http://dx.doi.org/10.1016/j.bpj.2013.10.043>.
- Ketchum, Christina et al. (2018). "Subcellular topography modulates actin dynamics and signaling in B-cells". In: *Molecular biology of the cell*. DOI: 10.1091/mbc.E17-06-0422. URL: <https://www-molbiolcell-org.gate2.inist.fr/doi/pdf/10.1091/mbc.E17-06-0422>.
- Kindt, T., R. A. Goldsby, and B. A. Osborne (2007). *Kuby Immunology 6th Edition*. W. H. Freeman and Company.
- Kirby, Tyler J. and Jan Lammerding (Apr. 2018). *Emerging views of the nucleus as a cellular mechanosensor*. DOI: 10.1038/s41556-018-0038-y.
- Klymenko, T. et al. (Feb. 2018). "Lamin B1 regulates somatic mutations and progression of B-cell malignancies". In: *Leukemia* 32.2, pp. 364–375. ISSN: 14765551. DOI: 10.1038/leu.2017.255. URL: www.nature.com/leu.
- K.M., Ansel et al. (2000). "A chemokine-driven positive feedback loop organizes lymphoid follicles". In: *Nature* 406.6793, pp. 309–314. URL: <http://ovidsp.ovid.com/ovidweb.cgi?T=JS&PAGE=reference&D=emed5&NEWS=N&AN=2000274660>.
- Köster, Darius Vasco et al. (2016). "Actomyosin dynamics drive local membrane component organization in an in vitro active composite layer". In: *Proceedings of the National Academy of Sciences of the United States of America* 113.12, E1645–E1654. ISSN: 10916490. DOI: 10.1073/pnas.1514030113.
- Kumar, Abhishek et al. (Jan. 2014). "Actomyosin contractility rotates the cell nucleus". In: *Scientific Reports* 4.1, p. 3781. ISSN: 20452322. DOI: 10.1038/srep03781. URL: <http://www.nature.com/articles/srep03781>.
- Kumari, Anita et al. (Jan. 2019). "Actomyosin-driven force patterning controls endocytosis at the immune synapse". In: *Nature Communications* 10.1, p. 2870. ISSN: 2041-1723. DOI: 10.1038/s41467-019-10751-7. URL: <https://doi.org/10.1038/s41467-019-10751-7><http://www.nature.com/articles/s41467-019-10751-7><http://biorxiv.org/content/early/2018/10/25/452896.abstract>.
- Kumari, Anita et al. (2020). "Traction force microscopy to study B lymphocyte activation". In: *Journal of Visualized Experiments* 2020.161, pp. 1–15. ISSN: 1940087X. DOI: 10.3791/60947.

- Kwak, Kihyuck et al. (2018). "Intrinsic properties of human germinal center B cells set antigen affinity thresholds". In: *Science immunology* 3. URL: <http://immunology.sciencemag.org/>.
- Lammerding, Jan et al. (Sept. 2006). "Lamins a and C but not lamin B1 regulate nuclear mechanics". In: *Journal of Biological Chemistry* 281.35, pp. 25768–25780. ISSN: 00219258. DOI: 10.1074/jbc.M513511200.
- Laplaud, Valentin et al. (2021). "Pinching the cortex of live cells reveals thickness instabilities caused by myosin II motors". In: *Sci. Adv* 7.2. URL: <http://advances.sciencemag.org/>.
- Le Roux, Delphine et al. (2007). "Syk-dependent Actin Dynamics Regulate Endocytic Trafficking and Processing of Antigens Internalized through the B-Cell Receptor". In: *Molecular biology of the cell* 18. ISSN: 1059-1524. DOI: 10.1091/mbc.E06. URL: <http://www.molbiolcell.org/cgi/doi/10.1091/mbc.E06>.
- Lebien, Tucker W. and Thomas F. Tedder (Sept. 2008). "B lymphocytes: How they develop and function". In: *Blood* 112.5, pp. 1570–1580. ISSN: 00064971. DOI: 10.1182/blood-2008-02-078071.
- Leduc, Cécile and Sandrine Etienne-Manneville (2017). "Regulation of microtubule-associated motors drives intermediate filament network polarization". In: *Journal of Cell Biology* 216.6, pp. 1689–1703. ISSN: 15408140. DOI: 10.1083/jcb.201607045. URL: <https://doi.org/10.1083/jcb.201607045>.
- Leeuw, Rebecca de, Yosef Gruenbaum, and Ohad Medalia (2018). "Nuclear Lamins: Thin Filaments with Major Functions". In: *Trends in Cell Biology* 28.1, pp. 34–45. ISSN: 18793088. DOI: 10.1016/j.tcb.2017.08.004. URL: <http://dx.doi.org/10.1016/j.tcb.2017.08.004>.
- Lehtimäki, J. I. et al. (2021). "Generation of stress fibers through myosin-driven reorganization of the actin cortex". In: *eLife* 10, pp. 1–43. ISSN: 2050084X. DOI: 10.7554/eLife.60710.
- Li, Fang and Henry N. Higgs (Aug. 2003). "The mouse formin mDia1 is a potent actin nucleation factor regulated by autoinhibition". In: *Current Biology* 13.15, pp. 1335–1340. ISSN: 09609822. DOI: 10.1016/S0960-9822(03)00540-2.
- Li, Jingwen et al. (Jan. 2019). "The Coordination Between B Cell Receptor Signaling and the Actin Cytoskeleton During B Cell Activation". In: *Frontiers in Immunology* 9.JAN, p. 3096. ISSN: 1664-3224. DOI: 10.3389/fimmu.2018.03096. URL: <https://www.frontiersin.org/article/10.3389/fimmu.2018.03096/full>.
- Lin, Kevin B.L. et al. (2008). "The Rap GTPases Regulate B Cell Morphology, Immune-Synapse Formation, and Signaling by Particulate B Cell Receptor Ligands". In: *Immunity* 28.1, pp. 75–87. ISSN: 10747613. DOI: 10.1016/j.immuni.2007.11.019.

- Linder, Stefan (Sept. 2009). "Invadosomes at a glance". In: *Journal of Cell Science* 122.17, pp. 3009–3013. ISSN: 0021-9533. DOI: 10.1242/jcs.032631. URL: <http://www.ncbi.nlm.nih.gov/pubmed/19692587>.
- Liu, Chaohong et al. (2011). "A Balance of Bruton's Tyrosine Kinase and SHIP Activation Regulates B Cell Receptor Cluster Formation by Controlling Actin Remodeling". In: *The Journal of Immunology* 187.1, pp. 230–239. ISSN: 0022-1767. DOI: 10.4049/jimmunol.1100157. URL: <http://www.jimmunol.org/content/187/1/230>.
- Liu, Chaohong et al. (2012). "Analyzing actin dynamics during the activation of the B cell receptor in live B cells". In: *Biochemical and Biophysical Research Communications* 427.1, pp. 202–206. ISSN: 0006291X. DOI: 10.1016/j.bbrc.2012.09.046.
- Liu, Chaohong et al. (2013a). "N-WASP Is Essential for the Negative Regulation of B Cell Receptor Signaling". In: *PLoS Biology* 11.11, p. 1001704. ISSN: 15449173. DOI: 10.1371/journal.pbio.1001704. URL: www.plosbiology.org.
- Liu, Peng et al. (2020). "Insights into the assembly and activation of the microtubule nucleator γ -TuRC". In: *Nature* 578.7795, pp. 467–471. ISSN: 14764687. DOI: 10.1038/s41586-019-1896-6. URL: <https://doi.org/10.1038/s41586-019-1896-6>.
- Liu, Wanli et al. (2010). "Antigen affinity discrimination is an intrinsic function of the B cell receptor". In: *Journal of Experimental Medicine* 207.5, pp. 1095–1111. ISSN: 00221007. DOI: 10.1084/jem.20092123. URL: www.jem.org/cgi/doi/10.1084/jem.20092123.
- Liu, Xin et al. (2013b). "Diacylglycerol promotes centrosome polarization in T cells via reciprocal localization of dynein and myosin II". In: *Proceedings of the National Academy of Sciences of the United States of America* 110.29, pp. 11976–11981. ISSN: 00278424. DOI: 10.1073/pnas.1306180110. URL: www.pnas.org/cgi/doi/10.1073/pnas.1306180110.
- Lohner, James et al. (2019). "Large and reversible myosin-dependent forces in rigidity sensing". In: *Nature Physics* 15.7, pp. 689–695. ISSN: 17452481. DOI: 10.1038/s41567-019-0477-9. URL: <http://dx.doi.org/10.1038/s41567-019-0477-9>.
- Luxton, G. W.Gant et al. (2010). "Linear arrays of nuclear envelope proteins harness retrograde actin flow for nuclear movement". In: *Science* 329.5994, pp. 956–959. ISSN: 00368075. DOI: 10.1126/science.1189072. URL: <http://science.sciencemag.org/>.
- Mandal, Kalpana et al. (Dec. 2014). "Cell dipole behaviour revealed by ECM sub-cellular geometry". In: *Nature Communications* 5.1, pp. 1–10. ISSN: 20411723. DOI: 10.1038/ncomms6749. URL: <https://www.nature.com/articles/ncomms6749>.
- Marion, Sabrina et al. (Apr. 2011). "Ezrin Promotes Actin Assembly at the Phagosome Membrane and Regulates Phago-Lysosomal Fusion". In: *Traffic* 12.4, pp. 421–437. ISSN: 13989219. DOI: 10.1111/j.1600-0854.2011.01158.x.

- Mason, T. G. and J. Bibette (Oct. 1996). "Emulsification in viscoelastic media". In: *Physical Review Letters* 77.16, pp. 3481–3484. ISSN: 10797114. DOI: 10.1103/PhysRevLett.77.3481. URL: <https://link.aps.org/doi/10.1103/PhysRevLett.77.3481>.
- Mayya, Viveka et al. (2018). "Durable Interactions of T Cells with T Cell Receptor Stimuli in the Absence of a Stable Immunological Synapse". In: *Cell Reports* 22.2, pp. 340–349. ISSN: 22111247. DOI: 10.1016/j.celrep.2017.12.052. URL: <https://doi.org/10.1016/j.celrep.2017.12.052>.
- McIntosh, Betsy B. and E Michael Ostap (2016). "Myosin-I molecular motors at a glance". In: *Journal of Cell Science* 129.14, pp. 2689–2695. ISSN: 14779137. DOI: 10.1242/jcs.186403.
- McIntosh, J. Richard et al. (2018). "Microtubules grow by the addition of bent guanosine triphosphate tubulin to the tips of curved protofilaments". In: *Journal of Cell Biology* 217.8, pp. 2691–2708. ISSN: 15408140. DOI: 10.1083/jcb.201802138. URL: <https://doi.org/10.1083/jcb.201802138>.
- Merino-Cortés, Sara V et al. (2020). "Diacylglycerol kinase ζ promotes actin cytoskeleton remodeling and mechanical forces at the B cell immune synapse". In: *Science signaling*. ISSN: 19379145. DOI: 10.1126/scisignal.aaw8214. URL: <http://stke.sciencemag.org/>.
- Mesdjian, Olivier (2017). "Étude des phénomènes d'adhésion entre des cellules B et des gouttes d'huile fonctionnalisées par des anticorps à l'aide de pièges microfluidiques". PhD thesis. Université Pierre et Marie Curie - Paris VI, 2017. URL: <https://tel.archives-ouvertes.fr/tel-01821875http://www.theses.fr/2017PA066502/document>.
- Monks, Colin R F et al. (1998). "Three-dimensional segregation of supramolecular activation clusters in T cells". In: *Nature* 395. ISSN: 00280836. DOI: 10.1038/25764.
- Montel, Lorraine, Léa Pinon, and Jacques Fattaccioli (2019). "A Multiparametric and High-Throughput Assay to Quantify the Influence of Target Size on Phagocytosis". In: *Biophysical Journal*. ISSN: 15420086. DOI: 10.1016/j.bpj.2019.06.021. URL: <https://doi.org/10.1016/j.bpj.2019.06.021>.
- Moreau, Hélène D. et al. (2012). "Dynamic in situ cytometry uncovers t cell receptor signaling during immunological synapses and kinapses in vivo". In: *Immunity* 37.2, pp. 351–363. ISSN: 10747613. DOI: 10.1016/j.immuni.2012.05.014.
- Moreau, Hélène D. et al. (Sept. 2015). "Signal strength regulates antigen-mediated T-cell deceleration by distinct mechanisms to promote local exploration or arrest". In: *Proceedings of the National Academy of Sciences of the United States of America* 112.39, pp. 12151–12156. ISSN: 10916490. DOI: 10.1073/pnas.1506654112. URL: www.pnas.org/cgi/doi/10.1073/pnas.1506654112.

- Moritz, Michelle et al. (2000). "Structure of the γ -tubulin ring complex: A template for microtubule nucleation". In: *Nature Cell Biology* 2.6, pp. 365–370. ISSN: 14657392. DOI: 10.1038/35014058. URL: www.nature.com/ncb.
- Murugesan, Sricharan et al. (2016). "Formin-generated actomyosin arcs propel t cell receptor microcluster movement at the immune synapse". In: *Journal of Cell Biology* 215.3, pp. 383–399. ISSN: 15408140. DOI: 10.1083/jcb.201603080.
- Nagasawa, Takashi (2006). "Microenvironmental niches in the bone marrow required for B-cell development". In: *Nature Reviews Immunology* 6.2, pp. 107–116. ISSN: 14741733. DOI: 10.1038/nri1780. URL: www.nature.com/reviews/immunol.
- Natkanski, Elizabeth et al. (2013). "B cells use mechanical energy to discriminate antigen affinities". In: *Science* 340.6140, pp. 1587–1590. DOI: 10.1126/science.1237572. B.
- Neuman, Keir C and Attila Nagy (2008). "Single-molecule force spectroscopy: optical tweezers, magnetic tweezers and atomic force microscopy". In: *Nature Methods*. DOI: 10.1038/NMETH.1218. URL: <http://www.nature.com/naturemethods>.
- Nobes, Catherine D. and Alan Hall (Mar. 1999). "Rho GTPases Control Polarity, Protrusion, and Adhesion during Cell Movement". In: *The Journal of Cell Biology* 144.6, p. 1235. DOI: 10.1083/JCB.144.6.1235. URL: [/pmc/articles/PMC2150589/](https://pmc/articles/PMC2150589/) [https://www.ncbi.nlm.nih.gov/pmc/articles/PMC2150589/](https://www.ncbi.nlm.nih.gov/pmc/articles/PMC2150589/?report=abstract) [?report=abstracthttps://www.ncbi.nlm.nih.gov/pmc/articles/PMC2150589/](https://www.ncbi.nlm.nih.gov/pmc/articles/PMC2150589/).
- Nomachi, Akira et al. (2013). "Moesin controls clathrin-mediated S1PR1 internalization in T cells". In: *PLoS ONE* 8.12, p. 82590. ISSN: 19326203. DOI: 10.1371/journal.pone.0082590. URL: www.plosone.org.
- Norcross, M. A. (Jan. 1984). "A synaptic basis for T-lymphocyte activation". In: *Annales de l'Institut Pasteur / Immunologie* 135.2, pp. 113–134. ISSN: 0769-2625. DOI: 10.1016/S0769-2625(84)81105-8.
- Núñez-Andrade, Norman et al. (2016). "HDAC6 regulates the dynamics of lytic granules in cytotoxic T lymphocytes". In: *Journal of Cell Science* 129.7, pp. 1305–1311. ISSN: 14779137. DOI: 10.1242/jcs.180885.
- Obino, Dorian and Ana-Maria Lennon-Duménil (2014). "A Critical Role for Cell Polarity in Antigen Extraction, Processing, and Presentation by B Lymphocytes". In: *Advances in immunology* 123, pp. 51–67. DOI: 10.1016/B978-0-12-800266-7.00001-7. URL: <http://dx.doi.org/10.1016/B978-0-12-800266-7.00001-7>.
- Obino, Dorian et al. (2016). "Actin nucleation at the centrosome controls lymphocyte polarity". In: *Nature Communications* 7. DOI: 10.1038/ncomms10969. URL: www.nature.com/naturecommunications.
- Obino, Dorian et al. (2017). "Vamp-7-dependent secretion at the immune synapse regulates antigen extraction and presentation in B-lymphocytes". In: *Molecular Biology*

- of the Cell* 28. DOI: 10.1091/mbc.E16-10-0722. URL: <https://www.molbiolcell.org/doi/pdf/10.1091/mbc.e16-10-0722>.
- O'Connell, Christopher B., Matthew J. Tyska, and Mark S. Mooseker (May 2007). "Myosin at work: Motor adaptations for a variety of cellular functions". In: *Biochimica et Biophysica Acta - Molecular Cell Research* 1773.5, pp. 615–630. ISSN: 01674889. DOI: 10.1016/j.bbamcr.2006.06.012.
- Oddos, Stephane et al. (2008). "High-speed high-resolution imaging of intercellular immune synapses using optical tweezers". In: *Biophysical Journal* 95.10, pp. L66–L68. ISSN: 15420086. DOI: 10.1529/biophysj.108.143198. URL: <http://dx.doi.org/10.1529/biophysj.108.143198>.
- Onabajo, Olusegun O. et al. (May 2008). "Actin-Binding Protein 1 Regulates B Cell Receptor-Mediated Antigen Processing and Presentation in Response to B Cell Receptor Activation". In: *The Journal of Immunology* 180.10, pp. 6685–6695. ISSN: 0022-1767. DOI: 10.4049/jimmunol.180.10.6685. URL: <https://www.jimmunol.org/content/180/10/6685><https://www.jimmunol.org/content/180/10/6685.abstract>.
- Pape, Kathryn A et al. (2007). "The Humoral Immune Response Is Initiated in Lymph Nodes by B Cells that Acquire Soluble Antigen Directly in the Follicles". In: *Immunity* 26, pp. 491–502. ISSN: 10747613. DOI: 10.1016/j.immuni.2007.02.011.
- Parent, Carole A and Peter N Devreotes (1999). "A Cell's Sense of Direction". In: *Science* 284. April.
- Paul, Danielle M. et al. (Sept. 2020). "In situ cryo-electron tomography reveals filamentous actin within the microtubule lumen". In: *Journal of Cell Biology* 219.9. ISSN: 15408140. DOI: 10.1083/JCB.201911154. URL: <https://doi.org/10.1083/jcb.201911154>.
- Pedersen, Ross T.A. and David G. Drubin (2019). "Type I myosins anchor actin assembly to the plasma membrane during clathrin-mediated endocytosis". In: *Journal of Cell Biology* 218.4, pp. 1138–1147. ISSN: 15408140. DOI: 10.1083/jcb.201810005.
- Peglion, Florent and Nathan W Goehring (2019). "Switching states: dynamic remodeling of polarity complexes as a toolkit for cell polarization". In: *Current Opinion in Cell Biology*. ISSN: 18790410. DOI: 10.1016/j.ceb.2019.05.002. URL: <https://doi.org/10.1016/j.ceb.2019.05.002>.
- Pollard, Thomas D and John A Cooper (2009). "Actin, a central player in cell shape and movement". In: *Science* 326.5957, pp. 1208–1212. ISSN: 00368075. DOI: 10.1126/science.1175862. URL: <http://science.sciencemag.org/>.
- Pore, Debasis and Neetu Gupta (2015). "Ezrin-Radixin-Moesin family proteins in the regulation of B cell immune response". In: *Critical Review in Immunology*.

- Reversat, Anne et al. (Apr. 2015). "Polarity protein Par3 controls B-cell receptor dynamics and antigen extraction at the immune synapse". In: *Molecular Biology of the Cell* 26.7. Ed. by Xueliang Zhu, pp. 1273–1285. ISSN: 1059-1524. DOI: 10.1091/mbc.e14-09-1373. URL: <https://www.molbiolcell.org/doi/prev/20180314-aop/pdf/10.1091/mbc.E14-09-1373><http://www.molbiolcell.org/doi/10.1091/mbc.e14-09-1373>.
- Rey-Suarez, Ivan et al. (2020). "WASP family proteins regulate the mobility of the B cell receptor during signaling activation". In: *Nature Communications* 11.1. ISSN: 20411723. DOI: 10.1038/s41467-020-14335-8. URL: <https://doi.org/10.1038/s41467-020-14335-8>.
- Reymann, Anne-Cécile et al. (2012). "Actin network architecture can determine Myosin motor activity". In: *Science* 304.5674, pp. 1158–1160. ISSN: 00368075. DOI: 10.1126/science.1096284. URL: www.sciencemag.org/cgi/content/full/science.1218632/DC1.
- Riedl, Julia et al. (July 2008). "Lifeact: a versatile marker to visualize F-actin". In: *Nat Meth* 5.7, pp. 605–607. ISSN: 1548-7091. URL: <http://dx.doi.org/10.1038/nmeth.1220>http://www.nature.com/nmeth/journal/v5/n7/supinfo/nmeth.1220_S1.html.
- Ritter, Alex T et al. (2015). "Actin Depletion Initiates Events Leading to Granule Secretion at the Immunological Synapse". In: *Immunity* 42, pp. 864–876. DOI: 10.1016/j.immuni.2015.04.013. URL: <http://dx.doi.org/10.1016/j.immuni.2015.04.013>.
- Ritter, Alex T et al. (2017). "Cortical actin recovery at the immunological synapse leads to termination of lytic granule secretion in cytotoxic T lymphocytes". In: *Proceedings of the National Academy of Sciences of the United States of America* 114.32, E6585–E6594. ISSN: 10916490. DOI: 10.1073/pnas.1710751114. URL: www.pnas.org/cgi/doi/10.1073/pnas.1710751114.
- Robert, Amélie, Caroline Hookway, and Vladimir I Gelfand (2016). "Intermediate filament dynamics: What we can see now and why it matters". In: *Bioessays*. ISSN: 15211878. DOI: 10.1002/bies.201500142.
- Roberts, Aleah D. et al. (Dec. 2020). "Structurally distinct endocytic pathways for B cell receptors in B lymphocytes". In: *Molecular Biology of the Cell* 31.25, pp. 2826–2840. ISSN: 1059-1524. DOI: 10.1091/mbc.e20-08-0532. URL: <https://www.molbiolcell.org/doi/abs/10.1091/mbc.E20-08-0532>.
- Roman-Garcia, Sara et al. (2018). "Distinct roles for Bruton's Tyrosine Kinase in B cell immune synapse formation". In: *Frontiers in Immunology* 9.SEP, p. 2027. ISSN: 16643224. DOI: 10.3389/fimmu.2018.02027. URL: www.frontiersin.org.

- Roper, Sophie I. et al. (2019). "B cells extract antigens at arp2/3-generated actin foci interspersed with linear filaments". In: *eLife* 8, pp. 1–24. ISSN: 2050084X. DOI: 10.7554/eLife.48093.
- Rotty, Jeremy D. et al. (2015). "Profilin-1 Serves as a gatekeeper for actin assembly by Arp2/3-Dependent and -Independent pathways". In: *Developmental Cell* 32.1, pp. 54–67. ISSN: 18781551. DOI: 10.1016/j.devcel.2014.10.026. URL: <http://dx.doi.org/10.1016/j.devcel.2014.10.026>.
- Roux, Kyle J et al. (2009). "Nesprin 4 is an outer nuclear membrane protein that can induce kinesin-mediated cell polarization". In: *Proceedings of the National Academy of Sciences of the United States of America* 106.7, pp. 2194–2199. ISSN: 00278424. DOI: 10.1073/pnas.0808602106. URL: www.pnas.org/cgi/content/full/.
- RStudio, Team (2020). *RStudio: Integrated Development Environment for R*. Boston, MA. URL: <http://www.rstudio.com/>.
- Sáez, Juan José et al. (2019). "The exocyst controls lysosome secretion and antigen extraction at the immune synapse of B cells". In: *The Journal of Cell Biology*, jcb.201811131. ISSN: 0021-9525. DOI: 10.1083/jcb.201811131. URL: <https://doi.org/10.1083/jcb.201811131><http://doi.org/10.1083/jcb.201811131><http://www.jcb.org/lookup/doi/10.1083/jcb.201811131>.
- Sage, Peter T et al. (2012). "Memory/Effector T Cells Invadosome-like Protrusions Formed by Antigen Recognition Is Facilitated by". In: *J Immunol* 188, pp. 3686–3699. DOI: 10.4049/jimmunol.1102594. URL: <http://www.jimmunol.org/content/188/8/3686><http://www.jimmunol.org/content/188/8/3686.full#ref-list-1>.
- Sawicka, Anna et al. (Nov. 2017). "Micropipette force probe to quantify single-cell force generation: application to T-cell activation". In: *Molecular Biology of the Cell* 28.23. Ed. by Manuel Théry, pp. 3229–3239. ISSN: 1059-1524. DOI: 10.1091/mbc.e17-06-0385. URL: <http://www.molbiolcell.org/doi/10.1091/mbc.e17-06-0385>.
- Schindelin, Johannes et al. (June 2012). "Fiji: An open-source platform for biological-image analysis". In: *Nature Methods* 9.7, pp. 676–682. ISSN: 15487091. DOI: 10.1038/nmeth.2019. URL: <https://www.nature.com/articles/nmeth.2019>.
- Schmoranzer, Jan et al. (2009). "Par3 and Dynein Associate to Regulate Local Microtubule Dynamics and Centrosome Orientation during Migration". In: *Current Biology* 19.13, pp. 1065–1074. ISSN: 09609822. DOI: 10.1016/j.cub.2009.05.065. URL: <http://dx.doi.org/10.1016/j.cub.2009.05.065>.
- Schnyder, Tim et al. (2011). "B Cell Receptor-Mediated Antigen Gathering Requires Ubiquitin Ligase Cbl and Adaptors Grb2 and Dok-3 to Recruit Dynein to the Signaling Microcluster". In: *Immunity* 34.6, pp. 905–918. ISSN: 10747613. DOI: 10.1016/j.immuni.2011.06.001.

- Schreiner, Sarah M. et al. (June 2015). "The tethering of chromatin to the nuclear envelope supports nuclear mechanics". In: *Nature Communications* 6. ISSN: 20411723. DOI: 10.1038/ncomms8159.
- Schroeder, Harry W and Lisa Cavacini (2010). "Structure and function of immunoglobulins". In: *Journal of Allergy and Clinical Immunology* 125.2 SUPPL. 2. ISSN: 00916749. DOI: 10.1016/j.jaci.2009.09.046.
- Seeley-Fallen, Margaret K. et al. (July 2014). "Actin-binding protein 1 links B-cell antigen receptors to negative signaling pathways". In: *Proceedings of the National Academy of Sciences of the United States of America* 111.27, pp. 9881–9886. ISSN: 10916490. DOI: 10.1073/pnas.1321971111. URL: <https://www.pnas.org/content/111/27/9881><https://www.pnas.org/content/111/27/9881.abstract>.
- Seetharaman, Shailaja et al. (2021). "Microtubules tune mechanosensitive cell responses". In: *bioRxiv*. DOI: 10.1101/2020.07.22.205203. URL: <https://doi.org/10.1101/2020.07.22.205203>.
- Sergé, Arnaud et al. (July 2008). "Dynamic multiple-target tracing to probe spatiotemporal cartography of cell membranes". In: *Nature Methods* 5.8, pp. 687–694. ISSN: 15487091. DOI: 10.1038/nmeth.1233. URL: <https://www.nature.com/articles/nmeth.1233>.
- Serrador, Juan M. et al. (2004). "HDAC6 deacetylase activity links the tubulin cytoskeleton with immune synapse organization". In: *Immunity* 20.4, pp. 417–428. ISSN: 10747613. DOI: 10.1016/S1074-7613(04)00078-0.
- Shaheen, Samina et al. (July 2017). "Substrate stiffness governs the initiation of B cell activation by the concerted signaling of PKC β and focal adhesion kinase". In: *eLife* 6, e23060. ISSN: 2050-084X. DOI: 10.7554/eLife.23060. URL: <https://elifesciences.org/articles/23060>.
- Sharma, Shruti, Gregory Orłowski, and Wenxia Song (2009). "Btk Regulates B Cell Receptor-Mediated Antigen Processing and Presentation by Controlling Actin Cytoskeleton Dynamics in B Cells". In: *The Journal of Immunology* 182.1, pp. 329–339. ISSN: 0022-1767. DOI: 10.4049/jimmunol.182.1.329.
- Shevchuk, Andrew I. et al. (2012). "An alternative mechanism of clathrin-coated pit closure revealed by ion conductance microscopy". In: *Journal of Cell Biology* 197.4, pp. 499–508. ISSN: 00219525. DOI: 10.1083/jcb.201109130. URL: www.jcb.org/cgi/doi/10.1083/jcb.201109130JCB499.
- Shiu, Jau Ye et al. (2018). "Nanopillar force measurements reveal actin-cap-mediated YAP mechanotransduction". In: *Nature Cell Biology* 20.3, pp. 262–271. ISSN: 14764679. DOI: 10.1038/s41556-017-0030-y. URL: <http://dx.doi.org/10.1038/s41556-017-0030-y>.

- Siegrist, Sarah E and Chris Q Doe (2007). "Microtubule-induced cortical cell polarity". In: *Genes and Development* 21.5, pp. 483–496. ISSN: 08909369. DOI: 10.1101/gad.1511207. URL: <http://www.genesdev.org/cgi/doi/10.1101/gad.1511207>..
- Skelley, Alison M et al. (2009). "Microfluidic control of cell pairing and fusion." In: *Nature methods* 6.2, pp. 147–52. ISSN: 1548-7105. DOI: 10.1038/nmeth.1290. URL: <http://www.ncbi.nlm.nih.gov/pubmed/19122668>.
- Sohn, Hae Won, Pavel Tolar, and Susan K. Pierce (July 2008). "Membrane heterogeneities in the formation of B cell receptor-Lyn kinase microclusters and the immune synapse." In: *The Journal of cell biology* 182.2, pp. 367–79. ISSN: 1540-8140. DOI: 10.1083/jcb.200802007. URL: <http://www.ncbi.nlm.nih.gov/pubmed/18644892><http://www.pubmedcentral.nih.gov/articlerender.fcgi?artid=PMC2483512>.
- Solinet, Sara et al. (2013). "The actin-binding ERM protein Moesin binds to and stabilizes microtubules at the cell cortex". In: *Journal of Cell Biology* 202.2, pp. 251–260. ISSN: 00219525. DOI: 10.1083/jcb.201304052.
- Spillane, Katelyn M and Pavel Tolar (2016). "B cell antigen extraction is regulated by physical properties of antigen-presenting cells". In: *The Journal of Cell Biology* 2, pp. 1–14. ISSN: 15408140. DOI: 10.1083/jcb.201607064.
- Stinchcombe, Jane C and Gillian M. Griffiths (2014). "Communication, the centrosome and the immunological synapse". In: *Philosophical Transactions of the Royal Society B* 369.1650. ISSN: 14712970. DOI: 10.1098/rstb.2013.0463. URL: <http://dx.doi.org/10.1098/rstb.2013.0463>.
- Suarez, Cristian and David R. Kovar (Sept. 2016). "Internetwork competition for monomers governs actin cytoskeleton organization". In: *Nature Reviews Molecular Cell Biology* 17.12, pp. 799–810. ISSN: 14710080. DOI: 10.1038/nrm.2016.106. URL: <https://www-nature-com.proxy.insermbiblio.inist.fr/articles/nrm.2016.106>www.nature.com/nrm.
- Suarez, Cristian et al. (2015). "Profilin regulates F-Actin network homeostasis by favoring formin over Arp2/3 complex". In: *Developmental Cell* 32.1, pp. 43–53. ISSN: 18781551. DOI: 10.1016/j.devcel.2014.10.027. URL: <http://dx.doi.org/10.1016/j.devcel.2014.10.027>.
- Suzuki, Kazuhiro et al. (July 2009). "Visualizing B cell capture of cognate antigen from follicular dendritic cells." In: *The Journal of experimental medicine* 206.7, pp. 1485–93. ISSN: 1540-9538. DOI: 10.1084/jem.20090209. URL: </pmc/articles/PMC2715076/?report=abstract><http://www.ncbi.nlm.nih.gov/pmc/articles/PMC2715076/><http://www.ncbi.nlm.nih.gov/pubmed/19506051><http://www.pubmedcentral.nih.gov/articlerender.fcgi?artid=PMC2715076>.

- Tan, John L et al. (2003). "Cells lying on a bed of microneedles: An approach to isolate mechanical force". In: *Proceedings of the National Academy of Sciences of the United States of America* 100.4. ISSN: 00278424. DOI: 10.1073/pnas.0235407100. URL: www.pnas.org/cgi/doi/10.1073/pnas.0235407100.
- Tariq, Zeshan et al. (July 2017). "Lamin A and microtubules collaborate to maintain nuclear morphology". In: *Nucleus* 8.4, pp. 433–446. ISSN: 1949-1034. DOI: 10.1080/19491034.2017.1320460. URL: <https://www.tandfonline.com/doi/full/10.1080/19491034.2017.1320460>.
- Teo, Jessica L. et al. (2020). "A Biologist's Guide to Traction Force Microscopy Using Polydimethylsiloxane Substrate for Two-Dimensional Cell Cultures". In: *STAR Protocols* 1.2, p. 100098. ISSN: 26661667. DOI: 10.1016/j.xpro.2020.100098. URL: <http://dx.doi.org/10.1016/j.xpro.2020.100098>.
- Thievensen, Ingo et al. (Nov. 2015). "Vinculin is required for cell polarization, migration, and extracellular matrix remodeling in 3D collagen". In: *FASEB Journal* 29.11, pp. 4555–4567. ISSN: 15306860. DOI: 10.1096/fj.14-268235.
- Tikhonenko, Irina et al. (Apr. 2013). "A kinesin-mediated mechanism that couples centrosomes to nuclei". In: *Cellular and Molecular Life Sciences* 70.7, pp. 1285–1296. ISSN: 1420682X. DOI: 10.1007/s00018-012-1205-0.
- Tinevez, Jean Yves et al. (Feb. 2017). "TrackMate: An open and extensible platform for single-particle tracking". In: *Methods* 115, pp. 80–90. ISSN: 10959130. DOI: 10.1016/j.ymeth.2016.09.016.
- Treanor, Bebhinn et al. (2010). "The Membrane Skeleton Controls Diffusion Dynamics and Signaling through the B Cell Receptor". In: *Immunity* 32.2, pp. 187–199. ISSN: 10747613. DOI: 10.1016/j.immuni.2009.12.005.
- Treanor, Bebhinn et al. (2011). "Dynamic cortical actin remodeling by ERM proteins controls BCR microcluster organization and integrity". In: *Journal of Experimental Medicine* 208.5, pp. 1055–1068. ISSN: 00221007. DOI: 10.1084/jem.20101125. URL: www.jem.org/cgi/doi/10.1084/jem.20101125.
- Trepat, Xavier et al. (May 2009). "Physical forces during collective cell migration". In: *Nature Physics* 5.6, pp. 426–430. ISSN: 17452481. DOI: 10.1038/nphys1269. URL: <https://www.nature.com/articles/nphys1269>.
- Tsui, Carlson et al. (Oct. 2018). "Dynamic reorganisation of intermediate filaments coordinates early B-cell activation". In: *Life Science Alliance* 1.5. ISSN: 25751077. DOI: 10.26508/lsa.201800060.
- Tukey, J. W. (1977). "Exploratory data analysis". In: *Reading Massachusetts: Addison-Wesley*. ISSN: 00257818. DOI: 10.4324/9781315311135-8.
- Ueda, Hironori et al. (2015). "Distinct Roles of Cytoskeletal Components in Immunological Synapse Formation and Directed Secretion". In: *Journal of Immunology*. ISSN:

- 0022-1767. DOI: 10.4049/jimmunol.1402175. URL: <http://www.jimmunol.org/content/195/9/4117>.
- Uhler, Caroline and G V Shivashankar (2017). "Regulation of genome organization and gene expression by nuclear mechanotransduction". In: *Nature Reviews Molecular Cell Biology* 18.12, pp. 717–727. ISSN: 14710080. DOI: 10.1038/nrm.2017.101. URL: www.nature.com/nrm.
- Ulloa, Romina et al. (Apr. 2021). "B cells adapt their nuclear morphology to organize the immune synapse and help antigen extraction". In: *bioRxiv*, p. 2021.04.20.440571. DOI: 10.1101/2021.04.20.440571. URL: <https://doi.org/10.1101/2021.04.20.440571>.
- Vascotto, Fulvia et al. (Mar. 2007). "The actin-based motor protein myosin II regulates MHC class II trafficking and BCR-driven antigen presentation". In: *Journal of Cell Biology* 176.7, pp. 1007–1019. ISSN: 00219525. DOI: 10.1083/jcb.200611147.
- Vu, Timothy Quang et al. (2017). "Bridging the gap: microfluidic devices for short and long distance cell-cell communication". In: *Lab on a Chip* 17.6, pp. 1009–1023. ISSN: 14730189. DOI: 10.1039/c6lc01367h.
- Wan, Zhengpeng et al. (2013). "B Cell Activation Is Regulated by the Stiffness Properties of the Substrate Presenting the Antigens". In: *The Journal of Immunology* 190.12, pp. 6711–6711. ISSN: 0022-1767. DOI: 10.4049/jimmunol.1390030. URL: <http://www.jimmunol.org/content/190/9/4661>.
- Wan, Zhengpeng et al. (2015). "The activation of IgM- or isotype-switched IgG- and IgE-BCR exhibits distinct mechanical force sensitivity and threshold". In: *eLife* 4.AUGUST2015, pp. 1–24. ISSN: 2050084X. DOI: 10.7554/eLife.06925.
- Wang, Jia C. et al. (Mar. 2017). "The Rap1-cofilin-1 pathway coordinates actin reorganization and MTOC polarization at the B cell immune synapse". In: *Journal of Cell Science* 130.6, pp. 1094–1109. ISSN: 14779137. DOI: 10.1242/jcs.191858.
- Wang, Junyi et al. (Aug. 2018). "Profiling the origin, dynamics, and function of traction force in B cell activation". In: *Science Signaling* 11.542, eaai9192. ISSN: 1945-0877. DOI: 10.1126/scisignal.aai9192. URL: <http://stke.sciencemag.org/lookup/doi/10.1126/scisignal.aai9192><http://stke.sciencemag.org/>.
- Wang, Xuefeng and Taekjip Ha (2013). "Defining single molecular forces required to activate integrin and notch signaling." In: *Science (New York, N.Y.)* 340.6135, pp. 991–4. ISSN: 1095-9203. DOI: 10.1126/science.1231041. URL: <http://www.ncbi.nlm.nih.gov/pubmed/23704575><http://www.pubmedcentral.nih.gov/articlerender.fcgi?artid=PMC3710701>.
- Wickstead, Bill and Keith Gull (2011). "The evolution of the cytoskeleton". In: *Journal of Cell Biology* 194.4, pp. 513–525. ISSN: 00219525. DOI: 10.1083/jcb.201102065. URL: www.jcb.org/cgi/doi/10.1083/jcb.201102065JCB513.

- Wodarz, Andreas and Inke Näthke (Sept. 2007). "Cell polarity in development and cancer". In: *Nature Cell Biology* 9.9, pp. 1016–1024. ISSN: 14657392. DOI: 10.1038/ncb433.
- Wojnacki, José et al. (Mar. 2014). "Rho GTPases at the crossroad of signaling networks in mammals: Impact of Rho-GTPases on microtubule organization and dynamics". In: *Small GTPases* 5. ISSN: 21541256. DOI: 10.4161/sgtp.28430.
- Woods, Benjamin and Daniel J Lew (2019). "Polarity establishment by Cdc42: Key roles for positive feedback and differential mobility". In: *Small GTPases* 10.2, pp. 130–137. ISSN: 21541256. DOI: 10.1080/21541248.2016.1275370. URL: <https://www.tandfonline.com/action/journalInformation?journalCode=ksgt20>.
- Woźniak, Marcin J. et al. (2009). "Role of kinesin-1 and cytoplasmic dynein in endoplasmic reticulum movement in VERO cells". In: *Journal of Cell Science* 122.12, pp. 1979–1989. ISSN: 00219533. DOI: 10.1242/jcs.041962. URL: <http://jcs.biologists.org/cgi/content/full/122/12/1979/DC1>.
- Yuseff, Maria-Isabel and Ana Maria Lennon-Dumenil (May 2015). "B Cells use Conserved Polarity Cues to Regulate Their Antigen Processing and Presentation Functions". In: *Frontiers in Immunology* 6, p. 251. ISSN: 1664-3224. DOI: 10.3389/fimmu.2015.00251. URL: http://www.frontiersin.org/Antigen_Presenting_Cell_Biology/10.3389/fimmu.2015.00251/abstract.
- Yuseff, Maria-Isabel et al. (Sept. 2011). "Polarized secretion of lysosomes at the B cell synapse couples antigen extraction to processing and presentation." In: *Immunity* 35.3, pp. 361–74. ISSN: 1097-4180. DOI: 10.1016/j.immuni.2011.07.008. URL: <http://www.ncbi.nlm.nih.gov/pubmed/21820334>.
- Yuseff, Maria-Isabel Isabel et al. (July 2013). "How B cells capture, process and present antigens: a crucial role for cell polarity". In: *Nat Rev Immunol* 13.7, pp. 475–486. ISSN: 1474-1733. DOI: 10.1038/nri3469. URL: <http://dx.doi.org/10.1038/nri3469><http://10.0.4.14/nri3469>.
- Zhu, De-Min et al. (2007). "Analysis of two-dimensional dissociation constant of laterally mobile cell adhesion molecules". In: *Biophysical Journal* 92.3, pp. 1022–1034. ISSN: 00063495. DOI: 10.1529/biophysj.106.089649.

Appendix A







Co-first author Research article

ARTICLE

<https://doi.org/10.1038/s41467-019-10751-7>

OPEN

Actomyosin-driven force patterning controls endocytosis at the immune synapse

Anita Kumari^{1,2,6}, Judith Pineau ^{1,2,6}, Pablo J. Sáez ¹, Mathieu Maurin¹, Danielle Lankar¹, Mabel San Roman¹, Katharina Hennig³, Vanessa F. Boura⁴, Raphael Voituriez⁵, Mikael C.I. Karlsson ⁴, Martial Balland ³, Ana-Maria Lennon Dumenil ¹ & Paolo Pierobon ¹

An important channel of cell-to-cell communication is direct contact. The immune synapse is a paradigmatic example of such type of interaction: it forms upon engagement of antigen receptors in lymphocytes by antigen-presenting cells and allows the local exchange of molecules and information. Although mechanics has been shown to play an important role in this process, how forces organize and impact on synapse function is unknown. We find that mechanical forces are spatio-temporally patterned at the immune synapse: global pulsatile myosin II-driven tangential forces are observed at the synapse periphery while localised forces generated by invadosome-like F-actin protrusions are detected at its centre. Noticeably, we observe that these force-producing actin protrusions constitute the main site of antigen extraction and endocytosis and require myosin II contractility to form. The interplay between global and local forces dictated by the organization of the actomyosin cytoskeleton therefore controls endocytosis at the immune synapse.

¹Institut Curie, PSL Research University, INSERM U932, 26 rue d'Ulm, 75248 Paris, Cedex 05, France. ²Université Paris Descartes, Paris 75006, France. ³Laboratoire Interdisciplinaire de Physique, Université Joseph Fourier (Grenoble 1), 38402 Saint, Martin d'Hères Cedex 9, France. ⁴Department of Microbiology, Tumor and Cell Biology, Karolinska Institutet, Stockholm 17177, Sweden. ⁵Laboratoire de Physique Théorique de la Matière Condensée, UMR 7600 CNRS /UPMC and Laboratoire Jean Perrin, UMR 8237 CNRS /UPMC, 4 Place Jussieu, 75255 Paris, Cedex 05, France. ⁶These authors contributed equally: Anita Kumari, Judith Pineau. Correspondence and requests for materials should be addressed to A.-M.L.D. (email: ana-maria.lennon@curie.fr) or to P.P. (email: paolo.pierobon@curie.fr)

Cells are endowed with the ability to internalize substrate-bound molecules, which they recognize through specific surface receptors. Although the role of substrate mechanics has been extensively investigated in the context of adhesion, its impact on receptor endocytosis remains unclear. A typical case of coupling between substrate mechanics and juxtacrine signaling (i.e., by direct contact) occurs at the immunological synapse, i.e., the tight contact zone that forms between a lymphocyte and an antigen-presenting cell^{1,2}. In the case of B lymphocytes, formation of the immunological synapse results from the engagement of the B-cell-antigen receptor (BCR) by antigens exposed at the surface of neighboring cells *in vivo*. The immune synapse provides a platform that facilitates signaling and leads to antigen internalization^{3–5}, which is needed for B cells to ultimately produce high-affinity antibodies and generate immune memory^{6,7}. As endocytosis often involves surface-tethered rather than soluble molecules when occurring in tissues, antigen internalization at the B-cell synapse provides a valuable model to study the impact of mechanics in this process.

Different experimental systems have been developed as surrogate antigen-presenting cells to study antigen extraction at the B-cell synapse *ex vivo*: planar lipid bilayers⁶, plasma membrane sheets⁸, and polystyrene beads⁹. On lipid bilayers, the immune synapse consists of a set of concentric patterns in which molecules and cytoskeletal components are partitioned: a distal supramolecular antigen cluster (dSMAC) with an actin ring, a peripheral supramolecular antigen cluster (pSMAC) enriched for adhesion molecules and a central supramolecular antigen cluster (cSMAC) in which antigens concentrate⁶. The first antigen extraction model to be proposed was based on the observation that B cells spread over antigen-coated substrates and then contract, allowing the transport of BCR-bound antigens towards the cSMAC¹⁰. A second model arose from Atomic Force Microscopy experiments monitoring interactions between the BCR and plasma membrane sheet-bound antigens. These experiments showed that B cells internalize these antigens by actively pulling on BCR-antigen complexes⁸. Both these mechanical models rely on the actin-based molecular motor non-muscular myosin II. In the first model, myosin II generates a global actomyosin contraction that drives antigen transport towards the cSMAC, whereas in the second model, myosin II acts locally by pulling on individual BCR-antigen complexes. Intriguingly, punctuated actin structures have also been observed in mouse B cells, where they were found to colocalize with BCR microclusters, and in human B cells, where they were shown to be involved in BCR signaling and antigen extraction^{11,12}. Whether and how these actin structures are related to myosin II activity is not understood.

Here we investigate the spatio-temporal organization of forces exerted by B lymphocytes during antigen extraction. We show that they display a stereotypical patterning profile that includes two components: (1) peripheral forces resulting from the centripetal flow of myosin II and (2) central forces exerted by local invadosome-like actin protrusions, which mediate antigen extraction. Noticeably, we find that these actin protrusions need myosin II-dependent peripheral forces to form, reconciling the models previously proposed for antigen extraction. We conclude that the interplay between global and local forces, governed by the dynamics of the actomyosin cytoskeleton, controls endocytosis at the immune synapse. Myosin II-dependent force patterning therefore emerges as a key regulator of cell–cell interactions.

Results

B cells exert pulsatile pulling forces on soft substrate. We used time-dependent traction force microscopy (TFM, see Methods)^{13–15} to analyse the spatio-temporal distribution of forces at the B-cell

synapse (Fig. 1a). Primary naive B cells freshly purified from the spleen of mice expressing a hen egg lysozyme (HEL)-specific BCR were plated on gels coated with HEL or with bovine serum albumin (BSA) as a negative control. A rigidity of 500 Pa that matches the physiological rigidity of the macrophages that present the antigen to B cells *in vivo* was chosen¹⁶, as B cells were previously shown to behave differently when plated on gels of different rigidities^{17,18}. Surprisingly, scanning electron microscopy (SEM) analysis showed no B-cell spreading on antigen-coated gels, spreading being observed on glass coated with equivalent amounts of antigen, as previously reported (Fig. 1b, see also Supplementary Fig. 1a). Instead, when B cells contacted antigen-coated gels, they exhibited pulsatile contractions (Supplementary Movie 1). To characterize this cell mechanical behavior, we quantified the stress (Fig. 1c) and the strain energy exerted on the substrate. We found that the strain energy displayed a growth phase lasting ~5 minutes followed by a plateau (Fig. 1d, e). This growth phase was barely observed in the absence of HEL (Fig. 1d, e, Supplementary Fig. 1b, Supplementary Movie 2) and the plateau displayed a clear antigen dose-dependence (Fig. 1f). Analyzing the single cell energy curve, we found that the plateau phase exhibited peaks in energy, corresponding to global cell contractions (Fig. 1g). Spectral analysis revealed a typical time-scale of 170 ± 10 s (median \pm IQR) between each contractile event (Fig. 1h and Supplementary Fig. 1c). Measurements of the bead displacement field flux through the cell boundaries revealed that the forces detected were mostly directed inward (Fig. 1i). We conclude that, on substrates of physiological rigidity, B cells exert pulsatile forces directed towards the synapse center in an antigen-dependent manner.

Force patterning at the immune synapse. An important hypothesis used to build the algorithm for force calculation in typical TFM experiments is that the displacement of cell-associated beads is accompanied by the displacement of its neighbors. However, we consistently observed that certain beads did not display movements parallel to the ones of their neighbors (Fig. 2a). These apparently aberrant bead movements did not result from a modification of gel elasticity as the gel relaxed to its initial state upon cell detachment (Supplementary Fig. 2a). We hypothesized that they rather result from locally applied forces, which may be perpendicular to the synaptic plan. To test this possibility, we investigated the nature of these local displacements by splitting the pool of beads into two groups based on r , the correlation between the directions of displacement vectors with its neighbors in a range of $1 \mu\text{m}$ (Fig. 2b). For each frame, we classified the beads in two groups: coordinated ($r > 0.5$) and non-coordinated ($r < 0.5$) (see also Supplementary Note 1, Analysis of the coordinated and non-coordinated bead movements). Remarkably, these two types of movements were spatially segregated, as observed from average bead density maps and radial scans (Fig. 2c): the coordinated pool was located at the periphery of the synapse (~2–3 μm from the center), whereas the non-coordinated one was located at its center. Of note, the number of beads moving in a coordinated manner increased with time, reaching a plateau at ~3 min (Supplementary Fig. 2c), suggesting that force patterning occurs early upon cell–gel contact, most likely during the rising phase of the strain energy curve. A similar spatial segregation was observed when analyzing the displacement field calculated from each group of beads (Fig. 2d). Of note, because the TFM algorithm cannot be used for localized forces but only for tangential ones (Supplementary Note 1, Underestimation of the non-coordinated pool of forces), we could not compute the stress field in this analysis. We conclude that forces transmitted to the substrate present a specific spatio-temporal pattern at the

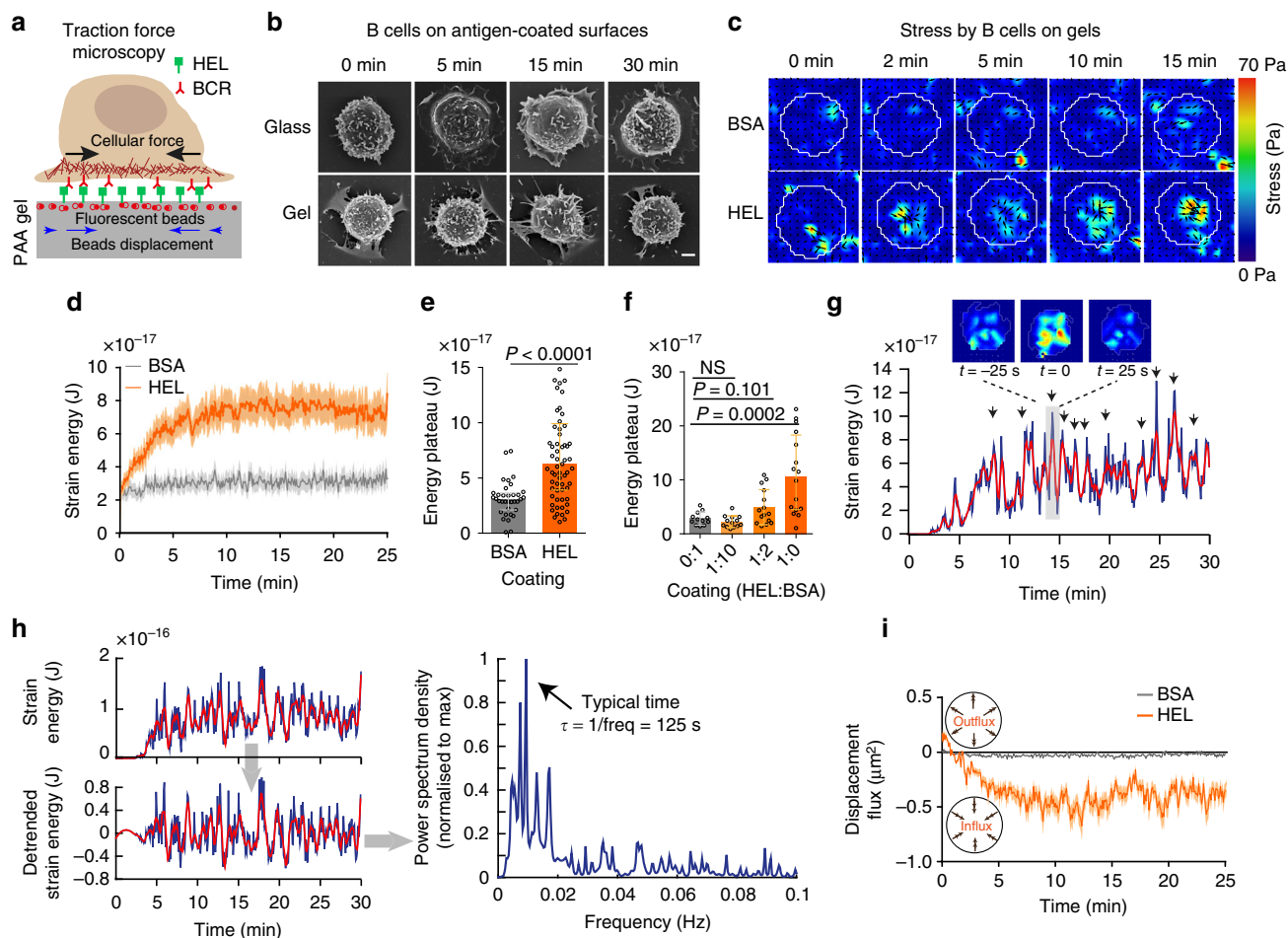


Fig. 1 B cells show antigen-specific pulsatile traction forces on PAA gels. **a** Cartoon of traction force microscopy showing B-cell plated on antigen-coated polyacrylamide (PAA) gel containing fiducial markers. **b** Scanning electron microscopy of fixed B lymphocytes on HEL-coated glass and PAA gels, scale bar is 2 μm . **c** Time-lapse color maps of stress for HEL and control BSA condition; contractile stress can reach 70 Pa. **d** Comparison of average strain energy profile for HEL and BSA conditions, error bars represent mean \pm SEM ($n = 65$ for HEL and $n = 35$ for BSA, five independent experiments, five mice), acquisitions were started before the arrivals of the cells to capture the initial time of contact and all cells were aligned at time zero. **e** Summary statistics of plateau of strain energy for HEL and BSA, error bar represents median \pm IQR ($n = 65$ for HEL and $n = 35$ for BSA, five independent experiments, five mice), Mann–Whitney test was performed for statistical analysis. **f** Concentration-dependent increase in strain energy, error bars representing median \pm IQR ($n = 12, 13, 15, 16, 3$ independent experiments, three mice), Mann–Whitney test was performed for statistical analysis. **g** Example of the strain energy curve for a single cell, plateau exhibit isolated peaks (see single stress maps). **h** Extraction of the typical pulsation frequency from the contractile energy: from the time series of a coordinated energy signal (smoothed in red), the signal is de-trended and the power spectrum density derived from it shows a maximum, hence a typical time scale for the pulsation. **i** Displacement flux showing the direction of displacement over time in HEL and BSA condition (mean \pm SEM, $n = 65$ for HEL and $n = 35$ for BSA, five independent experiments, five mice). Source data are provided as a Source Data file

immune synapse with a peripheral, centripetal, tangential pool opposed to a central, localized, and disorganized one.

Tangential forces rely on myosin II-driven cell contraction. We next investigated the role of the actomyosin cytoskeleton in force patterning. Monitoring myosin II-GFP dynamics showed that it displayed a pulsatile behavior similar to the one observed when analyzing the coordinated component of the cell contractile energy (Fig. 3a, b, Supplementary Movie 3). Zooming on a single energy peak showed that myosin II-GFP recruitment indeed coincided with maximal contractile stress (Fig. 3c). This was also visible when averaging the myosin II-GFP and energy signals over 40 different peaks (Fig. 3d). Cross-correlation analysis showed that myosin II-GFP peaks preceded the energy ones by few seconds, consistent with the motor being first recruited to the synapse and then triggering global contractions (Fig. 3d). These results strongly suggest that coordinated peripheral forces arise from global actomyosin contractions.

To assess the involvement of myosin II in force generation, we used conditional knockout mice in which *MYH9*, the gene coding for the main myosin II isoform expressed in lymphocytes (Immunological Genome Project, <http://www.immgen.org>), was deleted in B cells using the *CD21-cre* transgene (Fig. 4a, Supplementary Fig. 3a). No difference in the number of B cells in lymph nodes was observed between WT and myosin II KO mice (Fig. 4b). However, germinal centers were disorganized and reduced in number in the spleen and lymph nodes of immunized myosin II KO mice (Fig. 4c–e and Supplementary Fig. 3b). Thus, myosin II is required for B-cell responses *in vivo*, which is consistent with recently published results¹⁹, validating our experimental model. Remarkably, monitoring of the forces exerted on HEL-coated gels showed that the contractile strain energy of most myosin II-deficient B cells was considerably decreased (Fig. 4f–h, Supplementary Movie 4). Similar results were obtained when inhibiting myosin II with para-nitroblebbistatin (Supplementary Fig. 3c). SEM analysis showed that

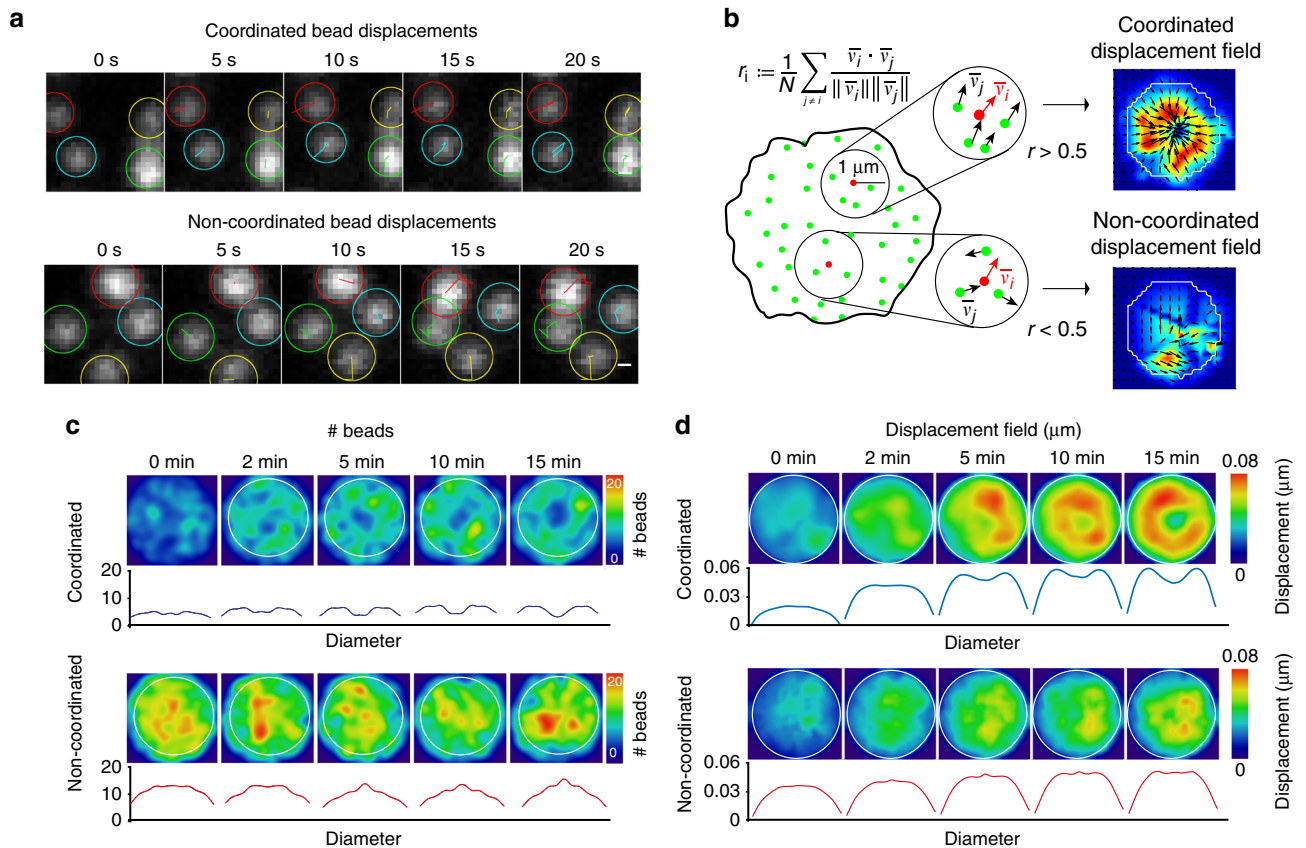


Fig. 2 Forces at the synapse exhibit two components. **a** Time-lapse images of individual beads showing displacement tracks in coordinated and non-coordinated type of movements, scale bar is 0.3 μm . **b** Scheme showing the method used to separate the bead population in two pools, allowing extraction of coordinated and non-coordinated displacements. **c** Mean bead distribution in coordinated and non-coordinated pool of stress ($n = 100$ cells). Below: radial profile of the density map obtained by average spatial distribution of the beads by resizing all cells and interpolating each bead with a Gaussian kernel. **d** Mean displacement field map obtained by resizing and averaging (over all cells) at the indicated time point the individuals coordinated and non-coordinated stress maps

myosin II KO spleen B cells did not show major morphological differences as compared with their wild-type counterpart (Supplementary Fig. 3d). We conclude that tangential forces exerted at the B-cell synapse are mediated by myosin II-driven centripetal cell contraction.

Localized forces result from protrusive actin patches. We next investigated the nature of the non-coordinated force component. By analyzing the Z displacements of each bead (quantified in the standard deviation of the position over 60 s), we observed that their movement in Z was indeed higher at the synapse center as compared with the periphery (Fig. 5a, b). This finding suggested that non-coordinated forces might result from local 3D movements of the cell. Strikingly, analysis of LifeAct-GFP dynamics at the cell–gel interface showed the presence of actin patches at the center of the synapse (Fig. 5c, d and Supplementary Movie 5), where most of bead movements in Z were detected (Fig. 5a). Accordingly, we found that actin patches and non-coordinated bead displacements were correlated in space and time (Fig. 5e, f). This result indicates that actin patches might be responsible for localized non-coordinated bead movements, suggesting that they correspond to protrusive structures. Consistent with this hypothesis, when presenting laterally pieces of antigen-coated gels to LifeAct-GFP B cells, we observed actin-rich protrusions that penetrated within the gel and were associated to bead movement (Fig. 6a). This experiment was motivated by the fact that the presence of the gel strongly limits imaging resolution in Z ,

compromising the analysis of these protrusive structures in B cells plated on 2D antigen-coated gels. However, we could confirm the existence of actin-rich protrusions in these cells by cryo-electron microscopy (Fig. 6b and Supplementary Fig. 4). Actin patches colocalized with phosphorylated Cortactin, a hallmark of invadosome-like protrusions previously observed in other cell types including T cells^{20,21} (Fig. 6c) and, partially, with clathrin (Fig. 6d), suggesting that clathrin-mediated endocytosis might locally take place. Other podosome hallmarks (vinculin, phosphorylated paxillin, and fascin) were not found to colocalize with actin (Supplementary Figs. 5a–c). We conclude that non-coordinated forces localized at the center of the immune synapse most likely result from the formation of protrusive actin patches that resemble invadosome-like protrusions.

Antigen extraction occurs in actin protrusive patches. We next investigated the dynamics of these actin patches in the presence or absence of antigen. We found that only few actin patches formed on BSA, which does not engage the BCR (Fig. 7a, b). In addition, actin patches were more peripheral in absence of BCR stimulation, compared with their central localization in presence of HEL (Fig. 7c). Patch tracking further showed that HEL increased their lifetime (Fig. 7d). Altogether, these data suggest that the presence of BCR-specific antigens facilitate the stable formation of actin patches that protrude into the gel and are localized at the center of the synapse.

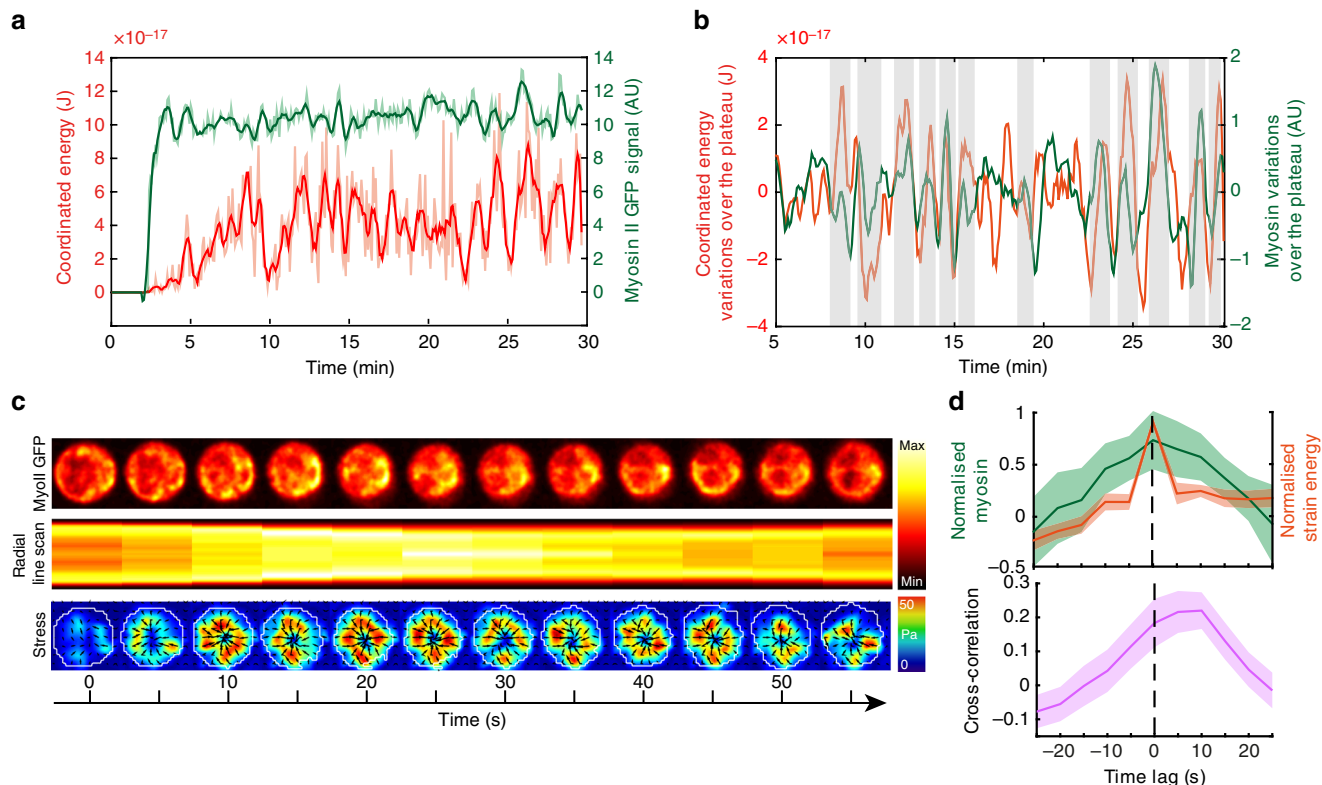


Fig. 3 Myosin II recruitment is associated to global contractions. **a** Example of strain energy and myosin II GFP signal at the synapse. **b** The two signals (once de-trended) show concomitant peaks. **c** Time-lapse images showing dynamics of myosin II GFP, radial linescan (presented as a kymograph, time in x axis) and corresponding stress map: a contraction peak is visible at times $t = 20\text{--}30$ s. **d** Average of different peaks and cross-correlation between strain energy and myosin II peak intensity: myosin peak precedes the energy peak of $\sim 5\text{--}10$ s (Mean \pm SEM, $n = 40$ peaks, from 15 cells, four independent experiments). Source data are provided as a Source Data file

These results prompted us to investigate whether antigen extraction occurs at these protrusive actin patches. For this, we recorded B cells plated on gels coated with fluorescently labeled HEL. Surprisingly, we observed that fluorescence was quenched when HEL was linked to the gel, being only detected upon HEL detachment (Supplementary Fig. 6a). This unexpected observation provided us with a robust system to monitor HEL extraction together with force generation or formation of actin patches. We observed a gradual antigen detachment starting as soon as B cells contact the gel surface and slowing down ~ 5 minutes later (Fig. 7e, f and Supplementary Movie 6). This crossover time corresponded to the time at which the plateau was reached in the energy curve. Strikingly, the appearance of actin patches at the center of the synapse coincided in space and time with the appearance of HEL clusters (Fig. 7g, h and Supplementary Movie 7). However, when coating the gel with both specific (HEL) and non-specific (Ovalbumin) fluorescent antigens, we observed that only HEL was extracted (Supplementary Fig. 6b). This result implies that antigen extraction does not only rely on the formation of actin patches but further requires specific antigen binding to the BCR. Altogether, our findings strongly support a model where actin protrusions that form at the center of the immune synapse allow the local extraction of BCR-associated antigens.

Actin patch formation and antigen extraction rely on myosin II. So far, our data show that myosin II-mediated pulsatile contractions account for tangential coordinated forces generated at the synapse periphery, whereas actin protrusions are responsible for localized 3D forces at the synapse center as well as for antigen extraction. To assess whether these two spatially segregated

functions of the actomyosin cytoskeleton are or not linked, we analyzed the impact of myosin II inhibition on actin patch formation. We found that Blebbistatin treatment strongly decreased the formation of actin patches and reduced the non-coordinated bead displacements localized at the synapse center (Fig. 5d). Consistently, myosin II inhibition almost cancelled the extraction of gel-associated HEL (Fig. 8a). Thus, myosin II is needed for actin patch formation and antigen extraction at the synapse center. Of note, antigens were not only detached from the substrate, but also internalized within B cells as shown by inside-out HEL staining (Fig. 8b). In agreement with these findings, myosin II was detected by cryoimmuno-electron microscopy at the cytosolic face of vesicles containing internalized HEL (Fig. 8c). In contrast, HEL was mainly found at the cell surface in myosin II KO B cells (Supplementary Fig. 6c).

Intriguingly, unlike actin-, myosin II-containing patches were not observed at the synapse center. This points to an indirect role of myosin II in patch formation rather than a direct one. We therefore hypothesized that myosin II-mediated contractions might facilitate the formation of the central actin patches for antigen extraction. To test this hypothesis, we evaluated the impact of myosin II-contraction stimulation on actin patch formation and antigen extraction. For this, we used MLSA1, an agonist of the lysosomal calcium channel TRPML1, which locally enhances myosin II flows and activity in dendritic cells²². We found that MLSA1-treated B cells showed increased contractile energy (Fig. 8d), both non-coordinated and coordinated displacement fields being enhanced (Fig. 8e). Noticeably, although MLSA1 treatment had a minor effect on the number of actin patches (Fig. 8f) and their distribution (Fig. 8g), it strongly decreased their diffusion coefficient (Fig. 8h), indicating that

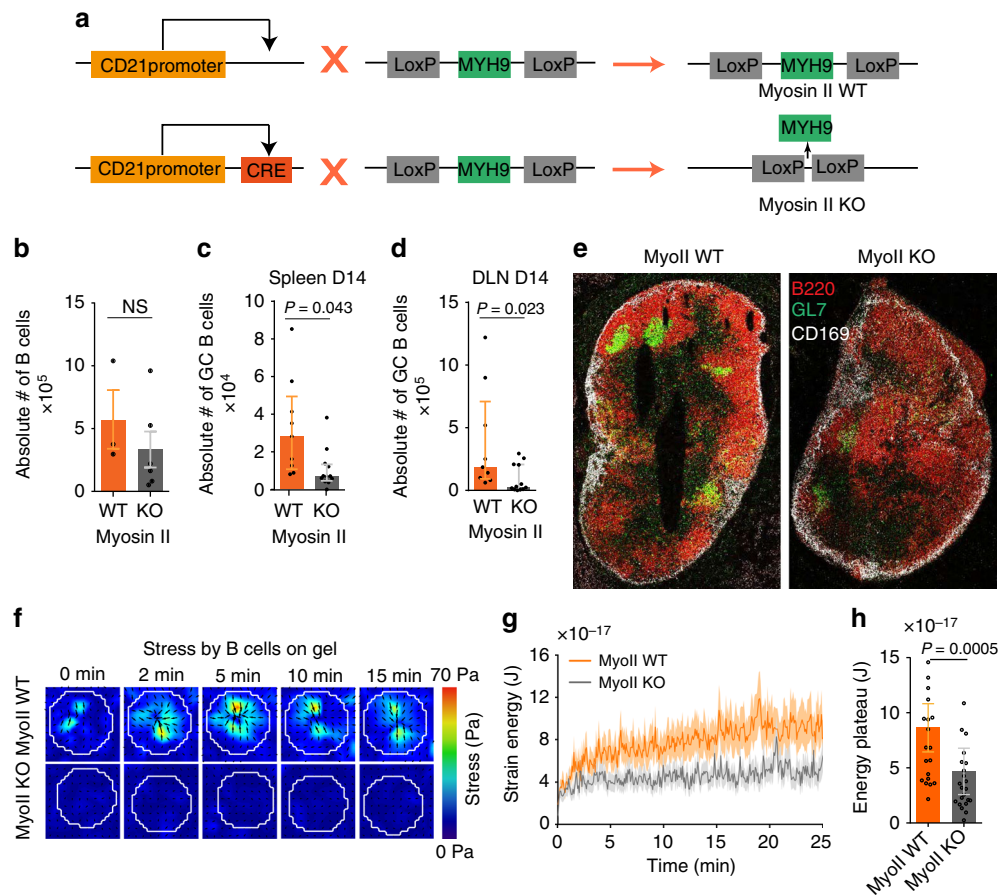


Fig. 4 Myosin II is essential for force generation by B cells. **a** Genetic approach used to ablate Myosin IIA specifically in B cells: Myosin II Flox mice are crossed with CRE + mice under CD21 promoter. **b** Absolute number of CD19-positive B cells in myosin II WT and KO mice inguinal lymph node (each dot represents one mice, two independent experiments, error bars represents mean \pm SEM, Mann-Whitney test was performed for statistical analysis). **c** Absolute number of germinal center B cells in inguinal lymph node and **d** draining lymph node in myosin II WT and KO beads immunized mice (each dot represents one mouse, two independent experiments, error bars represent median \pm IQR, Mann-Whitney test was performed for statistical analysis). **e** Histology image of draining lymph node from immunized mice showing B cells (B220), germinal centers (GL7), and sub-capsular sinus macrophages (CD169); images highlight scattered germinal center B cells in myosin II KO mice. **f** Time-lapse images of stress color maps for myosin II KO and WT conditions, forces are almost absent in myosin II KO cells. **g** Average energy profile for myosin II KO and WT conditions, error bars represent Mean \pm SEM ($n = 22, 23$, four independent experiments, four mice). **h** Summary statistics of plateau of strain energy for myosin II KO and WT, error bars represent median \pm IQR ($n = 22, 23$, four independent experiments, four mice), Mann-Whitney test was performed for statistical analysis. Source data are provided as a Source Data file

patches became more stable when myosin II contractility was enhanced. Consistent with this result, antigen extraction was significantly faster and more efficient in MLSA1-treated B cells (Fig. 8i). Thus, although inhibition of myosin II abolishes force generation, actin patch formation and antigen extraction, stimulation of its activity enhances these three events, strongly suggesting that they are most likely functionally linked.

To address the existence of this functional link, we built a theoretical model (Fig. 8j). The model considers that molecules associated to the membrane can both diffuse and be advected by an intermittent flow induced by actomyosin contractions. At the cellular scale, the diffusion time of these molecules (the time necessary for molecular patterns such as actin patches to disappear) is more than 5 min, i.e., it is longer than the typical period of the 2–3 min. pulsations detected (see Supplementary Note 1, myosin II-driven pulsatile contractions can lead to central patterns). Noticeably, calculations show that this condition is sufficient to generate a radial gradient of advected molecular components. This analytical argument therefore supports the idea that global myosin II pulsatile contractions promote the

centripetal transport/accumulation of molecules that in turn facilitate the formation of stable protrusive actin patches where antigen extraction occurs. This spatial organization of the actomyosin cytoskeleton leads to force patterning at the immune synapse, with pulsatile tangential (2D) peripheral forces resulting from global myosin II contraction and 3D disorganized central forces being produced by local actin protrusions.

Discussion

We here show that forces are patterned at the immune synapse of B lymphocytes. Consistent with others' findings²³, we observe the build up of a contractile concentric ring upon BCR activation, but in addition to this, we detect localized forces mainly located at the center of the synapse. We propose that force patterning results from centripetal pulsatile actomyosin contractions that lead to the segregation of molecular components at the cell-antigen interface. This scenario is distinct from the one described at the immune synapse formed by lymphocytes interacting with antigen-functionalized lipid bilayers, as molecular segregation is driven by centripetal actin flow in these cells^{10,24,25}, which were not

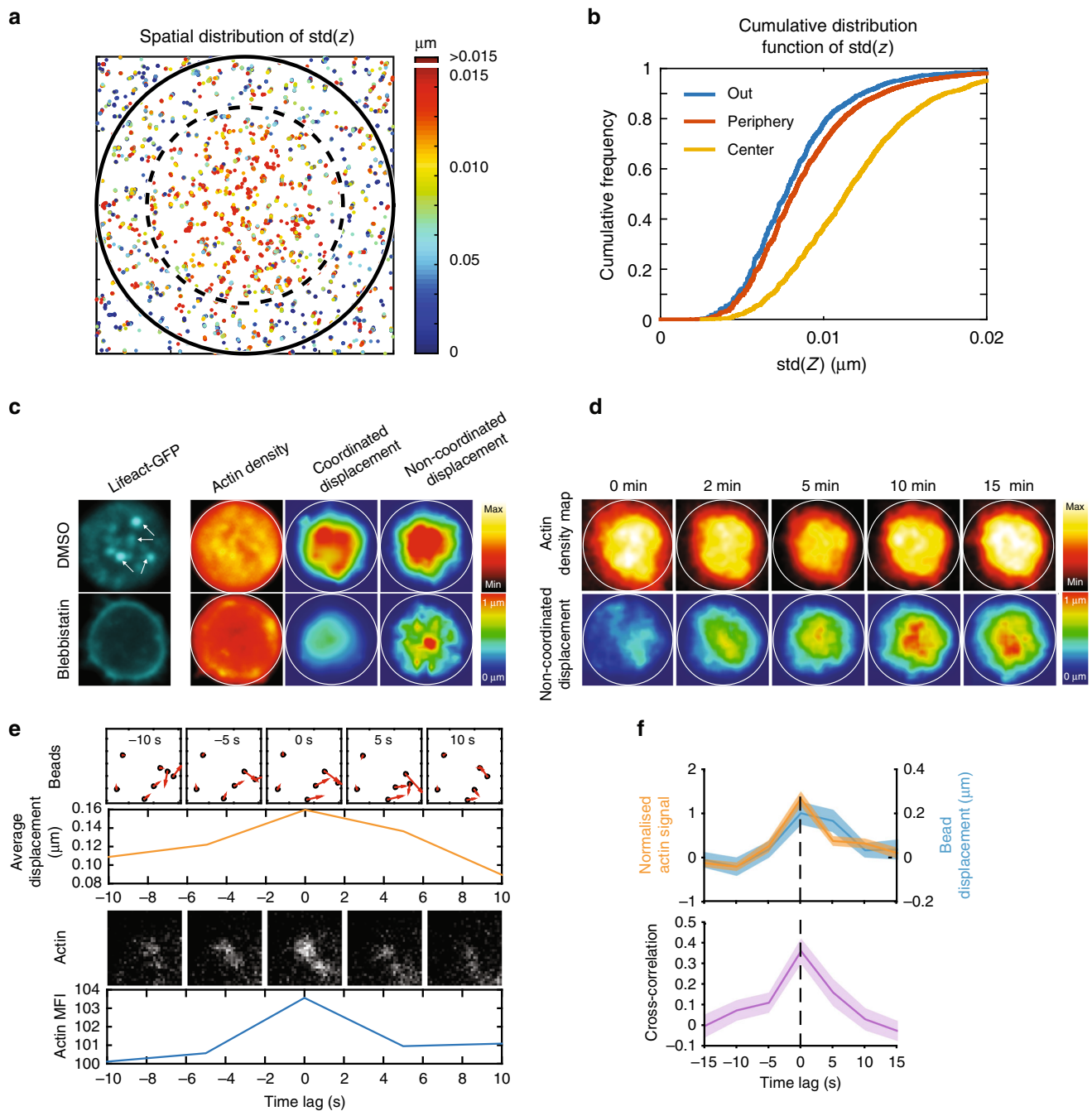


Fig. 5 Actin dynamics at the synapse. **a** Space distribution of bead displacement in the z direction: each point represents the standard deviation of the z position of a single bead on a 10 frame sequence; all beads have been projected on a size and aspect ratio normalized cell (inner circle at $2/3$ of the cell diameter) represents the central portion of the synapse: the figure show that the displacement in z is higher in the center of the synapse (8422 points, superposition of 14 cells, one representative experiment). **b** Cumulative distribution for the z displacement color-coded in figure **a**, the central fraction of beads shows significantly higher displacement in z ($P < 0.0001$ for all comparison, Kolmogorov-Smirnov test). **c** Left, single cell showing actin patches in the center of the cell which are lost in case of para-Nitroblebbistatin treated cells. Right, mean actin distribution, mean coordinated and mean non-coordinated force density color map in control and para-Nitroblebbistatin treated B cells ($n = 12$). **d** Actin distribution over time correlates with non-coordinated force distribution (images are average projection of 12 cells over all time points). **e** Time-lapse images showing simultaneous appearance of an actin patch and non-coordinated bead displacements, arrowhead showing direction and magnitude of displacement; graphs below the images represent the respective signals integrated over a square of $2\ \mu\text{m} \times 2\ \mu\text{m}$. **f** Average of the signals quantified in **e** and average cross-correlation: both signals appear simultaneously and show a peak simultaneously with no lag (mean \pm SEM, $n = 89$, from nine cells, two independent experiments). Source data are provided as a Source Data file

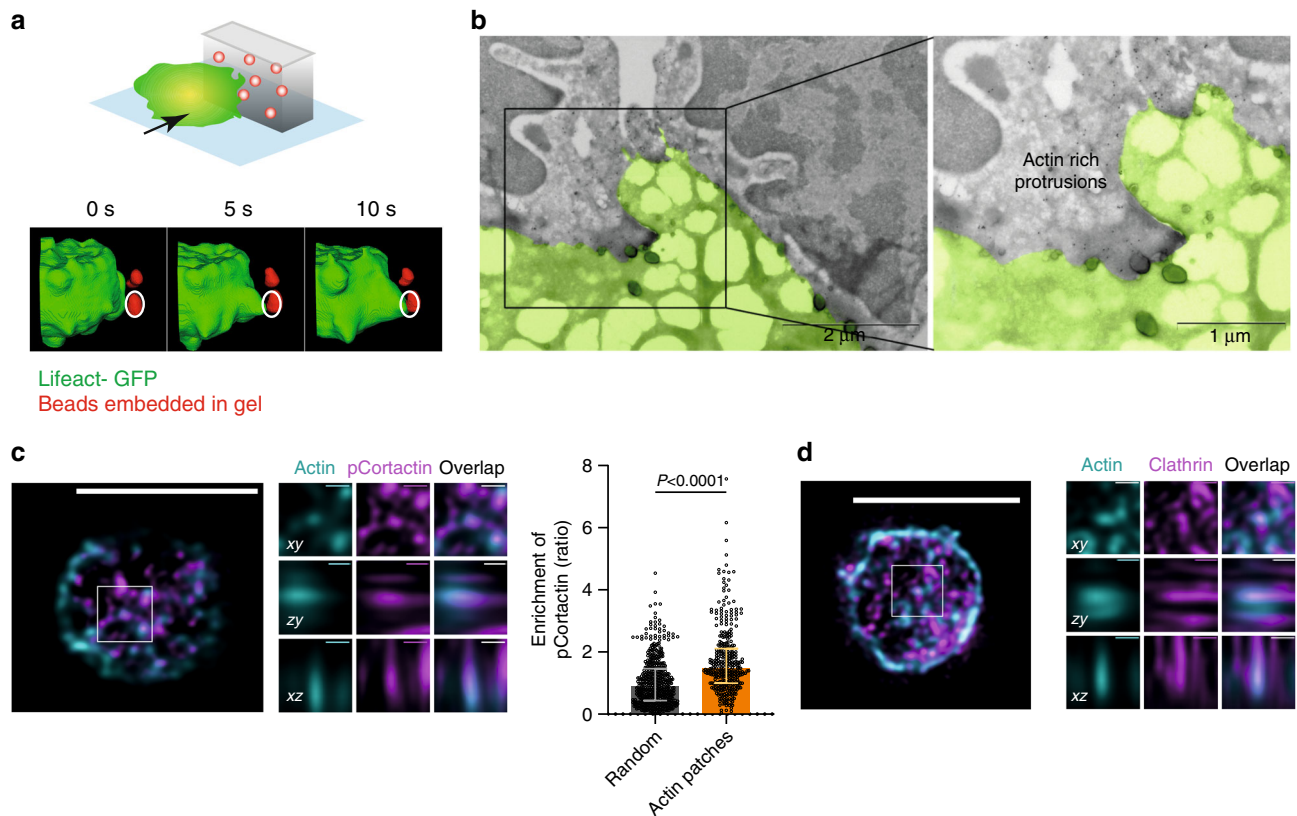


Fig. 6 Characterization of actin patches. **a** Protrusions associated with bead movement (red) on antigen-coated gel pieces presented laterally to B cell (green), 3D reconstruction. **b** Electron microscopy image showing actin-rich protrusions (marked by gold beads) through PAA gel (scale bar $0.2\ \mu\text{m}$). **c** Immunostaining of actin (cyan) and phospho-cortactin (magenta) and zoomed orthogonal projections on different planes (scale bar $5\ \mu\text{m}$, zoom $0.5\ \mu\text{m}$); images show colocalization (quantify on the right as ratio of magenta signal in the cyan region, control is the enrichment of the signal in random position, Median \pm IQR, 26 cells, two independent experiments, two mice, Mann-Whitney test). **d** Immunostaining of actin (cyan) and clathrin (magenta) and zoomed orthogonal projections on different planes (scale bar $5\ \mu\text{m}$, zoom $0.5\ \mu\text{m}$); images show partial colocalization (not quantified, scale bar $5\ \mu\text{m}$, zoom $0.5\ \mu\text{m}$). Source data are provided as a Source Data file

detected in B lymphocytes interacting with antigen-coated gels. This might result from the fact that (1) on gels, cells are anchored to the substrate, allowing force transmission, which is not the case in fluid lipid bilayers, and/or (2) gels are several orders of magnitude softer than glass surfaces.

We observed protrusive actin patches that form at the synapse center, where antigen extraction occurs, and which resemble invadosome-like protrusions. This is consistent with *in vitro* studies showing that when an actomyosin active gel is coupled to the cell membrane, it can indeed form actin patches as long as a sufficient number of contractile elements are present^{26,27}. It is therefore likely that shear coordinated forces generated by myosin II pulsatile contractions at the synapse periphery do not directly contribute to antigen extraction but rather help the cell building stable protrusive actin structures where extraction occurs (see Supplementary Note 1, force required for antigen extraction). It therefore appears that both global contractility and local force generation are involved in antigen extraction, reconciling the two models previously proposed. Interestingly, the growth-plateau regimes that we observed are reminiscent of the spreading-contraction phases observed on fluid substrates.

We found that the lifetime of protrusive actin patches increases in the presence of BCR-specific antigens. This suggests that similarly to T lymphocytes, B cells might probe their environment through unstable actin protrusions, which are then stabilized upon antigen binding to the BCR²⁸. Antigen internalization could occur by endocytosis at the tip of protrusions as described for both clathrin-mediated endocytosis²⁹ and clathrin-independent

IL2 receptor endocytosis³⁰. Interestingly, actin-rich pod-like structures have been recently described as sites of antigen internalization in human Light Zone B cells plated on activating plasma membrane sheets¹². Although it is not clear at this stage whether these actin pods are the protrusive structures we here describe, our data provide a putative mechanism for their formation.

Our results show that, in the presence of antigen, actin patches form at the center of the synapse, in agreement with previous studies showing that this is indeed a privileged site for antigen internalization. Actin-rich endocytic structures might preferentially form at the synapse center owing to a local drop in membrane tension, as recently described during phagocytosis in macrophages^{31–33}. In this context, pulsatile peripheral actomyosin ring could contribute creating a gradient of lipid and therefore of tension (even without need for a proper diffusion barrier) with a reduced membrane tension at the center of the synapse. Alternatively, the actomyosin peripheral ring might act as a mechanical dumper by sealing the synapse and isolate its center from external mechanical noise, for example, owing to lymph node/vessel contractions or cell movements/proliferation. This could improve antigen affinity mechanical discrimination by the BCR⁸ (see Supplementary Note 1, affinity discrimination and energy scales).

We observed that lysosomal calcium release enhances myosin II-driven peripheral forces as well as actin patch formation and subsequent antigen extraction. This is particularly appealing as lysosomes have been shown to be recruited upon centrosome

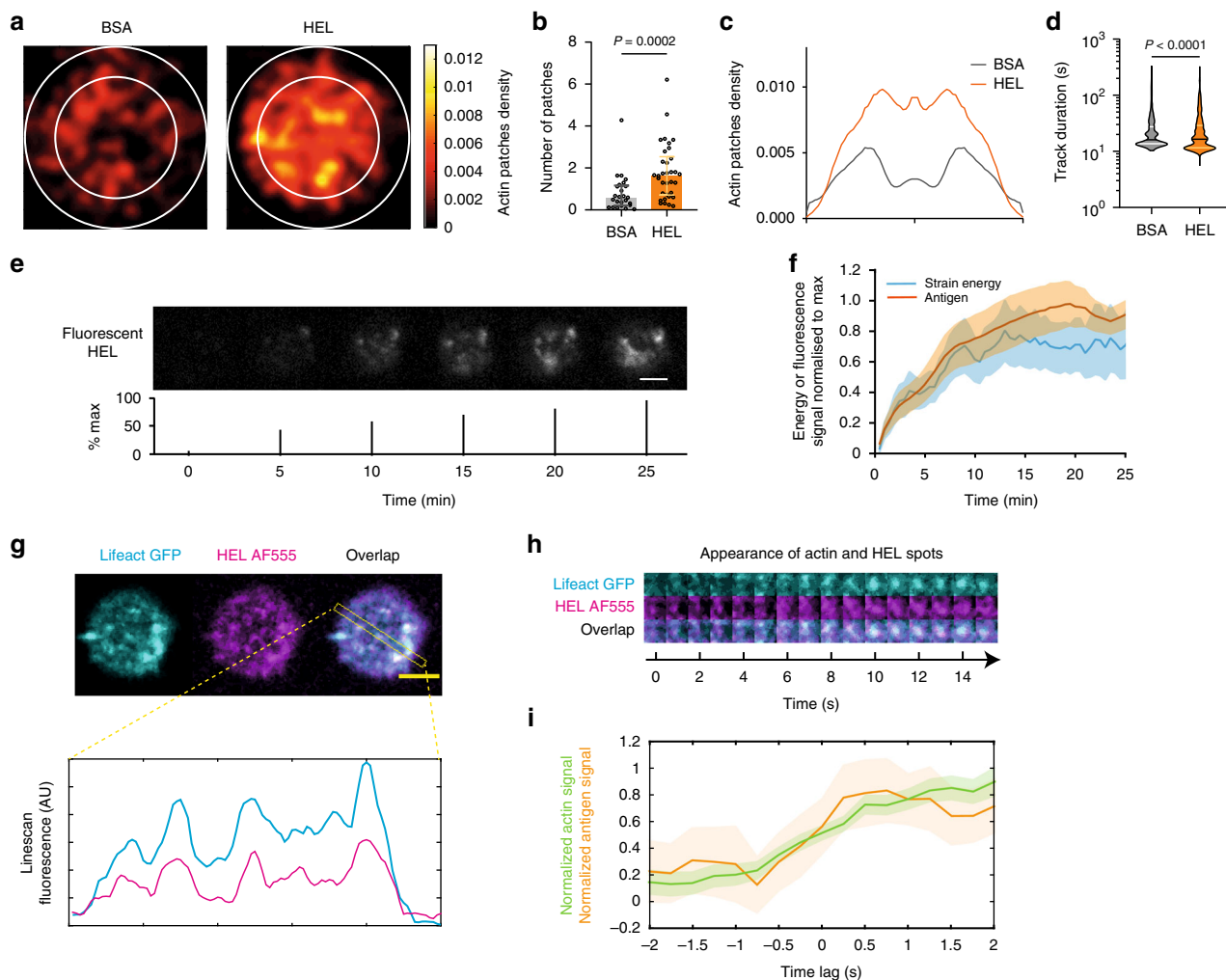
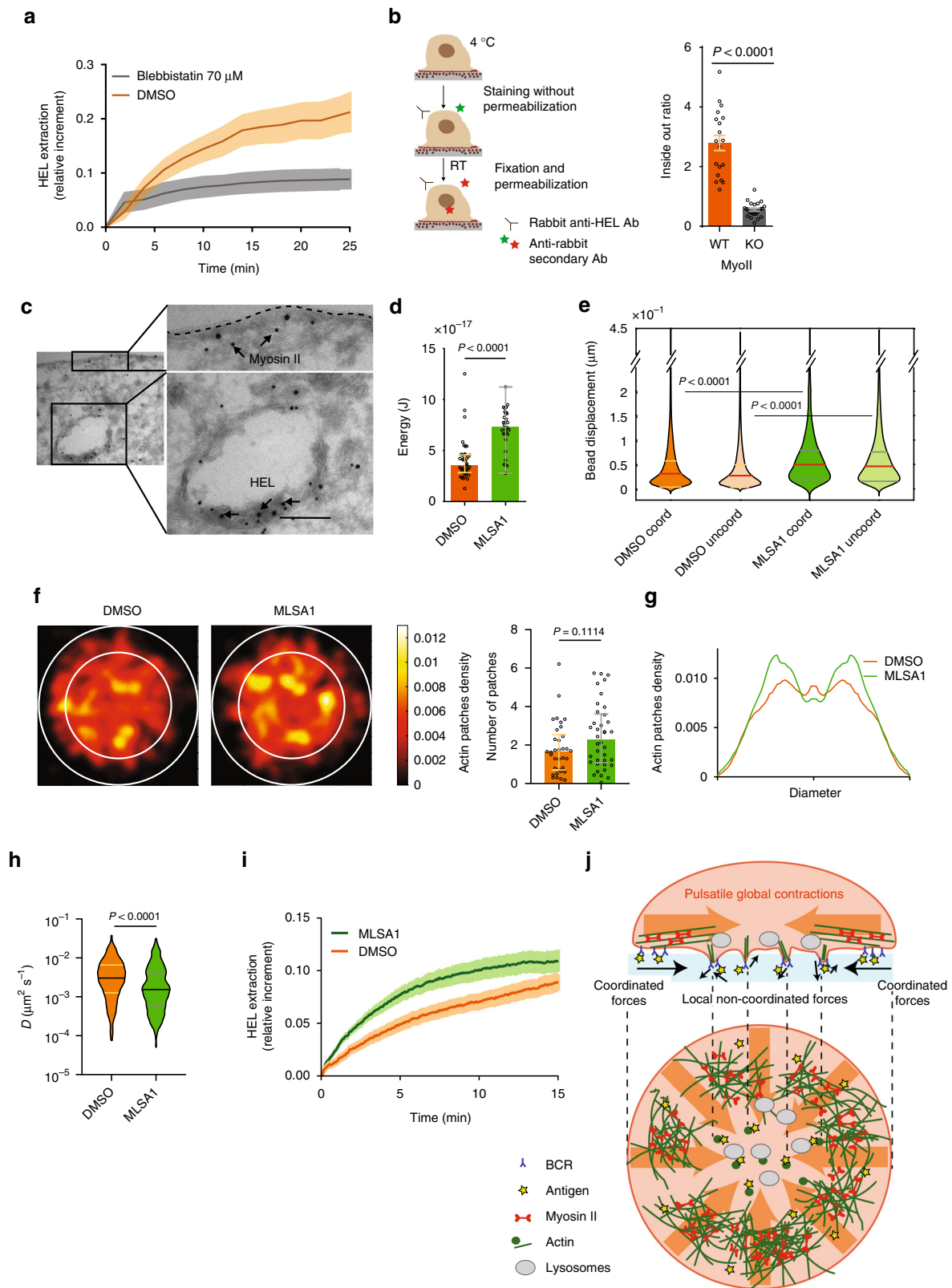


Fig. 7 Actin patches correlate with antigen internalization. **a** Average distribution of actin patches (obtained by tracking and convoluting the results with a Gaussian kernel): internal circle (2/3 cell diameter) corresponds to the central portion of the cell (scale bar represents the integrated density as number/cell/5 min). The distribution in HEL-coated gel is very different compared with the BSA coated gel in **b** number of beads (Mann-Whitney test, Median \pm IQR) and **c** radial distribution (BSA: 25 cells, HEL: 34 cells, three different mice). **d** Effective diffusion coefficient of actin patches (violin plot with Median \pm IQR, $n = 301$ trajectories (34 cells) for HEL and $n = 84$ trajectories (25 cells) for BSA, Mann-Whitney test). **e** Time lapse of the extraction of fluorescent HEL (below: percentage of the maximum, scale bar 3 μm). **f** Strain energy and antigen gathering (Mean \pm SEM, $n = 15$, five independent experiments); signals are normalized to the maximum to highlight similarity in the kinetics. **g** Example of colocalization of the actin patches (Lifeact-GFP) and fluorescent HEL (AF555), bottom linescan on the colocalization panel (scale bar 3 μm). **h** Zoom on an actin (and HEL) patch showing the concomitant arrival of the two signals. **i** Quantification of the signal in **g** measured over a square of 1 $\mu\text{m} \times 1 \mu\text{m}$: both signals appear simultaneously (mean \pm SEM, $n = 21$, from six cells). Source data are provided as a Source Data file

polarization to the B-cell immune synapse^{9,34}, which would then be locally available for calcium release. We do not exclude that local release of calcium might also promote the activity of other myosin motors such as class I myosins, which are typically required for clathrin-mediated endocytosis^{35–37}. This would help coupling global myosin II contractions at the cell periphery with local endocytosis at actin patches. Indeed, although the minimal force to activate the BCR is 16 pN (as measured by DNA tension sensors³⁸), the stall force of a single myosin motor is < 2 pN³⁹, indicating that the action of at least eight myosin motors is required to activate the receptor. Moreover, higher forces have been reported in antigen extraction: 56 pN rupture forces have been measured³⁸ as well as biotin–streptavidin bond ruptures⁸ (requiring 160 pN or 80 motors). Single contractile elements made of tens of motors can achieve large force peak (recent experiments report forces up to 1 nN⁴⁰), provided that the activity of several motors is properly

coordinated in order to achieve efficient antigen extraction, which could be orchestrated by local lysosomal calcium release. This further implies that lysosomal polarization to the immune synapse might be needed to stimulate mechanical extraction of surface-tethered antigens, in addition to their known role in antigen proteolysis and processing⁴¹.

Spatio-temporal force patterning was first highlighted in the context of tissues⁴², cell adhesion to substrate^{43–45}, and cell motility⁴⁶. Our study shows that it might be a more general and basic feature of cell–cell interfaces where the engagement of surface receptors leads to both juxtacrine signaling and ligand endocytosis. We found that myosin II intervenes in this process as a global master organizer of forces and actin organization, and thus as an indirect but key actor of endocytosis, which is essential for adaptive immunity. We anticipate that this study should set the ground for future work aimed at exploring force patterning in additional cell-to-cell communication models.



Methods

Mice and cells. Mice with a conditional deletion of myosin II in B cells were generated by backcrossing mice carrying a floxed myosin II allele (*MyosinII flox/flox*)⁴⁷ with mice expressing the Cre recombinase under the control of the CD21 promoter (*CD21-cre^{+/+}*). Mice expressing the HEL-specific MD4 receptor were also crossed with mice carrying a floxed myosin II allele. Mice were crossed at an age of 8–10 weeks, and Cre⁻ littermates were used as WT controls. The transgenic MD4, Lifeact-GFP and myosin II-GFP mouse lines have been described

elsewhere^{48,49}. This resulted in all the desired genetic combinations being obtained in the C57BL/6 background, and the corresponding breeding controls were systematically used. The experiments were performed on 8–10-week-old male or female mice. Animal care conformed strictly to European and French national regulations for the protection of vertebrate animals used for experimental and other scientific purposes (Directive 2010/63; French Decree 2013-118). Immunization experiments carried out at the Karolinska Institute were performed according to local ethical committee guidelines (N11/13). Mature spleen B cells

Fig. 8 Antigen is internalized through a myosin II-dependent mechanism. **a** Antigen gathering over time in control and para-Nitroblebbistatin treated cells (error bars show mean \pm SEM, $n = 15$ DMSO, $n = 9$ Blebbistatin). **b** Scheme of the inside-out experiment and relative quantification: ratio of internalized (inside) and not internalized (outside) antigen in myosin II KO and WT B cells (error bars show mean \pm SEM, $n = 29$ Myosin II WT, $n = 21$, Myosin II KO, three independent experiments, t test). **c** Scanning electron microscopy images showing internalized antigens and its proximity to myosin II (scale bar 0.2 μm). **d** Statistics of plateau of strain energy for MLSA1-treated (MLSA1) and untreated (DMSO) cells (error bar show median \pm IQR, $n = 41$ for DMSO and $n = 30$ for MLSA1, three independent experiments, three mice, Mann-Whitney test): contractile energy is strongly increased in the treated cells. **e** Statistics of the bead displacement in the coordinated and uncoordinated compartment for treated and untreated cells: both coordinated and uncoordinated movements are significantly increased in treated cells (in red median \pm IQR, Mann-Whitney test, $n = 41$ for DMSO and $n = 30$ for MLSA1, three independent experiments, three mice, total of > 4400 beads). **f** Average distribution of actin patches (obtained by tracking and convoluting the results with a Gaussian kernel): internal circle (2/3 cell diameter) corresponds to the central portion of the cell (scale bar represents the integrated density as number/cell/5 min). The distribution in MLSA1-treated cells is different compared with the untreated (DMSO) cells neither in number of beads (it increases but not significantly) nor **g** in radial profile (Mann-Whitney test, Median \pm IQR, $N = 34$ DMSO, $N = 38$ MLSA1, three independent experiments, three mice). **h** Apparent diffusion coefficient of actin patches: MLSA1-treated cells exhibit less mobile patches (number of tracks: N DMSO=301, N MLSA1=492, Mann-Whitney test). **i** Antigen extraction profile for MLSA1-treated and untreated cells: treated cells extract antigen faster than untreated ($N = 55$ DMSO, $N = 53$ MLSA1, three independent experiments, three mice). **j** Model: myosin II-driven global peripheral contractions (shear coordinated forces) allow the endocytic machinery to build up in the center, where antigen is extracted through actin protrusions associated to the generation of localized forces. Source data are provided as a Source Data file

were purified with the MACS kit (130-090-862). B cells were cultured⁹ in Rosewell Park Memorial Institute (RPMI) 1640—GlutaMax-I supplemented with 10% fetal calf serum, 1% penicillin–streptomycin, 0.1% b-mercaptoethanol and 2% sodium pyruvate.

Antibodies and reagents. The following reagents were used: 100 $\mu\text{g}/\text{ml}$ HEL (Sigma), 100 $\mu\text{g}/\text{ml}$ BSA (Euromedex), 40% polyacrylamide (PAA, Biorad), 2% bis-polyacrylamide (Biorad), 3-aminopropyltrimethoxysilane (Sigma), 0.2 μm Alexa647 Fluospheres (Thermo Fisher, F8807), SigmaCote (Sigma), ammonium persulfate (Sigma), TEMED (ICN Biomedicals), Sulfo-SANPAH (Thermo Fisher), and the Alexa555 protein labeling kit (A30007, Molecular Probes). The following primary antibodies were used: rabbit anti-HEL (Abcam, 1/100), human anti-GFP (Institut Curie, 1/200), rabbit Anti-phospho-Cortactin (pTyr⁴⁶⁶) (SAB4504373, Sigma-Aldrich, 1:200), rabbit anti Clathrin (Cell Signalling 4796, 1:50), Alexa Fluor 488 Phalloidin (A12379 Invitrogen 1:200), Alexa Fluor 647-conjugated anti-phalloidin (Thermo Fisher, 1/200), anti-myosin IIA heavy chain (Covance, 1/500). The following secondary antibodies were used: Alexa Fluor 488-conjugated goat anti-rabbit IgG (Life Technologies, 1/200), Alexa Fluor 488-conjugated goat anti-human IgG (Life Technologies, 1/200), Alexa Fluor 405 Goat anti-Rabbit IgG (H + L) (A31556 ThermoFisher 1:200), Alexa Fluor 546 Goat anti-Mouse IgG1 (A21123 ThermoFisher 1:200).

Inhibitors and drugs. Blebbistatin: cells were incubated with 70 μM para-nitro blebbistatin (Optopharma) for 40 minutes at 37 $^{\circ}\text{C}$ in RPMI media before the experiments, unless otherwise stated. MLSA1: cells were incubated with 10 μM mucolipin synthetic agonist 1 (MLSA1, TOCRIS) for 30 minutes at 37 $^{\circ}\text{C}$ in RPMI media before the experiments. Dimethyl sulfoxide (DMSO) was used as a control.

Live cell traction force microscopy. Fluorodishes containing gels were placed under a microscope focused on the plane of beads. In total, 1×10^5 B cells were added to the plate (time 0), and images were acquired over time. Images were acquired at 37 $^{\circ}\text{C}$, under an atmosphere containing 5% CO_2 , with an inverted spinning disk confocal microscope (Eclipse Ti Nikon/Roper spinning head) equipped with a $\times 60$ (1.4 numerical aperture) oil immersion objective and a CoolSNAP HQ2 camera (pixel size 6.4 μm) with MetaMorph software (Molecular Device, France); time lapse were typically 1 image/5 s and last minimum 15 mins.

Preparation of PAA gel substrates. PAA gels were produced in 35-mm FD35 fluorodishes (World Precision Instruments, Inc). These dishes were first treated by UV irradiation for 2 minutes, and then with 3-aminopropyltrimethoxysilane for 5 minutes. The dishes were washed thoroughly in distilled water and dried before preparation of the PAA gels. Hydrophobic 12mm diameter coverslips were prepared by incubation in SigmaCote for 3 minutes, followed by thorough washing and drying. A 500 Pa gel was prepared by diluting 40% PAA and 2% bis-acrylamide solutions to obtain stock solutions of 12% acrylamide/0.1% bis-acrylamide. We sonicated 167 μl of this solution with 1% of 0.2 μm carboxylated fluorescent (660/680) beads (ThermoFisher Scientific), and then added 1.67 μl of the 10% ammonium persulfate (APS) stock solution and 0.2 μl of TEMED and mixed thoroughly, to initiate polymerization. A volume of 9 μl of the PAA mixture was immediately pipetted onto the surface of the Fluorodish and a SigmaCote (Sigma-Aldrich) activated coverslip was carefully placed on top to squeeze the gel to a thickness of about 80 μm . Fluorodishes were immediately inverted, to bring the beads to the surface of the gel. Polymerization was completed in 45 min at room temperature and the top coverslip was then slowly peeled off and immediately immersed in phosphate-buffered saline (PBS). Sulfo-SANPAH (Sigma-Aldrich), a surface

functionalizing reagent with an amine-binding group and a photoactivable azide group, was used to crosslink molecules to the surface of the gel. Sulpho-SANPAH (150 μl of 0.5 mg/ml stock) was attached to the gel surface through UV light activation for 2 minutes followed by 2x PBS washing (procedure repeated 2 times). Gels were washed thoroughly with PBS 3 times and finally coated with 100 μl (100 $\mu\text{g}/\text{ml}$) HEL or BSA, by overnight incubation at 4 $^{\circ}\text{C}$. Gels were washed thoroughly with PBS 3 times and pre-incubated with medium at room temperature at least 30 min before experiments.

Characterization of the PAA gels. The Young's modulus of PAA gel was measured by bead indentation and calculated using a Hertz model for an elastic substrate with finite thickness⁵⁰. Glass beads of 0.25 mm radius were deposited on the gel and their indentation was measured using confocal stacks. Gel height was determined by focussing on the bottom and top of the gel. The force inserted in the Hertz formula was computed theoretically as the weight of the glass bead (density = 2.2 kg/m^3 and radius 0.25 mm) minus the buoyancy in water. PAA gels in our system remains in the range of 400–650 Pa.

Quantification of amount of antigen on PAA gel and glass. We ensured that the difference of spreading on gel and on glass was not owing to the amount of antigen-coated on different substrates (it is harder to coat gels with protein due to the inherent hydrophobicity of the PAA). We inferred the amount of antigen required for coating the glass with an equivalent concentration of antigen on gel (100 $\mu\text{g}/\text{ml}$) by taking images at different concentration on glass and comparing with the fluorescent intensity obtained on the gel of 100 $\mu\text{g}/\text{ml}$. Respective glasses and gels were coated with HEL overnight at 4 $^{\circ}\text{C}$ and later stained by using rabbit anti-HEL primary antibody at 37 $^{\circ}\text{C}$, eventually staining with anti-rabbit alexa-488 secondary antibody. Images were acquired using laser scanning microscope (Leica) with a $\times 40$ 1.4 NA oil immersion objective with 5% 488 laser. Mean fluorescence intensity at different point follows a logarithmic curve that suggests the equivalent concentration on glass is 0.14 $\mu\text{g}/\text{ml}$.

Immunofluorescence. B cells plated for 30 min on PAA gels were fixed by incubation with PFA for 15 min at RT, washed 3x with PBS, permeabilized 5 min with Triton 0.1%, washed 3x with PBS. The sample was blocked for 30 min with CLSM buffer (PBS, 20 mM Glycine, 3% BSA), washed, blocked 10 min with Mouse Fc block (1:100 in CLSM buffer), washed, then incubated overnight at 4 degrees with primary antibodies (anti-phospho-Cortactin and anti-Clathrin) diluted in CLSM buffer. Secondary antibodies were incubated 1 h at RT. Samples were mounted so that cells could be imaged without going through the PAA gel. Samples were imaged using a laser scanning microscope (Leica) with a $\times 60$, NA 1.3 oil immersion objective. Images were deconvoluted using Huygens software. Enrichment of p-Cortactin is quantified with custom-made ImageJ macro. Actin patches were detected average intensity of p-Cortactin in a disk around this patch was measured and then divided by the average intensity of p-Cortactin in the cell. This was compared with the same analysis, but taking random points in the cell instead of actin patches detection.

Inside-out immunofluorescence. B cells were plated on PAA gels and incubated for 15 min at 37 $^{\circ}\text{C}$. The cells were then transferred to 4 $^{\circ}\text{C}$ and Fc receptors were blocked for 10 min using Fc blocker (BD, 1/200). The cells were washed with PBS and incubated with rabbit anti-HEL antibody at 4 $^{\circ}\text{C}$ for one hour and then with Alexa Fluor 488-conjugated anti-rabbit IgG secondary antibody for one hour. The cells were moved to room temperature, fixed by incubation with 4% PFA for 10 minutes and permeabilized by incubation with PBS plus 0.2% BSA and 0.05%

saponin. The cells were then incubated with rabbit anti-HEL antibodies for 1 hour, washed with PBS–BSA–SAPONIN, and incubated with the Alexa 546-conjugated anti-rabbit IgG secondary antibody for one hour at room temperature. The cells were washed several times in PBS and then used for imaging. Images were acquired using laser scanning microscope (Leica) with a $\times 40$ 1.4 NA oil immersion objective.

SEM imaging. Cells were fixed overnight at 4 °C in 2.5% glutaraldehyde in phosphate buffer on 0.2 $\mu\text{g}/\text{ml}$ HEL coated on glass and 100 $\mu\text{g}/\text{ml}$ HEL coated on PAA gel. They were dehydrated in a graded series of ethanol solutions, then dried by the CO_2 critical-point method, with an EM CPD300 (Leica microsystems). Samples were mounted on an aluminum stub with silver lacquer and sputter-coated with a 5 nm layer of platinum, with an EM ACE600 (Leica Microsystems). Images were acquired with a GeminiSEM 500 (Zeiss).

Electron microscopy. Immunoelectron microscopy was performed by the Tokuyasu method (Slot & Geuze, 2007). Double-immunogold labeling was performed on ultrathin cryosections with protein A-gold conjugates (PAG) (Utrecht University, The Netherlands). Electron micrographs were acquired on a Tecnai Spirit electron microscope (FEI, Eindhoven, The Netherlands) equipped with a Quemesa (SIS) 4k CCD camera (EMSIS GmbH, Münster, Germany).

Western blotting. B cells were lysed at 4 °C in lysis buffer (10 mM Tris HCL pH 7.4, 150 mM NaCl, 0.5% NP40). Cell lysates were loaded onto mini-PROTEAN TGX sodium dodecyl sulfate polyacrylamide gel electrophoresis gels, which were run at 200 volts and 65 mA. The bands on the gel were transferred onto polyvinylidene fluoride membranes (Trans-Blot Turbo Transfer). Membranes were blocked with 5% BSA in 1 \times tris-buffered saline (TBS) (Tris-buffered saline)–0.05% Tween-20 and incubated overnight at 4 °C with primary antibodies and then for 60 min with secondary antibodies. Western blots were developed with Clarity Western ECL substrate, and chemiluminescence was detected with a ChemiDoc imager (all from BioRad).

Density map analysis. On movie reconstruction, individual cells were cropped with ImageJ software. For signal mapping, the images obtained for each individual cell were aligned in a single column. Cell size normalization was applied to each time point, based on mean cell size, with background subtraction. We obtained a mean behavior for each cell, by projecting every time point onto the average. The mean behavior of the population was then determined, by projecting the mean signal of every individual cell at a given time point. This procedure was performed with a custom-designed ImageJ-compatible macro. A similar procedure was used to map stresses, except that the real stress value was used, without normalization. For bead density analysis, we smoothed positions with a two-dimensional Gaussian kernel of radius 3 pixels to obtain a density map, as described by Schauer and coworkers⁵¹. These last two analyses were performed in Matlab. Similar analysis was carried out for the actin patches density (despite the normalization that was done per cell and on a time windows of 5 minutes, to pool observations done with different frame rates).

Myosin and energy peak analysis. Maxima of the coordinated energy were isolated manually and a sequence of 11 frames around each maximum isolated and aligned to the maximum. The average Myosin II-GFP fluorescence was integrated in the area of the cell and aligned blindly following the energy sequence alignment. The pieces of signals were offset to zero and normalised to the maximum, averaged and plotted. For the correlation analysis the signals were cross-correlated and the average cross-correlation plotted.

Actin patch and displacement analysis. Actin patches were isolated manually and the signal integrated in a square of $2 \times 2 \mu\text{m}$. In time sequence of 11 frames were considered separately. The signal of the displacement was computed as average absolute length of the displacement vector of the non-coordinated beads population in the same square used for the actin signal. Each sequence of actin signal was offset to zeros and aligned according to the maximum in fluorescence. The displacement signal was aligned blindly following actin ones. The pieces of signals were averaged and plotted. For the correlation analysis the signals were cross-correlated and the average cross-correlation plotted.

Actin and HEL patches analysis. To show the simultaneous appearance of HEL and actin patches we performed an analysis similar to the one described above (but at high acquisition rate, 2 fps), in a smaller sequence (11 frames) and in a smaller window ($1 \mu\text{m} \times 1 \mu\text{m}$) were performed. The only difference is that in this case the HEL signal was aligned first to the point of appearance and the actin signal was blindly translated.

Actin patches tracking. B cells from Lifeact-GFP MD4 mice were settled onto a PAA gel coated with either BSA or HEL. Cells were allowed to settle for 10 min before imaging with an inverted spinning disk confocal microscope (Eclipse Ti

Nikon/Roper Spinning head) equipped with a $\times 40$ Water immersion objective 1.4 NA and a CoolSNAP HQ2 camera (pixel size 6.4 μm) with Metamorph software (Molecular Device, France). Time lapse were typically 1 image/6 s, taking 10 images stack with $\text{dz} = 0.4 \mu\text{m}$, and last 6 min. The acquisition were bleach-corrected and projected in z , before cropping the cells. Patches were tracked, excluding the ones on the cortex, using ImageJ (TrackMate). Tracks were further analyzed on Matlab to extract the diffusion coefficient D (on tracks of length n frames ($n > 3$) it was obtained as a linear fit without offset of the first $\text{max}(10, n)$ points of the mean square displacement), the duration, and the localization relative to the center of the synapse. Maps were obtained as done for the beads map (using a gaussian kernel).

Antigen-stripping experiments. Round glass coverslips were coated with anti-HEL antibody by overnight incubation. The coverslips were washed with PBS and imaged to obtain the control image. They were then placed on the antigen-coated PAA gel for 30 s to 1 minute. They were stripped off the surface of the gel and imaged as soon as possible using laser scanning microscope (Leica) with a 40x 1.4 NA oil immersion objective. Fluorescence on these images indicated the presence of detached antigen. Absence of fluorescence in stripped gel suggests that quenching is not due to the presence of many layer of antigen.

Antigen extraction quantifications. Movies of fluorescent antigen were quantified by measuring the fluorescence intensity in the cell $S(t)$, subtracting the initial point $S(0)$ and dividing by $S(0)$. So the plotted quantity $(S(t) - S(0))/S(0)$ represents the relative increment in fluorescence. When compared with the energy, this quantity signal was further divided by the maximum of the signal to compare the trend in the curve.

TEM: energy and flux. The traction force algorithm was based on that used by Butler et al.⁵² and modified by Mandal et al.¹⁵. Force reconstruction was conducted with the assumption that the substrate is a linear elastic half space, using Fourier Transform Traction Cytometry with Tikhonov regularization (regularization parameter was set to 5×10^{-19}). The position of the beads in reference image and deformed one was measured using MTT algorithm⁵³. The problem of calculating the stress field from the displacement is solved in Fourier space then inverted back to real space. The final stress field is obtained on a grid with 0.432 μm spacing (four pixels). All calculations and image processing were performed in Matlab.

Given the size of B cells, the density of beads, the magnitude of displacement, some parameters needed optimization for the analysis. In particular for the detection algorithm (MTT): search window size (5 pixels), particle radius (2.5 pixels), and maximum distance for nearest neighbor (four pixels). Pixel size of spinning disk confocal microscope is 108 nm (we occasionally used another setup with pixel size 160 nm, but the parameters did not need adjustment). Same parameters were applied for noise detection by measuring force in a non-stressed area not too far from the cell. A quality check of the TFM algorithm is given by the non-equilibrated forces, i.e., by the ratio of the sum of forces vectors (which should be zero) to the sum of magnitude of the forces. Lower ratio signifies higher quality of the analysis. We checked that all analyzed data this ratio was below 0.15. Further calculations based on the output of the algorithm were performed to extract the total strain energy (defined as the sum over the entire cell area of the scalar product force by displacement). Fluxes were calculated by standard vector analysis (Green's theorem): the flux is the integral over the cell area of the divergence of the 2D field (displacement). An outward flux represents pushing forces and inward flux represents pulling forces.

Note that even if in theory the forces are supposed to be zero outside the cell, we decided not to introduce this constraint to avoid border effects. However, when we compute energy and fluxes, we use the mask of the cell extracted by using an ImageJ custom-made macro. The mask was increased by 10% (dilation of the binary image using Matlab morphological tools) to avoid excessive cropping of the force/displacement field.

In order to respect physiological rigidity, the Young modulus of the gel is $E \sim 500$ Pa. This which limits the number of particles that can be inserted within the gel without altering its properties and prevented us to use more resolute methods^{54,55}. However, our setup has the advantage of being relatively simple to implement on classical confocal microscopy keeping a relatively good resolution. The imaging conditions in soft gel are also the reason for a poor point spread function which prevented us to implement 2.5D force measurements as done by Legant et al.⁵⁶. This is also the reason for a statistical treatment of the z displacement in the 3D tracking experiment (see the quantification of the $\text{std}(z)$ in Fig. 5a).

TFM algorithm for coordinated and non-coordinated forces. We determined whether a bead belongs to the coordinated or non-coordinated group, by calculating the mean correlation between the displacement vector associated with the bead and its nearest neighbors (within 1 μm range). Beads with a correlation coefficient below 0.5 were considered to belong to the non-coordinated pool. Note that we define a correlation that does not depend on the magnitude of the displacement vectors but only of their relative orientation. This implies that beads moving a little or not at all have low correlations coefficient and build up the non-coordinated pool.

Spectral analysis. To extract a typical time-scale of the collective pulsatile dynamics (Fig. 3f) the coordinated energy was first de-trended subtracting the background obtained smoothing the original signal with a low pass filter (Savitsky–Golay filter with third degree polynomial and a window of 500 s, 101 frames). The filter was run a second time to eliminate high frequency noise (Savitsky–Golay filter with third degree polynomial and a window of 50 s, 11 frames). The power spectrum was then computed on the de-trended signal using maximum entropy algorithm (Matlab). The maximum (if present) was selected in frequencies between 1/50 Hz and 1/500 Hz (to avoid effects introduced by the smoothing).

Z movement measurement. B cells from MD4 mice were settled onto a PAA gel coated with HEL. Cells were allowed to settle for 10 min before imaging with an inverted spinning disk confocal microscope (Eclipse Ti Nikon/Roper Spinning head) equipped with a $\times 40$ water immersion objective 1.4 NA and a CoolSNAP HQ2 camera (pixel size 6.4 μm) with Metamorph software (Molecular Device, France). Stacks of 16 images were taken with $\text{dz} = 0.2 \mu\text{m}$, every 6 s for 60–360 s. We performed 3D single particle tracking (Trackmate, Fiji) and analyzed the trajectory in Matlab. We analyzed and plotted the standard deviation of the z position in subtrajectories of 10 frames (to pull together the movies that have different lengths). Center and radius of the cell were extracted from the mask and used to compute the “normalised position” of the trajectory in the average cell. The central region is considered having a radius $r = 2/3 \times (\text{cell radius})$.

Fluorescence-activated cell sorting antibodies. Cells were blocked with rat anti-mouse CD16/CD32 (BioLegend) and stained with: LIVE/DEAD[®] Fixable Aqua Dead Cell (ThermoFischer), PerCpCy5.5 Rat anti-mouse IgD (BioLegend), Pacific Blue Rat anti-mouse B220 (BioLegend), PE Cy7 Hamster anti-mouse CD95 (BD Biosciences), PE Rat anti-mouse T- and B-cell activation antigen (BD Biosciences). Samples were attained on BD LSRFortessa X20 and analyzed using FlowJo software.

Mice immunization. HEL (Sigma)-OVA (Sigma) coated beads used in immunization experiments were prepared as follows: 7.5 μg of biotinylated HEL + 7.5 μg of biotinylated OVA 647 were incubated overnight at 4 °C with 10^7 streptavidin-coated 200 nm beads (Sigma) in 500 μl , washed four times and re-suspended in PBS–BSA 1% at a concentration of 80×10^6 beads/ μl . Mice were injected subcutaneously in the left flank with 50 μl beads in Alum (ThermoScientific) in a ratio 1:1 (mice received 4×10^9 beads or 3 μg HEL + 3 μg OVA). Draining (inguinal) lymph nodes were collected on day 14.

Lymph node immunofluorescence. Eight micrometer-thick lymphnode sections were blocked for 30 minutes with 5% goat serum (DakoCytomation) in PBS. GL7 antibody was incubated overnight at 4 °C, followed by washing with PBS and staining of the remaining directly conjugated antibodies for 1 h at room temperature. The following antibodies were used: Alexa Fluor 488-conjugated rat anti-mouse T and B-cell activation antigen (BioLegend) and PE-conjugated rat anti-mouse B220 (BioLegend), Alexa Fluor 647-conjugated anti-mouse CD169 (BioLegend). Afterwards, the tissue sections were washed with PBS and mounted with Prolong Diamond mounting medium (Invitrogen). Images were collected using a confocal microscope (Zeiss LSM880) and analyzed using ImageJ software.

Statistics. All graphs and statistical analyses were performed with GraphPad Prism 5 (GraphPad Software) and MATLAB. In most cases non-parametric test (Mann–Whitney) test was used to determine statistical significance unless otherwise stated. Bar graphs show the median \pm interquartile range (IQR) or mean \pm standard error mean (SEM). Graphs representing strain energy and displacement flux were aligned to start at time zero, dot plots of strain energy show the average of each cell at the plateau.

Reporting summary. Further information on research design is available in the Nature Research Reporting Summary linked to this article.

Data availability

The raw and treated data are available from the corresponding authors upon request. The source data underlying Figs. 1d–i, 3a–b, 3d, 4b–d, 4g–h, 5a–b, 5e–f, 6c, 7b–d, 7f, 7i, 8a, 8d–i and Supplementary Figs 1b–c, 2a–b, 3c and 6b are provided as a Source Data file.

Code availability

TFM analysis codes (Matlab) and image quantification tools (ImageJ and Matlab) are available from the corresponding authors upon request.

Received: 27 March 2019 Accepted: 30 May 2019

Published online: 28 June 2019

References

- Griffiths, G. M., Tsun, A. & Stinchcombe, J. C. The immunological synapse: a focal point for endocytosis and exocytosis. *J. Cell Biol.* **189**, 399–406 (2010).
- Batista, F. D. & Dustin, M. L. Cell: cell interactions in the immune system. *Immunol. Rev.* **251**, 7–12 (2013).
- Batista, F. D., Iber, D. & Neuberger, M. S. B cells acquire antigen from target cells after synapse formation. *Nature* **411**, 489–494 (2001).
- Qi, H., Egen, J. G., Huang, A. Y. C. & Germain, R. N. Extrafollicular activation of lymph node B cells by antigen-bearing dendritic cells. *Science* **312**, 1672–1676 (2006).
- Suzuki, K., Grigorova, I., Phan, T. G., Kelly, L. M. & Cyster, J. G. Visualizing B cell capture of cognate antigen from follicular dendritic cells. *J. Exp. Med.* **206**, 1485–1493 (2009).
- Carrasco, Y. R., Fleire, S. J., Cameron, T., Dustin, M. L. & Batista, F. D. LFA-1/ICAM-1 interaction lowers the threshold of B cell activation by facilitating B cell adhesion and synapse formation. *Immunity* **20**, 589–599 (2004).
- Batista, F. D. & Harwood, N. E. The who, how and where of antigen presentation to B cells. *Nat. Rev. Immunol.* **9**, 15–27 (2009).
- Natkanski, E. et al. B cells use mechanical energy to discriminate antigen affinities. Materials and methods. *Science* **340**, 1587–1590 (2013).
- Yuseff, M. et al. Polarized secretion of lysosomes at the B cell synapse couples antigen extraction to processing and p. *Immunity* **35**, 361–374 (2011).
- Fleire, S. J. et al. B cell ligand discrimination through a spreading and contraction response. *Science* **312**, 738–741 (2006).
- Mattila, P. K. et al. The actin and tetraspanin networks organize receptor nanoclusters to regulate B cell receptor-mediated signaling. *Immunity* **38**, 461–474 (2013).
- Kwak, K. et al. Intrinsic properties of human germinal center B cells set antigen affinity thresholds. *Sci. Immunol.* **3**, 1–14 (2018).
- Dembo, M. & Wang, Y. L. Stresses at the cell-to-substrate interface during locomotion of fibroblasts. *Biophys. J.* **76**, 2307–2316 (1999).
- Sabass, B., Gardel, M. L., Waterman, C. M. & Schwarz, U. S. High resolution traction force microscopy based on experimental and computational advances. *Biophys. J.* **94**, 207–220 (2008).
- Mandal, K., Wang, I., Vitiello, E., Orellana, L. A. C. & Balland, M. Cell dipole behaviour revealed by ECM sub-cellular geometry. *Nat. Commun.* **5**, 5749 (2014).
- Buñi, N. et al. Human primary immune cells exhibit distinct mechanical properties that are modified by inflammation. *Biophys. J.* **108**, 2181–2190 (2015).
- Wan, Z. et al. B Cell Activation Is Regulated by the Stiffness Properties of the Substrate Presenting the Antigens. *J. Immunol.* **190**, 4661–4675 (2013).
- Zeng, Y. et al. Substrate stiffness regulates B-cell activation, proliferation, class switch and T-cell-independent antibody responses in vivo. *Eur. J. Immunol.* **45**, 1621–1634 (2015).
- Hoogeboom, R. et al. Myosin IIa promotes antibody responses by regulating B cell activation, acquisition of antigen, and proliferation. *Cell Rep.* **23**, 2342–2353 (2018).
- Sage, P. T. et al. Antigen recognition is facilitated by invadosome-like protrusions formed by memory/effector T cells. *J. Immunol.* **188**, 3686–3699 (2012).
- Di Martino, J. et al. The microenvironment controls invadosome plasticity. *J. Cell Sci.* **129**, 1759–1768 (2016).
- Bretou, M. et al. Lysosome signaling controls the migration of dendritic cells. *Sci. Immunol.* **2**, eaak9573 (2017).
- Wang, J. et al. Profiling the origin, dynamics, and function of traction force in B cell activation. *Sci. Signal.* **11**, pii: eaai9192 (2018).
- Liu, C. et al. Analyzing actin dynamics during the activation of the B cell receptor in live B cells. *Biochem. Biophys. Res. Commun.* **427**, 202–206 (2012).
- Murugesan, S. et al. Formin-generated actomyosin arcs propel T cell receptor microcluster movement at the immune synapse. *J. Cell Biol.* **215**, 383–399 (2016).
- Chaudhuri, A., Bhattacharya, B., Gowrishankar, K., Mayor, S. & Rao, M. Spatiotemporal regulation of chemical reactions by active cytoskeletal remodeling. *Proc. Natl Acad. Sci. USA* **108**, 14825–14830 (2011).
- Gowrishankar, K. et al. Active remodeling of cortical actin regulates spatiotemporal organization of cell surface molecules. *Cell* **149**, 1353–1367 (2012).
- Cai, E. et al. Visualizing dynamic microvillar search and stabilization during ligand detection by T cells. *Science* **356**, eaal3118 (2017).
- Shevchuk, A. I. et al. An alternative mechanism of clathrin-coated pit closure revealed by ion conductance microscopy. *J. Cell Biol.* **197**, 499–508 (2012).
- Basquin, C. et al. Membrane protrusion powers clathrin-independent endocytosis of interleukin-2 receptor. *EMBO J.* **34**, 2147–2161 (2015).
- Trimble, W. S. & Grinstein, S. Barriers to the free diffusion of proteins and lipids in the plasma membrane. *J. Cell Biol.* **208**, 259–271 (2015).
- Freeman, S. A. et al. Integrins form an expanding diffusional barrier that coordinates phagocytosis. *Cell* **164**, 128–140 (2016).

33. Maxson, M. E. et al. Integrin-based diffusion barrier separates membrane domains enabling the formation of microbiostatic frustrated phagosomes. *Elife* **7**, 1–37 (2018).
34. Reversat, A. et al. Polarity protein Par3 controls B-cell receptor dynamics and antigen extraction at the immune synapse. *Mol. Biol. Cell* **26**, 1273–1285 (2015).
35. Kaksonen, M., Toret, C. P. & Drubin, D. G. Harnessing actin dynamics for clathrin-mediated endocytosis. *Nat. Rev. Mol. Cell Biol.* **7**, 404–414 (2006).
36. Cheng, J., Grassart, A. & Drubin, D. G. Myosin 1E coordinates actin assembly and cargo trafficking during clathrin-mediated endocytosis. *Mol. Biol. Cell* **23**, 2891–2904 (2012).
37. Pedersen, R. T. A. & Drubin, D. G. Type I myosins anchor actin assembly to the plasma membrane during clathrin-mediated endocytosis. *J. Cell Biol.* **218**, 1138–1147.
38. Wan, Z. et al. The activation of IgM- or isotype-switched IgG- and IgE-BCR exhibits distinct mechanical force sensitivity and threshold. *Elife* **4**, 1–24 (2015).
39. McIntosh, B. B. & Ostap, E. M. Myosin-I molecular motors at a glance. *J. Cell Sci.* **129**, 2689–2695 (2016).
40. Lohner, J. et al. Myosin filaments reversibly generate large forces in cells. *Nat. Phys.* (2019) <https://doi.org/10.1038/s41567-019-0477-9>.
41. Watts, C. Antigen processing in the endocytic compartment. *Curr. Opin. Immunol.* **13**, 26–31 (2001).
42. Heisenberg, C. P. & Bellaïche, Y. Forces in tissue morphogenesis and patterning. *Cell* **153**, 948–962 (2013).
43. Plotnikov, S. V., Pasapera, A. M., Sabass, B. & Waterman, C. M. Force fluctuations within focal adhesions mediate ECM-rigidity sensing to guide directed cell migration. *Cell* **151**, 1513–1527 (2012).
44. Yang, B. et al. Mechanosensing controlled directly by tyrosine kinases. *Nano Lett.* **16**, 5951–5961 (2016).
45. Shiu, J., Aires, L., Lin, Z. & Vogel, V. Nanopillar force measurements reveal actin-cap-mediated YAP mechanotransduction. *Nat. Cell Biol.* **20**, 262–271 (2018).
46. Treppe, X. et al. Physical forces during collective cell migration. *Nat. Phys.* **5**, 426–430 (2009).
47. Jacobelli, J. et al. Confinement-optimized three-dimensional T cell amoeboid motility is modulated via myosin IIA-regulated adhesions. *Nat. Immunol.* **11**, 953–961 (2010).
48. Riedl, J. et al. Lifeact: a versatile marker to visualize F-actin. *Nat. Methods* **5**, 605–607 (2008).
49. Goodnow, C. C. et al. Altered immunoglobulin expression and functional silencing of self-reactive B lymphocytes in transgenic mice. *Nature* **334**, 676–682 (1988).
50. Long, R., Hall, M. S., Wu, M. & Hui, C. Y. Effects of gel thickness on microscopic indentation measurements of gel modulus. *Biophys. J.* **101**, 643–650 (2011).
51. Schauer, K. et al. Probabilistic density maps to study global endomembrane organization. *Nat. Methods* **7**, 560–566 (2010).
52. Butler, J. P., Tolic, I. V. A. M., Fabry, B. E. N. & Fredberg, J. J. Traction fields, moments, and strain energy that cells exert on their surroundings. *Am. J. Physiol. Cell Physiol.* **282**, 595–605 (2002).
53. Bertaux, N., Marguet, D. & Serge, A. Dynamic multiple-target tracing to probe spatiotemporal cartography of cell membranes. *Nat. Methods* **5**, 687–694 (2008).
54. Waithe, D. et al. Super-resolved traction force microscopy (STFM). *Nano Lett.* **16**, 2633–2638 (2016).
55. Plotnikov, S. V., Sabass, B., Schwarz, U. S. & Waterman, C. M. High-Resolution Traction Force Microscopy. *Methods in Cell Biology* **123**, 367–394 (2014).
56. Legant, W. R. et al. Multidimensional traction force microscopy reveals out-of-plane rotational moments about focal adhesions. *Proc. Natl Acad. Sci.* **110**, 881–886 (2013).

Acknowledgements

We acknowledge Y. Bellaïche, G. Cappello, M. Cosentino-Lagomarsino, C. Hivroz, J. Husson, I. Lavi, M. Leoni, O. Malbec, H. Moreau, M. Piel, J. Prost and P.H. Puech for discussions, advices about experiments and critical reading of the paper. We thank D. Vignjevic, G. Montagnac, and C. Hivroz for helping with antibodies. We acknowledge the Nikon Imaging Center@CNRS-Institut Curie and PICT-IBISA, Institut Curie, Paris, member of the France-BioImaging national research infrastructure, for support in image acquisition and the Curie Mouse Facility. PP was supported by CNRS. AK and JP were supported by Paris Descartes PhD fellowship and Ecole Doctorale FIRE—Programme Bettencourt. This project was funded by grants to PP (ANR-10-JCJC-1504-Immuphy), AMLD (ANR-PoLyBex-12-BSV3-0014-001, ERC-Strapacemi-GA 243103), MCIC (Swedish Research Council).

Author contributions

A.K. performed and analyzed most experiments, prepared figures, and participated in writing the first draft. J.P. performed experiments, quantifications and figures on MLSA1 and actin patches characterization and participated in writing the second draft. P.J.S. helped with the initial experimental setup and cell manipulation. M.M. performed image analysis. D.L. performed immunostaining and SEM experiments, M.S.-R. performed and analyzed TEM experiments. R.V. built the analytical model and contributed to analytical arguments. K.H. performed preliminary TFM analysis. V.F.B. performed and analyzed in vivo experiments. M.C.I.K. supervised the in vivo experiments. M.B. provided TFM expertise and analytical tools. A.-M.L.D. designed experiments, wrote the manuscript, and supervised the whole research. P.P. designed experiments, performed formal and data analysis, prepared figures, wrote the manuscript, and supervised the whole research. Drawings in Figs. 1a, 8b and Supp. 6a were created by A.K., model in Fig. 8j was created by P.P.

Additional information

Supplementary Information accompanies this paper at <https://doi.org/10.1038/s41467-019-10751-7>.

Competing interests: The authors declare no competing interests.

Reprints and permission information is available online at <http://npg.nature.com/reprintsandpermissions/>

Peer review information: *Nature Communications* would like to thank the anonymous reviewers for their contributions to the peer review of this work. Peer reports are available

Publisher's note: Springer Nature remains neutral with regard to jurisdictional claims in published maps and institutional affiliations.



Open Access This article is licensed under a Creative Commons Attribution 4.0 International License, which permits use, sharing, adaptation, distribution and reproduction in any medium or format, as long as you give appropriate credit to the original author(s) and the source, provide a link to the Creative Commons license, and indicate if changes were made. The images or other third party material in this article are included in the article's Creative Commons license, unless indicated otherwise in a credit line to the material. If material is not included in the article's Creative Commons license and your intended use is not permitted by statutory regulation or exceeds the permitted use, you will need to obtain permission directly from the copyright holder. To view a copy of this license, visit <http://creativecommons.org/licenses/by/4.0/>.

© The Author(s) 2019

Appendix B

Published Protocol article

Traction Force Microscopy to Study B Lymphocyte Activation

Anita Kumari¹, Judith Pineau¹, Ana-Maria Lennon-Duménil¹, Martial Balland², Paolo Pierobon¹

¹ Institut Curie, PSL Research University, INSERM U932 ² Laboratoire Interdisciplinaire de Physique, Université Joseph Fourier (Grenoble 1)

Corresponding Author

Paolo Pierobon

Paolo.Pierobon@curie.fr

Citation

Kumari, A., Pineau, J., Lennon-Duménil, A.M., Balland, M., Pierobon, P. Traction Force Microscopy to Study B Lymphocyte Activation. *J. Vis. Exp.* (161), e60947, doi:10.3791/60947 (2020).

Date Published

July 23, 2020

DOI

10.3791/60947

URL

jove.com/video/60947

Abstract

Traction force microscopy (TFM) enables the measurement of forces produced by a cell on a substrate. This technique infers traction force measurements from an experimentally observed displacement field produced by a cell pulling on an elastic substrate. Here, we adapted TFM to investigate the spatial and temporal structure of the force field exerted by B cells when activated by antigen engagement of the B cell receptor. Gel rigidity, bead density, and protein functionalization must be optimized for the study of relatively small cells (~ 6 μm) that interact with, and respond specifically to ligands for cell surface receptors.

Introduction

B cells are the antibody-producing cells of the immune system. To activate the adaptive immune response, they first acquire the antigen in a native form (i.e., non-processed) through a specific receptor called B cell receptor (BCR)¹. This process occurs in the lymph node B cell zone. Even if some antigens can reach the B cell through lymphatic fluids, most antigens, especially with high molecular weight (>70 kDa, which is the limit size for lymphatic conduits) are indeed presented in their native form on the surface of an antigen presenting cell (APC), typically a subcapsular sinus

macrophage or follicular dendritic cell, through lectin or Fc receptors (non-specific). The contact with this cell leads to the formation of an immune synapse where the BCR exerts force on the APC-associated antigens. The binding of an antigen to the BCR initiates BCR signaling, which may activate force-generating mechanisms. These forces could be important for amplifying BCR signaling, but are also essential for B cells to extract and then internalize the antigen.

Recent studies have shown that the BCR is indeed mechanosensitive². For example, stiffer substrates elicit

enhanced BCR signaling³. Moreover, force generated at the immune synapse pulls on single BCRs to probe its affinity to antigen and thereby ensure affinity discrimination⁴. It is therefore interesting to investigate the mechanical response of B cells to antigen presentation and to dissect this response in terms of type of receptors implicated (IgG/IgM)⁵, adhesion molecules (integrin ligands) or in pharmacologically and genetically modified cells (i.e., silencing of a protein downstream of BCR signaling or cytoskeleton dynamics)⁶.

A simple method to observe the response of a cell to a substrate of physiological rigidity and, at the same time, study forces exerted on the substrate is Traction Force Microscopy (TFM). TFM consists of observing the displacement field produced by the cell pulling on an elastic substrate. Originally the deformation of the gel was observed through wrinkles of the elastomer itself by phase-contrast microscopy⁷, but the insertion of fluorescence microbeads as fiducial markers allowed for better resolution and has since become the standard⁸. This method has been used to investigate the traction force exerted by adherent cells, tissues, and even organoids embedded in gels. Several variations of TFM have been developed⁹ including, combination with superresolution microscopy (i.e., STED¹⁰ or SRRF¹¹), modification of the refractive index of the gel to allow for TIRF microscopy¹², replacing beads by nano-printed patterns¹³, and using nanopillars instead of flat surface¹⁴. For a complete review of these variations, see Colin-York et al.¹⁵.

The protocol presented here describes a procedure to measure forces exerted by B cells on an antigen-coated substrate. These forces are applied on the ligands (antigen) in order to cluster them and subsequently extract them from the antigen-presenting substrate. We have adapted the standard TFM protocol to mimic the rigidity of physiological

antigen-presenting substrates, the size and the relevant coating for the B cells. This protocol allows for the study of several cells simultaneously and can be used in conjunction with fluorescence microscopy techniques and chemical treatments. However, it does not aim to probe single molecule force measurements, for which optical tweezers¹⁶, molecular tension probes^{17, 18}, biomembrane force probes¹⁹, and atomic force microscopy²⁰ are more suitable techniques. Compared to other single cell force measurement methods (e.g., micropipettes²¹ or microplates²²) TFM allows for the reconstruction of a complete map of the forces exerted at the synapse with a resolution of ~300 nm. This is useful to identify spatio-temporal patterns in the forces exerted on the surface and, as the gel is compatible with confocal imaging, to correlate them with the recruitment of specific proteins (for example, cytoskeleton and signaling proteins).

Although 3D TFM is possible, it is not compatible with the rigidity and the setup we used. Deformations in 3D are achievable by other more complex setups such as protrusion force microscopy (AFM scanning a deformable membrane where the cells are plated)^{23, 24} and elastic resonator interference stress microscopy (ERISM, a gel acting as resonating cavity for light and highlighting deformations of the substrate with accuracy of a few nanometers)²⁵. Although these techniques are very promising, they have not yet been employed in B cells. Other types of TFM, such as on nanopillars¹⁴, could be used to have more reproducible substrates. However, this geometry is not adapted to soft cells as the cell interpenetrates the pillars, which complicates the analysis. This approach has indeed been used in T cells to observe the capability of the cell to build structures around the pillars²⁶.

Despite its simplicity, TFM using polyacrylamide gels allows for the simultaneous observation of many cells and can be easily and inexpensively implemented in any lab equipped with a bench and an epifluorescence microscope (although we recommend confocal/spinning disk).

To mimic the physiological rigidity of an APC, we used polyacrylamide gels with a rigidity of $\sim 500 \text{ Pa}^{27}$ and functionalized the gel with activating antigens. In this protocol, we functionalized the surface of the polyacrylamide gel with hen egg lysozyme (HEL). This allows for the measurement of forces generated by stimulation of the BCR through engagement of the antigen binding site. The use of this antigen and the HEL-specific B cells from MD4 mice ensures relatively uniform force generation in response to antigen ligation²⁸. However, other molecules (such as anti-IgM for B6 mice) can be grafted onto the gel, but the forces generated in these cases could be more heterogeneous and less intense. Because B cells are small cells (diameter $\sim 6 \mu\text{m}$), the number of beads has been optimized to be maximal but still trackable. For large cells that exert $\sim \text{kPa}$ forces on their substrates, one can achieve satisfactory results using relatively sparse beads or performing simple particle image velocimetry (PIV) to reconstruct the deformation field. However, for small cells such as B lymphocytes that exert stress as small as $\sim 50 \text{ Pa}$, the use of single particle tracking is required (particle tracking velocimetry, PTV) to achieve the desired accuracy when reconstructing the deformation field. In order to reliably track beads individually, the magnification of the objective lens needs to be at least 60x and its numerical aperture around 1.3. Thus, the gels must be relatively thin ($< 50 \mu\text{m}$), otherwise the beads are not visible as they are above the working distance of the objective.

The main protocol consists of three sections: gel preparation, gel functionalization and imaging; two more sections are optional and are dedicated to the antigen extraction quantification and imaging of fluorescent cells.

Protocol

1. Gel preparation

1. Silanization of the gel support
 1. Activate the coverslip or glass-bottom Petri dish (which will be used as gel support) with a UV lamp for 2 min (wait 30 s before exposure to the UV lamp to avoid exposure to residual ozone).
 2. Silanize the coverslip/glass-bottom dish using 200 μL aminopropyltrimethoxysilane (APTMS) for 5 min. This will prepare the support for the covalent binding of the gel.
 3. Thoroughly wash the coverslip/glass-bottom dish with ultra-pure water.
 4. Dry the coverslip/glass-bottom dish using vacuum aspiration.
2. Preparation of the 18mm coverslip used to flatten the gel
 1. To prepare the coverslips, first put them into a ceramic coverslip holder. Then put the coverslip holder into a small beaker (50 mL) and pour siliconizing reagent (stored at 4 °C, reusable) over the coverslips, being sure to completely cover them.
 2. Cover the beaker with aluminum foil and incubate for 3 min at room temperature. While waiting, fill a large beaker (500 mL) with ultra-pure water. After 3 min of incubation in siliconizing reagent, transfer the coverslip holder with coverslips to the beaker of water.

3. Thoroughly rinse the coverslips with ultra-pure water, dry them well and keep on paper wipes. For best results, proceed immediately to the next section.

3. Gel polymerization

1. For gels of 0.5 kPa, mix 75 μL of 40% acrylamide with 30 μL of 2% bisacrylamide (crosslinker) and 895 μL of phosphate-buffered saline (PBS). This premix can be stored for up to one month at 4 $^{\circ}\text{C}$.

2. To 167 μL of 0.5 kPa gel premix, add 1% (1.67 μL) of beads, vortex and sonicate for 5 min in a bath sonicator (standard bench ultrasonic cleaner with power of 50–100 W and frequency 40 kHz). Keep the mix protected from light using aluminum foil.

NOTE: The premix does not polymerize until the initiator (TEMED) is added.

3. To catalyze polymerization, add 1% (1.67 μL) of 10% w/v ammonium persulfate (APS).

4. To initiate polymerization, add 0.1% (0.2 μL) N,N,N',N'-Tetramethylethylenediamine (TEMED). Mix with a pipette. Once APS and TEMED have been added, the gel rapidly polymerizes so proceed quickly to gel casting.

4. Gel casting

1. Pipet 9 μL of gel mix onto each coverslip/glass-bottom dish (drop in the center, **Figure 1A**)
2. Place the silanized/hydrophobic coverslip and flatten the gel (**Figure 1B**). Using forceps, press the coverslip to ensure the gel spreads across the entire area of the coverslip (**Figure 1C**) until it starts leaking out.

3. Invert the coverslip/glass-bottom dish into a large Petri dish and tap it on the bench to force beads going towards the gel surface (**Figure 1D**).

4. Cover with aluminum foil and leave for 1 h to polymerize at room temperature in a humid chamber (i.e., put a wet tissue above the dish to prevent evaporation).

5. After 1 h, add PBS to the sample to facilitate coverslip release. Carefully, remove the coverslip using a needle (the coating with different silanes should allow easy peeling off of the coverslip from the gel, **Figure 1E**).

6. Leave the gel in PBS.

NOTE: Gels can now be stored in PBS at 4 $^{\circ}\text{C}$ for 5–7 days, but it is recommended to use them within 48 h.

2. Gel functionalization

1. Prepare sulfosuccinimidyl 6-(4'-azido-2'-nitrophenylamino)hexanoate (Sulfo SANPAH) solution at 0.5 mg/mL in 10 mM HEPES buffer. This can be stored at 4 $^{\circ}\text{C}$ covered with aluminum foil for up to one week.

2. Aspirate the PBS from gels.

3. Add 150 μL of Sulfo SANPAH to the gel at room temperature (**Figure 1F**).

4. Expose the gel to UV treatment for 2 min to photoactivate the sites of Sulfo SANPAH and make it stick to the gel surface.

5. Wash with PBS three times (**Figure 1G**).

6. Repeat steps 2.2–2.5.

7. Add 250 μL of HEL (100 $\mu\text{g}/\text{mL}$) to each gel and incubate overnight in a humid chamber at 4 $^{\circ}\text{C}$ overnight while keeping covered with aluminum foil (**Figure 1H**).

8. Remove HEL antigen and wash with PBS three times.

NOTE: HEL acts both as an antigen and as an adhesion molecule. It can be replaced by other molecules that bind to the receptor (e.g., an anti-mouse IgM, Bovine Serum Albumin, Ovalbumin) or mixed with integrin ligands (e.g., ICAM1 binding to LFA1). If needed, antigen extraction can be observed with a fluorescent version of the HEL (obtained by staining the molecule with a protein labeling kit, see step 4). Note that a given concentration in bulk might not yield the same surface concentration on the gel as on the glass: this needs to be quantified with secondary staining if direct comparison is required.

3. Cell loading and imaging

1. Before imaging, remove PBS from the gels and add 500 μ L of B cell media (RPMI 1640, 10% decompemented fetal calf serum, 1% penicillin-streptomycin, 2% Sodium Pyruvate, 50uM Mercaptoethanol and 1X Non Essential Amino Acids) and let them to equilibrate to RT.

2. Cell preparation

1. Purify primary B cells from spleen according to a negative selection protocol (see **Table of Materials**). Typical final B cell yield is around 1×10^7 cells. Concentrate this to 3×10^6 cells/mL in B cell medium (RPMI-1640 supplemented with 10% fetal calf serum, 1% penicillin-streptomycin, 0.1% mercaptoethanol and 2% sodium pyruvate).

2. Store cells as needed for up to 6 h at 4 °C.

3. Keep the cells at 37 °C for 30 min before image acquisition.

3. Imaging

1. Use a confocal microscope with thermal and (possibly) CO₂ control.

NOTE: Regardless of whether a confocal or spinning-disk microscope is used, it is important to use an objective/pinhole that allows a pixel size <200 nm to comfortably track the beads in the analysis phase (e.g., 60x, NA 1.3). Epifluorescence microscopy can also be used, however it provides lower signal to noise ratio and may make individual bead tracking harder.

2. Two main layers of beads will appear on the bottom and the top of the gel. Focus on the gel plane.

NOTE: A nice gel will appear as a starry sky, with beads approximately uniformly distributed on the same plane.

3. Program the acquisition for 30 min with a frame rate of 5 s (this is adaptable to the needs of the experiment, e.g., acquire other colors, acquire z stack, etc.)

4. Aspirate the media from the gel, leaving about 200 μ L of media on the gel. Position the gel on the microscope and find the surface layer of beads and a nice even area on the gel.

5. Add 80 μ L of cells (avoid touching the gel to maintain focus).

6. Ensure that the focus is still correct and that cells can be seen descending in the area (under transmitted light). Launch the acquisition before the cells reach the gel.

7. In case of accidental contact with gel, vibrations, or focus drift, adjust the focus.

NOTE: It is crucial to collect an image of the relaxed gel and this can be any image taken before the arrival of the cells on the gel.

4. Fluorescent HEL extraction experiment

1. Prepare fluorescent HEL by binding a fluorescent dye (of a color different from the beads one such as Alexa 555), see the **Table of Materials**.
2. In step 2.7, replace conventional HEL with the fluorescent HEL.
3. Acquire images with low illumination settings or low frame rate (e.g., 2 frames per minute) to avoid photo-bleaching.
4. To quantify HEL extraction, compute the intensity integrated over the cell area for each frame $I(t)$ corrected and normalized by the intensity $I(0)$ of frame 0 according to the formula:

$$Q(t) = \frac{I(t) - I(0)}{I(0)}$$

NOTE: The antigen conjugated with a fluorophore is not visible (probably due to quenching of the fluorophore at the gel surface), but its presence on the gel can be verified with an anti-HEL and a fluorescent secondary antibody. It can be verified that the fluorophore is indeed fluorescent when detached by stripping it from the gel with a coverslip coated with anti-HEL and revealing it with a secondary fluorescent antibody (on the coverslip)⁶. The signal of the extracted antigen is very dim and is sometimes masked by leaking of the beads. If one is interested only in antigen extraction, it is recommended to prepare the gel without beads (skip steps 1.3.2 and 1.4.3).

5. Fluorescence imaging

1. Obtain fluorescent B cells by purifying B cell from the spleens of genetically modified mice as done for the wild type (e.g., from Lifeact-GFP or Myosin II GFP mice).

2. For imaging fluorescent cells, use (if possible) a spinning disk microscope with a water immersion long-distance 40x–100x objective.
3. Keep exposure duration and frame rate low to avoid bleaching.

NOTE: The point spread function in Z is highly degraded by the presence of the gel, hence we suggest using a water immersion objective. Live upright microscopy with water-dipping objectives suffers from strong spherical aberrations induced by the presence of the (spherical) cell (and cell nucleus) in the emission path.

6. Analysis

NOTE: Data analysis is in general performed by first correcting the whole stack for drift, finding the beads in each frame, tracking their movements with respect to a reference frame (taken in absence of cells), interpolating the displacement field and inverting the problem to obtain the stress using Fourier transform²⁹. To this end, we suggest using a combination of ImageJ Macro and MATLAB programs downloadable from an online repository³⁰.

1. Open the movie in ImageJ as stack of images
2. Run the macro “Crop_and_save.ijm”
 1. Select the regions of interest (ROI) with the “Rectangle” tool and add them to the ROI list using the ‘t’ key.
 2. When cropping the cell, be sure to include a region of at least 5–10 pixels of immobile beads. Exclude cells that are too close to the boundaries or to other cells from the analysis. When finished click on ‘OK’.
 3. The macro proposes a mask of the cell: if this is satisfactory click on “OK”. If not satisfactory, click on

“Not ok” and then manually select a closed region with any selection tool (e.g. “Freehand” or “Oval”) and click on “Continue”.

3. Open MATLAB and run “TFM_v1.m”.
 1. Input the required parameters: in particular check the image properties (pixel size, time interval of acquisition) and the gel properties (Young modulus E, Poisson ratio).
 2. The reference image is set to be the first by default. Set it to another frame if needed or set it to “0” to load an external file.
 3. Locate the outputs of the software in the same directory as the original file (for a description see the User_notice.pdf file). This includes a preliminary track of the beads (“FILENAME.fig”), a plot of the contractile energy over time (“FILENAME_energy.fig”), a table of several quantities integrated over the cell (energy, area, moments, etc) “FILENAME_finaletable.mat”, a structure containing the displacement and force field, movies of the bead, displacement field, stress and energy (that can be opened with any avi reader).

NOTE: In the input parameters, the “Window size” is the window over which the displacement is interpolated, hence the final resolution of the stress and displacement field. This is set to a few (by default four) pixels. It is not advisable to reduce this as it would artificially increase the resolution by interpolating regions where there are no beads.

Representative Results

Given the size of the cells, algorithms that extract the displacement map of the beads via correlative techniques (such as particle image velocimetry) are in general not very

precise. However depending on the degree of resolution required, one can easily obtain qualitative results using a free Fiji/ImageJ plugin^{31, 32}. While this approach is sufficient to compare stimulating versus non-stimulating conditions, for a thorough analysis we recommend using our software downloadable from an online repository³⁰, that tracks the beads individually and provides the displacement field map at a given time point as the interpolation of the individual bead displacements³³. Several quantifications are possible at this point. For example (by assuming the displacement is caused only by stress tangential to the gel surface) the software also provides the stress at each point causing that specific displacement map. This is a type of “inversion problem”: the displacement at a certain point depends on the sum of all the forces applied all over the other points. The “inversion algorithm” takes into account the physical parameters of the substrate: its rigidity (Young modulus) and Poisson ratio. Direct algorithms are typically very accurate but computationally expensive. Algorithms based on Fourier transform, like ours, perform essentially a deconvolution in Fourier space and are more efficient but prone to some errors (mainly due to the interpolation step). These algorithms generally require the tuning of a parameter that prevents small local (and potentially artifactual) displacements to become too relevant in the computation of the stress field (Tikhonov regularization parameter^{8, 29}; “Regularization” variable in the dialog window; here we typically set equal to 5×10^{-19}). For more advanced interpretation and analysis, such as spatio-temporal correlations, local movements, correlations with fluorescent channels, we recommend collaborating with experts in the field. For a review on computational methods see Schwarz et al.⁹.

As mentioned above, correct bead images look like a “starry sky”, a uniform and random distribution of bright spots (**Figure**

2A). Data and analysis are not reliable when the number of beads is too low (**Figure 2B**) or the image is out of focus (**Figure 2C**). Once B cells have settled onto the surface of the gel, the beads underneath the cells start to move due to the traction force exerted by the cell on the gel. Frames for which the beads are not trackable should be discarded.

As a check, it is possible to observe by eye the movement of beads comparing the “reference frame”, typically the one preceding the first contact of the cell with the substrate. Approximate results can be obtained from the single particle tracking (e.g., Trackmate, Fiji ³⁴) as done in **Figure 3A**. The analysis provides a segmentation of the beads in the reference image (“FILENAME.fig”) as a control.

With the software we propose, one can obtain the displacement (**Figure 3B**) and stress field (the vector of the local stress at each pixel and each time point obtained by inversion from the displacement field, **Figure 3C**). Scalar product of the displacement and force fields integrated on the

area of the cell provides total work exerted by the cell on the substrate (**Figure 4A**). This computation requires the mask of the cell introduced in step 6.2 of the protocol.

To compare two biological conditions (as activating HEL versus non-activating substrate BSA, or wild type versus knock-out) it is useful to compute the average curve (**Figure 4B**) or, even more synthetically, an average value over the last time points (20 min) where the energy reaches a plateau (**Figure 4C**). When the spatial information of the forces is relevant it is possible to compare single time points of each condition (**Figure 4D**). Refer to Kumari et al.⁶ for deeper analysis.

An example of fluorescence antigen extraction time lapse is shown in **Figure 5A**: the progressive appearance of fluorescence signals at the synapse indicated antigen detachment from the gel. The average extraction curve with its confidence interval (standard error of the mean) over 15 cells is shown in **Figure 5B**.

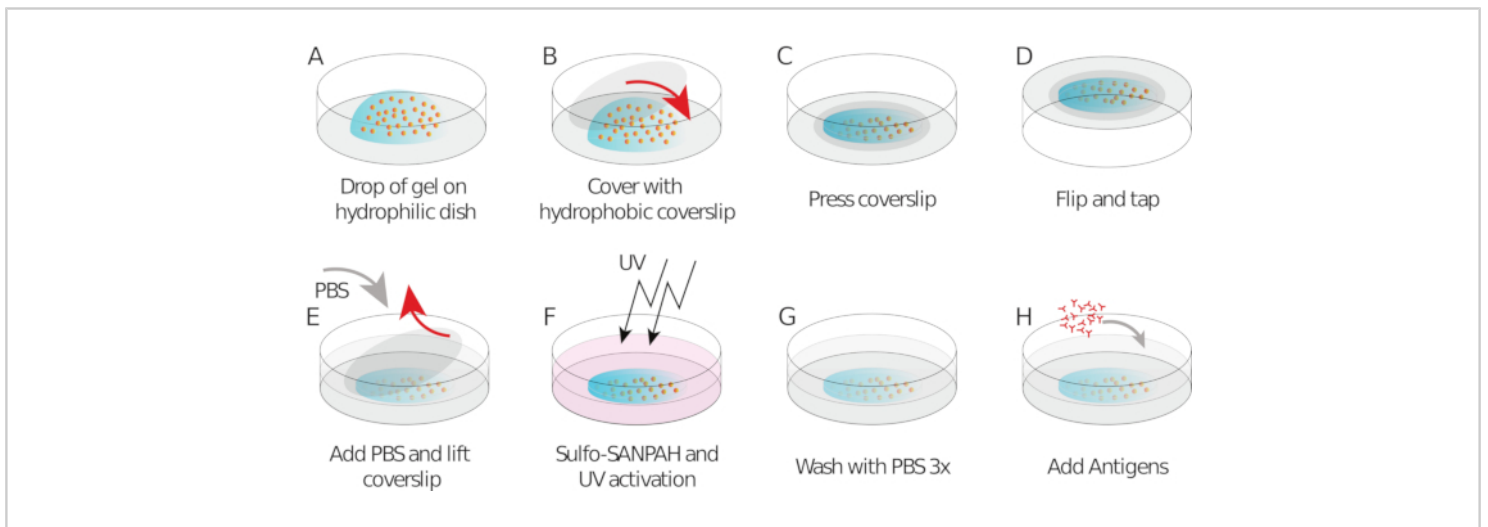


Figure 1: Schematic showing of the preparation of the gel and its functionalization. Steps are described in the protocol. [Please click here to view a larger version of this figure.](#)

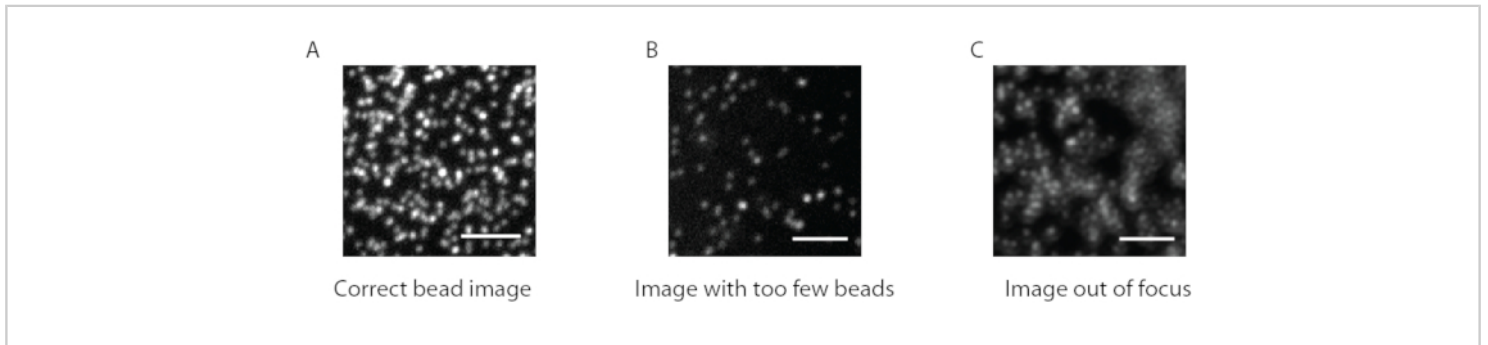


Figure 2: Three examples of bead images of different qualities. (A) Example of bead image with the correct signal to noise ratio and the correct density. **(B)** Examples of images with a too insufficient number of beads and **(C)** out of focus plane. [Please click here to view a larger version of this figure.](#)

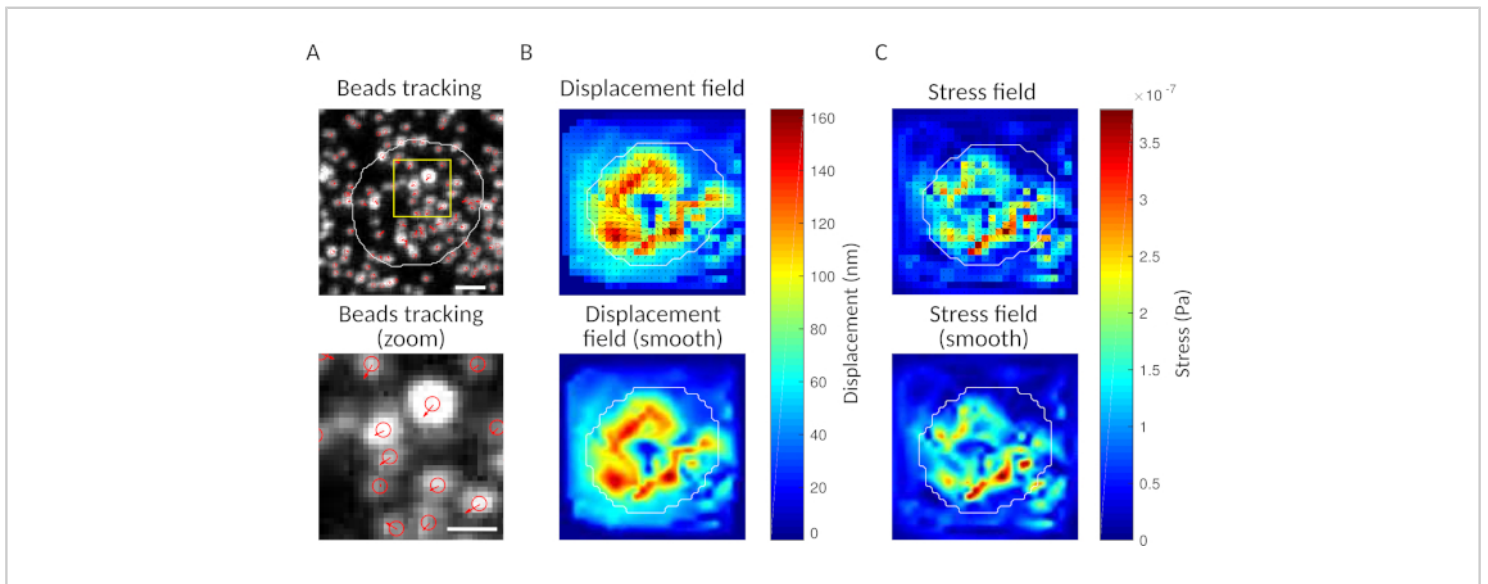


Figure 3: Processing of the images to extract the force field. (A) Example of an image of the beads (outline of the cell in white, extracted from the transmission image), bead tracking at time $t = 5$ min (red overlay) and displacement (arrows) relative to time $t = 0$ min (scale bar $5 \mu\text{m}$). **(B)** Interpolated displacement field (represented as vector quiver and magnitude map, arrows are proportional to the displacement [nm]; see the color bar on the right); bottom: a smoother image of the magnitude (obtained by interpolation with a bicubic function). **(C)** Stress field from displacement field in panel B (represented as vector quiver and magnitude map; arrows are proportional to the shear stress [Pa]; see the color bar on the right); bottom: a smoother image of the magnitude (obtained by interpolation with a bicubic function). [Please click here to view a larger version of this figure.](#)

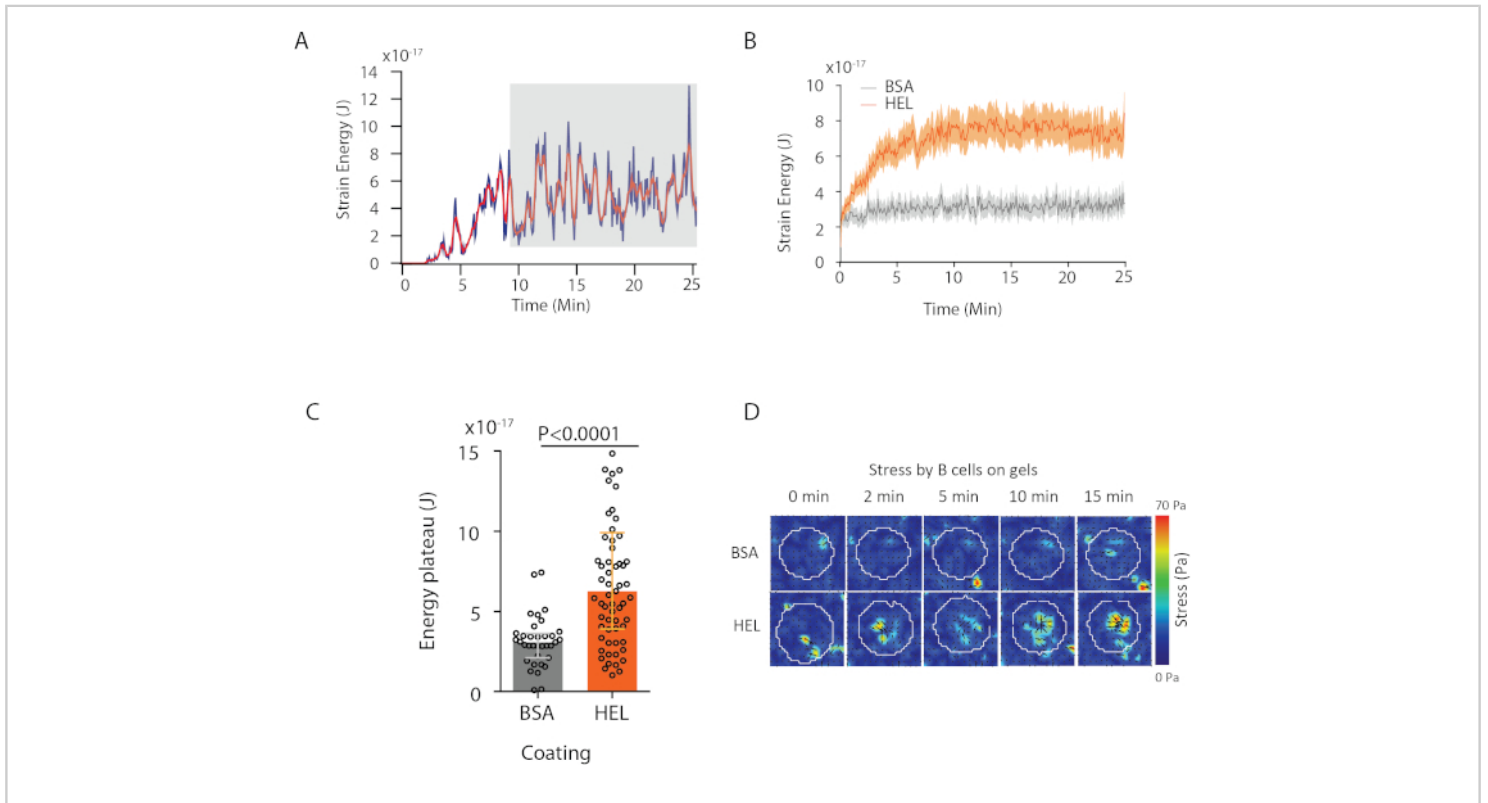


Figure 4: Example of information that can be extracted from force and displacement fields. (A) Example of evolution of energy in time for a single cell: a plateau phase (highlighted in gray) shows up after about 10 min. **(B)** Comparison of the average energy curves and **(C)** of the relative plateau levels for 65 cells plated on HEL (activating) coated gel and 35 cells on BSA (non-activating) coated gel (median \pm interquartile ranges are shown, Mann-Whitney test was used for statistical significance). **(D)** Time-lapse color maps of stress for HEL and control BSA condition; both magnitude and quiver plots are shown. These images have been adapted from Kumari et al.⁶. [Please click here to view a larger version of this figure.](#)

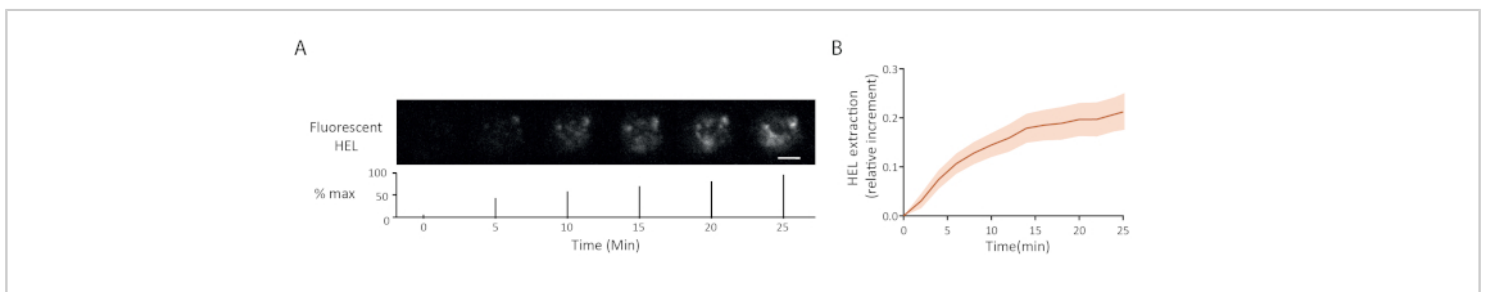


Figure 5: Example of experiments with fluorescent antigen. (A) Time lapse of the extraction of fluorescent HEL (below: percentage of the maximum, scale bar = 3 μ m). **(B)** Antigen gathering over time (Mean \pm SEM, n = 15). These images have been adapted from Kumari et al.⁶. [Please click here to view a larger version of this figure.](#)

Discussion

The TFM method described here allows for the systematic study of the active mechanical capabilities of B cells. In the context of B cells, this is related to the ability to extract and internalize the antigen. Compared to other TFM methods, the protocol presented here is simple and rather reproducible: the rigidity, measured by indentation of a glass microsphere and using Hertz model, is between 400 and 600 Pa. Similar protocols have been successfully used not only for B cells³⁵ but also for T cells³⁶. In comparison to nanopillars (also used for T lymphocytes³⁷) it provides a flat homogeneous surface, hence the results are easier to interpret as the interaction of the gel are mainly constrained to be tangential to the surface.

The protocol we described gives access to the spatiotemporal dynamics of the forces exerted by B cells on antigen-presenting substrates. On the spatial level this provides information of the localization of forces, and in combination with fluorescence microscopy, enables the experimenter to correlate local forces with the presence of specific molecules (i.e., components of the cytoskeleton or BCR signaling cascade). At the temporal level, it is possible to integrate quantities (such as total energy or total stress) to provide one value per time point and reduce the noise. This allows for observation of the evolution of the traction force in time (growth and plateau) and the presence of pulsatile patterns.

Critical experimental aspects for the analysis are described as following. (i) Cell density: to perform a correct analysis, cells should be sufficiently separated. We consider a cell to be analyzable if it has an empty region of its own size around it. (ii) Transmission image: it is advisable to collect at least a transmission image of the cells during the experiment to be used as a mask in the analysis. (iii) Number of beads in the image: we suggest analyzing only

images where the number of beads in the synapse is between 30 and 200 (i.e., 1–8 beads/ μm^2). Lower densities do not allow for adequate map displacement reconstruction. High bead densities make single particle tracking unreliable. (iv) Number of beads should be constant during the experiment; however, fluctuations can occur due to small variability in the imaging conditions (especially in beads that are too close to each other). Focus drift, if occurring, must be corrected and problematic frames should be discarded. (v) Gel quality: gels with too many cracks, variability in beads distribution or gels that are too thick should be discarded. (vi) Depending on the cell type, after repeated exposures, cells at late time points (>300 frames) may suffer phototoxic effects. It is advisable to run the program on a mask devoid of cells as a “baseline” to be compared with the data. This provides a magnitude of the noise level solely due to the experimental conditions.

Gels used to measure traction force in classical adhesion allow for the investigation of processes that occur at the focal adhesion (actin flows and recruitment of signaling molecules)—the points where forces are applied^{38, 39}. However, forces at the synapse are not applied through focal adhesions. The spatiotemporal pattern of force generation at the B cell immune synapse has not been quantitatively investigated using this method until recently. Using TFM, we observed for the first time, force patterning at the B cell immune synapse, as presented in our recent study⁶, opening encouraging perspectives in the study of lymphocytes.

Notably, this method employs an image taken before the arrival of the cells on the gel as a reference image for the force computation. Usual TFM protocols suggest taking the reference image at the end of the experiment, after detaching the cells with trypsin; this allows the experimenter to look for a region rich in cells. Although this is possible here too, trypsin

is rather inefficient at detaching B cells from antigen-coated gel, one needs to wait long for detachment and the risk of gel modification and movements (that make the whole data set unexploitable) is higher.

The method presented here is flexible and can be applied to study the effect of other signals at the immune synapse as it allows for grafting other proteins onto the gel surface (e.g., integrin ligands and immunoglobulins have been tested) and even fluorescent antigen (see section 4). Moreover, cells remain accessible to the experimenter for drug treatment and local perturbations. Finally, the method is also compatible with imaging fixed cells. For these observations, it is recommended to make the gel on a coverslip, stain the cells, glue the coverslip on a slide and only then add mounting media and another coverslip. Observation will then be done with the gel on top to avoid the degradation of the image through the gel.

Possible pitfalls are the variability in gel in polymerization and coating. Polymerization problems are mainly due to the quality of initiator/catalyst. Also, the gel can inflate, especially if not used right after assembly. This problem does not seem to dramatically affect the mechanical properties of the gel, but it can make the bead layer unreachable for the objective, effectively making the gel useless. We recommend preparing extra gels for each condition when this problem appears. There might be also a certain variability in the coating, and it is crucial to have freshly diluted Sulfo SANPAH.

In conclusion, we have described a simple, cheap and reproducible method to measure the forces exerted by B cells at the immunological synapse when activated by BCR ligand. It can be adapted to study the reaction to other ligands and

other kinds of lymphocytes (memory B cells, T cells, etc.) with the use of the proper receptor ligand.

Disclosures

The authors have nothing to disclose.

Acknowledgments

The authors thank M. Bolger-Munro for critical reading and acknowledge the Nikon Imaging Center@CNRS-InstitutCurie and PICT-IBISA, Institut Curie, Paris, member of the France-BioImaging national research infrastructure, for support in image acquisition and the Curie Animal Facility. PP was supported by CNRS. AK and JP were supported by Paris Descartes PhD fellowship and Ecole Doctorale FIRE—Programme Bettencourt. This project was funded by grants to PP (ANR-10-JCJC-1504-Immuphy) and AMLD (ANR-PoLyBex-12-BSV3-0014-001, ERC-Strapacemi-GA 243103).

References

1. Yuseff, M.-I., Pierobon, P., Reversat, A., Lennon-Duménil, A.-M. How B cells capture, process and present antigens: a crucial role for cell polarity. *Nature Reviews Immunology*. **13** (7), 475-486, (2013).
2. Spillane, K. M., Tolar, P. B cell antigen extraction is regulated by physical properties of antigen-presenting cells. *The Journal of Cell Biology*. **216** (1), 217-230, (2017).
3. Shaheen, S., Wan, Z., et al. Substrate stiffness governs the initiation of B cell activation by the concerted signaling of PKC β and focal adhesion kinase. *eLife*. **6**, (2017).

4. Natkanski, E., et al. B cells use mechanical energy to discriminate antigen affinities. *Science*. **340** (6140), 1587-1590, (2013).
5. Wan, Z., Chen, X., et al. The activation of IgM- or isotype-switched IgG- and IgE-BCR exhibits distinct mechanical force sensitivity and threshold. *eLife*. **4**, (2015).
6. Kumari, A., Pineau, J., et al. Actomyosin-driven force patterning controls endocytosis at the immune synapse. *Nature Communications*. **10** (1), 2870, (2019).
7. Dembo, M., Wang, Y. L. Stresses at the cell-to-substrate interface during locomotion of fibroblasts. *Biophysical Journal*. **76** (4), 2307-2316, (1999).
8. Sabass, B., Gardel, M. L., Waterman, C. M., Schwarz, U. S. High resolution traction force microscopy based on experimental and computational advances. *Biophysical Journal*. **94** (1), 207-220, (2008).
9. Schwarz, U. S., Soiné, J. R. D. Traction force microscopy on soft elastic substrates: A guide to recent computational advances. *Biochimica et Biophysica Acta*. **1853** (11 Pt B), 3095-3104, (2015).
10. Colin-York, H., Shrestha, D., et al. Super-Resolved Traction Force Microscopy (STFM). *Nano Letters*. **16** (4), 2633-2638, (2016).
11. Stubb, A., Laine, R. F., Guzmán, C., Henriques, R., Jacquemet, G., Ivaska, J. Fluctuation-Based Super-Resolution Traction Force Microscopy. *BioRxiv*. , (2019).
12. Gutierrez, E., Tkachenko, E., et al. High refractive index silicone gels for simultaneous total internal reflection fluorescence and traction force microscopy of adherent cells. *Plos One*. **6** (9), e23807, (2011).
13. Bergert, M., Lendenmann, T., et al. Confocal reference free traction force microscopy. *Nature Communications*. **7**, 12814, (2016).
14. Schoen, I., Hu, W., Klotzsch, E., Vogel, V. Probing cellular traction forces by micropillar arrays: contribution of substrate warping to pillar deflection. *Nano Letters*. **10** (5), 1823-1830, (2010).
15. Colin-York, H., Fritzsche, M. The future of traction force microscopy. *Current Opinion in Biomedical Engineering*. **5**, 1-5, (2018).
16. Feng, Y., et al. Mechanosensing drives acuity of $\alpha\beta$ T-cell recognition. *Proceedings of the National Academy of Sciences of the United States of America*. **114** (39), E8204-E8213, (2017).
17. Spillane, K. M., Tolar, P. DNA-Based Probes for Measuring Mechanical Forces in Cell-Cell Contacts: Application to B Cell Antigen Extraction from Immune Synapses. *Methods in Molecular Biology*. **1707**, 69-80, (2018).
18. Stabley, D. R., Jurchenko, C., Marshall, S. S., Salaita, K. S. Visualizing mechanical tension across membrane receptors with a fluorescent sensor. *Nature Methods*. **9** (1), 64-67, (2011).
19. Merkel, R., Nassoy, P., Leung, A., Ritchie, K., Evans, E. Energy landscapes of receptor-ligand bonds explored with dynamic force spectroscopy. *Nature*. **397** (6714), 50-53, (1999).
20. Hinterdorfer, P., Dufrêne, Y. F. Detection and localization of single molecular recognition events using atomic force microscopy. *Nature Methods*. **3** (5), 347-355, (2006).
21. Sawicka, A., Babataheri, A., et al. Micropipette force probe to quantify single-cell force generation: application

- to T-cell activation. *Molecular Biology of the Cell*. **28** (23), 3229-3239, (2017).
22. Desprat, N., Guiroy, A., Asnacios, A. Microplates-based rheometer for a single living cell. *Review of Scientific Instruments*. **77** (5), 055111, (2006).
 23. Labernadie, A., Bouissou, A., et al. Protrusion force microscopy reveals oscillatory force generation and mechanosensing activity of human macrophage podosomes. *Nature Communications*. **5**, 5343, (2014).
 24. Bouissou, A., Proag, A., et al. Protrusion force microscopy: A method to quantify forces developed by cell protrusions. *Journal of Visualized Experiments*. (136), (2018).
 25. Kronenberg, N. M., Liehm, P., et al. Long-term imaging of cellular forces with high precision by elastic resonator interference stress microscopy. *Nature Cell Biology*. **19** (7), 864-872, (2017).
 26. Basu, R., Whitlock, B. M., et al. Cytotoxic T cells use mechanical force to potentiate target cell killing. *Cell*. **165** (1), 100-110, (2016).
 27. Bufi, N., Saitakis, M., et al. Human Primary Immune Cells Exhibit Distinct Mechanical Properties that Are Modified by Inflammation. *Biophysical Journal*. **108** (9), 2181-2190, (2015).
 28. Goodnow, C. C., Crosbie, J., et al. Altered immunoglobulin expression and functional silencing of self-reactive B lymphocytes in transgenic mice. *Nature*. **334** (6184), 676-682, (1988).
 29. Butler, J. P., Tolić-Nørrelykke, I. M., Fabry, B., Fredberg, J. J. Traction fields, moments, and strain energy that cells exert on their surroundings. *American Journal of Physiology. Cell Physiology*. **282** (3), C595-605, (2002).
 30. MBPPlab/TFM_v1: Software for Time dependent Traction Force Microscopy. at <https://github.com/MBPPlab/TFM_v1> (2019).
 31. Tseng, Q., Duchemin-Pelletier, E., et al. Spatial organization of the extracellular matrix regulates cell-cell junction positioning. *Proceedings of the National Academy of Sciences of the United States of America*. **109** (5), 1506-1511, (2012).
 32. ImageJ plugins by Qingzong TSENG. at <<https://sites.google.com/site/qingzongtseng/>> (2019).
 33. Plotnikov, S. V., Sabass, B., Schwarz, U. S., Waterman, C. M. High-resolution traction force microscopy. *Methods in Cell Biology*. **123**, 367-394, (2014).
 34. Schindelin, J., Arganda-Carreras, I., et al. Fiji: an open-source platform for biological-image analysis. *Nature Methods*. **9** (7), 676-682, (2012).
 35. Wang, J., Lin, F., et al. Profiling the origin, dynamics, and function of traction force in B cell activation. *Science Signaling*. **11** (542), (2018).
 36. Hui, K. L., Balagopalan, L., Samelson, L. E., Upadhyaya, A. Cytoskeletal forces during signaling activation in Jurkat T-cells. *Molecular Biology of the Cell*. **26** (4), 685-695, (2015).
 37. Bashour, K. T., Gondarenko, A., et al. CD28 and CD3 have complementary roles in T-cell traction forces. *Proceedings of the National Academy of Sciences of the United States of America*. **111** (6), 2241-2246, (2014).
 38. Gardel, M. L., Sabass, B., Ji, L., Danuser, G., Schwarz, U. S., Waterman, C. M. Traction stress in focal adhesions correlates biphasically with actin retrograde flow speed. *The Journal of Cell Biology*. **183** (6), 999-1005, (2008).

39. Stricker, J., Sabass, B., Schwarz, U. S., Gardel, M. L.
Optimization of traction force microscopy for micron-sized
focal adhesions. *Journal of Physics. Condensed Matter*.
22 (19), 194104, (2010).

Appendix C

Collaborative Research articles

C.1 Collaborative Research article 1



Actin filaments regulate microtubule growth at the centrosome

Daisuke Inoue^{1,‡}, Dorian Obino^{2,†,‡} , Judith Pineau² , Francesca Farina¹, Jérémie Gaillard^{1,3}, Christophe Guerin^{1,3}, Laurent Blanchoin^{1,3,*} , Ana-Maria Lennon-Duménil^{2,**} & Manuel Théry^{1,3,***}

Abstract

The centrosome is the main microtubule-organizing centre. It also organizes a local network of actin filaments. However, the precise function of the actin network at the centrosome is not well understood. Here, we show that increasing densities of actin filaments at the centrosome of lymphocytes are correlated with reduced amounts of microtubules. Furthermore, lymphocyte activation resulted in disassembly of centrosomal actin and an increase in microtubule number. To further investigate the direct crosstalk between actin and microtubules at the centrosome, we performed *in vitro* reconstitution assays based on (i) purified centrosomes and (ii) on the co-micropatterning of microtubule seeds and actin filaments. These two assays demonstrated that actin filaments constitute a physical barrier blocking elongation of nascent microtubules. Finally, we showed that cell adhesion and cell spreading lead to lower densities of centrosomal actin, thus resulting in higher microtubule growth. We therefore propose a novel mechanism, by which the number of centrosomal microtubules is regulated by cell adhesion and actin-network architecture.

Keywords actin; cell adhesion; centrosome; microtubule

Subject Categories Cell Adhesion, Polarity & Cytoskeleton; Immunology

DOI 10.15252/embj.201899630 | Received 13 April 2018 | Revised 5 February 2019 | Accepted 21 February 2019 | Published online 22 March 2019

The EMBO Journal (2019) 38: e99630

See also: F Farina *et al* (June 2019)

Introduction

The growth of the microtubule network and its architecture regulates cell polarization, migration and numerous key functions in differentiated cells (Mimori-Kiyosue, 2011; de Forges *et al*, 2012;

Etienne-Manneville, 2013; Sanchez & Feldman, 2017). Microtubule growth first depends on microtubule nucleation, which is regulated by large complexes serving as microtubule templates and proteins that stabilize early protofilament arrangements (Wieczorek *et al*, 2015; Roostalu & Surrey, 2017). Then, microtubule elongation becomes regulated by microtubule-associated proteins and molecular motors acting at the growing end of microtubules (Akhmanova & Steinmetz, 2015). The architecture of the microtubule network—the spatial distribution and orientation of microtubules—is heavily influenced by its biochemical interactions and physical interplay with actin filaments (Rodriguez *et al*, 2003; Coles & Bradke, 2015; Huber *et al*, 2015; Colin *et al*, 2018; Dogterom & Koenderink, 2019). Although the physical cross-linking of the two networks can occur at any points along microtubule length (Mohan & John, 2015), the sites of intensive crosstalk occur at the growing ends of microtubules (Akhmanova & Steinmetz, 2015; Dogterom & Koenderink, 2019).

The growth of microtubules can also be directed by actin-based structures (Kaverina *et al*, 1998; Théry *et al*, 2006; López *et al*, 2014). They can force the alignment of microtubules (Elie *et al*, 2015), resist their progression (Burnette *et al*, 2007), capture, bundle or stabilize them (Zhou *et al*, 2002; Hutchins & Wray, 2014), submit them to mechanical forces (Gupton *et al*, 2002; Fakhri *et al*, 2014; Robison *et al*, 2016) or define the limits in space into which they are confined (Katrukha *et al*, 2017). The actin–microtubule interplay mostly takes place at the cell periphery, because most actin filaments are nucleated at and reorganized into actin-based structures near the plasma membrane (Blanchoin *et al*, 2014). We recently have identified a subset of actin filaments that form at the centrosome at the cell centre (Farina *et al*, 2016). The centrosome is the main microtubule nucleating and organizing centre of the cell and sustains the highest concentration of microtubules in the cell. Centrosomal actin filaments have been shown to be involved in several functions including centrosome anchoring to the nucleus (Obino *et al*, 2016), centrosome separation in mitosis (Au *et al*, 2017) and ciliary-vesicle transport in the early stages of ciliogenesis

1 CEA, CNRS, INRA, Biosciences & Biotechnology Institute of Grenoble, UMR5168, CytoMorpho Lab, Univ. Grenoble-Alpes, Grenoble, France

2 INSERM, U932 Immunité et Cancer, Institut Curie, PSL Research University, Paris, France

3 INSERM, CEA, Hôpital Saint Louis, Institut Universitaire d'Hématologie, UMR51160, CytoMorpho Lab, Univ. Paris Diderot, Paris, France

*Corresponding author. Tel: +33 4 38 78 32 90; E-mail: laurent.blanchoin@cea.fr

**Corresponding author. Tel: +33 1 56 24 64 27; E-mail: ana-maria.lennon@curie.fr

***Corresponding author. Tel: +33 1 71 20 70 44; E-mail: manuel.thery@cea.fr

‡These authors contributed equally to this work

†Present address: Pathogenesis of Vascular Infections Unit, INSERM, Institut Pasteur, Paris, France

(Wu *et al.*, 2018). Whether centrosomal actin filaments affect centrosomal microtubules is not yet known.

Here, we investigated how the processes of actin and microtubule growth at the centrosome influence each other. We provide *in vivo* and *in vitro* evidence that centrosomal actin network blocks microtubule growth, most likely as a result of physical hindrance. Our results further suggest that the regulation by centrosomal actin filaments restricts microtubule growth in response to cell adhesion.

Results

The centrosomal actin network appears to negatively regulate the microtubule network in B lymphocytes

B-lymphocyte polarization can be achieved by B-cell receptor (BCR) activation from binding surface-tethered cognate antigens and requires the local reduction of centrosomal actin density (Obino *et al.*, 2016). To evaluate how microtubules were affected in resting and activated B lymphocytes, we examined, by fluorescent microscopy of fixed cells, microtubule density throughout the cell in comparison with changes to the density of centrosomal actin filaments (Fig 1A). As expected, B-lymphocyte activation was associated with a lower density (by 30%) of actin at the centrosome (Obino *et al.*, 2016). It appeared to be also associated with a higher density (by 20%) of microtubules at the centrosome and in the entire cytoplasm (Fig 1B and C). A closer analysis by single cells showed a clear negative correlation between centrosomal actin density and microtubule density in resting ($r = -0.44$) and activated lymphocytes ($r = -0.34$) (Fig 1D), suggesting that the interplay between the two networks is not specific to the activation but an intrinsic relationship. Noteworthy, the amount of cortical actin did not vary during the activation (Fig EV1A), and the amount of cortical actin could not be correlated to the amount of microtubules in single cells (Fig EV1B and C), reinforcing the hypothesis of an early regulation at the centrosome. The labelling of actin filaments and microtubules in resting cells revealed the presence at the centrosome of dense actin puncta, from which microtubules were excluded, suggesting they act as a physical barrier through which microtubule cannot grow (Fig 1E).

To test the hypothesis that the density of centrosomal actin is driving the reduction in microtubule density, B lymphocytes were

treated with actin filament inhibitors (Fig 2A). Treatment with the actin polymerization inhibitors (Arp2/3 inhibitor CK666) or latrunculin A reduced the centrosomal actin density and increased the microtubule density at the centrosome (Fig 2B and C) and throughout the cell (Fig EV2A), thus supporting the hypothesis. Conversely, treatment with the formin inhibitor, SMFH2, increased centrosomal actin density, by an unknown mechanism possibly related to the actin homeostasis supporting Arp2/3-based nucleation of actin filament, notably at the centrosome (Farina *et al.*, 2016), when formin is inhibited (Suarez & Kovar, 2016). This increase in centrosomal actin led to a marginally decreased microtubule density at the centrosome and throughout the cell (Figs 2B and C, and EV2A), thus confirming the negative relationship between the two networks. Overall, the analysis of individual cells showed a negative correlation between centrosomal actin filaments and microtubules. The inhibition of formin and Arp2/3 induced higher and lower actin densities at the centrosome, respectively, and thus expanded the range in which the negative correlation could be observed (Fig 2D).

Noteworthy, local perturbations to the actin network could have affected other actin networks in the same cell by a process of actin-network homeostasis that operates throughout the cell (Burke *et al.*, 2014; Suarez *et al.*, 2014; Suarez & Kovar, 2016). Therefore, an increase in actin density at the centrosome could have been offset by a corresponding decrease in actin density elsewhere in the cell (e.g. in cytoplasmic and cortical networks). To evaluate this effect, we measured the impact of CK666 on the growth of microtubules at the centrosome and along the cortex by quantifying the dynamics of EB3-mCherry, which labelled microtubule plus ends (Fig 2E, Movie EV1). We found no major difference in the residency time of EB3 comets, and therefore in the microtubule growth, at the cortex (Fig 2F), suggesting that the changes in the cortical actin induced by Arp2/3 inhibition were not responsible for the overall increase in microtubule number. By contrast, treatment with CK666 significantly increased the number of microtubules growing out of the centrosome (Fig 2F), confirming the involvement of centrosomal actin in this regulation.

To assess more directly the role of centrosomal actin filaments, we next examined B lymphocytes which expressed a fusion protein (centrin1-VCA-GFP; Obino *et al.*, 2016) that promotes actin filament nucleation at the centrosome specifically (Fig 2G). Hence, the expression of centrin1-VCA-GFP strongly increased the density of centrosomal actin filaments and decreased the microtubule density

Figure 1. Cytoskeleton remodelling in B lymphocytes upon antigen stimulation.

- A IIA1.6 B lymphoma cells were stimulated with BCR-ligand⁻ (anti-IgM) or BCR-ligand⁺ (anti-IgG) beads for 60 min, fixed and stained for F-actin (top) and α -tubulin (bottom). Scale bar: 3 μ m.
- B Histograms show the quantifications of the polymerized tubulin and F-actin at the centrosome (dashed outline on the image, values correspond to the fraction of fluorescence in a 2-micron-wide area around the centrosome relative to the total fluorescence in the cell) and the total amount of polymerized tubulin (bottom right, values were normalized with respect to the mean of control condition). Measurements were pooled from three independent experiments; anti-IgM (BCR-ligand⁻): $n = 88$; anti-IgG (BCR-ligand⁺): $n = 93$. Error bars correspond to standard deviations. P values were calculated with Mann-Whitney test. Scale bar: 2 μ m.
- C Percentage differences of centrosomal F-actin and centrosomal microtubule fluorescence intensities in cells stimulated with BCR-ligand⁺ beads with respect to cells stimulated with BCR-ligand⁻ beads. The data set is identical to panel (B). Measurements were pooled from three independent experiments; anti-IgM (BCR-ligand⁻): $n = 88$; anti-IgG (BCR-ligand⁺): $n = 93$. Error bars correspond to standard deviations. P values were calculated with one-sample t -test (i.e. comparison to a theoretical mean of "0").
- D The graph shows the variations of the total amount of polymerized tubulin per cell with respect to the content of F-actin at the centrosome in an XY representation of individual measurements. The two lines correspond to linear regressions of the two sets of data relative to cells stimulated with BCR-ligand⁺ (activated cells) or BCR-ligand⁻ (resting cells) beads.
- E IIA1.6 B lymphoma cells were fixed and immuno-stained for F-actin (red) and α -tubulin (green). Images show the projection of maximal intensity of three confocal slices spaced by 0.5 μ m apart from the centrosome. Scale bars: 2 μ m (0.5 μ m in the zoomed insets).

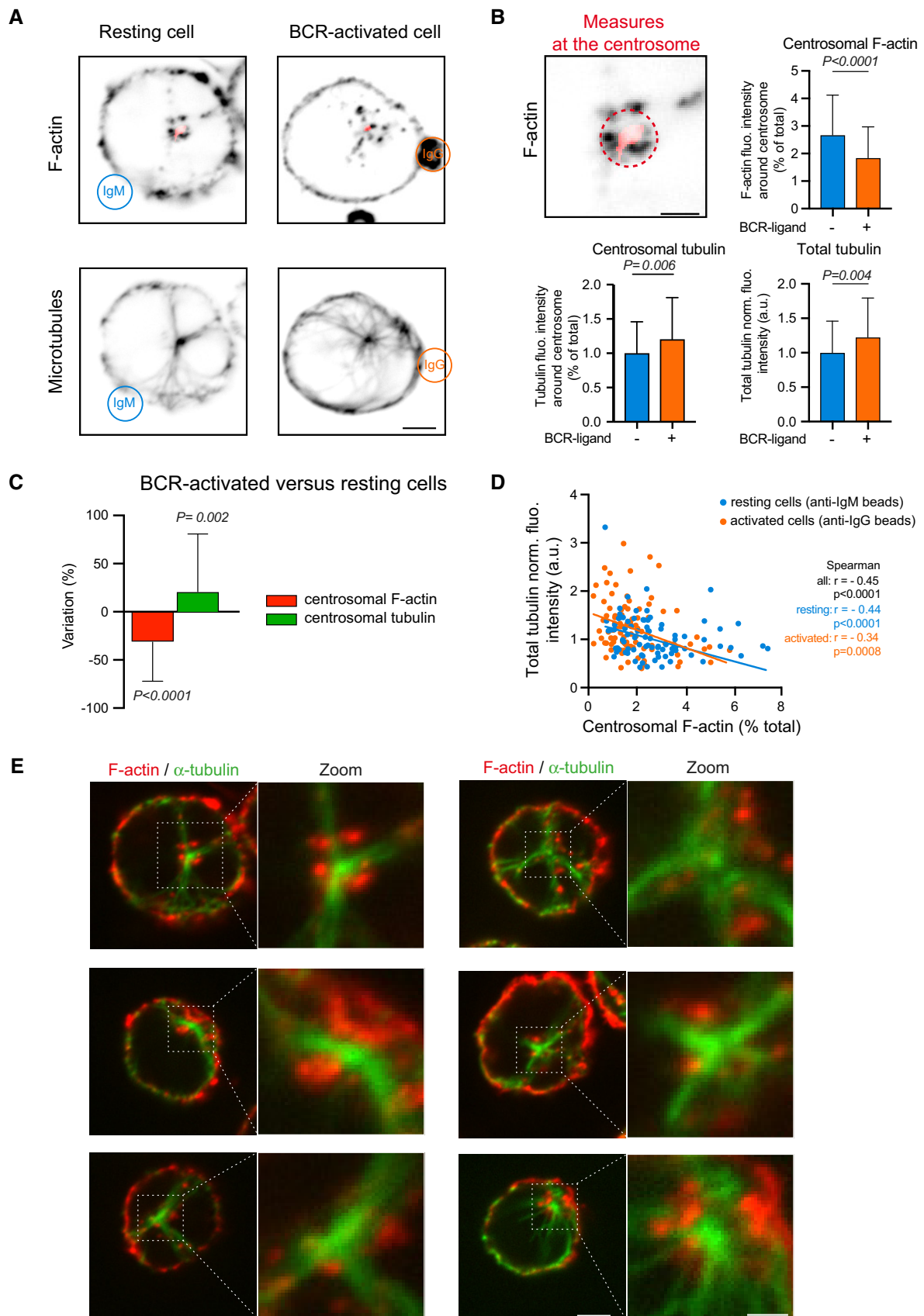


Figure 1.

at the centrosome and throughout the cell demonstrating the specific role of actin filaments at the centrosome in the negative regulation of the microtubule network (Figs 2H–J and EV2B).

The centrosomal actin network perturbs the elaboration of the microtubule network *in vitro*

A limitation to the interpretation of the B-lymphocyte experiments was that on top of the influence of subcellular actin networks on each other, actin and microtubule networks share numerous signalling pathways (Dogterom & Koenderink, 2019). It was therefore not possible to distinguish purely sterical effects at the centrosome from the modulation of cross-signalling pathways. To circumvent this limitation, we used an *in vitro* model that reconstituted actin and microtubule networks from actin monomers and tubulin dimers incubated in the presence of a centrosome labelled with centrin1-GFP. In this model and as expected (Farina *et al.*, 2016), 25% of the centrosomes (i.e. centrin1-GFP-positive puncta) were associated with actin and microtubule networks (Fig 3A). Among those centrosomes, the actin density per centrosome was negatively correlated with the number of microtubules per centrosome (Fig 3B). Actin filament density at the centrosome was then altered by incubating centrosomes in different concentrations of free actin monomers, with tubulin dimer concentration kept constant (Fig 3C). Consistent with the hypothesis, higher actin concentrations were associated with lower microtubule numbers per centrosome (Fig 3D). Moreover, the highest actin concentration almost completely inhibited microtubule growth (Fig 3D). These changes were not due to the interference of dense actin networks with microtubule growth rate, which did not seem to depend on the density of actin network (Fig 3E). They were neither due to the removal of microtubule nucleation complexes from the centrosome since the intensity of

gamma-tubulin staining appeared independent on the presence of actin filaments (Fig 3F). These results from *in vitro* experiments rather suggest that actin filaments perturb the early stages of microtubule elongation at the centrosome. Therefore, it is plausible that in B-lymphocyte experiments, the centrosomal actin network had direct and antagonistic effects on the microtubule network emanating from the centrosome.

To further explore the dynamics of the interaction between the centrosomal actin network and the microtubule network, the *in vitro* model was manipulated by sequential addition of the network components. By incubating with tubulin dimers first, microtubules formed in the absence of actin filaments (Fig 4A and B). When actin monomers were introduced afterwards (together with tubulin dimers to maintain the tubulin dimer concentration), the number of microtubules increased on all centrosomes, irrespective of whether centrosomes triggered the formation of actin filaments or not (Fig 4C). An explanation for this unexpected observation was that the addition of new tubulin dimers increased the effective concentration of free tubulins. Furthermore, not all centrosomes were capable of nucleating actin filaments, and there was no difference in the microtubule numbers per centrosome between those centrosomes with and those without actin filaments (Fig 4C). This suggested that in this model, the stability of preassembled microtubules may not be sensitive to actin filaments that form at the microtubule ends proximal to the centrosome, and newly assembled microtubules could form in spaces along pre-existing microtubules or in spaces created from depolymerized microtubules.

In a second experiment, tubulin dimers were initially added to quantify the number of microtubules per centrosome and, in effect, to select those centrosomes with the capability to nucleate microtubules. The tubulin dimers and microtubules were then removed

Figure 2. The impact of modulating centrosomal actin network on microtubules in B lymphocytes.

- A IIA1.6 B lymphoma cells were treated 45 min with indicated inhibitors (CK666 at 25 μ M, SMIFH2 at 25 μ M) or DMSO as control prior to being fixed and stained for α -tubulin (left column) and F-actin (right column). Scale bar: 3 μ m.
- B Histograms show the quantifications of the amount of polymerized tubulin (right, values were normalized with respect to the mean of control condition) and F-actin at the centrosome (left, values correspond to the fraction of fluorescence in a 2-micron-wide area around the centrosome relative to the total fluorescence in the cell). Measurements were pooled from three independent experiments; DMSO: $n = 91$, CK666: $n = 82$, SMIFH2: $n = 74$, latrunculin A: $n = 96$. Error bars correspond to standard deviations. P values were calculated with Mann–Whitney test.
- C Percentage differences of centrosomal F-actin and microtubule fluorescence intensities in cells treated with cytoskeleton inhibitors in comparison with the respective densities in cells treated with DMSO. Error bars represent standard deviations. P values were calculated with one-sample t -test (i.e. comparison to a theoretical mean of “0”).
- D The graph shows the same measurements as in panel (B) in an XY representation of individual measurements. The three lines correspond to linear regressions of the three sets of data relative to cells treated with each actin drug.
- E IIA1.6 B lymphoma cells were transfected to transiently express centrin1-GFP (red) and EB3-mCherry (green) and video-recorded at the contact site with the glass coverslip (left) and at the centrosome (right). Scale bar: 3 μ m.
- F The duration of EB3-positive comets' presence in the bottom plane was measured in DMSO- and CK666-treated cells (left). Error bars correspond to standard deviations. The number of EB3-positive comets exiting a 2- μ m-wide centrosomal area was also compared between the two conditions (right). In both cases, P values were calculated with Mann–Whitney test.
- G IIA1.6 B lymphoma cells were transfected to transiently express centrin1-VCA-GFP (bottom) or centrin1-GFP (top) as control prior to be fixed and stained for α -tubulin (left column) and F-actin (middle column). The GFP signal of centrin1 or centrin1-VCA is shown in the right column to illustrate the proper centrosome targeting. Scale bar: 3 μ m.
- H Histograms show the quantifications of the amount of polymerized tubulin (right) and F-actin at the centrosome (left). Values correspond to the fraction of fluorescence in a 2-micron-wide area around the centrosome relative to the total fluorescence in the cell. Measurements were pooled from three independent experiments; centrin1-GFP: $n = 88$, centrin1-VCA-GFP: $n = 87$. Error bars represent standard deviations. P values were calculated with Mann–Whitney test.
- I Percentage differences of F-actin and polymerized tubulin fluorescence intensities at the centrosome were compared in cells transfected either with centrin1-VCA-GFP or with centrin1-GFP. Error bars represent standard deviations. P values were calculated with one-sample t -test (i.e. comparison to a theoretical mean of “0”).
- J The graph shows the variations of the total amount of polymerized tubulin per cell with respect to the content of F-actin at the centrosome. The two lines correspond to linear regressions of the two sets of data relative to cells transfected with centrin1-VCA-GFP or centrin1-GFP.

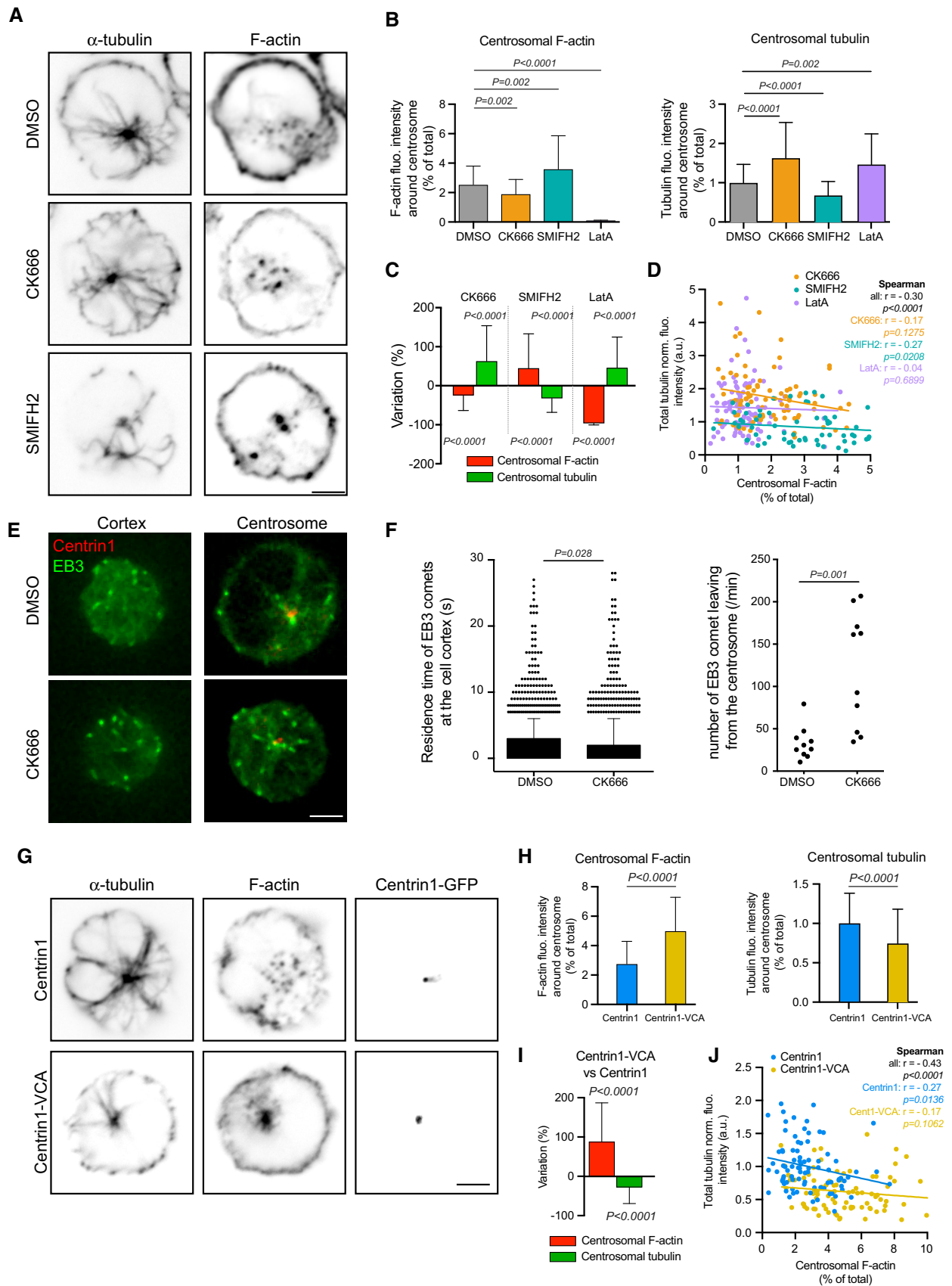


Figure 2.

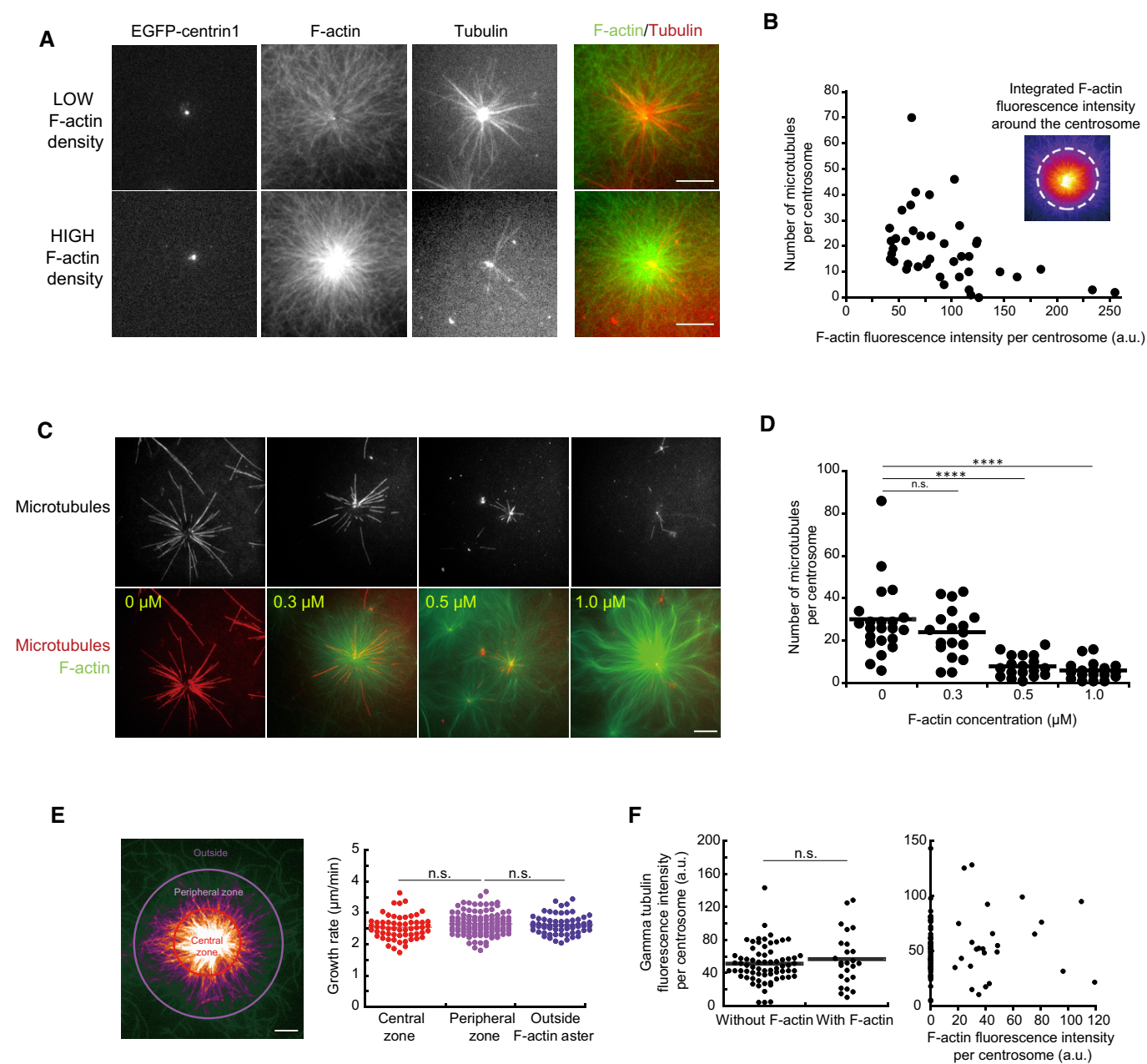


Figure 3. Assembly of microtubules and F-actin on isolated centrosomes.

- A Two sets of representative images showing fluorescent microtubules and F-actin assembled from isolated centrosomes. Centrosomes were isolated from Jurkat cells expressing centrin1-GFP. Upper and lower lines show F-actin and microtubules radiating from two distinct centrosomes with low (top) and high (bottom) densities of F-actin. Scale bars: 10 μm .
- B The graph shows the number of microtubules per centrosome relative to the density of actin filaments. Inset shows F-actin at the centrosome with a FIRE look-up table and a 20- μm -wide circle in which F-actin fluorescence intensity is measured. Measurements were pooled from five independent experiments; $n = 50$.
- C Microtubules (top line) and F-actin (bottom line) assembly from isolated centrosomes in the presence of increasing concentration of monomeric actin (from left to right). Scale bar: 20 μm .
- D The graph shows the number of microtubules per centrosome in response to increasing concentrations of monomeric actin. Data were pooled from two independent experiments; 0 μM : $n = 21$; 0.3 μM : $n = 17$; 0.5 μM : $n = 17$; 1.0 μM : $n = 17$. **** $P < 0.001$ Mann–Whitney test.
- E The image shows the density of F-actin (in the presence of 1 μM of actin monomers) at the centrosome colour-coded with the FIRE look-up table and the definition of central, peripheral and distal regions corresponding to decreasing concentrations of F-actin. Scale bar: 20 μm . The graph shows the measurements of microtubule growth rate in each region. Data were pooled from three independent experiments: central zone: $n = 58$, peripheral: $n = 104$, outside: $n = 61$; n.s. means no statistical difference between the data set according to Mann–Whitney test.
- F The graphs show the various intensities of centrosome immuno-staining with antibodies against gamma-tubulin on the same coverslip depending on the presence/absence of F-actin (left) or on the amount of F-actin (right). Data were pooled from three independent experiments. Left graph: without F-actin $n = 69$, with F-actin $n = 26$, right graph $n = 26$. n.s. means no statistical difference between the data set according to Mann–Whitney test.

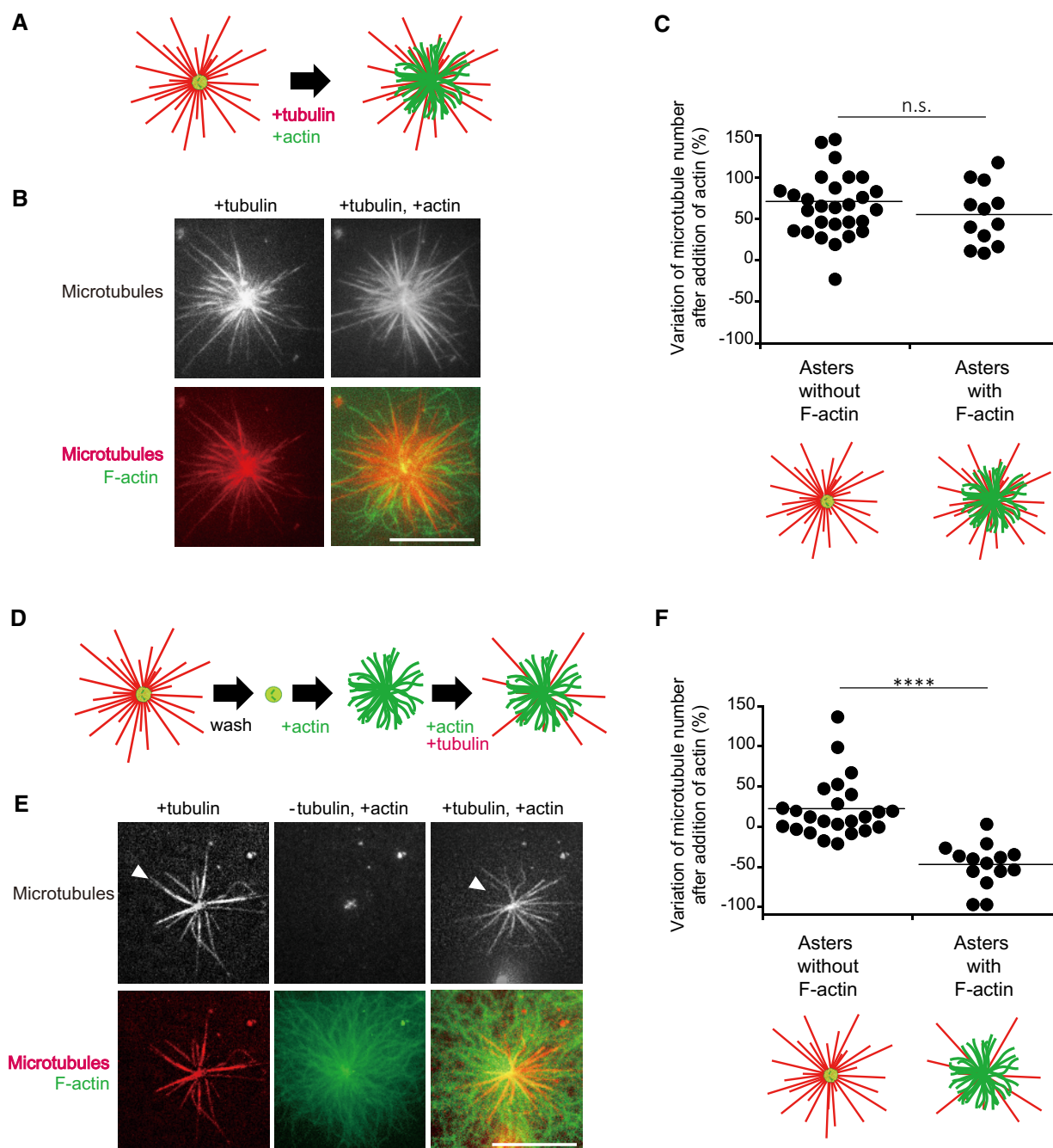


Figure 4. Blockage of microtubule growth by F-actin on isolated centrosomes.

- A Schematic illustration of the first dynamic assay: sequential addition of tubulin followed by tubulin and actin on isolated centrosomes.
- B Representative images showing microtubules (top line) and the merged images of F-actin and microtubules (bottom line) for the two steps of the assay; in the presence of tubulin only (left column) and in the presence of tubulin and actin (right column). Scale bar: 10 μm .
- C Quantification of the differences in the number of microtubules per centrosome between the two stages of the experiment described above on centrosomes capable (first condition), or not (second condition), to grow F-actin. Data were collected from a single experiment; asters without F-actin: $n = 29$; asters with F-actin: $n = 13$. Data were analysed using Mann–Whitney test.
- D Schematic illustration of the second dynamic assay: tubulin is added to measure centrosome nucleation capacity and washed out. Then, actin is added followed by actin and tubulin.
- E Representative images showing microtubules (top line) and the merged images of F-actin and microtubule (bottom line) during the three steps of the assay; in the presence of tubulin only (left column), in the absence of tubulin and presence of actin (middle column) and in the presence of tubulin and actin (right column). Scale bar: 10 μm . Arrowheads indicate microtubules unable to re-grow after assembly of F-actin.
- F Quantification of the differences in the number of microtubules per centrosome between the first and last steps of the experiment described above (panels D and E) on centrosomes capable (first condition), or not (second condition), to grow F-actin. Data were pooled from two independent experiments; asters without F-actin: $n = 24$; asters with F-actin: $n = 13$. **** $P < 0.001$ Student's t -test.

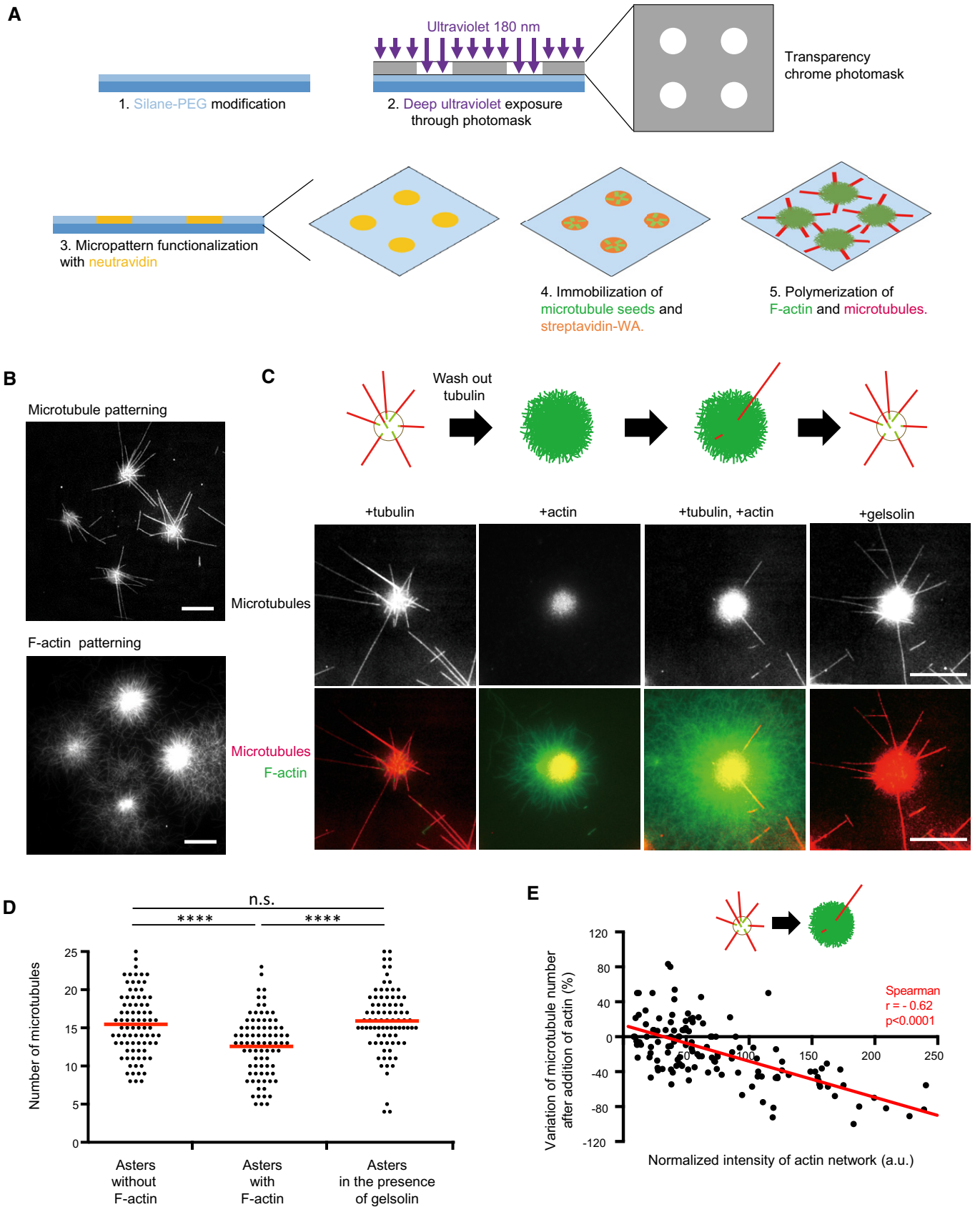


Figure 5.

Figure 5. Reconstitution of the interplay between F-actin and microtubules on micropatterns.

- A Schematic illustration of the micropatterning method used to graft microtubule seeds (green) via neutravidin (yellow) and F-actin-nucleation-promoting complexes (streptavidin-WA) (orange) on 8-micron-wide discoidal micropatterns. A glass coverslip (deep blue) coated with polyethyleneglycol (PEG) (light blue) was placed in contact with a transparency photomask and exposed to deep UV light. The exposed coverslip was then immersed with neutravidin to fix biotinylated microtubule seeds (green) on exposed regions. Streptavidin-WA was immobilized on microtubule seeds via their interaction with biotin. Tubulin dimers and actin monomers were then added to allow filaments elongation.
- B Representative images of microtubules (top) and F-actin (bottom) growth from micropatterns. Scale bars: 20 μm .
- C Schematic illustration of the assay on micropatterned substrate. Tubulin was first added alone to measure the nucleation capacity of each micropattern, and then washed out. Later on, actin was added followed by actin and tubulin. Finally, actin was rinsed out and gelsolin was added to fully disassemble F-actin. Representative images showing microtubules (top line) and the merged images of actin filaments and microtubules (bottom line) during the four steps of the assay; in the presence of tubulin only, in the absence of tubulin and presence of actin, in the presence of tubulin and actin, and finally in the presence of tubulin and gelsolin but in the absence of actin (from left to right). Scale bars: 10 μm .
- D Quantification of the number of microtubules per micropattern in the presence of tubulin only (left), actin and tubulin (middle) and tubulin only after actin filament disassembly (right). Data were pooled from 2 independent experiments; $n = 133$. **** $P < 0.001$ Student's *t*-test.
- E The graph shows the same measurements as in panel (D) in an XY representation of individual measurements. It illustrates the differences in the number of microtubules per micropattern between the first to the second step (tubulin only versus actin and tubulin together) with respect to the density of F-actin per micropattern.

by rinsing the centrosomes in buffer. Actin monomers were then added, followed by tubulin dimers again (Fig 4D–F). For those centrosomes devoid of actin filaments, the microtubule number was not significantly different between the initial and final stages of the experiment (Fig 4F). By contrast, for centrosomes which nucleated actin filaments, the microtubule number was significantly reduced at the final stage compared to the initial stage (Fig 4F). This effect was not due to actin filaments impact on the centrosome itself since the number of microtubules was not reduced if actin filaments were disassembled prior to microtubule regrowth (Fig EV3). These experiments confirmed that microtubule regrowth was impaired in the presence of pre-existing actin filaments.

Actin filaments block microtubule growth in a biochemical model

In the above *in vitro* model, only 25% of the isolated centrosomes had the capability of nucleating microtubules, reflecting the difficulties in centrosome purification. Despite the optimization steps to improve the quality of the centriole (Gogendeau *et al*, 2015), the isolation step results in centrosome with more or less fragmented peri-centriolar material. As a consequence, the investigation of their nucleation capacities was informative but intrinsically biased. Therefore, to directly test steric competition between actin and microtubules during the first stages of microtubule growth, we combined two distinct biochemical assays in which short microtubule seeds and actin nucleators were grafted onto the same microfabricated spot on a planar surface *in vitro* (Reymann *et al*, 2010; Portran *et al*, 2013) (Fig 5A).

In the biochemical model, the addition of free tubulin dimers and actin monomers led to the growth of both actin filaments and microtubules from each micropattern (Fig 5B). As with the *in vitro* model above, the micropatterns were treated according to the following sequence: addition of tubulin dimers and growth of microtubules; microtubule count; wash; addition of actin monomers and growth of actin filaments; addition of tubulin dimers and microtubule regrowth (Fig 5C). The model showed again that microtubule formation was perturbed by the presence of actin filaments (Fig 5D). Interestingly, the addition of gelsolin to promote the disassembly of actin filaments overcame the perturbation, indicating that the nucleation of actin filaments did not detach microtubule seeds (Fig EV4) but blocked their elongation (Fig 5C and D). Moreover, the relative density of actin

was negatively correlated with microtubule numbers (Fig 5E). Therefore, given the absence of signalling pathways or cross-linking proteins, the actin filaments physically blocked microtubule growth, and the denser the actin network, the stronger the barrier.

Actin filament density at the centrosome is negatively affected by the degree of cell spreading

The experiments above supported the model in which actin filaments perturb the formation of microtubules at the centrosome by forming a physical barrier. This led us to investigate how actin density at the centrosome is regulated in living cells. We have previously shown that with B lymphocyte forming an immune synapse with antigen-presenting cells, actin nucleation is decreased at the centrosome (Obino *et al*, 2016). Because immune synapses are enriched for actin and adhesion molecules such as integrins (Carrasco *et al*, 2004; Bretou *et al*, 2016), we hypothesized that the actin filament density at the centrosome is inversely related to the degree of cell adhesion and spreading because actin nucleating structures compete for available actin monomers in the cell (Suarez & Kovar, 2016). Hence, minimal cell spreading permits a high amount of actin filaments to form at the centrosome, thus perturbing microtubule growth, whereas extensive cell spreading sequesters most of the available actin monomers, reducing the number of actin filaments at the centrosome and thus favouring microtubule growth (Fig 6A).

For highly adherent RPE1 cells, three states of cell spreading (low, medium and high) were dictated by the degree of substrate adhesiveness (by tuning fibronectin concentration in PEG; Fig 6B). For low-adherent B lymphocytes, three states of cell adhesion and spreading were dictated by plating on poly-L-lysine, fibronectin and ICAM-1 (Carrasco *et al*, 2004) (Fig 6C). For both cell types, the degree of cell adhesion and/or spreading (i.e. the area occupied by the cell on the substrate) was negatively correlated with centrosomal actin density and positively correlated with the density of microtubules at the centrosome and throughout the cell (Fig 6D and E). Although these results do not indicate the exact mechanism by which cell spreading modulates the amount of microtubules, and notably do not exclude the possibility that microtubules were stabilized by contact with focal adhesions (Byron *et al*, 2015; Bouchet *et al*, 2016), they support a model in which microtubule growth from the centrosome is modulated by the adhesion state of the cell

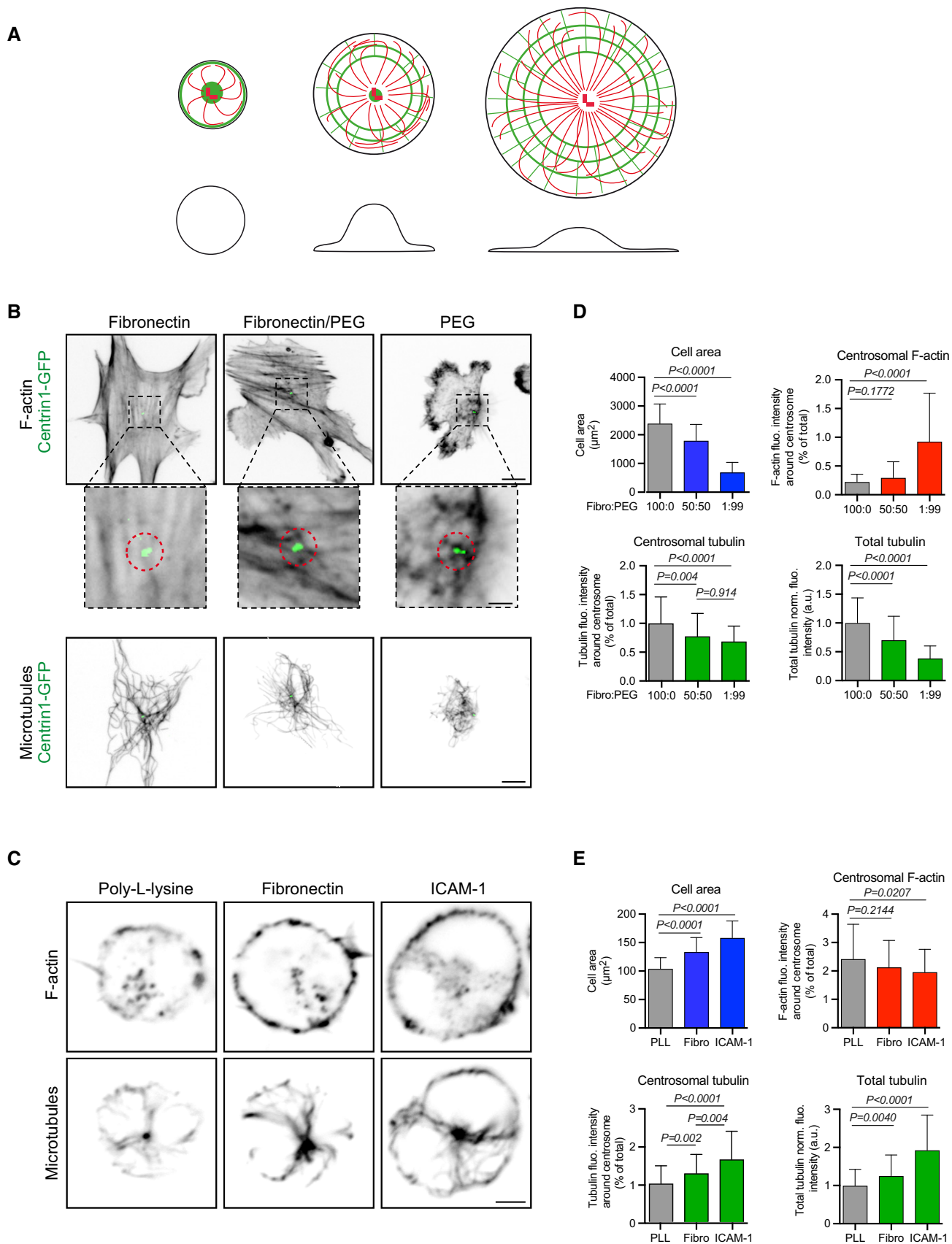


Figure 6.

Figure 6. Modulation of microtubule growth by cell spreading and centrosomal actin filaments.

- A Schematic illustration of our model according to which cell spreading sequesters monomeric actin to the cortex and thereby enables the centrosome to grow more microtubules. Drawings show top (top line) and side views (bottom line) of cells with increased spreading from left to right. Actin filaments are in green; microtubules are in red.
- B RPE1 cells stably expressing centrin1-GFP were plated for 3 h on coverslips coated with different ratios (100:0; 50:50 or 1:99) of fibronectin and PLL-PEG prior to fixation and staining for F-actin (top line and magnified views around centrosome below. Scale bars: 10 μm and 2 μm , respectively) and α -tubulin (bottom line. Scale bar: 10 μm).
- C IIA1.6 B lymphoma cells were plated for 60 min on poly-L-lysine, fibronectin or ICAM-1-coated cover slides prior to be fixed and stained for F-actin (top line) and α -tubulin (bottom line). Scale bar: 3 μm .
- D Quantification of the area occupied by RPE1 cells on the substrate (top left), F-actin content at the centrosome (top right), polymerized tubulin at the centrosome (bottom left) and in the entire cell (bottom right) for the three conditions of cell adhesion described in (B). Measurements came from three independent experiments with more than 60 analysed cells in each. Error bars represent standard deviations. F-actin and microtubule contents were compared using Mann–Whitney test, and variations of the cell area were compared using unpaired *t*-test.
- E Quantification of the area occupied by B lymphoma cells on the substrate (top left), F-actin content at the centrosome (top right), polymerized tubulin at the centrosome (bottom left) and in the entire cell (bottom right) for the three conditions of cell adhesion described in (D). Measurements came from three independent experiments with more than 80 analysed cells in each. Error bars represent standard deviations. F-actin and microtubule contents were compared using Mann–Whitney test, and variations of the cell area were compared using unpaired *t*-test.

via the degree to which actin filaments are prevented from forming at the centrosome.

Discussion

Actin is the most abundant protein in the cytoplasm and as such has long been considered as a major contaminant of centrosome proteomic studies (Bornens & Moudjou, 1999; Andersen *et al*, 2003). However, actin filaments have been directly observed at the poles of mitotic spindles (Stevenson *et al*, 2001; Chodagam *et al*, 2005) and at the centrosome of several cell types in interphase (Farina *et al*, 2016; Obino *et al*, 2016; Au *et al*, 2017). Centrosomal actin filaments have been shown to anchor the centrosome to the nucleus (Bornens, 1977; Burakov & Nadezhkina, 2013; Obino *et al*, 2016), support the transport of vesicles during ciliogenesis (Assis *et al*, 2017; Wu *et al*, 2018), connect basal bodies to the actin cortex in ciliated cells (Pan *et al*, 2007; Antoniadis *et al*, 2014; Walentek *et al*, 2016; Mahuzier *et al*, 2018) and power centrosome splitting in prophase (Uzbekov *et al*, 2002; Wang *et al*, 2008; Au *et al*, 2017).

The results of our study identify a new function for actin filaments at the centrosome. Noteworthy, in the lymphocytes we analysed, actin filaments formed dense clouds in close proximity to the centrosome, i.e. within a micrometre from the centre of the microtubule array, but did not seem to colocalize with the centrosome (Fig 1E), raising some doubts about the actual origin of these filaments. It is still unclear whether actin filaments were nucleated at the centrosome, which would be consistent with the localization of Arp2/3 at the centrosome (Farina *et al*, 2016) or at endosomes, where WASH also triggers actin filament assembly (Derivery *et al*, 2009), which were later gathered around the centrosome. Regardless of their actual origin, we propose a model in which these centrosomal, or peri-centrosomal, actin filaments provide a conduit through which changes to actin networks at the cell periphery modulate the formation and growth of microtubules emanating from the centrosome. The centrosomal actin filaments primarily perturb the formation of microtubules by physically blocking the early stages of their elongation. Although the actin networks adopted quite different architectures in cells and in reconstituted experiments *in vitro*, i.e. tiny clouds and radial array, respectively, in both

cases the density of the network blocked microtubule elongation. Although we cannot exclude that other mechanisms, such as shared signalling pathways or competition for common resources, support the negative impact of centrosomal actin filaments on microtubules in cells, we favoured the interpretation based on the role of physical constraints since they exist in cells and were proven to be capable to block microtubule growth in our *in vitro* assays. But these physical constraints may not be the only mechanism co-regulating the two networks at the centrosome. Noteworthy, these results add to pre-existing body of evidences showing that physical constraints imposed by actin filaments (Huber *et al*, 2015) can limit microtubule growth (Colin *et al*, 2018), microtubule's shape fluctuations (Brangwynne *et al*, 2006; Katrukha *et al*, 2017) and centrosome displacement (Piel *et al*, 2000). Interestingly, by contrast with previous descriptions of physical barriers blocking microtubule growth locally (Katrukha *et al*, 2017; Colin *et al*, 2018) our observations show that centrosomal actin filaments, by preventing microtubule growth at the organizing centre, affect the entire microtubule network throughout the cell.

Our results expand the description of cytoskeleton changes during B-lymphocyte activation (Obino *et al*, 2016) and show that centrosomal actin filament disassembly promotes the growth of microtubules. Interestingly, the increase in microtubules may contribute to B-cell polarization, a hallmark of their activation (Yuseff *et al*, 2011), by promoting centrosome off-centring. Indeed, a high quantity of microtubules can break network symmetry and force centrosome off-centring and its displacement to the cell periphery through the reorientation of pushing forces produced at the centrosome by microtubule growth (Letort *et al*, 2016; Burute *et al*, 2017; Pitaval *et al*, 2017). Therefore, centrosomal actin filament disassembly could be involved both in the disengagement of the centrosome from the nucleus (Obino *et al*, 2016) and in the stimulation and reorganization of microtubule-based pushing forces to drive centrosome motion towards the cell periphery.

The regulation of microtubule growth at the cell centre complements those mechanisms that regulate microtubule stability at the cell periphery, where microtubule stability is promoted by cell adhesions and their associated actin networks (Akhmanova & Steinmetz, 2015; Byron *et al*, 2015; Bouchet *et al*, 2016). Those mechanisms ensure a form of regulation that can bias microtubule network organization locally (Gundersen *et al*, 2004; Etienne-Manneville, 2013).

At the cell centre, the actin network can adapt the entire microtubule network to cell shape, cell adhesion and cell spreading (Fig 6A). An explanation for this is that cell adhesion and cell spreading trigger the elaboration of actin networks at the cortex, hence reducing the pool of available actin monomers, and potentially sequestering from the centrosome actin filament nucleation and branching factors such as Arp2/3 and WASH (Farina *et al*, 2016; Obino *et al*, 2016; Suarez & Kovar, 2016). The reduction in the centrosomal actin network thus allows more microtubules to be nucleated at the centrosome. The interplay at the centrosome between actin filaments and microtubules in response to cell spreading may have important implications for the ability of the cell to sense and adapt to external cues.

Materials and Methods

Cell culture and chemical treatments

Stable Jurkat cell lines expressing centrin1-GFP (Farina *et al*, 2016) were cultured in RPMI 1640 (Gibco). Cells were not sorted based on GFP fluorescence. The mouse B lymphoma cell line IIA1.6 (derived from the A20 cell line (American Type Culture Collection #: TIB-208)) was cultured as reported (Obino *et al*, 2016) in CLICK medium (RPMI 1640—GlutaMax-I), supplemented with 0.1% β -mercaptoethanol and 2% sodium pyruvate. The RPE1 cell line stably expressing centrin1-GFP (Farina *et al*, 2016) was cultured in DMEM/F-12. All media were supplemented with 10% foetal calf serum and penicillin/streptomycin. Cells were cultured at 37°C and 5% CO₂. All cell lines were tested monthly for mycoplasma contamination.

Two million IIA1.6 cells were electroporated with 2 μ g of EB3-mCherry plasmid and 2 μ g centrin1-GFP plasmid using the Amaxa Cell Line Nucleofector Kit R (T-016 programme, Lonza). Cells were incubated in CLICK medium for 8–12 h before analysis.

Cytoskeleton inhibitors (CK666 at 25 μ M, SMIFH2 at 25 μ M; Latrunculin A at 5 μ M; all from Tocris Bioscience) were added in the cell medium for 45 min at 37°C.

For the coating of glass coverslips, fibronectin (Sigma-Aldrich) was used at 10 μ g/ml and PLL-PEG (JenKem Technologies, Texas) at 10 μ g/ml in HEPES 10 mM, poly-L-Lysine (Invitrogen) was used at 10 μ g/ml, and ICAM-1 (R&D System) was used at 10 μ g/ml.

Preparation of BCR-ligand-coated beads

Latex NH₂-beads 3 μ m in diameter (Polyscience) were activated with 8% glutaraldehyde (Sigma-Aldrich) for 2 h at room temperature (4×10^7 beads/ml). Beads were washed with PBS and incubated overnight at 4°C with 100 μ g/ml of either F(ab')₂ goat anti-mouse IgG (BCR-ligand⁺ beads) or F(ab')₂ goat anti-mouse IgM (BCR-ligand⁻ beads; MP Biomedical).

Cell fixation and immuno-staining

Cells were extracted by incubation for 15 sec with cold cytoskeleton buffer (10 mM MES pH 6.1, 138 mM KCl, 3 mM MgCl₂, 2 mM EGTA) supplemented with 0.5% Triton X-100 and fixed with cytoskeleton buffer supplemented with 0.5% glutaraldehyde for 10 min at room

temperature. Glutaraldehyde was reduced with 0.1% sodium borohydride (NaBH₄) in 1 \times PBS for 7 min, and unspecific binding sites were saturated using a solution of 1 \times PBS supplemented with 2% BSA and 0.1% Triton X-100 for 10 min. The following primary antibodies were used: monoclonal rat anti- α -tubulin (AbD Serotec, Clone YL1/2, 1/1,000) and VHH anti-green fluorescent protein (GFP)-human Fc (Recombinant Antibodies Platform (TAB-IP), Institut Curie, Paris, France, 1/200). The following secondary antibodies were used: AlexaFluor647-conjugated F(ab')₂ donkey anti-rat and AlexaFluor488-conjugated donkey anti-human (Life Technologies, both 1/200). Actin filaments were stained using AlexaFluor546-conjugated phalloidin (Life Technologies, #A22283, 1/100).

Isolation of centrosomes

Centrosomes were isolated from Jurkat cells by modifying a previously published protocol (Moudjou & Bornens, 1998; Gogendeau *et al*, 2015). In brief, cells were treated with nocodazole (0.2 μ M) and cytochalasin D (1 μ g/ml) followed by hypotonic lysis. Centrosomes were collected by centrifugation onto a 60% sucrose cushion and further purified by centrifugation through a discontinuous (70, 50 and 40%) sucrose gradient. The composition of the sucrose solutions was based on a TicTac buffer (Farina *et al*, 2016), in which the activity of tubulin, actin and actin-binding proteins is maintained: 10 mM HEPES, 16 mM Pipes (pH 6.8), 50 mM KCl, 5 mM MgCl₂, 1 mM EGTA. The TicTac buffer was supplemented with 0.1% Triton X-100 and 0.1% β -mercaptoethanol. After centrifugation on the sucrose gradient, supernatant was removed until only about 5 ml remained in the bottom of the tube. Centrosomes were stored at -80°C after flash freezing in liquid nitrogen.

Protein expression and purification

Tubulin was purified from fresh bovine brain by three cycles of temperature-dependent assembly/disassembly in Brinkley Buffer 80 (BRB80 buffer: 80 mM Pipes pH 6.8, 1 mM EGTA and 1 mM MgCl₂) (Shelanski, 1973). Fluorescently labelled tubulins (ATTO-488- and ATTO-565-labelled tubulin) were prepared by following previously published method (Hyman *et al*, 1991).

Actin was purified from rabbit skeletal-muscle acetone powder. Monomeric Ca-ATP-actin was purified by gel-filtration chromatography on Sephacryl S-300 at 4°C in G buffer (2 mM Tris-HCl, pH 8.0, 0.2 mM ATP, 0.1 mM CaCl₂, 1 mM NaN₃ and 0.5 mM dithiothreitol (DTT)). Actin was labelled on lysines with Alexa-488 and Alexa-568. Recombinant human profilin, mouse capping protein, the Arp2/3 complex and GST-streptavidin-WA were purified in accordance with previous methods (Michelot *et al*, 2007; Achard *et al*, 2010).

In vitro assays with isolated centrosomes

Experiments were performed in polydimethylsiloxane (PDMS) stencils in order to add/exchange sequentially experimental solutions when needed. PDMS (Sylgard 184 kit, Dow Corning) was mixed with the curing agent (10:1 ratio), degassed, poured into a Petri dish to a thickness of 5 mm and cured for 2 h at 80°C on a hot plate. The PDMS layer was cut to square shape with dimension of 10 \times 10 mm and punched using a hole puncher (Ted Pella) with an outer

diameter of 6 mm. The PDMS chamber was oxidized in an oxygen plasma cleaner for 40 s at 60W (Femto, Diener Electronic) and brought it into contact with clean coverslip (24 × 30 mm) via a double-sided tape with 6-mm hole.

Isolated centrosomes were diluted in TicTac buffer and incubated for 20 min. To remove excess of centrosomes and coating the surface of coverslips, TicTac buffer supplemented with 1% BSA was perfused into the PDMS chamber, which was followed by a second rinsing step with TicTac buffer supplemented with 0.2% BSA and 0.25% w/v methylcellulose. Microtubules and actin assembly at the centrosome were induced using a reaction mixture containing tubulin dimers (labelled with ATTO-565, 18 μM final) and actin monomers (labelled with Alexa-488, 0.3–1.0 μM final) in TicTac buffer supplemented with 1 mM GTP and 2.7 mM ATP, 10 mM DTT, 20 μg/ml catalase, 3 mg/ml glucose, 100 μg/ml glucose oxidase and 0.25% w/v methylcellulose. In addition, a threefold molar equivalent of profilin to actin and 60 nM Arp2/3 complex were added in the reaction mixture.

Sequential microtubule and actin filament assembly experiments were carried out based on the aforementioned method. In brief, after assembling microtubules by adding tubulin in the reaction mixture (18 μM final) for 15 min, microtubules were removed by exchanging the reaction mixture with TicTac buffer supplemented with 0.2% BSA and 0.25% w/v methylcellulose. Subsequently, the reaction mixture of actin (1 μM final) with profilin and Arp2/3 was applied to assemble the actin aster. After 15-min incubation, the tubulin reaction mixture with actin, profilin and Arp2/3 complex was added to assemble both microtubules and actin asters together.

Micropatterning

Micropatterning of microtubules and actin filaments was performed in accordance with previously published methods with modification (Reymann *et al*, 2010; Portran *et al*, 2013). In brief, cleaned glass coverslips were oxidized with oxygen plasma (5 min, 60 W, Femto, Diener Electronic) and incubated with polyethyleneglycol silane (5 kDa, PLS-2011, Creative PEGWorks, 1 mg/ml in ethanol 96.5 and 0.02% of HCl) solution for overnight incubation. PEGylated coverslips were placed on a chromium quartz photomask (Toppan Photomasks, Corbeil, France) using a vacuum holder. The mask-covered coverslips were then exposed to deep ultraviolet light (180 nm, UVO Cleaner, Jelight Company, Irvine, CA) for 5 min. The PDMS open chamber was assembled as described above. Neutravidin (0.2 mg/ml in 1× HKEM [10 mM HEPES pH 7.5, 50 mM KCl, 5 mM MgCl₂, 1 mM EGTA]) was perfused in PDMS chamber and incubated for 15 min. The biotinylated microtubule seeds, which were prepared with 25% of fluorescent-dye-labelled tubulin and 75% biotinylated tubulin in presence of 0.5 mM of GMPCPP as previously described (Portran *et al*, 2013), were deposited on neutravidin-coated surface. Subsequently, 1 μM of streptavidin-WA in 1× HKEM was added into the PDMS chamber. After each step, the excess of unbound proteins was washed away using wash buffer. Microtubules and actin filaments were assembled according to the above protocol (see *In vitro assays*), except that 120 nM of Arp2/3 complex was used instead of 60 nM. To disassemble actin filaments on the micropatterns, gelsolin (1.6 μM, gift from Robert Robinson laboratory, IMCB, Singapore) was added into the reaction mixture at the last step of the experiment.

Imaging and analysis

Cell imaging was performed on an inverted spinning disc confocal microscope (Nikon) with a EMCCD QuantEM (Photometrics) camera. Z-stack images (0.5 μm spacing) of fixed cells were acquired with a 60× oil immersion objective (NA 1.4). Live cell images were acquired using ×100 oil immersion objective (NA 1.4) every second at the two planes (centrosome and cortex). Image processing was performed with Fiji (ImageJ) software. Centrosomal actin filaments were quantified as previously described (Obino *et al*, 2016). Briefly, after selecting manually the centrosome plane, we performed a background subtraction (rolling ball 50 px) on the z-projection (by calculation of pixel average intensity) of the three planes above and below the centrosome. The total fluorescence of centrosomal actin filaments was measured in a 1.6-μm-wide disc centred on the centrosome, and the total fluorescence of microtubules was measured in the entire cell.

The imaging of microtubules, actin filaments and centrosomes in the *in vitro* experiments was performed with a total internal reflection fluorescence (TIRF) microscope (Roper Scientific) equipped with an iLasPulsed system and an Evolve camera (EMCCD) using 60× Nikon Apo TIRF oil-immersion objective lens (N.A = 1.49). The microscope stage was maintained at 37°C by means of a temperature controller to obtain an optimal microtubule growth. Multi-stage time-lapse movies were acquired using Metamorph software (version 7.7.5, Universal Imaging). Actin-nucleation activity was quantified by measuring the actin filament fluorescence intensity integrated over a 20 μm diameter at the centre of the actin aster and normalized with respect to initial background intensity. The number of microtubules was manually counted from fluorescence microscopy images. All the measurements were done using Adobe Photoshop CC, and the corresponding graphs were produced using KaleidaGraph 4.0.

Statistics

For the *in vitro* experiments (Figs 3–5), statistical differences were identified using the unpaired *t*-test with Welch's correction and KaleidaGraph software. For the cellular studies (Figs 1, 2 and 6), statistical differences were computed using GraphPad Prism 7 Software. No statistical method was used to determine sample size. Kolmogorov–Smirnov test was used to assess normality of all data sets. The following tests were used to determine statistical significance: Figs 1B, 2B, F and H, 3D, 4C and 6C (actin and microtubules) and 6E (actin and microtubules): Mann–Whitney test; Figs 3E and F, 4A, 5D and 6C (cell area) and 6E (cell area): unpaired *t*-test; Figs 1C and 2C and I: one-sample *t*-test (comparison to a theoretical mean of zero, where zero represents no difference between conditions); Figs 1D, 2D and H, and 5E: Spearman's correlation test. Bar graphs describe the mean ± standard deviation.

Expanded View for this article is available online.

Acknowledgements

We acknowledge the Recombinant Antibodies Platform (TAB-IP) at Institut Curie, Paris, France for providing the VHH anti-GFP-human Fc antibody. We thank Pablo Saez (Institut Curie, France) for providing the EB3-mCherry plasmid and Robert Robinson (IMCB, Singapore) for providing the purified gelsolin.

DI was supported by a fellowship from the Uehara Memorial Foundation (Japan). DO was supported by a fellowship from the Fondation pour la Recherche Médicale (FDT20150532056). Funding was obtained from the Association Nationale pour la Recherche (ANR-PoLyBex-12-BSV3-0014-001 to A-ML-D and ANR-Mitotube-12-BSV5-0004-01 to MT) and the European Research Council (ERC-Strapacemi-GA 243103 to A-ML-D and ERC-SpiCy 310472 to MT).

Author contributions

DI performed all experiments in reconstituted systems. DO performed all experiments in living cells except those related to EB3 dynamics, which were performed by JP. FF performed preliminary experiments in reconstituted systems. JG and CG were involved in experiments in reconstituted systems. A-ML-D, LB and MT designed the project, obtained the funding to support it and supervised the work. MT wrote the manuscript. All authors reviewed/edited the manuscript.

Conflict of interest

The authors declare that they have no conflict of interest.

References

- Achard V, Martiel J-L, Michelot A, Guérin C, Reymann A-C, Blanchoin L, Boujemaa-Paterski R (2010) A “primer”-based mechanism underlies branched actin filament network formation and motility. *Curr Biol* 20: 423–428
- Akhmanova A, Steinmetz MO (2015) Control of microtubule organization and dynamics: two ends in the limelight. *Nat Rev Mol Cell Biol* 16: 711–726
- Andersen JS, Wilkinson CJ, Mayor T, Mortensen P, Nigg EA, Mann M (2003) Proteomic characterization of the human centrosome by protein correlation profiling. *Nature* 426: 570–574
- Antoniades I, Stylianou P, Skourides PA (2014) Making the connection: ciliary adhesion complexes anchor basal bodies to the actin cytoskeleton. *Dev Cell* 28: 70–80
- Assis LHP, Silva-Junior RMP, Dolce LG, Alborghetti MR, Honorato RV, Nascimento AFZ, Melo-Hanchuk TD, Trindade DM, Tonoli CCC, Santos CT, Oliveira PSL, Larson RE, Kobarg J, Espreafico EM, Giuseppe PO, Murakami MT (2017) The molecular motor Myosin Va interacts with the cilia-centrosomal protein RPGRIPL1. *Sci Rep* 7: 43692
- Au FK, Jia Y, Jiang K, Grigoriev I, Hau BKT, Shen Y, Du S, Akhmanova A, Qi RZ (2017) GAS2L1 is a centriole-associated protein required for centrosome dynamics and disjunction. *Dev Cell* 40: 81–94
- Blanchoin L, Boujemaa-Paterski R, Sykes C, Plastino J (2014) Actin dynamics, architecture, and mechanics in cell motility. *Physiol Rev* 94: 235–263
- Bornens M (1977) Is the centriole bound to the nuclear membrane? *Nature* 270: 80–82
- Bornens M, Moudjou M (1999) Studying the composition and function of centrosomes in vertebrates. *Methods Cell Biol* 61: 13–34
- Bouchet BP, Gough RE, Ammon Y-C, van de Willige D, Post H, Jacquemet G, Altaalar AFM, Heck AJR, Goult BT, Akhmanova A (2016) Talin-KANK1 interaction controls the recruitment of cortical microtubule stabilizing complexes to focal adhesions. *Elife* 5: e18124
- Brangwynne CP, MacKintosh FC, Kumar S, Geisse NA, Talbot J, Mahadevan L, Parker KK, Ingber DE, Weitz DA (2006) Microtubules can bear enhanced compressive loads in living cells because of lateral reinforcement. *J Cell Biol* 173: 733–741
- Bretou M, Kumari A, Malbec O, Moreau HD, Obino D, Pierobon P, Randrian V, Sáez PJ, Lennon-Duménil AM (2016) Dynamics of the membrane-cytoskeleton interface in MHC class II-restricted antigen presentation. *Immunol Rev* 272: 39–51
- Burakov AV, Nadezhdina ES (2013) Association of nucleus and centrosome: magnet or velcro?. *Cell Biol Int* 37: 95–104
- Burke TA, Christensen JR, Barone E, Suarez C, Sirotkin V, Kovar DR (2014) Homeostatic actin cytoskeleton networks are regulated by assembly factor competition for monomers. *Curr Biol* 24: 579–585
- Burnette DT, Schaefer AW, Ji L, Danuser G, Forscher P (2007) Filopodial actin bundles are not necessary for microtubule advance into the peripheral domain of Aplysia neuronal growth cones. *Nat Cell Biol* 9: 1360–1369
- Burute M, Prioux M, Blin G, Truchet S, Letort G, Tseng Q, Bessy T, Lowell S, Young J, Filhol O, Théry M (2017) Polarity reversal by centrosome repositioning primes cell scattering during epithelial-to-mesenchymal transition. *Dev Cell* 40: 168–184
- Byron A, Askari JA, Humphries JD, Jacquemet G, Koper EJ, Warwood S, Choi CK, Stroud MJ, Chen CS, Knight D, Humphries MJ (2015) A proteomic approach reveals integrin activation state-dependent control of microtubule cortical targeting. *Nat Commun* 6: 6135
- Carrasco YR, Fleire SJ, Cameron T, Dustin ML, Batista FD (2004) LFA-1/ICAM-1 interaction lowers the threshold of B cell activation by facilitating B cell adhesion and synapse formation. *Immunity* 20: 589–599
- Chodagani S, Royou A, Whitfield W, Karess R, Raff JW (2005) The centrosomal protein CP190 regulates myosin function during early *Drosophila* development. *Curr Biol* 15: 1308–1313
- Coles CH, Bradke F (2015) Coordinating neuronal actin-microtubule dynamics. *Curr Biol* 25: R677–R691
- Colin A, Singaravelu P, Théry M, Blanchoin L, Gueroui Z (2018) Actin-network architecture regulates microtubule dynamics. *Curr Biol* 28: 2647–2655.e4
- Derivery E, Sousa C, Gautier JJ, Lombard B, Loew D, Gautreau A (2009) The Arp2/3 activator WASH controls the fission of endosomes through a large multiprotein complex. *Dev Cell* 17: 712–723
- Dogterom M, Koenderink GH (2019) Actin-microtubule crosstalk in cell biology. *Nat Rev Mol Cell Biol* 20: 38–54
- Elie A, Prezel E, Guérin C, Denarier E, Ramirez-Rios S, Serre L, Andrieux A, Fourest-Lieuvain A, Blanchoin L, Arnal I (2015) Tau co-organizes dynamic microtubule and actin networks. *Sci Rep* 5: 9964
- Etienne-Manneville S (2013) Microtubules in cell migration. *Annu Rev Cell Dev Biol* 29: 471–499
- Fakhri N, Wessel AD, Willms C, Pasquali M, Klopfenstein DR, MacKintosh FC, Schmidt CF (2014) High-resolution mapping of intracellular fluctuations using carbon nanotubes. *Science* 344: 1031–1035
- Farina F, Gaillard J, Guérin C, Couté Y, Sillibourne J, Blanchoin L, Théry M (2016) The centrosome is an actin-organizing centre. *Nat Cell Biol* 18: 65–75
- de Forges H, Bouissou A, Perez F (2012) Interplay between microtubule dynamics and intracellular organization. *Int J Biochem Cell Biol* 44: 266–274
- Gogondeau D, Guichard P, Tassin AM (2015) Purification of centrosomes from mammalian cell lines. *Methods Cell Biol* 129: 171–189
- Gundersen GG, Gomes ER, Wen Y (2004) Cortical control of microtubule stability and polarization. *Curr Opin Cell Biol* 16: 106–112
- Gupton SL, Salmon WC, Waterman-Storer CM (2002) Converging populations of f-actin promote breakage of associated microtubules to spatially regulate microtubule turnover in migrating cells. *Curr Biol* 12: 1891–1899
- Huber F, Boire A, López MP, Koenderink GH (2015) Cytoskeletal crosstalk: when three different personalities team up. *Curr Opin Cell Biol* 32: 39–47

- Hutchins BI, Wray S (2014) Capture of microtubule plus-ends at the actin cortex promotes axophilic neuronal migration by enhancing microtubule tension in the leading process. *Front Cell Neurosci* 8: 1–8
- Hyman A, Drechsel D, Kellogg D, Salser S, Sawin K, Steffen P, Wordeman L, Mitchison TJ (1991) Preparation of modified tubulins. *Methods Enzymol* 196: 478–485
- Katrakha EA, Mikhaylova M, van Brakel HX, van Bergen en Henegouwen PM, Akhmanova A, Hoogenraad CC, Kapitein LC (2017) Probing cytoskeletal modulation of passive and active intracellular dynamics using nanobody-functionalized quantum dots. *Nat Commun* 8: 14772
- Kaverina I, Rottner K, Small JV (1998) Targeting, capture, and stabilization of microtubules at early focal adhesions. *J Cell Biol* 142: 181–190
- Letort G, Nedelec F, Blanchoin L, Théry M (2016) Centrosome centering and decentering by microtubule network rearrangement. *Mol Biol Cell* 27: 2833–2843
- López MP, Huber F, Grigoriev I, Steinmetz MO, Akhmanova A, Koenderink GH, Dogterom M (2014) Actin-microtubule coordination at growing microtubule ends. *Nat Commun* 5: 4778
- Mahuzier A, Shihavuddin A, Fournier C, Lansade P, Faucourt M, Menezes N, Meunier A, Garfa-Traoré M, Carlier M-F, Voituriez R, Genovesio A, Spassky N, Delgehr N (2018) Ependymal cilia beating induces an actin network to protect centrioles against shear stress. *Nat Commun* 9: 2279–2294
- Michelot A, Berro J, Guérin C, Boujemaa-Paterski R, Staiger CJ, Martiel J-L, Blanchoin L (2007) Actin-filament stochastic dynamics mediated by ADF/cofilin. *Curr Biol* 17: 825–833
- Mimori-Kiyosue Y (2011) Shaping microtubules into diverse patterns: molecular connections for setting up both ends. *Cytoskeleton* 68: 603–618
- Mohan R, John A (2015) Microtubule-associated proteins as direct crosslinkers of actin filaments and microtubules. *IUBMB Life* 67: 395–403
- Moudjou M, Bornens M (1998) Method of centrosome isolation from cultured animal cells. In *Cell biology: a laboratory handbook*, Celis J (ed.), pp 111–119. San Diego, CA: Academic Press
- Obino D, Farina F, Malbec O, Sàez PJ, Maurin M, Gaillard J, Dingli F, Loew D, Gautreau A, Yuseff M-I, Blanchoin L, Théry M, Lennon-Duménil A-M (2016) Actin nucleation at the centrosome controls lymphocyte polarity. *Nat Commun* 7: 10969
- Pan J, You Y, Huang T, Brody SL (2007) RhoA-mediated apical actin enrichment is required for ciliogenesis and promoted by Foxj1. *J Cell Sci* 120: 1868–1876
- Piel M, Meyer P, Khodjakov A, Rieder CL, Bornens M (2000) The respective contributions of the mother and daughter centrioles to centrosome activity and behavior in vertebrate cells. *Cell* 101: 317–329
- Pitaval A, Senger F, Letort G, Gidrol X, Guyon L, Sillibourne J, Théry M (2017) Microtubule stabilization drives 3D centrosome migration to initiate primary ciliogenesis. *J Cell Biol* 216: 3713–3728
- Portran D, Gaillard J, Vantard M, Théry M (2013) Quantification of MAP and molecular motor activities on geometrically controlled microtubule networks. *Cytoskeleton* 70: 12–23
- Reymann A, Martiel J, Cambier T, Blanchoin L, Boujemaa-Paterski R, Théry M (2010) Nucleation geometry governs ordered actin networks structures. *Nat Mater* 9: 827–832
- Robison P, Caporizzo MA, Ahmadzadeh H, Bogush AI, Chen CY, Margulies KB, Shenoy VB, Prosser BL (2016) Detyrosinated microtubules buckle and bear load in contracting cardiomyocytes. *Science* 352: aaf0659
- Rodriguez OC, Schaefer AW, Mandato CA, Forscher P, Bement WM, Waterman-storer CM (2003) Conserved microtubule–actin interactions in cell movement and morphogenesis. *Nat Cell Biol* 5: 599–609
- Roostalu J, Surrey T (2017) Microtubule nucleation: beyond the template. *Nat Rev Mol Cell Biol* 18: 702–710
- Sanchez AD, Feldman JL (2017) Microtubule-organizing centers: from the centrosome to non-centrosomal sites. *Curr Opin Cell Biol* 44: 93–101
- Shelanski M (1973) Chemistry of the filaments and tubules of brain. *J Histochem Cytochem* 21: 529–539
- Stevenson VA, Kramer J, Kuhn J, Theurkauf WE (2001) Centrosomes and the Scrambled protein coordinate microtubule-independent actin reorganization. *Nat Cell Biol* 3: 68–75
- Suarez C, Carroll RT, Burke TA, Christensen JR, Bestul AJ, Sees JA, James ML, Sirotkin V, Kovar DR (2014) Profilin regulates F-actin network homeostasis by favoring formin over Arp2/3 complex. *Dev Cell* 32: 43–53
- Suarez C, Kovar DR (2016) Internetwork competition for monomers governs actin cytoskeleton organization. *Nat Rev Mol Cell Biol* 17: 799–810
- Théry M, Racine V, Piel M, Pépin A, Dimitrov A, Chen Y, Sibarita J-B, Bornens M (2006) Anisotropy of cell adhesive microenvironment governs cell internal organization and orientation of polarity. *Proc Natl Acad Sci USA* 103: 19771–19776
- Uzbekov R, Kireyev I, Prigent C (2002) Centrosome separation: respective role of microtubules and actin filaments. *Bilo Cell* 94: 275–288
- Walentek P, Quigley IK, Sun DI, Sajjan UK, Kintner C, Harland RM (2016) Ciliary transcription factors and miRNAs precisely regulate Cp110 levels required for ciliary adhesions and ciliogenesis. *Elife* 5: e17557
- Wang W, Chen L, Ding Y, Jin J, Liao K (2008) Centrosome separation driven by actin-microfilaments during mitosis is mediated by centrosome-associated tyrosine-phosphorylated cortactin. *J Cell Sci* 121: 1334–1343
- Wieczorek M, Bechstedt S, Chaaban S, Brouhard GJ (2015) Microtubule-associated proteins control the kinetics of microtubule nucleation. *Nat Cell Biol* 17: 907–916
- Wu C-T, Chen H-Y, Tang TK (2018) Myosin-Va is required for preciliary vesicle transportation to the mother centriole during ciliogenesis. *Nat Cell Biol* 20: 175–185
- Yuseff MI, Reversat A, Lankar D, Diaz J, Fanget I, Pierobon P, Randrian V, Larochette N, Vascotto F, Desdouets C, Jauffred B, Bellaïche Y, Gasman S, Darchen F, Desnos C, Lennon-Duménil AM (2011) Polarized secretion of lysosomes at the B cell synapse couples antigen extraction to processing and presentation. *Immunity* 35: 361–374
- Zhou FQ, Waterman-Storer CM, Cohan CS (2002) Focal loss of actin bundles causes microtubule redistribution and growth cone turning. *J Cell Biol* 157: 839–849

C.2 Collaborative Research article 2

IMMUNOLOGY

Diacylglycerol kinase ζ promotes actin cytoskeleton remodeling and mechanical forces at the B cell immune synapse

Sara V. Merino-Cortés¹, Sofia R. Gardeta¹, Sara Roman-García¹, Ana Martínez-Riaño², Judith Pineau^{3,4}, Rosa Liebana¹, Isabel Merida¹, Ana-Maria Lennon Dumenil³, Paolo Pierobon³, Julien Husson⁵, Balbino Alarcon², Yolanda R. Carrasco^{1*}

Copyright © 2020
The Authors, some
rights reserved;
exclusive licensee
American Association
for the Advancement
of Science. No claim
to original U.S.
Government Works

Diacylglycerol kinases (DGKs) limit antigen receptor signaling in immune cells by consuming the second messenger diacylglycerol (DAG) to generate phosphatidic acid (PA). Here, we showed that DGK ζ promotes lymphocyte function-associated antigen 1 (LFA-1)-mediated adhesion and F-actin generation at the immune synapse of B cells with antigen-presenting cells (APCs), mostly in a PA-dependent manner. Measurement of single-cell mechanical force generation indicated that DGK ζ -deficient B cells exerted lower forces at the immune synapse than did wild-type B cells. Nonmuscle myosin activation and translocation of the microtubule-organizing center (MTOC) to the immune synapse were also impaired in DGK ζ -deficient B cells. These functional defects correlated with the decreased ability of B cells to present antigen and activate T cells in vitro. The in vivo germinal center response of DGK ζ -deficient B cells was also reduced compared with that of wild-type B cells, indicating that loss of DGK ζ in B cells impaired T cell help. Together, our data suggest that DGK ζ shapes B cell responses by regulating actin remodeling, force generation, and antigen uptake-related events at the immune synapse. Hence, an appropriate balance in the amounts of DAG and PA is required for optimal B cell function.

INTRODUCTION

Diacylglycerol kinases (DGKs) convert the lipid diacylglycerol (DAG) into phosphatidic acid (PA), shaping the pools of both second messengers. There are 10 mammalian DGK isoforms, which are classified into five subgroups based on their distinct regulatory domains. DGKs are soluble enzymes that translocate to specific cellular locations to regulate the relative amounts of DAG and PA (1, 2). Enrichment of DAG or PA at the plasma membrane supports the localized recruitment of effector proteins. DAG-dependent effectors include conventional protein kinase C (PKC), PKD, and Ras guanyl nucleotide-releasing protein (RasGRP), which drive the activation of nuclear factor κ B (NF- κ B) and extracellular signal-regulated kinase 1 and 2 (ERK1/2) signaling cascades and subsequent gene expression. PA acts as a lipid anchor for distinct effectors through the binding of its negatively charged region to cationic regions on those proteins. PA-binding proteins, such as the Rac activator/dedicator of cytokinesis protein 1 (DOCK1), Rho GDP-dissociation inhibitor (RhoGDI), atypical PKC ζ , and partitioning defective protein 3 (Par3), are involved in cytoskeletal remodeling and cell polarity (1, 2).

In immune cells, DGKs are well known for limiting the intensity of DAG-regulated signals downstream of antigen receptor stimulation. DGK α and DGK ζ are the most studied isoforms, both of which are expressed in B and T cells (1, 3). Recognition by lymphocytes of antigen on the surface of antigen-presenting cells (APCs) triggers the formation of the immune synapse at the interface between the lymphocyte and the APC. Establishment of the immune synapse

requires actin cytoskeletal remodeling and protein segregation into two concentric regions: the central supramolecular activation cluster (cSMAC), which is characterized by the central accumulation of antigen-bound antigen receptors together with certain signaling molecules, and the peripheral ring-shaped domain [peripheral SMAC (pSMAC)], which is enriched in the integrin lymphocyte function-associated antigen 1 (LFA-1) [bound to its ligand intercellular adhesion molecule-1 (ICAM-1)], filamentous actin (F-actin), and other proteins involved in adhesion and cytoskeletal rearrangements, including vinculin, talin, and Wiskott-Aldrich syndrome protein (WASP) (4–7). In T cells, phospholipase C- γ (PLC- γ) generates a localized DAG pool at the immune synapse to trigger downstream signaling (8). Both DGK α and DGK ζ translocate to the immune synapse to regulate DAG abundance, thus decreasing the intensity of T cell receptor (TCR) signaling (9, 10). DGK ζ -deficient B cells show enhanced activation of the Ras-ERK1/2 pathway after stimulation of the B cell receptor (BCR), leading to increased B cell responses (3).

In nonimmune cells, DGKs participate in actin cytoskeletal rearrangements, cell polarity, and integrin recycling. DGK α -mediated PA generation at the plasma membrane recruits PKC ζ , which phosphorylates RhoGDI. This promotes the release and activation of Rac1 and, thus, actin polymerization for the generation of invasive protrusions by epithelial cells (11). Similarly, DGK ζ -produced PA facilitates Rac1 activation through the p21-activated kinase 1 (PAK1)-mediated phosphorylation of RhoGDI in neuronal and skeletal muscle cells (12, 13). PA generation by DGKs stimulates integrin recycling and tumor invasiveness through a Rab11-dependent pathway (14). PA also targets phosphatidylinositol-4-phosphate 5-kinase I (PIP5KI), promoting its lipid kinase activity to produce phosphatidylinositol-4,5-bisphosphate (PIP₂) at the plasma membrane (15, 16); PIP₂ is a substrate for PLC- γ and phosphatidylinositol 3-kinase (PI3K), and promotes adhesion and actin dynamics (17). Actomyosin reorganization, integrin clustering, and polarized membrane trafficking all occur at the immune synapse. DGKs are linked to T cell polarization

¹Department of Immunology and Oncology, Centro Nacional de Biotecnología (CNB)-CSIC, Madrid, Spain. ²Department of Cell Biology and Immunology, Centro de Biología Molecular Severo Ochoa (CBMSO), CSIC-UAM, Madrid, Spain. ³Institut Curie, PSL Research University, INSERM U932, Paris, France. ⁴Université de Paris, 75006, Paris, France. ⁵Laboratoire d'Hydrodynamique (LadHyx), Ecole polytechnique, CNRS, Institut Polytechnique de Paris, Paris, France.

*Corresponding author. Email: ycarrasco@cnb.csic.es

events because microtubule-organizing center (MTOC) translocation and polarized secretion at the immune synapse are impaired in the absence of DGK α or DGK ζ (18, 19). Nonetheless, PA-related DGK functions at the immune synapse are largely unknown.

Here, we investigated the roles of DGKs in the assembly of the B cell immune synapse. We used primary mouse B cells deficient in DGK ζ (DGK $\zeta^{-/-}$) or DGK α (DGK $\alpha^{-/-}$) or treated with a DGK inhibitor. In addition, we used a B cell line overexpressing green fluorescent protein (GFP)-tagged DGK ζ constructs. We found that DGK ζ promoted LFA-1-mediated adhesion and F-actin accumulation at the immune synapse mainly through PA generation and that the DOCK2 and PAK1 regulation of Rac activity was also involved. Furthermore, we used traction force microscopy (TFM) and micropipette force probe (MFP) technique to study single-cell force generation at the immune synapse (20, 21). We detected decreased mechanical forces for DGK $\zeta^{-/-}$ B cells and inhibitor-treated B cells. Forces are critical to acquire antigen at the B cell immune synapse (22). These results, together with the finding of impaired myosin activation and MTOC translocation to the immune synapse, correlated with the diminished ability of DGK ζ -defective B cells to extract antigen and present it to T cells in vitro. In immunocompetent mice, DGK $\zeta^{-/-}$ B cells exhibited reduced germinal center (GC) responses compared with those of wild-type (WT) B cells. Our data suggest pivotal functions for DGK ζ in cytoskeletal remodeling, mechanical force generation, and antigen uptake at the immune synapse to determine B cell responses.

RESULTS

DGK ζ stimulates LFA-1-mediated adhesion and F-actin accumulation at the B cell immune synapse

We first analyzed the relative amounts of DGK α and DGK ζ in B cells by Western blotting. Both isoforms were detected in WT B cells (fig. S1A), which is consistent with previous findings at the RNA level (3). Treatment with the DGK inhibitor R59949 (R59) had no substantial effect on the abundance of either DGK (fig. S1A). We investigated the ability of DGK $\zeta^{-/-}$, DGK $\alpha^{-/-}$, or R59-treated B cells to trigger immune synapse formation and maturation compared with that of WT B cells. For inhibitor experiments, the B cells were pretreated with 10 μ M R59 for 30 min at 37°C and washed before use. We used artificial planar lipid bilayers that contained the glycosylphosphatidylinositol (GPI)-linked adhesion molecule ICAM-1, various densities of tethered surrogate antigen [su-Ag; anti- κ LC antibody (Ab)], and were coated with the chemokine CXCL13. This system mimics an APC surface and was used to evaluate immune synapse formation by confocal microscopy (4). Splenic B cells were isolated by negative selection (<90% CD19⁺). WT and DGK $\zeta^{-/-}$ B cells showed similar cell surface amounts of immunoglobulin M (IgM) and IgD, whereas DGK $\alpha^{-/-}$ B cells displayed slightly increased amounts of IgM (fig. S1, B and C). B cells were left in contact with the lipid bilayer for 10 min at 37°C and then were imaged. The frequency of B cells that formed an immune synapse was analyzed on the basis of two criteria: the formation of a central su-Ag cluster (cSMAC) and of a cell contact with the substrate (immune synapse contact area), which were estimated by su-Ag-associated fluorescence and by interference reflection microscopy (IRM), respectively. At a density of su-Ag of 20 molecules/ μ m², we found a small increase in the percentage of DGK $\zeta^{-/-}$ B cells that formed an immune synapse compared with controls (Fig. 1, A and B). R59-treated B cells showed

a similar tendency (Fig. 1, A and B). In immune synapse-forming B cells, contact areas (estimated by IRM) were statistically significantly reduced in DGK $\zeta^{-/-}$ and R59-treated B cells compared with those for WT B cells (Fig. 1, C and D). In contrast, the area and the total quantity of su-Ag accumulated at the immune synapse (both estimated by fluorescence) were comparable between DGK $\zeta^{-/-}$, R59-treated, and WT B cells (Fig. 1, C and D). Similar results were obtained when lower su-Ag densities were used at the lipid bilayer (fig. S1, D to I).

Because the contact area is the sum of the su-Ag central cluster area (cSMAC) and the surrounding region of LFA-1 interactions with ICAM-1 (pSMAC), these data imply that impaired DGK ζ function caused pSMAC defects. We analyzed other pSMAC features, namely, vinculin and F-actin content, at the lipid bilayers by immunofluorescence. DGK $\zeta^{-/-}$ B cells had less vinculin and F-actin at the pSMAC than did controls for the su-Ag densities tested, and the reductions were greater for R59-treated B cells (Fig. 1, E to H). In contrast, DGK $\alpha^{-/-}$ B cells showed unimpaired immune synapse formation (pSMAC/cSMAC; vinculin/F-actin content) (fig. S2). We then centered our study on the DGK ζ isoform. Lack of DGK ζ did not affect the abundance of DGK α protein (fig. S1A). We also determined that a su-Ag density of 20 molecules/ μ m² was optimal for immune synapse formation, so this concentration was used going forward.

We set out to study the effect of an excess of DGK ζ activity on immune synapse formation. A20 B cells were transiently transfected with plasmids encoding GFP-tagged DGK ζ -WT or a kinase-deficient mutant (DGK ζ -KD). GFP-expressing and nontransfected (GFP^{neg}) A20 cells were included as controls (fig. S3A). Using the aforementioned experimental approach, we found that the percentage of cells expressing either DGK ζ construct that formed an immune synapse was decreased (fig. S3, B and C). Whereas the immune synapse contact areas were larger in the DGK-overexpressing cells, there were no differences in su-Ag cluster area or the total quantity of su-Ag (fig. S3, D and E). By immunofluorescence microscopy, we detected a statistically increased amount of F-actin at the pSMAC of A20 B cells overexpressing DGK ζ -WT but not at the pSMAC of cells expressing DGK ζ -KD (fig. S3F). For vinculin, we observed increased frequency of A20 cells overexpressing either DGK ζ -WT or DGK ζ -KD with a well-formed ring as well as increased vinculin abundance (fig. S3G). These data, thus, suggest a role for DGK ζ in mediating LFA-1-mediated adhesion, vinculin recruitment, and increased F-actin content at the B cell immune synapse.

DGK ζ -derived PA shapes LFA-1-mediated adhesion and the DOCK2-Rac-F-actin pathway at the B cell immune synapse

We next investigated whether an excess of PA could rescue the defects in LFA-1-mediated adhesion and F-actin abundance caused by impaired DGK ζ function. To do so, we allowed WT and DGK $\zeta^{-/-}$ B cells, untreated or treated with R59, to form an immune synapse and then added 0.1 mM PA to the medium. After 30 min of PA exposure, we imaged the cells and detected larger immune synapse contact areas in all instances (Fig. 2, A and B). The su-Ag area values and total quantities of su-Ag at the immune synapse were reduced after PA treatment (fig. S4, A and B). By immunofluorescence microscopy, we detected increased F-actin content at the immune synapse of PA-exposed B cells (Fig. 2, C and D). Increasing the abundance of PA, thus, resulted in enhanced LFA-1-mediated adhesion and actin polymerization at the immune synapse and altered su-Ag central cluster dynamics.

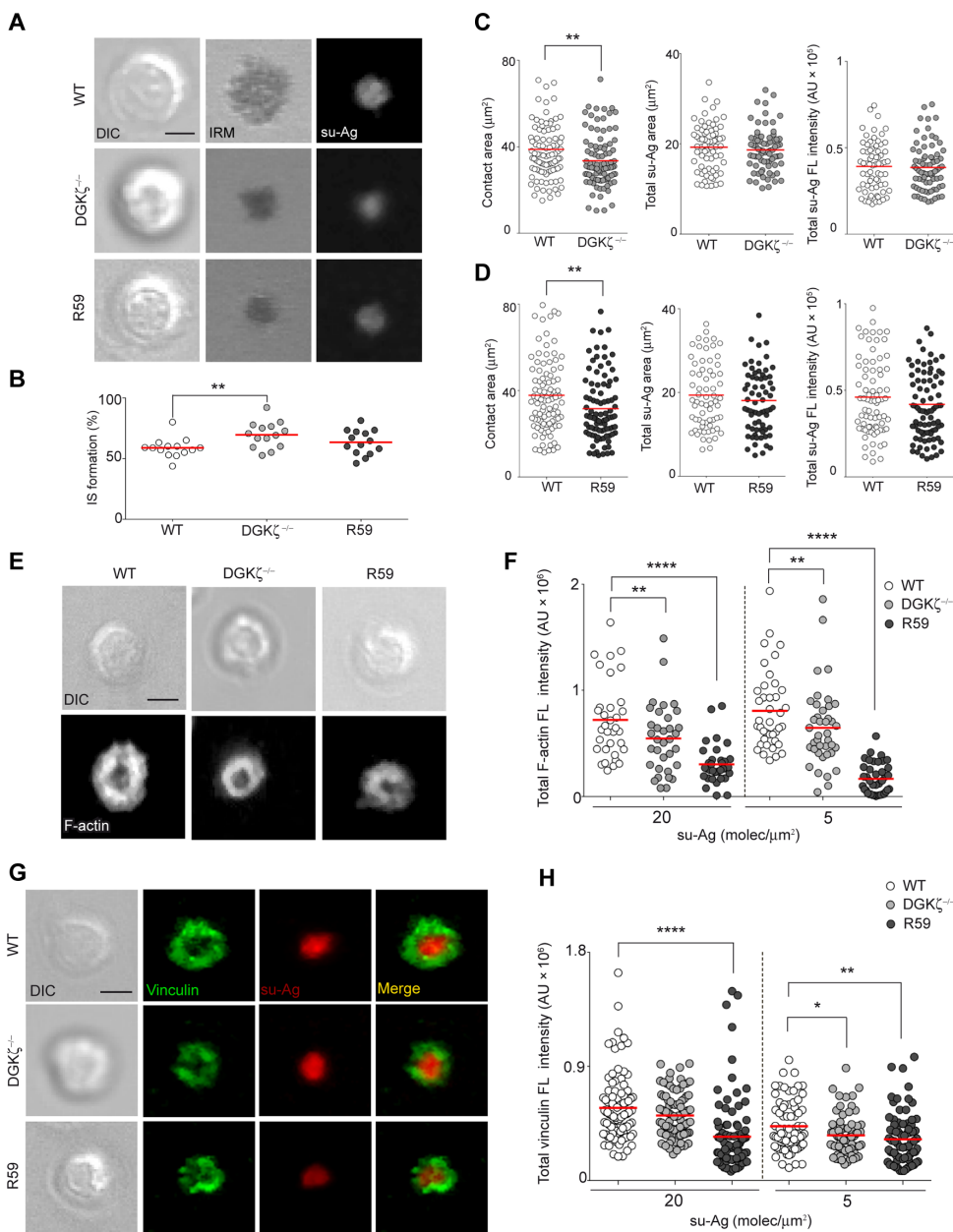


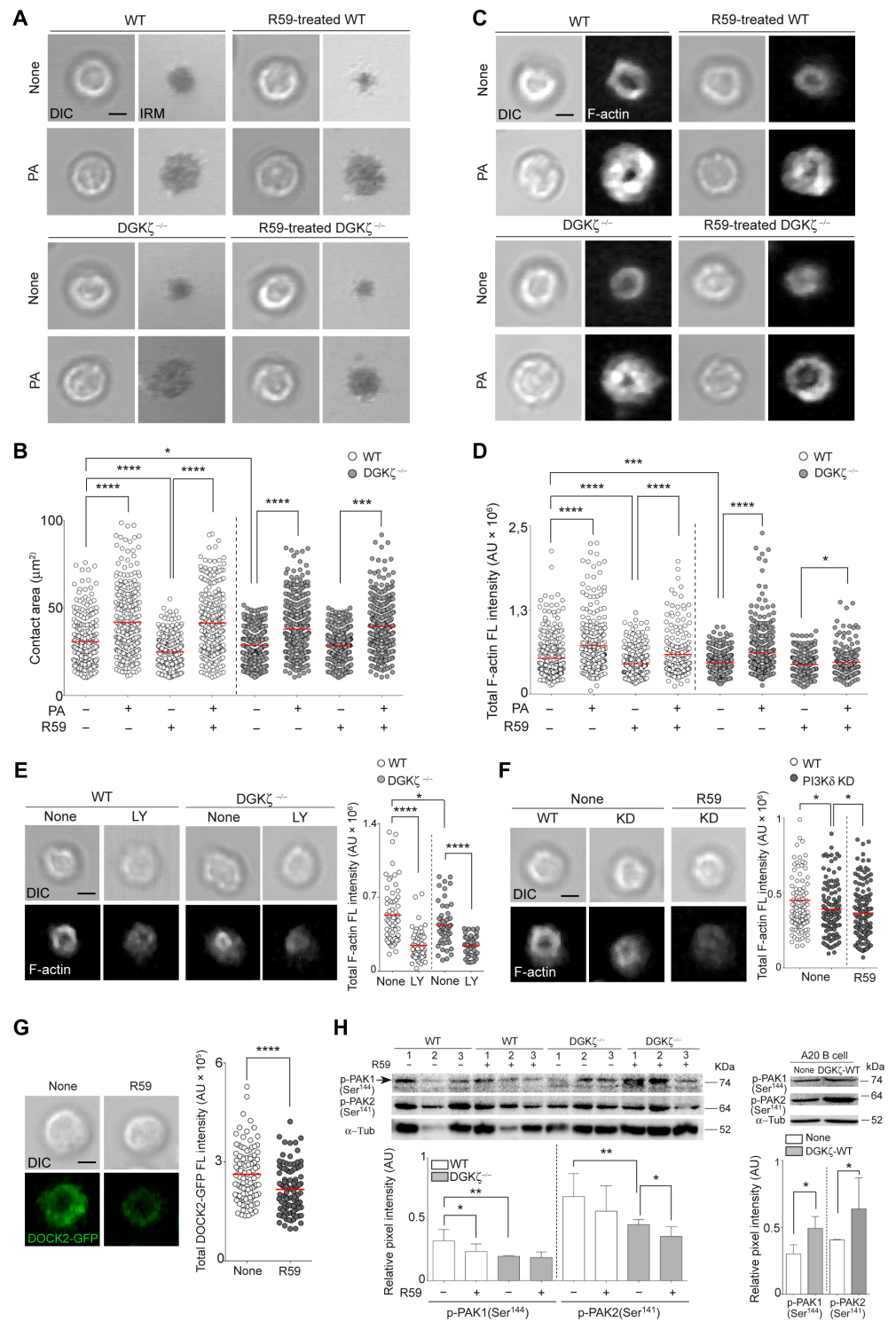
Fig. 1. DGK ζ dysfunction alters LFA-1-mediated adhesion and F-actin content at the B cell synapse. (A to H) B cells were allowed to settle on ICAM-1-coated and CXCL13-coated planar lipid bilayers loaded with su-Ag (20 molecules/ μm^2) for 10 min before being imaged or fixed for immunofluorescence analysis. (A) Differential interference contrast (DIC), IRM, and fluorescence su-Ag images at the contact plane of representative immune synapse-forming WT, DGK $\zeta^{-/-}$, and R59-treated B cells. (B) Percentages of the indicated cells that exhibited immune synapse formation. (C and D) Contact area (left), su-Ag central cluster area (cSMAC, middle), and total su-Ag fluorescence (FL) in arbitrary units (AU, right) for (C) DGK $\zeta^{-/-}$ B cells and (D) R59-treated B cells with established immune synapses compared with WT B cells. Each dot in (B) represents a single image field, whereas each dot in (C) and (D) represents a single cell. (E) DIC and FL images of F-actin (white) for representative immune synapse-forming WT, DGK $\zeta^{-/-}$, and R59-treated B cells, which were fixed at 10 min. (F) Values of total F-actin FL at the immune synapse in each case and in the presence of distinct su-Ag densities (20 and 5 molecules/ μm^2). (G) DIC and FL images of vinculin (green) and su-Ag (red) for representative immune synapse-forming WT, DGK $\zeta^{-/-}$, and R59-treated B cells, which were fixed at 10 min. (H) Values of total vinculin FL at the immune synapse in each case and in the presence of distinct su-Ag densities (20 and 5 molecules/ μm^2). Each dot in (F) and (H) represents a single cell. Data in (B) and (H) are pooled from two experiments from a total of four experiments. Data are representative of three (C and D) or four (F) experiments. Scale bars, 2.5 μm . * $P < 0.05$, ** $P < 0.01$, **** $P < 0.0001$ by two-tailed, unpaired Student's *t* test.

Previous studies noted the relevance of PI3K-derived phosphatidylinositol-3,4,5-trisphosphate (PIP₃) in regulating F-actin ring assembly at the T cell immune synapse. PIP₃ recruits DOCK2 to the periphery of the immune synapse, which promotes actin polymerization through the Rac guanosine 5'-triphosphatases (GTPases) (23). Thus, we addressed the interplay between PIP₃ and DGK ζ -derived PA in B cell immune synapse formation. PI3K activity in WT and DGK ζ -impaired (knockout and R59-treated) B cells was assessed by measuring Akt phosphorylation after BCR stimulation with anti-mouse IgM Ab-coated plates. We found no statistically significant differences in the abundance of Akt phosphorylated at Ser⁴⁷³ (Akt-pSer⁴⁷³) between the three cell types (fig. S5A). We treated WT and DGK $\zeta^{-/-}$ B cells with 10 μM LY294002 (a PI3K inhibitor) for 30 min at 37°C and then allowed them to settle on lipid bilayers for immune synapse formation. Treatment with this inhibitor caused a reduction in immune synapse area and in su-Ag cluster size in both cell types (fig. S5, B to D), as well as reducing total F-actin content (Fig. 2E). Within class I PI3Ks, the PI3K δ isoform (which contains the p110 δ catalytic subunit) was previously identified as the major contributor for PIP₃ production to regulate F-actin remodeling at the immune synapse (23). Thus, we isolated splenic B cells from knock-in mice expressing a kinase-deficient p110 δ catalytic subunit (PI3K δ KD), treated them with or without R59, and then evaluated immune synapse formation. PI3K δ KD B cells displayed reduced immune synapse contact area and F-actin content compared with WT control B cells (fig. S5, E and F, and Fig. 2F). We also detected increased su-Ag aggregation in PI3K δ KD B cells (fig. S5, E and G). Treatment of PI3K δ KD B cells with R59 further decreased immune synapse area and F-actin content compared with that in untreated cells, without modifying su-Ag clustering (fig. S5, E to G, and Fig. 2F).

We studied DOCK2 recruitment to the immune synapse in splenic B cells isolated from DOCK2-GFP knock-in mice, which were left untreated or were treated with R59. We observed a ring-shaped DOCK2-GFP structure at the immune synapse, and quantification of total

Fig. 2. PA generation promotes LFA-1-mediated adhesion and F-actin polymerization.

(A to D) The indicated B cells were in contact for 10 min with ICAM-1-containing and CXCL13-containing planar lipid bilayers loaded with su-Ag (20 molecules/ μm^2) to establish immune synapses, imaged, and then exposed to 0.1 mM PA for 30 min and either imaged or fixed for immunofluorescence. (A) DIC and IRM images for representative WT and $\text{DGK}\zeta^{-/-}$ B cells that were left untreated or were treated with R59 before (none) and after PA exposure. (B) Contact areas for B cells from the experiments shown in (A). (C) DIC and FL images of F-actin for WT and $\text{DGK}\zeta^{-/-}$ B cells that were left untreated or were treated with R59 before (none) and after PA exposure. (D) Values of total F-actin FL at the immune synapse in the indicated cells from the experiments shown in (C). (E) Left: DIC and FL images of F-actin for representative WT and $\text{DGK}\zeta^{-/-}$ B cells, which were left untreated or were treated with LY294002 and then fixed 10 min after contact with planar bilayer as described in (A). Right: Values of total F-actin FL at the immune synapse in the indicated cells. (F) Left: DIC and FL images of F-actin for representative WT and PI3K δ KD B cells, which were left untreated or were treated with R59. Right: Values of total F-actin FL at the immune synapse in the indicated cells. (G) Left: DIC and FL images of DOCK2-GFP for representative immune synapse-forming DOCK2-GFP knock-in B cells, which were left untreated or were treated with R59, after 10 min in contact with a su-Ag-loaded (20 molecules/ μm^2) planar bilayer. Right: Values of total DOCK2-GFP FL at the immune synapse in the indicated cells. (H) Top: Untreated and R59-treated (1 hour) WT and $\text{DGK}\zeta^{-/-}$ B cells as well as transfected A20 B cells sorted for the nontransfected (GFP^{neg}, none) or for the expression of GFP-DGK ζ -WT (DGK ζ -WT) were analyzed by Western blotting with specific antibodies against the indicated proteins. For primary B cells, lysates from three mice of each genotype are shown. Bottom: Quantification of phosphorylated-PAK1 (p-PAK1) and p-PAK2 band intensities, which were normalized to that of α -tubulin (α -Tub), which was used as a loading control. Each dot in (B) to (G) represents a single cell. Data in (B) and (D) pooled from two experiments from a total of four experiments. Data are representative of three (E and F) and two (G) experiments. Data in (H) are means \pm SD of three mice and of three A20 cell transfection experiments. Scale bars, 2.5 μm . * $P < 0.05$, ** $P < 0.01$, *** $P < 0.001$, **** $P < 0.0001$ by two-tailed, unpaired Student's t test.



DOCK2-GFP fluorescence at the immune synapse plane revealed a statistically significant reduction in B cells that were treated with R59 (Fig. 2G). $\text{DGK}\zeta$ -dependent PAK1 activation promotes RhoGDI/Rac dissociation and, thus, Rac activation (24). We assessed PAK1/2 activation by measuring the relative amounts of phosphorylated

PAK1/2 (p-PAK1/2) by Western blotting. We found that $\text{DGK}\zeta^{-/-}$ and R59-treated B cells had lower amounts of p-PAK1/2 than that of controls, whereas the overexpression of $\text{DGK}\zeta$ -WT in A20 B cells resulted in increased p-PAK1/2 abundance (Fig. 2H). PA did not increase the amount of p-PAK1/2 in WT B cells (fig. S4C). This suggests

that DGK ζ associates with the PAK/RhoGDI complex and promotes its activation, as was previously described for fibroblasts (24). Hence, our data suggest that DGK ζ promotes actin polymerization at the B cell immune synapse by increasing Rac function in a DOCK2- and PAK1/2-dependent manner.

DGK ζ stimulates mechanical forces at the B cell immune synapse

Several studies revealed the relevance of mechanical forces at the immune synapse for B and T cell effector function (20, 25). The robust actin polymerization and remodeling at the immune synapse induces force generation. LFA-1 and antigen receptors act as mechanosensitive proteins because their function and signaling properties are shaped by these mechanical forces. DGK $\zeta^{-/-}$ B cells and R59-treated WT B cells had defects in LFA-1-mediated adhesion and F-actin abundance at the immune synapse. We asked whether these defects affected the mechanical forces generated at the synapse of these B cells compared with those of WT B cells. To do that, we used two complementary methods: TFM and MFP. We used TFM to measure the forces exerted by B cells when they were in contact with polyacrylamide (PAA) hydrogels loaded with su-Ag alone or in combination with ICAM-1-Fc. Displacements of the fluorescent microbeads embedded on the hydrogel, monitored over time, enabled us to calculate the magnitude of the applied forces (fig. S6A) and the cell strength on the substrate at each time point. Traction energy values were statistically significantly greater in the presence of ICAM-1 at the substrate compared with the values in the presence of su-Ag alone (Fig. 3, A and B, and movies S1 and S3), pointing to the importance of LFA-1-mediated adhesion for force generation at the immune synapse. DGK $\zeta^{-/-}$ B cells exhibited reduced traction forces compared with those of control B cells in the presence of both su-Ag and ICAM-1 (Fig. 3, A and B, and movies S2 and S4).

To define the three-dimensional components of the forces involved, we delineated B cell mechanical behavior and quantified the forces generated at the immune synapse over time by MFP (21). In this technique, a bead coated with stimulatory ligands is aspirated at the tip of a flexible micropipette used as a sensitive force transducer, and brought in contact with the cell, which is aspirated at the tip of another micropipette (fig. S6B). We used silica beads (5- μ m diameter) coated with lipid bilayers containing GPI-ICAM-1 and tethered su-Ag. After contact with the stimulatory bead, WT B cells pushed it away during the first 40 s (positive values of bead displacement, X_{bead} , relative to initial bead position) (Fig. 3, C and D, fig. S6C, and movies S5 and S6) at a pushing speed of 0.025 ± 0.010 μ m/s (Fig. 3E). DGK $\zeta^{-/-}$ B cells showed a reduced pushing phase that correlated with lower pushing speed values (0.015 ± 0.005 μ m/s; Fig. 3, C to E, and movie S7). After the pushing phase, WT B cells pulled on the bead (X_{bead} reached negative values) and formed a cup-like structure on it (Fig. 3, C and D, fig. S6C, and movie S6), whereas the pulling ability of the DGK $\zeta^{-/-}$ B cells was decreased (Fig. 3D). MFP also enables the measurement of cell rigidity just upon cell contact with the bead, before the pushing phase begins (Young's modulus parameter) (21). We found that values were higher with su-Ag compared with nonantigen (Fig. 3F), indicating increased cell stiffness after BCR stimulation. Young's modulus values for DGK $\zeta^{-/-}$ B cells were lower than for WT in presence of su-Ag (Fig. 3F). To measure cell mechanical changes at the immune synapse, we monitored B cell elastic properties by quantifying cell stiffness through the K' parameter. Compared with WT B cells, DGK $\zeta^{-/-}$ B cells had lower

K' values (Fig. 3G), indicating an impaired ability to undergo cytoskeletal remodeling, which changed their mechanical properties upon immune synapse formation. Similarly, we detected mechanical defects in R59-treated B cells (Fig. 3, H to J, and movie S8). Therefore, data obtained from both TFM and MFP experiments suggest that DGK ζ is required for the mechanical properties and force generation at the B cell immune synapse.

DGK ζ activity limits immune synapse-triggered B cell activation

A previous study reported that the lack of DGK ζ enhances activation of DAG-dependent pathways upon B cell stimulation with soluble antigen *in vitro*, with ERK1/2 activation, CD69 abundance, and cell proliferation being increased (3). We investigated the effects of impaired DGK ζ function for B cell activation with regard to the immune synapse. We loaded WT, DGK $\zeta^{-/-}$, and R59-treated B cells with a Ca^{2+} -sensitive fluorescent probe and monitored Ca^{2+} influx during immune synapse formation by real-time fluorescence microscopy. Peak and sustained Ca^{2+} influx were enhanced in DGK $\zeta^{-/-}$ and R59-treated B cells compared with those in control cells (Fig. 4, A and B), which might be due to increased stimulation of DAG-dependent Ca^{2+} channels (26). We evaluated ERK1/2 activation by measuring the relative amounts of phosphorylated ERK1/2 (p-ERK) at the immune synapse by immunofluorescence (Fig. 4C). We found that DGK ζ absence or inhibition resulted in increased p-ERK abundance (Fig. 4, C and D). DGK $\zeta^{-/-}$ B cells had similar amounts of p-ERK at the immune synapse as did R59-treated WT B cells. This finding supports the major role of the DGK ζ isoform in limiting DAG-related signaling downstream of the BCR, as was previously reported (3). The lack of DGK α in B cells did not modify p-ERK abundance at the immune synapse compared with that of WT B cells (fig. S6D). The increased amount of p-ERK in R59-treated DGK $\zeta^{-/-}$ B cells compared with that in untreated cells implies the contribution of another DGK isoform in absence of DGK ζ .

We incubated B cells in contact with planar lipid bilayers, which were unloaded or su-Ag loaded, for 20 hours and then analyzed the cell surface expression of the activation markers CD69, CD25, and CD86 by flow cytometry. DGK $\zeta^{-/-}$ B cells expressed more of those markers at the cell surface than did WT B cells, although the increase was statistically significant only for CD69, and treatment with R59 had a similar effect (Fig. 4, E and F). To evaluate cell proliferation, we modified the experimental approach (fig. S7A) by using silica beads (5- μ m diameter) coated with lipid bilayers containing GPI-ICAM-1, a CXCL13 coating, and tethered su-Ag, because these beads were suitable for longer coculture periods. We refer to these beads as pseudo-APCs. We increased the su-Ag density (1000 molecules/ μm^2) at the pseudo-APC surface to promote greater B cell proliferation, thus facilitating detection. WT, DGK $\zeta^{-/-}$, and R59-treated B cells were stained with CFSE (carboxyfluorescein succinimidyl ester) and cocultured with pseudo-APCs at different ratios (1:1 and 1:5) in the presence of interleukin-4 (IL-4) for 96 hours. Compared with WT B cells, DGK $\zeta^{-/-}$ B cells showed increased proliferation, although treatment of these cells with R59 did not lead to further changes (Fig. 4, G and H; for the gating strategy, see fig. S7A).

DGK ζ deficiency diminishes the antigen presentation capacity of B cells *in vitro*

B cell immunity against T cell-dependent antigens entails antigen acquisition, degradation, and presentation to T cells in the form of antigenic peptides by the major histocompatibility complex (MHC)

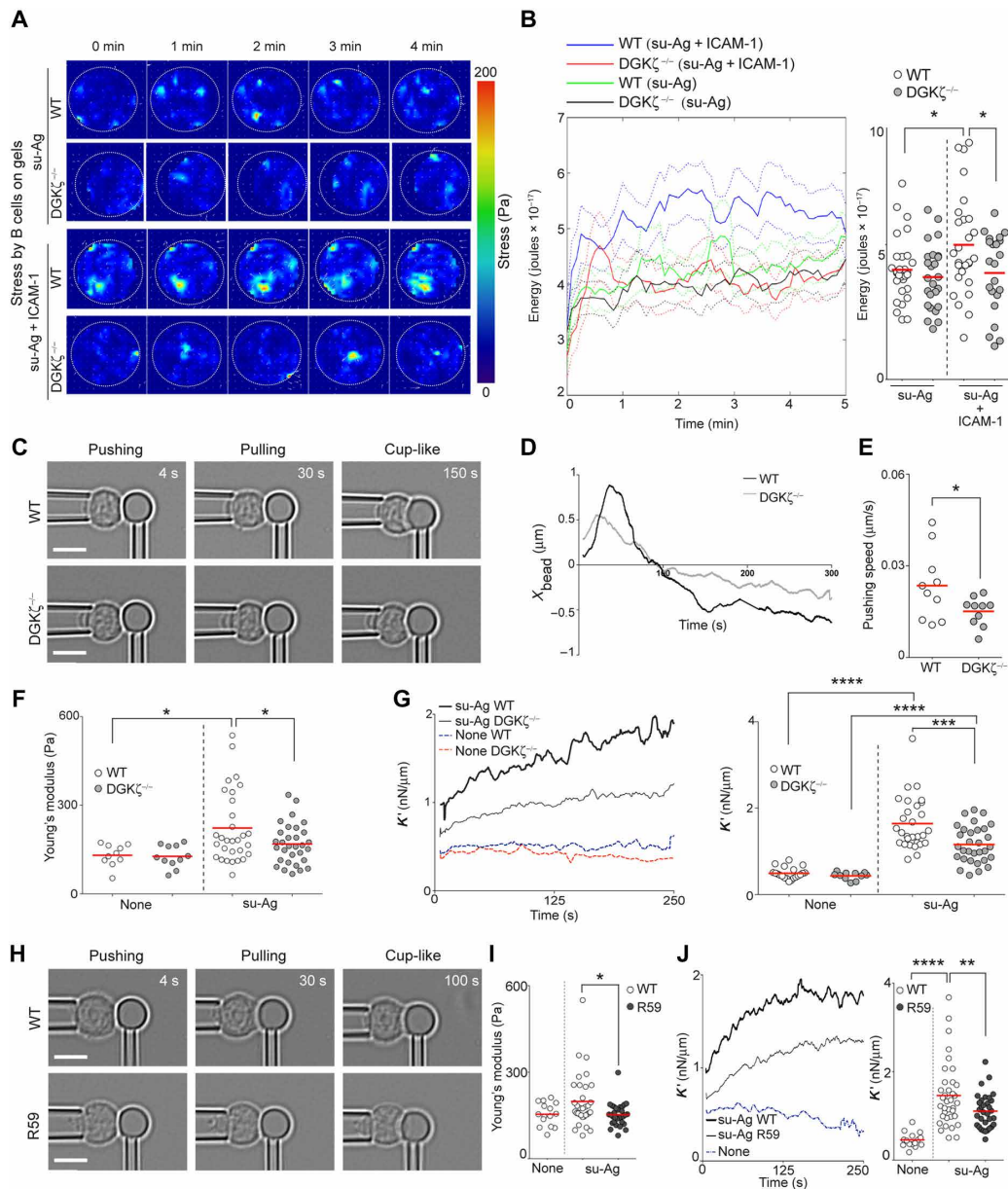
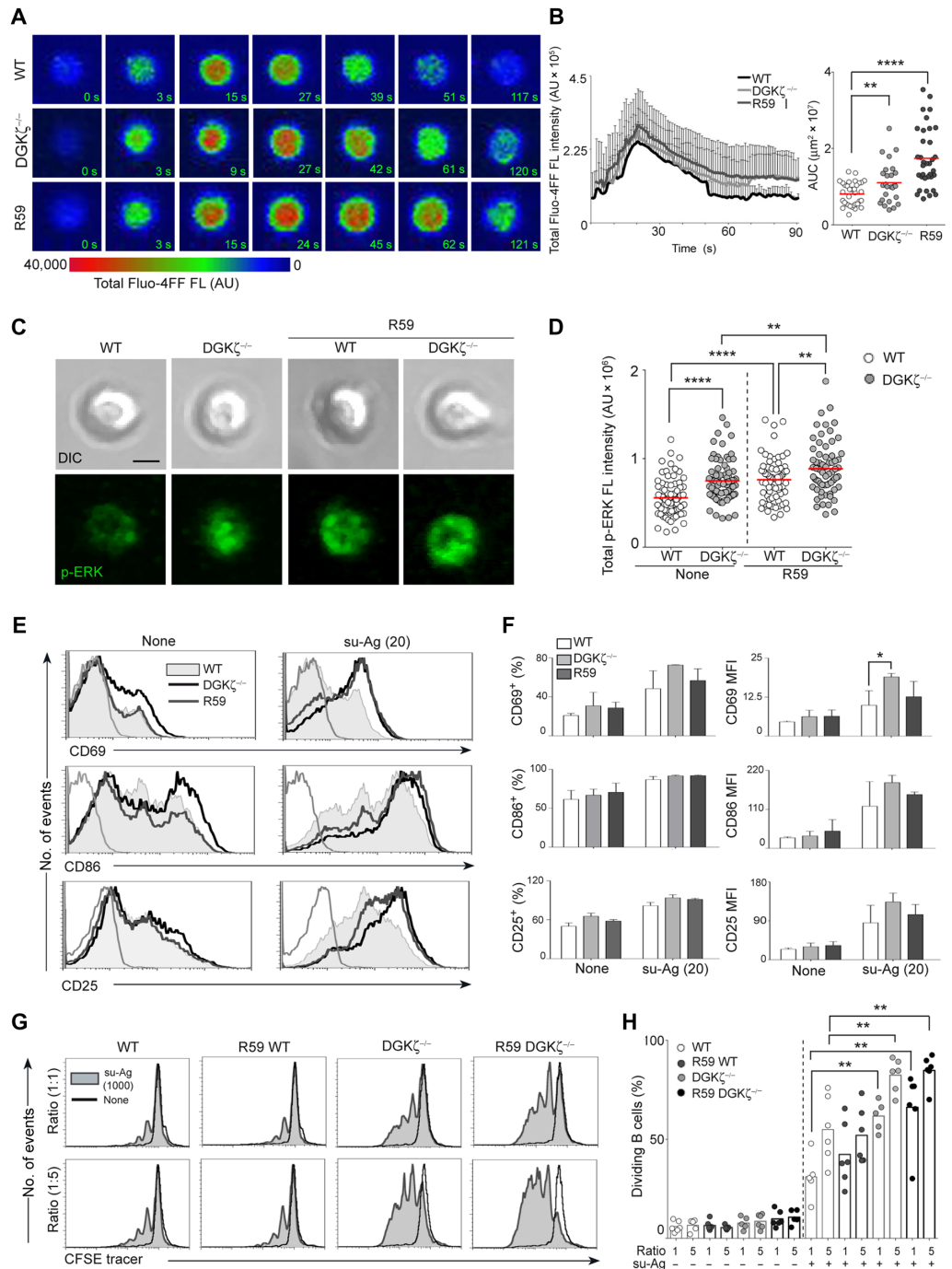


Fig. 3. Mechanical force generation at the B cell immune synapse is mediated by DGK ζ . (A) B cells were allowed to settle on PAA gels coated with su-Ag alone or with ICAM-1-Fc and then were monitored for up to 15 min. Time-lapse color maps of stress (in pascal) for representative WT and DGK ζ ^{-/-} B cells on PAA gels under the indicated conditions are shown. (B) Left: Average values of synaptic traction forces (in joules) over time for WT and DGK ζ ^{-/-} B cells under the indicated conditions. Each solid line corresponds to the mean of 25 to 30 measured cells; dotted lines represent \pm SD (confidence interval). Right: Average value of synaptic traction forces per cell over time. Each dot represents a single cell. Data are pooled from three experiments. (C to J) B cells were monitored by MFP while in contact with silica beads that were coated with ICAM-1-containing lipid bilayers and either unloaded (none) or loaded with su-Ag (100 molecules/ μm^2). (C) Bright-field microscopy images (processed using a high-pass filter for better visualization using ImageJ software) for representative WT and DGK ζ ^{-/-} B cells that were activated by a su-Ag-loaded bead. In both examples, the cells are submitted to an oscillatory force of 50-pN average, 25-pN amplitude, and 1-Hz frequency. (D) Time trace of the su-Ag-loaded bead position (X_{bead} , in micrometers) for WT and DGK ζ ^{-/-} B cells. Each line corresponds to the average value of 10 cells. Data are from a single experiment that is representative of three independent experiments. (E) Values of pushing speed (in micrometers per second) per cell when in contact with the su-Ag-loaded bead. Each dot represents a single cell. Data are from a single experiment that is representative of three independent experiments. (F to G) Mechanical changes during activation. (F) Values of Young's modulus (in pascal) per cell when contacting beads under the indicated conditions (none, in the absence of tethered su-Ag). Each dot represents a single cell. Data are pooled from three experiments. (G) Left: Time evolution of cell stiffness K' (in nanonewtons per micrometer) averaged over cells. Each line corresponds to the average value of 20 cells. Data are pooled from two experiments ($n = 3$). Right: Cell stiffness K' averaged over 250 s after cell contact with a bead. Each dot represents a single cell. Data are pooled from three experiments. (H) Bright-field microscopy images processed as described for (C) for representative untreated and R59-treated WT B cells activated by a su-Ag-loaded bead, as described in (C). (I) Values of Young's modulus were determined as described in (F) but for untreated and R59-treated (R59) WT B cells. (J) Left: Time evolution of cell stiffness K' (in nanonewtons per micrometer) averaged over untreated and R59-treated WT B cells. Each line corresponds to the average value of 30 cells. Data are pooled from three experiments. Right: Cell stiffness K' averaged over 250 s after cell contact with a bead. Each dot represents a single cell. Data are pooled from three experiments. Data in (I) and (J) are pooled from three experiments. Scale bars, 5 μm . * $P < 0.05$, ** $P < 0.01$, *** $P < 0.001$, **** $P < 0.0001$ by two-tailed, unpaired Student's t test.

Fig. 4. DGK ζ diminishes BCR-dependent B cell activation in the context of the immune synapse.

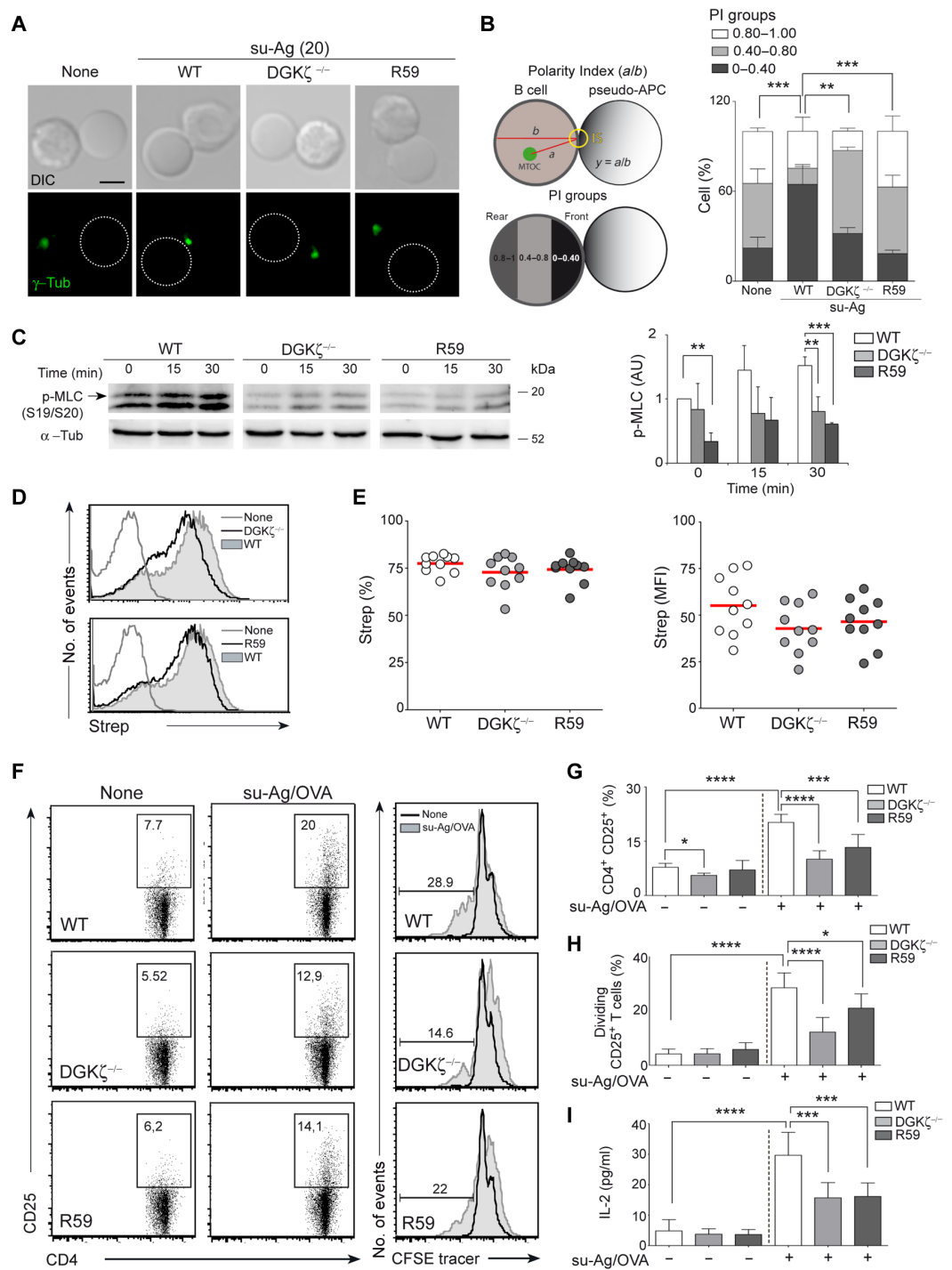
(A) Fluo-4FF-labeled WT, DGK $\zeta^{-/-}$, and R59-treated B cells were monitored for Ca²⁺ influx at early times of immune synapse formation on ICAM-1-containing and CXCL13-containing planar lipid bilayers loaded with su-Ag (20 molecules/ μ m²). Fluorescence Fluo-4FF images of representative B cells over time are shown. **(B)** Left: Values of total Fluo-4FF FL (in AU) over time. Data are means \pm SD of 30 B cells per condition. Right: To statistically compare the Fluo-4FF FL data, we calculated the area under the curve (AUC) per B cell and per condition. Each dot represents a single cell. **(C)** WT and DGK $\zeta^{-/-}$ B cells, which were left untreated (none) or were treated with R59, were in contact with su-Ag-loaded (20 molecules/ μ m²), ICAM-1-containing, and CXCL13-containing planar lipid bilayers for 10 min and then were fixed for immunofluorescence. DIC and FL images of phosphorylated ERK1/2 (p-ERK, green) for representative immune synapse-forming B cells are shown. **(D)** Values of total p-ERK FL at the immune synapse for the indicated cells. Each dot represents a single cell. **(E and F)** B cells were cultured on ICAM-1-containing and CXCL13-containing planar lipid bilayers, which were either unloaded (none) or loaded with su-Ag [20 molecules/ μ m²; su-Ag (20)], for 20 hours and then were collected for flow cytometry analysis. **(E)** Representative profiles of CD69, CD25, and CD86 staining for the indicated cells. **(F)** Percentages of B cells expressing CD69, CD25, or CD86 (left) and mean fluorescence intensity (MFI) values for these markers (right) in each condition and for each B cell type. **(G and H)** CFSE tracer-labeled WT and DGK $\zeta^{-/-}$ B cells, which were left untreated or were treated with R59, were cocultured with pseudo-APCs (silica beads coated with ICAM-1-containing and CXCL13-containing lipid bilayers), which were unloaded (none) or loaded with su-Ag [1000 molecules/ μ m², su-Ag (1000)] at ratios of 1:1 and 1:5 in the presence of IL-4 for 72 hours. **(G)** Representative profiles of CFSE tracer for the indicated conditions. **(H)** Percentages of dividing B cells (as determined by monitoring CFSE dilution) in each condition and for each B cell type. Data in (D) are from a single experiment and are representative of two experiments. Each dot represents a cell. Data are pooled from two (B), four (F), and six (H) experiments. Scale bars, 2.5 μ m. **P* < 0.05, ***P* < 0.01, *****P* < 0.0001 by two-tailed, unpaired Student's *t* test.



class II complex. In this process, B cells receive T cell help, mainly through CD40 stimulation, which triggers B cell survival, proliferation, and class switching. We investigated the role of DGK ζ in the molecular events related to antigen acquisition, processing, and presentation. MTOC polarization to the immune synapse supports the membrane trafficking needed for these events (27). We incubated WT, DGK $\zeta^{-/-}$, and R59-treated B cells with pseudo-APCs, unloaded or loaded with su-Ag, at a ratio of 1:1 for 30 min at 37°C, and then

fixed the cells and analyzed MTOC location by γ -tubulin staining. The distance of the MTOC from the immune synapse for each B cell was measured and normalized to the cell diameter. We found that su-Ag promoted MTOC relocation in most WT B cells (70%), whereas this was reduced in DGK ζ -defective cells (20% in DGK $\zeta^{-/-}$ B cells; 30% in R59-treated B cells) (Fig. 5, A and B). The nonmuscle motor protein myosin II is involved in antigen extraction at the B cell immune synapse (22). Therefore, we used Western blotting to

Fig. 5. MTOC translocation, myosin activation, and antigen presentation ability are reduced in $DGK\zeta^{-/-}$ and R59-treated B cells.



The indicated B cells were mixed with unloaded (none) or $su-Ag$ -loaded [20 molecules/ μm^2 ; $su-Ag$ (20)] pseudo-APCs at a 1:1 ratio, cultured for 30 min on poly-L-lysine-coated coverslips, and then fixed for immunofluorescence. DIC and FL γ -tubulin (γ -tub; green) images are shown for representative B cell-pseudo-APC conjugates for each indicated condition. Dashed circle, pseudo-APC. Scale bar, 2.5 μm .

Percentages of B cells from the experiments shown in (A) in the specified polarity index (PI) groups. The PI per B cell was estimated as the ratio of "a" and "b" distances (left). Data are means \pm SD of 40 B cells in each case. (C) Left: WT, $DGK\zeta^{-/-}$, and R59-treated B cells stimulated on Ab-coated plates for the indicated times were analyzed by Western blotting with specific antibodies against the indicated proteins. Right: Quantification of phosphorylated-MLC (p-MLC) band intensity was normalized to that of the loading control α -tubulin (α -Tub).

(D and E) WT, $DGK\zeta^{-/-}$, and R59-treated B cells were cultured for 2 hours in contact with ICAM-1-containing and CXCL13-containing planar lipid bilayers, which were coated with Alexa Fluor 647-streptavidin (strep) and were either unloaded (none) or loaded with $su-Ag/OVA$ ($su-Ag/OVA$; 2500 molecules/ μm^2). The B cells were then collected, treated with trypsin for 5 min, and analyzed by flow cytometry for strep fluorescence as a readout of $su-Ag/OVA$ extraction. (D) Representative profiles of strep for each case. (E) Percentages of strep⁺ B cells (left) and mean fluorescence intensity (MFI) strep values (right) in the presence of $su-Ag/OVA$ for each B cell type. Data are pooled from three experiments (four WT and four $DGK\zeta^{-/-}$ mice were used in total). (F to I) Experiments were performed as described for (D), but, after 2 hours of incubation with the planar bilayers, the B cells were collected, washed, and cocultured with CFSE-labeled OTII CD4⁺ T cells at a ratio 1:1 for 72 hours. Cell culture medium was then collected to analyze secreted IL-2, and the cells were analyzed by flow cytometry. (F) Left: Representative CD25 and CD4 dot plots for CD4-gated OTII T cells in each case and for each condition: B cells exposed to unloaded planar bilayers, none; B cells exposed to $su-Ag/OVA$ -loaded bilayers, $su-Ag/OVA$. Right: Representative profiles of CFSE for CD4⁺CD25⁺ T cells in each case and for each condition. (G) Percentages of CD4⁺CD25⁺ T cells and (H) of dividing CD25⁺ T cells in each case. (I) Amounts of T cell-secreted IL-2 in the medium of the indicated cell cocultures. Data in (G) to (I) are means \pm SD of three experiments. * $P < 0.05$, ** $P < 0.01$, *** $P < 0.001$, **** $P < 0.0001$ by two-tailed, unpaired Student's t test.

analyze phosphorylation of the regulatory subunit myosin light chain (MLC) after BCR triggering with Ab-coated plates and found that $DGK\zeta^{-/-}$ and R59-treated B cells had impaired MLC activation compared with that of control cells (Fig. 5C).

(D and E) WT, $DGK\zeta^{-/-}$, and R59-treated B cells were cultured for 2 hours in contact with ICAM-1-containing and CXCL13-containing planar lipid bilayers, which were coated with Alexa Fluor 647-streptavidin (strep) and were either unloaded (none) or loaded with $su-Ag/OVA$ ($su-Ag/OVA$; 2500 molecules/ μm^2). The B cells were then collected, treated with trypsin for 5 min, and analyzed by flow cytometry for strep fluorescence as a readout of $su-Ag/OVA$ extraction. (D) Representative profiles of strep for each case. (E) Percentages of strep⁺ B cells (left) and mean fluorescence intensity (MFI) strep values (right) in the presence of $su-Ag/OVA$ for each B cell type. Data are pooled from three experiments (four WT and four $DGK\zeta^{-/-}$ mice were used in total). (F to I) Experiments were performed as described for (D), but, after 2 hours of incubation with the planar bilayers, the B cells were collected, washed, and cocultured with CFSE-labeled OTII CD4⁺ T cells at a ratio 1:1 for 72 hours. Cell culture medium was then collected to analyze secreted IL-2, and the cells were analyzed by flow cytometry. (F) Left: Representative CD25 and CD4 dot plots for CD4-gated OTII T cells in each case and for each condition: B cells exposed to unloaded planar bilayers, none; B cells exposed to $su-Ag/OVA$ -loaded bilayers, $su-Ag/OVA$. Right: Representative profiles of CFSE for CD4⁺CD25⁺ T cells in each case and for each condition. (G) Percentages of CD4⁺CD25⁺ T cells and (H) of dividing CD25⁺ T cells in each case. (I) Amounts of T cell-secreted IL-2 in the medium of the indicated cell cocultures. Data in (G) to (I) are means \pm SD of three experiments. * $P < 0.05$, ** $P < 0.01$, *** $P < 0.001$, **** $P < 0.0001$ by two-tailed, unpaired Student's t test.

We evaluated B cell-mediated antigen extraction and presentation to T cells in vitro. We prepared planar lipid bilayers containing GPI-ICAM-1 and CXCL13 that were left unloaded or were loaded with a mixture of $su-Ag$ and Alexa Fluor 488-conjugated ovalbumin

Percentages of CD4⁺CD25⁺ T cells and (H) of dividing CD25⁺ T cells in each case. (I) Amounts of T cell-secreted IL-2 in the medium of the indicated cell cocultures. Data in (G) to (I) are means \pm SD of three experiments. * $P < 0.05$, ** $P < 0.01$, *** $P < 0.001$, **** $P < 0.0001$ by two-tailed, unpaired Student's t test.

Percentages of CD4⁺CD25⁺ T cells and (H) of dividing CD25⁺ T cells in each case. (I) Amounts of T cell-secreted IL-2 in the medium of the indicated cell cocultures. Data in (G) to (I) are means \pm SD of three experiments. * $P < 0.05$, ** $P < 0.01$, *** $P < 0.001$, **** $P < 0.0001$ by two-tailed, unpaired Student's t test.

analyze phosphorylation of the regulatory subunit myosin light chain (MLC) after BCR triggering with Ab-coated plates and found that $DGK\zeta^{-/-}$ and R59-treated B cells had impaired MLC activation compared with that of control cells (Fig. 5C).

We evaluated B cell-mediated antigen extraction and presentation to T cells in vitro. We prepared planar lipid bilayers containing GPI-ICAM-1 and CXCL13 that were left unloaded or were loaded with a mixture of $su-Ag$ and Alexa Fluor 488-conjugated ovalbumin

(OVA) protein (see Materials and Methods). To quantify BCR-mediated antigen extraction, we measured the fluorescence intensity of the Alexa Fluor 647–conjugated streptavidin (strep) used to tether su-Ag and OVA to the lipid bilayer (see Materials and Methods). We also assessed OVA acquisition by monitoring Alexa Fluor 488 fluorescence intensity. We incubated WT B cells in the absence or presence of su-Ag and OVA at different densities (ranging from 20 to 2500 molecules/ μm^2) for 2 hours at 37°C, followed by collecting the cells, treating them with trypsin, and analyzing them by flow cytometry. We detected strep/OVA extraction at densities of 500 and 2500 molecules/ μm^2 (~30 and 70% strep⁺ B cells, respectively), which was dependent on BCR stimulation by tethered su-Ag (fig. S7B). We then evaluated the antigen extraction ability of DGK ζ ^{-/-} and R59-treated B cells using the highest density to improve the detection of streptavidin. Strep⁺ B cell frequencies were similar, but the mean fluorescence intensity values were lower, for DGK ζ ^{-/-} and R59-treated B cells compared with those of WT B cells (Fig. 5, D and E), which is suggestive of reduced antigen acquisition, although the difference was not statistically significant. The addition of PA did not modify the ability of WT B cells to extract antigen (fig. S7C).

To assess T cell antigen presentation, we incubated WT, DGK ζ ^{-/-}, and R59-treated B cells in contact with unloaded or su-Ag/OVA-loaded planar lipid bilayers for 2 hours at 37°C. The B cells were then collected and cocultured with CFSE-labeled OTII CD4⁺ T cells at a 1:1 ratio (fig. S7D). The TCR of OTII CD4⁺ T cells recognizes OVA-derived peptides (residues 323 to 339) in the context of MHC class II (I-A^b) on the B cell surface, triggering T cell activation. After 72 hours, we evaluated the cell surface expression of CD25 as a marker of T cell activation, T cell proliferation (for the gating strategy, see fig. S7D), and the amount of IL-2 secreted into the cell culture medium. Using this system, we detected increased CD4⁺ CD25⁺ T cell frequencies (up to 25%) in presence of su-Ag/OVA compared with the control condition for WT B cells (Fig. 5, F and G), whereas the frequencies were statistically significantly reduced for DGK ζ ^{-/-} and R59-treated B cells (Fig. 5, F and G). T cell proliferation and IL-2 production were reduced in the context of DGK ζ ^{-/-} and R59-treated B cells (Fig. 5, F, H, and I). These results suggest that DGK ζ stimulates antigen presentation by mediating antigen acquisition- and antigen processing-related molecular events at the immune synapse.

The absence of DGK ζ in B cells impairs the GC response in vivo

We investigated whether the antigen presentation defects found in B cells with altered DGK ζ function limited GC responses to T-dependent antigens in vivo. We isolated WT or DGK ζ ^{-/-} B cells (CD45.2⁺) and adoptively transferred them to CD45.1⁺ immunocompetent recipient mice. One day later, the mice were immunized with 4-hydroxy-3-iodo-5-nitrophenylacetyl (NIP)–OVA embedded in alum, and the splenic GC response was evaluated by flow cytometry at day 7 after immunization (for the gating strategy used, see Fig. 6A for CD45.2⁺ B cell analysis). The frequency of NP-specific GC (GL7⁺Fas⁺NP⁺) B cells was statistically significantly less in mice that received DGK ζ ^{-/-} B cells compared with that in mice that received WT B cells (Fig. 6, B and C). We then determined the frequency of plasma cells (PCs; CD138⁺) and IgG1⁺ B cells within the CD45.2⁺ B cell population. The transferred DGK ζ ^{-/-} B cells showed reduced frequencies of both populations in comparison to transferred control B cells (Fig. 6, D and E). Transferred DGK ζ ^{-/-} B cells exhibited preferential generation of IgM⁺ PCs as opposed to IgG1⁺ PCs

when compared with transferred WT B cells (Fig. 6, F and G). The memory-like CD138⁺IgG1⁺ B cell subset was reduced for DGK ζ ^{-/-} B cells compared with that for WT B cells, although this was not statistically significant (Fig. 6, H and I). As expected, the recipient CD45.1⁺ B cell response was comparable between animals that received CD45.2⁺ WT B cells or CD45.2⁺ DGK ζ ^{-/-} B cells (fig. S8). These results suggest that DGK ζ ^{-/-} B cells have a competitive disadvantage for T cell help, which results in diminished GC responses.

DISCUSSION

This study reports a pivotal role for DGK ζ in the regulation of actin polymerization and LFA-1–mediated adhesion at the B cell immune synapse and, consequently, in the generation of mechanical forces at the immune synapse. Impaired MTOC translocation to the immune synapse also suggests that DGK ζ mediates cell polarity-related events in this context. Traction forces and cell polarization are necessary for the acquisition and processing of antigen at the B cell immune synapse (22, 28, 29). The ability of B cells to present antigenic peptides determines the chances of receiving costimulatory T cell help and the subsequent fate of the B cell response. Data from in vitro and in vivo assays support a role for DGK ζ in shaping the ability of B cells to extract antigen from the APC surface and, thus, to receive T cell help and facilitate an appropriate GC response.

Immune synapse formation induces robust actin polymerization and the assembly of a peripheral F-actin ring, which provides a framework for signaling events, membrane trafficking, and adhesion support. In T cells, PI3K-mediated PIP₃ production at the periphery of the immune synapse plays a major role in the maintenance of the F-actin ring (23). PIP₃ recruits DOCK2, promoting Rac activation, and thus, actin polymerization. Our data support a similar role for PIP₃ in regulating F-actin ring formation at the B cell immune synapse. DGK ζ ^{-/-} B cells and DGK-inhibited WT or PI3K δ KD B cells showed reduced amounts of F-actin at the immune synapse, whereas treatment with PA or overexpression of DGK ζ increased the size and content of the F-actin ring. DGK ζ and its product, PA, are thus involved in the regulation of F-actin ring formation at the B cell immune synapse. Previous reports of nonimmune cells showed the importance of DGK ζ in connecting lipid signaling with actin reorganization through its kinase and scaffold activities. DGK ζ associates with the PAK1-RhoGDI-Rac1 complex and promotes Rac activation, a process that requires both its scaffold and kinase functions (24). DGK ζ also stimulates RhoA activation through a scaffolding mechanism, forming a complex with PKC α and RhoGDI (30). We propose that DGK ζ affects Rac function and actin polymerization at the immune synapse by mediating DOCK2 recruitment and PAK1/2 activation. Our data from experiments with the DGK ζ KD construct, the addition of exogenous PA addition, and the reduction in DOCK2-GFP abundance in R59-treated B cells provide evidence of a major contribution of DGK ζ -kinase activity. In addition, the lack of increase in p-PAK1/2 abundance upon PA exposure suggests the involvement of DGK ζ scaffold properties. PAK1/2 are also targets of active Rac and coordinate actin cytoskeleton remodeling (31, 32); however, whether they are involved in immune synapse assembly downstream of Rac requires further study. In neutrophil migration, DOCK2 dynamics at the plasma membrane is sequentially regulated by PIP₃ and PA. Upon stimulation, PIP₃ rapidly recruits DOCK2 to the plasma membrane, whereas the PA that is generated stabilizes DOCK2 at the membrane promoting its local accumulation

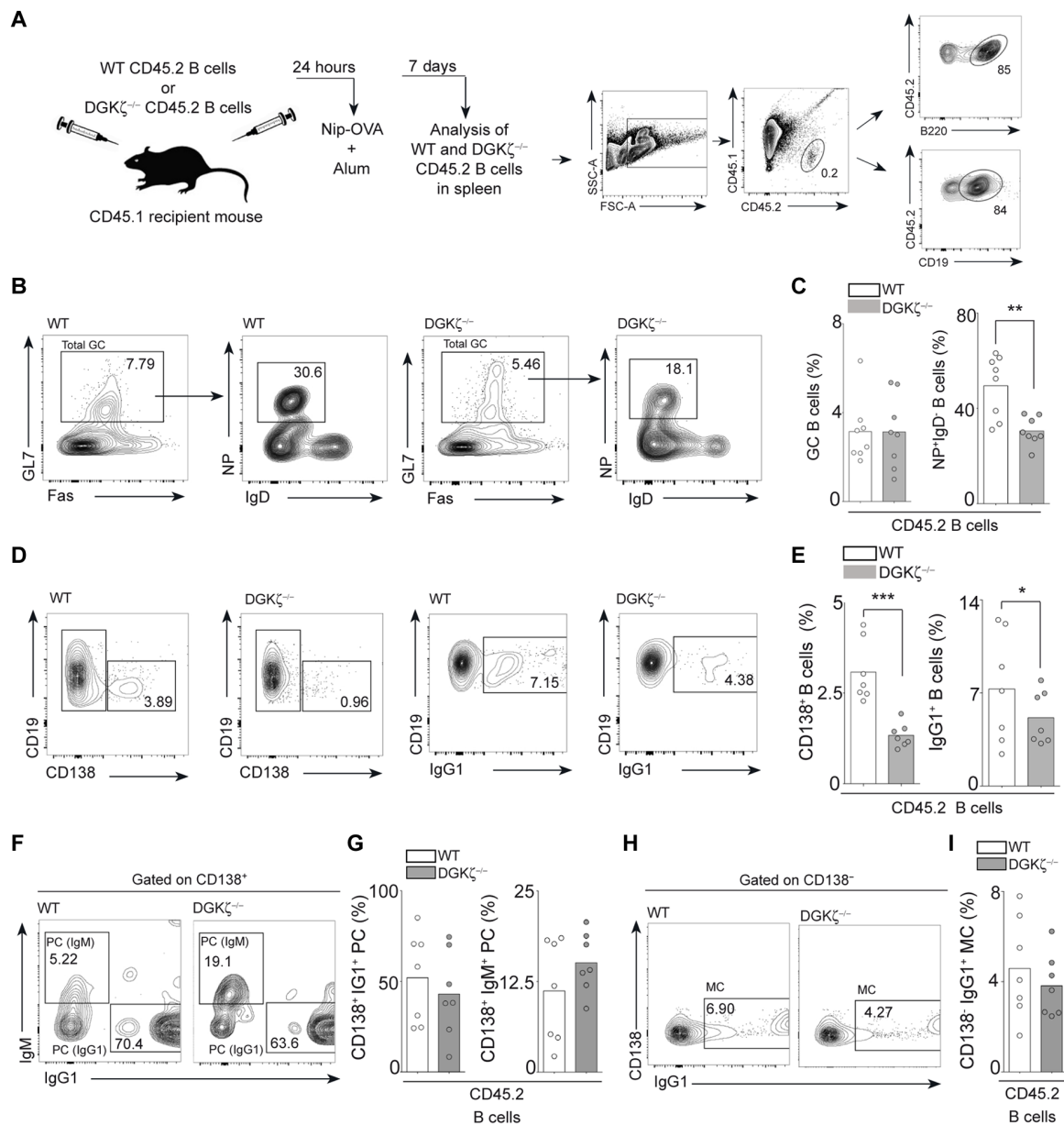


Fig. 6. $DGK\zeta^{-/-}$ B cells exhibit a decreased GC response in vivo. (A) Experimental design for comparing the in vivo responses of $DGK\zeta^{-/-}$ and WT $CD45.2^+$ B cells in immunocompetent $CD45.1^+$ mice. Right: Gating strategies to analyze $CD45.2^+$ B cells ($CD45.2^+ CD19^+$ or $CD45.2^+ B220^+$) isolated from the spleen. (B) Representative strategy to measure by flow cytometry the percentages of total GC ($GL7^+ Fas^+$) and NP-specific GC ($GL7^+ Fas^+ IgD^{neq} NP^+$) $CD45.2^+ B220^+$ B cells generated 7 days after immunization with the T cell-dependent antigen Nip-OVA with Alum. Representative density plots for WT and $DGK\zeta^{-/-}$ B cells are shown. The percentages of the gated cells are indicated. (C) Percentages of total GC B cells (left) and of NP-specific GC B cells (right) in the $CD45.2^+ B220^+$ WT or $DGK\zeta^{-/-}$ B cell populations in the spleen. Each dot represents a single mouse. (D) Representative density plots of PC ($CD19^+ CD138^+$) and class-switched IgG1 B cell ($CD19^+ IgG1^+$) generation for adoptively transferred $CD45.2^+$ WT or $DGK\zeta^{-/-}$ B cells. The percentages of the gated cells are indicated. (E) Percentages of PC and IgG1⁺ B cells in the $CD45.2^+ CD19^+$ WT or $DGK\zeta^{-/-}$ B cell populations in the spleen. Each dot represents a single mouse. (F) Representative density plots of IgM and IgG1 surface expression on PCs (gated as $CD19^+ CD138^+$; PC) for transferred $CD45.2^+$ WT or $DGK\zeta^{-/-}$ B cells. The percentages of the gated cells are indicated. (G) Percentages of IgG1⁺ PCs (left) and IgM⁺ PCs (right) for the indicated conditions. (H) Representative profile of IgG1 surface expression on $CD19^+ CD138^+$ B cells [memory-like cells (MC)] for transferred $CD45.2^+$ WT or $DGK\zeta^{-/-}$ B cells. The percentages of the gated cells are indicated. (I) Percentages of $CD138^+ IgG1^+$ MCs for the indicated conditions. Each dot in (G) to (I) represents a single mouse. Data in (C), (E), (G), and (I) are pooled from two independent experiments. * $P < 0.05$, ** $P < 0.01$, *** $P < 0.001$, by two-tailed, unpaired Student's *t* test.

and Rac activation (33). We propose that, in a similar fashion, the sequential actions of PIP_3 and PA determine DOCK2 dynamics and, thus, F-actin ring maintenance at the B cell immune synapse. BCR signaling initially leads to PI3K activation and PIP_3 production, whereas the PLC- $\gamma 2$ -mediated degradation of PIP_2 produces

the DAG that activates classical PKC. In turn, PKC phosphorylates $DGK\zeta$, driving its activation and relocation to the plasma membrane, where it produces PA (fig. S9).

$DGK\zeta^{-/-}$ and R59-treated B cells exhibited increased BCR-dependent Ca^{2+} influx. Ca^{2+} influx downstream of the BCR is mainly

driven by the PLC- γ 2-dependent and IP₃-dependent activation of store-operated Ca²⁺ channels (SOCs). Nonetheless, B cells express several members of the family of Ca²⁺-permeable transient receptor potential channels (TRPCs) (34). TRPC activation seems to be Ca²⁺ store independent and DAG sensitive (35–37). Previous work in the DT40 B cell line showed that DAG-dependent Ca²⁺ influx by TRPC3 enhances Ca²⁺ signaling downstream of the BCR and that TRPC3 promotes PLC- γ 2 translocation to the plasma membrane and activation, maintaining IP₃ and DAG production (26, 38). In addition, active TRPC3 retains PKC β at the plasma membrane through a direct interaction, which sustains ERK1/2 activation (26). The lack of DGK ζ activity enables DAG accumulation, which might amplify Ca²⁺ influx and signaling downstream of the BCR by inducing TRPC3 activation.

Cell polarization at the B cell immune synapse orchestrates the membrane-trafficking events that are required for antigen processing and presentation to T cells. MHC class II-containing lysosomes translocate together with the MTOC to the immune synapse, where their local secretions promote antigen extraction (29). The polarization of the MTOC and lysosomes depends on the GTPase Cdc42 and its effector, the atypical PKC ζ , which is part of the Par polarity complex together with Par3 and Par6 (29). Par3 is enriched at the B cell immune synapse and is involved in the transport of the MTOC and lysosomes to the immune synapse interface (39). DGK-derived PA promotes PKC ζ location and activity in nonimmune cells (11). In DGK ζ ^{-/-} OTI CD8⁺ cytotoxic T cells, impaired MTOC recruitment to the immune synapse correlates with reduced amounts of active (phosphorylated) PKC ζ (18). DAG accumulates at the CD4⁺ T cell immune synapse and establishes an intracellular gradient that drives MTOC polarization, which involves three novel PKC isoforms (ϵ , η , and θ) and the motor protein dynein (40, 41). DGK α has a major role in shaping the DAG gradient at the immune synapse and establishing T cell polarity (19). A report showed that Arp2/3-dependent F-actin nucleation at the MTOC connects this organelle with the nucleus in resting B cells and that BCR stimulation reduces F-actin content at the MTOC, enabling its detachment from the nucleus and polarization to the immune synapse (42). The defects in MTOC translocation in DGK ζ ^{-/-} and DGK-inhibited B cells suggest that DGK ζ promotes cell polarization events. More studies are necessary to relate DGK ζ with the PKC ζ /Par3 axis, F-actin nucleation at the MTOC, or the DAG gradient in B cells.

Actin cytoskeleton remodeling drives force generation in cells. Actin polymerization per se generates pushing forces, whereas F-actin, in combination with the contractile activity of myosin II, produces pulling forces. To generate and exert forces against the extracellular matrix, or another cell, cells connect protrusive and contractile F-actin dynamics to adhesion structures (43). Lymphocytes link actin dynamics to LFA-1-mediated adhesion at the immune synapse, which involves vinculin and talin. Our data point to DGK ζ being a regulator of force generation at the B cell immune synapse, which may be achieved by influencing LFA-1-mediated adhesion, actin polymerization, and myosin II activity downstream of the BCR. In T cells, F-actin flow and mechanical forces are important for LFA-1 activity at the immune synapse (44). DGK ζ might affect LFA-1-mediated adhesion through the activities of Rac, myosin, or both. In addition, DGK-produced PA promotes PIP5K activity and the subsequent generation of PIP₂, which recruits to the plasma membrane proteins that are involved in actin polymerization and adhesion site dynamics, such as vinculin, talin, and WASP

(4, 17, 45). Although further investigations are required to dissect the underlying mechanisms, DGK ζ appears to use the DOCK2-PAK1-Rac and PIP5K-PIP₂ axes to support mechanical force generation at the immune synapse. Our studies using the MFP technique showed sequential pushing, pulling, and cup-like stages during B cell immune synapse formation, similar to T cells (21, 46). Experiments involving inhibitor treatment of T cells indicate a main role of the actin cytoskeleton in generating pushing forces, whereas myosin activity is needed for the pulling/contractile stage, with PI3K-DOCK2 signaling also participating in the pulling phase (47). The reduced pushing and pulling forces values that we observed in DGK ζ ^{-/-} B cells correlated with impaired actin polymerization at the immune synapse and reduced myosin activation.

Two mutually nonexclusive mechanisms support antigen acquisition from the APC surface by B cells: local secretion of lysosomes at the immune synapse interface, which liberates proteases to facilitate antigen extraction (29), and myosin II-mediated pulling forces that promote the internalization of antigen-BCR complexes (22). Myosin II-derived forces enable discrimination of BCR affinity for the antigen, which is crucial for the T cell-dependent selection of high-affinity GC B cells (28). Our results suggest that the DGK ζ -mediated regulation of mechanical forces and MTOC translocation at the B cell immune synapse facilitate antigen acquisition and presentation to T cells. In our in vitro system, OVA was present with su-Ag at the planar lipid bilayer without the two components being physically attached to each other. This implies that lysosomal secretion and/or strong forces able to detach a piece of artificial membrane are required for OVA acquisition and degradation.

In a competitive in vivo environment, we demonstrated that the lack of DGK ζ resulted in reduced GC B cell activity and diminished numbers of antigen-specific GC B cells, PCs, and IgG1 class-switched B cells. A previous study addressed the role of DGK ζ in the B cell response with experiments involving the immunization of DGK ζ ^{-/-} mice with NP-Ficolin, a T-independent, type 2 antigen (3). This study reported increased numbers of antigen-specific IgM- and IgG₃-secreting PCs and increased serum concentrations of IgM and IgG₃ in DGK ζ ^{-/-} mice compared with those in WT mice, suggesting that DGK ζ limits the early PC response. In addition, the previous report used MD4 BCR (HEL-specific) transgenic B cells, WT (CD45.1) and DGK ζ ^{-/-} (CD45.2) mixed at 1:1 ratio, for adoptive transfer into immunocompetent mice. Mice were then immunized with HEL mutants of low and medium affinity conjugated to SRBC, a T cell-dependent antigen. The authors found increased numbers of GC B cells and IgM⁺ PCs generated by DGK ζ ^{-/-} B cells compared with those generated by WT B cells at the beginning of the Ab response (day 5) (3). Their model precluded analysis at later time points because MD4 B cells are unable to undergo class switching. The authors suggested that DGK ζ limits early PC generation in T cell-dependent responses by promoting antigen affinity discrimination by DAG signaling. Note that we evaluated later stages of the GC response. In our system, the reduced production of IgG1 B cells, supported by the in vitro data on antigen acquisition and presentation, provides evidence that DGK ζ determines the ability of B cells to acquire antigen and compete for T cell help. Nevertheless, the increased number of IgM⁺ PCs might reflect the enhanced early generation of PCs by DGK ζ -deficient B cells, which was previously described (3). In addition, our data showed that in vitro DAG-related activation (as determined by measuring Ca²⁺ influx, ERK1/2 activation, and CD69/CD25/CD86 expression) and proliferation in DGK ζ ^{-/-}

B cells are enhanced when compared with WT B cells after BCR stimulation, as also reported in that study (3). The later timing of analysis and impaired ability to receive T cell help might account for the reduced GC frequencies in our model compared with those in the previous study. B cell clone frequency and antigen affinity determine B cell recruitment to and interclonal competition at the GC (48). The affinity values reported for HEL^{3X} (low-affinity mutant) and NP are similar (K_D values are in the micromolar range), but distinct B cell precursor frequency might also explain the differences in results. B cell competition for antigen is likely lower in the previously published model than in the model use here, as all (and only) the transferred B cells recognize the antigen (HEL) used for immunization, which was not the case in our experimental approach. The method used for antigen administration (NIP-OVA in alum versus HEL on SRBCs) may also account for some of the differences between the two studies.

DGKs are currently considered as therapeutic targets to manipulate T cell function in autoimmune diseases and to subvert tumor immunosuppression. Increased amounts of DGK α and DGK ζ correlate with reduced effector function in tumor-infiltrating lymphocytes (49, 50). Pharmacological intervention to manipulate DGKs focuses on the capacity of drugs to limit DAG-mediated signals and subsequent gene transcription. Our study underlines the relevance of DGK ζ functions pertaining to PA generation for B cell function. The described roles for DGK ζ in organizing the B cell:APC interface might also apply to other immune cell interactions and should be considered when targeting DGKs therapeutically.

MATERIALS AND METHODS

Mice and B cell isolation

Primary B lymphocytes were isolated from the spleens of adult (10- to 20-week-old) WT, DGK $\zeta^{-/-}$ (51), DGK $\alpha^{-/-}$ (52), PI3K δ kinase-deficient knock-in [provided by D. F. Barber, Centro Nacional de Biotecnología (CNB)-Consejo Superior de Investigaciones Científicas (CSIC), Spain; (53)], and DOCK2-GFP knock-in [provided by J. Stein, University of Bern, Switzerland, and Y. Fukui, Kyushu University, Japan; (54)] mice, all of in which are on a C57BL/6 genetic background. Splenic B cells were purified by negative selection with mouse pan-T Dynabeads (DynaI Biotech, Invitrogen) after a Lympholyte step (Cedarlane Laboratories); we enriched to >90% B cells. Primary OTII CD4⁺ T cells were isolated from the spleens of adult OTII transgenic (OVA 323-339-specific TCR) mice (55) by negative selection using a CD4⁺ T cell isolation kit [magnetic-activated cell sorting (MACS), Miltenyi Biotec; purity, >90% CD4⁺ T cells]. Animal procedures were approved by the CNB-CSIC Bioethics Committee and conform to institutional, national, and European Union (EU) regulations. The A20 mouse B cell line was transiently transfected with plasmids encoding for GFP or Cherry fluorescent protein alone, or GFP- or cherry-tagged DGK ζ -WT or -DGK ζ -kinase-deficient (KD) constructs (9) by electroporation (260 mV, 950 μ F) and were used 20 hours later. Cells were cultured in complete RPMI (10 mM Hepes, 2 mM L-glutamine, and 50 μ M β -mercaptoethanol) supplemented with 10% fetal calf serum (FCS).

Real-time microscopy on planar lipid bilayers

Artificial planar lipid bilayers were assembled in FCS2 chambers (Bioptechs) as described previously (56). Briefly, unlabeled murine GPI-linked ICAM-1-containing 1,2-dioleoyl-PC (DOPC) liposomes

and DOPC liposomes containing biotinylated lipids were mixed with DOPC liposomes at distinct ratios to obtain specified molecular densities (ICAM-1 at 200 molecules/ μ m²; biotin lipids, as indicated in the figure legends). Artificial planar lipid bilayers were assembled on sulphochromic solution-treated coverslips in FCS2 closed flow chambers (Bioptechs) and blocked with phosphate-buffered saline (PBS)/2% FCS for 1 hour at room temperature. su-Ag was tethered to membranes by incubation with Alexa Fluor 647- or Alexa Fluor 555-conjugated streptavidin (Molecular Probes), which was followed by monobiotinylated rat anti- κ light chain monoclonal Ab (mAb; clone187.1). Monobiotinylation was achieved by labeling the Ab (0.5 mg/ml; 1 ml) with NHS-LC-LC-biotin (1 μ g/ml; 30 min, room temperature, in PBS; Pierce), followed by dialysis and analysis by flow cytometry. We estimated the number of molecules per square micrometer of GPI-ICAM-1 or anti- κ Ab at the lipid bilayers by immunofluorometric assay with anti-ICAM-1 or anti-rat IgG antibodies, respectively. We obtained the standard values from microbeads with distinct calibrated IgG-binding capacities (Bangs Laboratories). Before imaging, membranes were coated with murine recombinant CXCL13 (100 nM, Peptotech) for 20 min at room temperature. Lipids stock in chloroform were obtained from Avanti Polar Lipids Inc. WT and genetically modified B cells (4×10^6) were coinjected into the warmed chamber (37°C) for imaging. To distinguish them, one cell type was violet tracer labeled (0.1 μ M, 10 min, 37°C; Molecular Probes). Where indicated in the figure legends, B cells were pretreated with the pan-DGK inhibitor R59949 [10 μ M, 30 min, 37°C; half maximal inhibitory concentration (IC₅₀), 3.3 μ M; Sigma] or with the PI3K inhibitor LY294002 (10 μ M, 30 min, 37°C; Sigma) and washed before use. Confocal FL (1- μ m optical section), DIC, and IRM images were acquired every 30 s for 10 to 20 min. Consecutive videos were acquired when needed. Similarly, transfected A20 B cells (2×10^6) were injected and imaged. For Ca²⁺ flux measurements, B cells were labeled with Fluo-4FF (1 μ M, Molecular Probes) for 30 min at room temperature, injected into the warmed FCS2 chamber, and imaged every 10 s for 15 min at low quality to speed up acquisition. Assays were performed in chamber buffer [PBS, 0.5% FCS, D-glucose (0.5 g/liter), 2 mM MgCl₂, and 0.5 mM CaCl₂]. For exogenous PA assays, we used freshly prepared 10 mM PA stock [in 10 mM tris-HCl (pH 8.0) and 150 mM NaCl]. The cells were left in contact with the lipid bilayers for 10 min to form the immune synapse and then were imaged. At the 15-min time point, 0.1 mM PA (1 ml) was injected into the chamber buffer. After 30 min, the B cells were imaged. Images were acquired on an Axiovert LSM 510 META inverted microscope with a 40 \times oil immersion objective (Zeiss).

Immunofluorescence

Primary B cells or transfected A20 B cells were in contact with ICAM-1/CXCL13 lipid bilayers containing tethered su-Ag for 10 min, fixed with 4% paraformaldehyde for 10 min, at 37°C, permeabilized with PBS/0.1% Triton X-100 for 5 min at room temperature, blocked with PBS/2% FCS/2% bovine serum albumin (BSA) overnight at 4°C, and stained with Alexa Fluor 647-conjugated phalloidin (Molecular Probes) and the following antibodies: rabbit anti-phospho-ERK1/2 (Cell Signaling) with Alexa Fluor 488-conjugated goat anti-rabbit IgG (Southern Biotechnology), mouse anti-vinculin (clone hVIN-1; Sigma) with fluorescein isothiocyanate (FITC)-conjugated goat anti-mouse IgG1 (BD Biosciences). For PA assays, B cells were fixed at 30 min after PA exposure and stained for phalloidin as

described earlier. For MTOC analysis, B cells were mixed with unloaded or su-Ag-loaded pseudo-APCs (20 molecules/ μm^2) at a 1:1 ratio, cultured for 30 min at 37°C on poly-L-lysine-coated coverslips, fixed, permeabilized, and blocked as described earlier, stained with rabbit anti- γ -tubulin (T5192, Sigma) and Alexa Fluor 488-conjugated goat anti-rabbit IgG, and mounted using Fluoromount (Southern Biotech). FCS2 chambers and coverslips were imaged by confocal fluorescence microscopy as previously described.

Cell conjugates and activation assays

For cell activation assays, freshly isolated B cells (2×10^5) were cocultured with unloaded or su-Ag-loaded (20 molecules/ μm^2) planar lipid bilayers, assembled in glass-bottom p96-size wells for 20 hours, and then collected and analyzed by flow cytometry. To prepare pseudo-APCs, silica beads (5×10^6 ; 5- μm diameter; Bangs Laboratories) were washed in distilled water (2600g, 1 min, room temperature), incubated with 20 μl of DOPC liposomes containing GPI-linked ICAM-1 (200 molecules/ μm^2) and biotin lipids (20 or 1000 molecules/ μm^2) for 10 min at room temperature, washed twice with chamber buffer, blocked with PBS/2% FCS for 30 min, washed twice, incubated with the monobiotinylated su-Ag and 10 nM CXCL13 for 20 min, washed twice, and counted. All incubations were done in a rotary shaker at room temperature. For cell proliferation assays, B cells were labeled with CFSE tracer (0.1 μM , 10 min, 37°C), washed with complete RPMI/10% FCS, and cocultured with unloaded or su-Ag-loaded pseudo-APCs at specified ratios and with recombinant murine IL-4 (10 ng/ml; Peprotech) in flat-bottom p96 wells for 96 hours. The cells were collected, stained with APC-conjugated CD19, and analyzed for CFSE tracer dilution with a FACSCalibur cytometer (BD Biosciences). To assess antigen acquisition and T cell presentation, freshly isolated B cells (5×10^5) were cultured for 2 hours in contact with ICAM-1/CXCL13 planar lipid bilayers and assembled in glass-bottom p96-size wells. These planar bilayers contained distinct densities of biotinylated lipids (20, 100, 500, or 2500 molecules/ μm^2) and were loaded with a mixture of monobiotinylated su-Ag (5 $\mu\text{g}/\text{ml}$) and monobiotinylated Alexa Fluor 488-conjugated OVA (10 $\mu\text{g}/\text{ml}$; Molecular Probes) by previous coating with Alexa Fluor 647-conjugated streptavidin (Molecular Probes). OVA monobiotinylation was performed as described earlier for su-Ag. B cells were then collected; one-half of them (2.5×10^5) was treated with trypsin for 5 min at 37°C, washed with complete RPMI/10% FCS, and analyzed by flow cytometry for streptavidin and OVA fluorescence signals to measure antigen extraction. The other half of the B cells (2.5×10^5) was washed with complete RPMI/10% FCS and cocultured with CFSE tracer-labeled CD4⁺ OTII T cells (2.5×10^5) at 1:1 ratio in round-bottom p96 wells. After 72 hours, the culture medium was collected for IL-2 detection by enzyme-linked immunosorbent assay (ELISA) kit (IL-2 ELISA Max 413005, BioLegend), and the cells were collected, stained with Pacific Blue-conjugated rat anti-mouse B220, APC-conjugated rat anti-mouse CD4, and PE (phycoerythrin)-Cy7-conjugated rat anti-mouse CD25, and analyzed for CFSE tracer dilution and CD25 expression in the CD4⁺ T cell population with a fluorescence-activated cell sorting (FACS) LSR-II cytometer (BD Biosciences). When required, B cells were pretreated with the DGK inhibitor R59949 for 30 min before adding them to the planar lipid bilayers. The inhibitor was kept during the antigen extraction time (2 hours). When indicated in the figure legends, B cells were exposed to 0.1 mM PA for the 2 hours of antigen extraction.

Imaging data analysis

The frequency of immune synapse formation per imaged field was estimated as [number of B cells showing a central su-Ag cluster and IRM contact/total number of B cells (estimated by DIC)] \times 100, using Fiji [National Institutes of Health (NIH)] software. Confocal images (1- μm optical sections) were acquired at the contact plane or immune synapse plane. We used the IRM confocal image to focus on the B cell-artificial membrane contact plane and to define the immune synapse plane. Imaris 7.0 software (Bitplane) was used for the qualitative and quantitative analyses of fluorescence signals, as well as for cell contact area (IRM area) and su-Ag cluster area measurements. To set up the background of the fluorescence intensity signal, we used the fluorescence signal of the lipid bilayer in each case. To apply statistical analysis to the Ca²⁺ influx curves, we calculated the area under de curve (AUC) for each cell in each condition (WT, DGK $\zeta^{-/-}$, and R59 treated) and then compared the obtained AUC values with those of the control condition (untreated WT). To obtain the AUC value per cell, we sectioned the area in three trapezoids and calculated the area of each one; the AUC is the sum of the three trapezoid areas.

Western blotting analysis

Freshly isolated primary B cells (5×10^6) were cultured on a p48 plate in depletion medium (0.5 ml of complete RPMI) for 1 hour in the presence of 10 μM R59 when needed and then stimulated in an Ab-coated (goat anti-mouse IgM, μ -specific; Jackson ImmunoResearch) p48 plate for the times indicated in the figure legends. Wells were precoated with the appropriate Ab (5 $\mu\text{g}/\text{ml}$) in PBS for 1 hour at 37°C, washed, and used for analysis. To detect DGK isoforms or phosphorylated PAK1/2, isolated B cells (5×10^6) were cultured in complete RPMI, 10% FCS, without or with 10 μM R59 or 0.1 mM PA for 1 hour, and then were collected. Cells were lysed in lysis buffer [10 mM tris-HCl (pH 7.4), 150 mM NaCl, and 1 mM EDTA]/1% Triton X-100 with protease and phosphatase inhibitors (Roche) for 30 min at 4°C. Lysates were centrifuged at 20,000g for 30 min at 4°C, and the supernatants were collected and stored at -80°C. Total protein was quantified with the Micro BCA Protein Assay Kit (Thermo Scientific). Proteins were resolved by SDS-polyacrylamide gel electrophoresis (PAGE) and transferred to polyvinylidene difluoride membranes (Bio-Rad). Blots were blocked with TBS-T [10 mM tris-HCl (pH 8.0), 150 mM NaCl, and 0.1% Tween 20]/5% BSA for 1 hour at room temperature and incubated with rabbit anti-DGK ζ (ab105195; Abcam), anti-DGK α (11547-1-AP; Proteintech), anti-phospho (S473)-Akt (Cell Signaling), anti-phospho (Thr¹⁸/Ser¹⁹)-MLC (Cell Signaling), anti-phospho (S144)-PAK1/ (S141)-PAK2 (Cell Signaling), or loading control mouse anti- α -tubulin (clone DM1A; Sigma) or rabbit anti-glyceraldehyde-3-phosphate dehydrogenase (GAPDH) (FL305, Santa Cruz Biotech) overnight at 4°C. The blots were then incubated for 1 hour at room temperature with horseradish peroxidase-conjugated secondary antibodies (DAKO). Signals were detected with the enhanced chemiluminescence (ECL) detection system (GE Healthcare). Signal intensity values in arbitrary units (AU) for each protein were quantified with Fiji (NIH) software and were normalized to that of tubulin.

Immunization

Freshly isolated CD45.2⁺ WT or DGK $\zeta^{-/-}$ B cells (5×10^6 to 8×10^6) were adoptively transferred to CD45.1⁺ immunocompetent mice by intravenous injection. Twenty-four hours later, the mice were

immunized intraperitoneally with NIP-OVA (200 μ g; N-5041-10, Biosearch Technology) complexed with Alum (100 μ l; 77161, Thermo Scientific) diluted 1:1 in PBS (0.2 ml of final volume). Seven days after immunization, the spleens were harvested and processed for CD45.2⁺ B cell population analysis by flow cytometry.

Flow cytometry

B cells were stained with fluorochrome-conjugated (FITC, PE, or APC) rat anti-mouse IgD, CD19, CD25, CD69, or CD86 (BioLegend), and DyLight-649-conjugated Fab fragment goat anti-mouse IgM, μ -specific (Jackson ImmunoResearch) for 30 min at 4°C. Samples were acquired with a FACSCalibur cytometer (BD Biosciences). Splenocytes obtained from the immunizations were stained with the following fluorochrome-conjugated Ab mixes: rat anti-mouse CD45.1 (APC-Cy7), CD45.2 (APC), B220 (V450), CD95 (PE-Cy7), and GL7 (FITC), and with PE-conjugated NP(36) (N-5070-1, Biosearch Technology) for GC B cell analysis; rat anti-mouse CD45.1 (APC-Cy7), CD45.2 (Per-CP5.5), CD19 (PE-Cy7), CD138 (APC), IgG1 (PE), IgD (V450), and IgM (biotin) together with FITC-conjugated streptavidin for PC and IgG1⁺ B cell analysis; all antibodies were obtained from BD Biosciences. Samples were acquired in a FACSCanto II cytometer. Data were analyzed with FlowJo software (BD Biosciences).

Traction force microscopy

PAA gels were produced in 35-mm FD35 fluorodishes (World Precision Instruments Inc.). Dishes were first treated by ultraviolet (UV) irradiation for 2 min and then with 3-aminopropyltrimethoxysilane for 5 min and, lastly, washed thoroughly in distilled water before PAA gel preparation. Hydrophobic coverslips were prepared by incubation in Sigmacote (Sigma-Aldrich) for 3 min, which is followed by thorough washing and drying. A 500-Pa gel was prepared by diluting 40% PAA and 2% bis-acrylamide solutions to obtain stock solutions of 12% PAA/0.1% bis-acrylamide. We sonicated 167 μ l of this solution with 1% of 0.2- μ m-diameter carboxylated fluorescent (660/680) beads (Thermo Fisher Scientific) and then added 0.2 μ l of TEMED and 1% ammonium persulfate and mixed vigorously to initiate polymerization. A volume of 9 μ l of the PAA mixture was immediately pipetted onto the surface of the Fluorodish, and a Sigmacote-activated coverslip was carefully placed on top. Fluorodishes were immediately inverted to bring the beads to the surface of the gel. Polymerization was completed in 45 min. The top coverslip was then slowly peeled off and the gel was immediately immersed in PBS. Sulfo-SANPAH (Sigma-Aldrich), a surface functionalizing reagent with an amine-binding group and a photoactivable azide group, was used to crosslink molecules to the surface of the gel. Sulpho-SANPAH [150 μ l of stock (0.5 mg/ml) in 10 mM Hepes] was attached to the gel surface through UV light activation for 2 min. The gels were then washed with PBS, and the process was repeated. The gel was washed thoroughly with PBS and coated with 100 μ l of su-Ag (10 μ g/ml; rat anti- κ light chain mAb; clone187.1; BD Biosciences) alone or mixed with recombinant mouse ICAM-1-Fc (10 μ g/ml; BioLegend) by overnight incubation at 4°C. Freshly isolated WT and DGK ζ ^{-/-} B cells were mixed at 1:1 ratio (1×10^6), with one set of cells labeled with CFSE tracer to distinguish between them, and then added to the gels and imaged. Assays were performed in complete RPMI/10% FCS medium. All TFM movies were acquired at 37°C/4.5% CO₂ on an inverted spinning disk confocal microscope (Eclipse Ti Nikon/Roper spinning head) with a 60 \times /1.4 numerical aperture (NA) oil immersion objective (pixel size, 108 nm) with MetaMorph software

(Molecular Device, France) and a HQ2 Coolsnap Photometric camera. Time lapse was typically at a frame rate of one image per 5 s and lasted for 15 min. The traction force algorithm was based on that used by Butler *et al.* (57) and modified by Mandal *et al.* (58). Force reconstruction was conducted with the assumption that the substrate is a linear elastic half space, using Fourier transform traction cytometry with Tikhonov regularization (regularization parameter was set to 5×10^{-19}). The bead position in the reference image and the deformed one was measured using the multi-target tracking (MTT) algorithm (59). The problem of calculating the stress field from the displacement was solved in Fourier space and then inverted back to real space. The final stress field was obtained on a grid with 0.432- μ m spacing (four pixels). All calculations and image processing were performed in MATLAB. The mask of the cell (defined by the user based on fluorescence or bright field images) increased by 10% (dilation of the binary image using MATLAB morphological tools) and was used as domain of integration for the energy. Given the B cell size, the density of beads, and the magnitude of displacement, some parameters needed optimization for the analysis, in particular for the detection algorithm (MTT): search window size (5 pixels), particle radius (2.5 pixels), and maximum distance for nearest neighbor (4 pixels). The same parameters were applied for noise detection by measuring force in a non-stressed area not too far from the cell. Further calculations based on the output of the algorithm were performed to extract the total strain energy (scalar product force by displacement integrated over the entire cell area). Noise greater than a certain threshold (chosen at 3×10^{-17} J) indicated poorly acquired data (for example, due to defocus); the corresponding frames were, thus, eliminated from the analysis.

Micropipette force probe

MFP (21) uses a flexible glass micropipette as a cantilever to measure pushing and pulling forces generated by a single cell. We added supplementary, single-cell rheometer capabilities to measure the mechanical properties of the cell during its activation. Micropipettes were prepared as described previously (21, 47, 60, 61) by pulling borosilicate glass capillaries (Harvard Apparatus) with a P-97 micropipette puller (Sutter Instruments), cutting them with an MF-200 microforge (World Precision Instruments) and bending them at a 45° angle with an MF-900 microforge (Narishige). Micropipettes were held by micropipette holders (IM-H1, Narishige) placed at a 45° angle relative to a horizontal plane, so that their tips were in the focal plane of an inverted microscope under bright-field illumination (TiE, Nikon Instruments) equipped with a 100 \times oil immersion, 1.3 NA objective (Nikon Instruments), and placed on an air suspension table (Newport). The flexible micropipette was linked to a nonmotorized micropositioner (Thorlabs, Newton, NJ, USA) placed on top of a single-axis stage controlled with a piezo actuator (TPZ001; Thorlabs). The bending stiffness k of the flexible micropipette (about 0.2 nN/ μ m) was measured against a standard microindenter previously calibrated with a commercial force probe (model 406A; Aurora Scientific). The flexible micropipette aspirates a GPI-ICAM-1-containing lipid-coated bead with tethered su-Ag (100 molecules/ μ m²), while a second (rigid) micropipette holds a B cell at its tip. The B cell is brought in an adequate position using a motorized micromanipulator (MP-285; Sutter Instruments). Experiments were performed in glass-bottom petri dishes (Fluorodish, WPI) filled with about 5 ml of complete RPMI/10% FCS at room temperature. Images were acquired using

a Flash 4.0 complementary metal-oxide semiconductor (CMOS) camera (Hamamatsu Photonics). To perform rheological experiments, the setup automatically detects, at a rate of 400 to 500 Hz, the position of the bead at the tip of the force probe (X_{bead}) and imposes the position of the base of the flexible micropipette by regulating the position of the piezo stage. The deflection of the force probe is the difference between the position of the bead and the position of the piezo stage. The force applied to the cell is the product of this deflection by the bending stiffness k . A retroaction implemented in MATLAB (MathWorks) regulating both the camera by the Micromanager software (Edelstein 2014) and the piezo stage moves the latter in reaction to the measurement of the bead position to maintain a desired deflection of the cantilever. In this way, a controlled force is applied to the cell at any given time. The experiment was decomposed in two phases. During a first phase, the base of the force probe was translated at constant velocity $v = 1 \mu\text{m/s}$ toward the cell, leading to an increasing compressive force until a maximum compressive force of 240 pN was reached. Young's modulus of the cell was obtained by postprocessing the recordings made during this phase, as previously described (60). Then, the algorithm automatically switched to a second phase, during which an oscillatory force F was applied to the cell with an average force $F_0 = 60 \text{ pN}$, an amplitude $\Delta F = 20 \text{ pN}$, and at a frequency $f = 1 \text{ Hz}$. Knowing the position of the bead, we could deduce the changes in cell length (L) over time. L was approximately sinusoidal with an average value L_0 , an amplitude ΔL , and a phase lag φ relative to the imposed force. This phase lag results from the fact that the cell is not purely elastic but also viscous. In this study, we focused on the variations of the elastic properties of the cell, which we quantified with the stiffness K' of the cell that is expressed as $K' = (\Delta F/\Delta L) \cos \varphi$ (see the Supplementary Materials for K' parameter quantification). The average length L_0 evolves over time, and its measurement enables monitoring of cell growth or shrinkage.

Statistical analysis

Graphs and statistical analyses were performed using GraphPad Prism 6.0f software. Two-tailed unpaired Student's t tests were applied. $*P < 0.05$; $**P < 0.01$; $***P < 0.001$; $****P < 0.0001$.

SUPPLEMENTARY MATERIALS

stke.sciencemag.org/cgi/content/full/13/627/eaaw8214/DC1
 K' parameter quantification

Fig. S1. DGK ζ mediates LFA-1–dependent adhesion at the B cell immune synapse.

Fig. S2. DGK $\alpha^{-/-}$ B cells have no defects in immune synapse formation.

Fig. S3. DGK ζ overexpression enhances LFA-1–mediated adhesion as well as vinculin and F-actin content at the A20 B cell immune synapse.

Fig. S4. Exogenous PA modifies the su-Ag central cluster at the B cell immune synapse.

Fig. S5. DGK ζ -derived PA in combination with PI3K-generated PIP $_3$ mediates F-actin polymerization at the B cell immune synapse.

Fig. S6. TFM and MFP experimental setup and analysis of relative p-ERK abundance at the immune synapse of WT and DGK $\alpha^{-/-}$ B cells.

Fig. S7. Experimental setup for the evaluation of antigen extraction by B cells and presentation to OTII CD4 $^+$ T cells.

Fig. S8. GC response of recipient CD45.1 $^+$ B cells.

Fig. S9. Model for DGK ζ roles and lipid signaling interplay at the B cell immune synapse.

Movie S1. Stress maps generated by WT B cells contacting su-Ag–coated substrates.

Movie S2. Stress maps generated by DGK $\zeta^{-/-}$ B cells contacting su-Ag–coated substrates.

Movie S3. Stress maps generated by WT B cells contacting su-Ag– and ICAM-1-Fc–coated substrates.

Movie S4. Stress maps generated by DGK $\zeta^{-/-}$ B cells contacting su-Ag– and ICAM-1-Fc–coated substrates.

Movie S5. MFP assay of a WT B cell in the absence of su-Ag.

Movie S6. MFP assay of a WT B cell in the presence of su-Ag.

Movie S7. MFP assay of a DGK $\zeta^{-/-}$ B cell in the presence of su-Ag.

Movie S8. MFP assay of an R59-treated WT B cell in the presence of su-Ag.

Reference (62)

[View/request a protocol for this paper from Bio-protocol.](#)

REFERENCES AND NOTES

1. I. Merida, E. Andrada, S. I. Gharbi, A. Avila-Flores, Redundant and specialized roles for diacylglycerol kinases α and zeta in the control of T cell functions. *Sci. Signal.* **8**, re6 (2015).
2. G. Baldanzi, V. Bettio, V. Malacarne, A. Graziani, Diacylglycerol kinases: Shaping diacylglycerol and phosphatidic acid gradients to control cell polarity. *Front. Cell Dev. Biol.* **4**, 140 (2016).
3. M. L. Wheeler, M. B. Dong, R. Brink, X. P. Zhong, A. L. DeFranco, Diacylglycerol kinase zeta limits B cell antigen receptor-dependent activation of ERK signaling to inhibit early antibody responses. *Sci. Signal.* **6**, ra91 (2013).
4. J. Saez de Guinoa, L. Barrio, Y. R. Carrasco, Vinculin arrests motile B cells by stabilizing integrin clustering at the immune synapse. *J. Immunol.* **191**, 2742–2751 (2013).
5. Y. R. Carrasco, S. J. Fleire, T. Cameron, M. L. Dustin, F. D. Batista, LFA-1/ICAM-1 interaction lowers the threshold of B cell activation by facilitating B cell adhesion and synapse formation. *Immunity* **20**, 589–599 (2004).
6. A. Grakoui, S. K. Bromley, C. Sumen, M. M. Davis, A. S. Shaw, P. M. Allen, M. L. Dustin, The immunological synapse: a molecular machine controlling T cell activation. *Science* **285**, 221–227 (1999).
7. C. R. Monks, B. A. Freiberg, H. Kupfer, N. Sciaky, A. Kupfer, Three-dimensional segregation of supramolecular activation clusters in T cells. *Nature* **395**, 82–86 (1998).
8. M. Spitaler, E. Emslie, C. D. Wood, D. Cantrell, Diacylglycerol and protein kinase D localization during T lymphocyte activation. *Immunity* **24**, 535–546 (2006).
9. S. I. Gharbi, E. Rincon, A. Avila-Flores, P. Torres-Ayuso, M. Almena, M. A. Cobos, J. P. Albar, I. Merida, Diacylglycerol kinase zeta controls diacylglycerol metabolism at the immunological synapse. *Mol. Biol. Cell* **22**, 4406–4414 (2011).
10. R. P. Joshi, A. M. Schmidt, J. Das, D. Pytel, M. J. Riese, M. Lester, J. A. Diehl, E. M. Behrens, T. Kambayashi, G. A. Koretzky, The zeta isoform of diacylglycerol kinase plays a predominant role in regulatory T cell development and TCR-mediated ras signaling. *Sci. Signal.* **6**, ra102 (2013).
11. F. Chianale, E. Rainero, C. Cianflone, V. Bettio, A. Pighini, P. E. Porporato, N. Filigheddu, G. Serini, F. Sinigaglia, G. Baldanzi, A. Graziani, Diacylglycerol kinase α mediates HGF-induced Rac activation and membrane ruffling by regulating atypical PKC and RhoGDI. *Proc. Natl. Acad. Sci. U.S.A.* **107**, 4182–4187 (2010).
12. Y. Yakubchik, H. Abramovici, J. C. Maillet, E. Daher, C. Obagi, R. J. Parks, M. K. Topham, S. H. Gee, Regulation of neurite outgrowth in N1E-115 cells through PDZ-mediated recruitment of diacylglycerol kinase zeta. *Mol. Cell. Biol.* **25**, 7289–7302 (2005).
13. H. Abramovici, A. B. Hogan, C. Obagi, M. K. Topham, S. H. Gee, Diacylglycerol kinase-zeta localization in skeletal muscle is regulated by phosphorylation and interaction with syntrophins. *Mol. Biol. Cell* **14**, 4499–4511 (2003).
14. E. Rainero, P. T. Caswell, P. A. Muller, J. Grindlay, M. W. McCaffrey, Q. Zhang, M. J. Wakelam, K. H. Vousden, A. Graziani, J. C. Norman, Diacylglycerol kinase α controls RCP-dependent integrin trafficking to promote invasive migration. *J. Cell Biol.* **196**, 277–295 (2012).
15. G. H. Jenkins, P. L. Fiset, R. A. Anderson, Type I phosphatidylinositol 4-phosphate 5-kinase isoforms are specifically stimulated by phosphatidic acid. *J. Biol. Chem.* **269**, 11547–11554 (1994).
16. A. N. Roach, Z. Wang, P. Wu, F. Zhang, R. B. Chan, Y. Yonekubo, G. Di Paolo, A. A. Gorfe, G. Du, Phosphatidic acid regulation of PIPKI is critical for actin cytoskeletal reorganization. *J. Lipid Res.* **53**, 2598–2609 (2012).
17. G. Di Paolo, P. De Camilli, Phosphoinositides in cell regulation and membrane dynamics. *Nature* **443**, 651–657 (2006).
18. E. Andrada, M. Almena, J. S. de Guinoa, S. V. Merino-Cortés, R. Liebana, R. Arcos, S. Carrasco, Y. R. Carrasco, I. Merida, Diacylglycerol kinase zeta limits the polarized recruitment of diacylglycerol-enriched organelles to the immune synapse in T cells. *Sci. Signal.* **9**, ra127 (2016).
19. A. Chauveau, A. Le Floch, N. S. Bantilan, G. A. Koretzky, M. Huse, Diacylglycerol kinase α establishes T cell polarity by shaping diacylglycerol accumulation at the immunological synapse. *Sci. Signal.* **7**, ra82 (2014).
20. R. Basu, M. Huse, Mechanical communication at the immunological synapse. *Trends Cell Biol.* **27**, 241–254 (2017).
21. A. Sawicka, A. Babataheri, S. Dogniaux, A. I. Barakat, D. Gonzalez-Rodriguez, C. Hivroz, J. Husson, Micropipette force probe to quantify single-cell force generation: application to T-cell activation. *Mol. Biol. Cell* **28**, 3229–3239 (2017).

22. E. Natkanski, W. Y. Lee, B. Mistry, A. Casal, J. E. Molloy, P. Tolar, B cells use mechanical energy to discriminate antigen affinities. *Science* **340**, 1587–1590 (2013).
23. A. Le Floch, Y. Tanaka, N. S. Bantilan, G. Voisinne, G. Altan-Bonnet, Y. Fukui, M. Huse, Annular PIP3 accumulation controls actin architecture and modulates cytotoxicity at the immunological synapse. *J. Exp. Med.* **210**, 2721–2737 (2013).
24. H. Abramovici, P. Mojtabaie, R. J. Parks, X. P. Zhong, G. A. Koretzky, M. K. Topham, S. H. Gee, Diacylglycerol kinase zeta regulates actin cytoskeleton reorganization through dissociation of Rac1 from RhoGDI. *Mol. Biol. Cell* **20**, 2049–2059 (2009).
25. J. Wang, F. Lin, Z. Wan, X. Sun, Y. Lu, J. Huang, F. Wang, Y. Zeng, Y. H. Chen, Y. Shi, W. Zheng, Z. Li, C. Xiong, W. Liu, Profiling the origin, dynamics, and function of traction force in B cell activation. *Sci. Signal.* **11**, eaai9192 (2018).
26. T. Numaga, M. Nishida, S. Kiyonaka, K. Kato, M. Katano, E. Mori, T. Kurosaki, R. Inoue, M. Hikida, J. W. Putney Jr., Y. Mori, Ca²⁺ influx and protein scaffolding via TRPC3 sustain PKC β and ERK activation in B cells. *J. Cell Sci.* **123**, 927–938 (2010).
27. M. I. Yuseff, A. M. Lennon-Dum enil, B cells use conserved polarity cues to regulate their antigen processing and presentation functions. *Front. Immunol.* **6**, 251 (2015).
28. C. R. Nowosad, K. M. Spillane, P. Tolar, Germinal center B cells recognize antigen through a specialized immune synapse architecture. *Nat. Immunol.* **17**, 870–877 (2016).
29. M. I. Yuseff, A. Reversat, D. Lankar, J. Diaz, I. Fanget, P. Pierobon, V. Randrian, N. Larochette, F. Vascotto, C. Desdouets, B. Jauffred, Y. Bellaiche, S. Gasman, F. Darchen, C. Desnos, A. M. Lennon-Dum enil, Polarized secretion of lysosomes at the B cell synapse couples antigen extraction to processing and presentation. *Immunity* **35**, 361–374 (2011).
30. R. Ard, K. Mulatz, H. Abramovici, J. C. Maillet, A. Fottinger, T. Foley, M. R. Byham, T. A. Iqbal, A. Yoneda, J. R. Couchman, R. J. Parks, S. H. Gee, Diacylglycerol kinase ζ regulates RhoA activation via a kinase-independent scaffolding mechanism. *Mol. Biol. Cell* **23**, 4008–4019 (2012).
31. V. D. Delorme-Walker, J. R. Peterson, J. Chernoff, C. M. Waterman, G. Danuser, C. DerMardirossian, G. M. Bokoch, Pak1 regulates focal adhesion strength, myosin IIA distribution, and actin dynamics to optimize cell migration. *J. Cell Biol.* **193**, 1289–1303 (2011).
32. S. Dharmawardhane, L. C. Sanders, S. S. Martin, R. H. Daniels, G. M. Bokoch, Localization of p21-activated kinase 1 (PAK1) to pinocytotic vesicles and cortical actin structures in stimulated cells. *J. Cell Biol.* **138**, 1265–1278 (1997).
33. A. Nishikimi, H. Fukuhara, W. Su, T. Hongu, S. Takasuga, Y. Mihara, Q. Cao, F. Sanematsu, M. Kanai, H. Hasegawa, Y. Tanaka, M. Shibasaki, Y. Kanaho, T. Sasaki, M. A. Frohman, Y. Fukui, Sequential regulation of DOCK2 dynamics by two phospholipids during neutrophil chemotaxis. *Science* **324**, 384–387 (2009).
34. Y. Mori, M. Wakamori, T. Miyakawa, M. Hermosura, Y. Hara, M. Nishida, K. Hirose, A. Mizushima, M. Kurosaki, E. Mori, K. Gotoh, T. Okada, A. Fleig, R. Penner, M. Iino, T. Kurosaki, Transient receptor potential 1 regulates capacitative Ca²⁺ entry and Ca²⁺ release from endoplasmic reticulum in B lymphocytes. *J. Exp. Med.* **195**, 673–681 (2002).
35. P. Lucas, K. Ukhanov, T. Leinders-Zufall, F. Zufall, A diacylglycerol-gated cation channel in vomeronasal neuron dendrites is impaired in TRPC2 mutant mice: mechanism of pheromone transduction. *Neuron* **40**, 551–561 (2003).
36. T. Hofmann, A. G. Obukhov, M. Schaefer, C. Harteneck, T. Gudermann, G. Schultz, Direct activation of human TRPC6 and TRPC3 channels by diacylglycerol. *Nature* **397**, 259–263 (1999).
37. T. Okada, R. Inoue, K. Yamazaki, A. Maeda, T. Kurosaki, T. Yamakuni, I. Tanaka, S. Shimizu, K. Ikenaka, K. Imoto, Y. Mori, Molecular and functional characterization of a novel mouse transient receptor potential protein homologue TRP7. Ca²⁺-permeable cation channel that is constitutively activated and enhanced by stimulation of G protein-coupled receptor. *J. Biol. Chem.* **274**, 27359–27370 (1999).
38. M. Nishida, K. Sugimoto, Y. Hara, E. Mori, T. Morii, T. Kurosaki, Y. Mori, Amplification of receptor signalling by Ca²⁺ entry-mediated translocation and activation of PLC γ 2 in B lymphocytes. *EMBO J.* **22**, 4677–4688 (2003).
39. A. Reversat, M. I. Yuseff, D. Lankar, O. Malbec, D. Obino, M. Maurin, N. V. Penmarcha, A. Amoroso, L. Sengmanivong, G. G. Gundersen, I. Mellman, F. Darchen, C. Desnos, P. Pierobon, A. M. Lennon-Dum enil, Polarity protein Par3 controls B-cell receptor dynamics and antigen extraction at the immune synapse. *Mol. Biol. Cell* **26**, 1273–1285 (2015).
40. E. J. Quann, E. Merino, T. Furuta, M. Huse, Localized diacylglycerol drives the polarization of the microtubule-organizing center in T cells. *Nat. Immunol.* **10**, 627–635 (2009).
41. E. J. Quann, X. Liu, G. Altan-Bonnet, M. Huse, A cascade of protein kinase C isozymes promotes cytoskeletal polarization in T cells. *Nat. Immunol.* **12**, 647–654 (2011).
42. D. Obino, F. Farina, O. Malbec, P. J. Saez, M. Maurin, J. Gaillard, F. Dingli, D. Loew, A. Gautreau, M. I. Yuseff, L. Blanchoin, M. Thery, A. M. Lennon-Dum enil, Actin nucleation at the centrosome controls lymphocyte polarity. *Nat. Commun.* **7**, 10969 (2016).
43. M. Huse, Mechanical forces in the immune system. *Nat. Rev. Immunol.* **17**, 679–690 (2017).
44. W. A. Comrie, A. Babich, J. K. Burkhardt, F-actin flow drives affinity maturation and spatial organization of LFA-1 at the immunological synapse. *J. Cell Biol.* **208**, 475–491 (2015).
45. K. Ling, N. J. Schill, M. P. Wagoner, Y. Sun, R. A. Anderson, Movin' on up: the role of PtdIns(4,5)P(2) in cell migration. *Trends Cell Biol.* **16**, 276–284 (2006).
46. J. Husson, K. Chemin, A. Bohineust, C. Hivroz, N. Henry, Force generation upon T cell receptor engagement. *PLOS ONE* **6**, e19680 (2011).
47. R. Basu, B. M. Whitlock, J. Husson, A. Le Floch, W. Jin, A. Oyler-Yaniv, F. Dotiwala, G. Giannone, C. Hivroz, N. Biais, J. Lieberman, L. C. Kam, M. Huse, Cytotoxic T cells use mechanical force to potentiate target cell killing. *Cell* **165**, 100–110 (2016).
48. R. K. Abbott, J. H. Lee, S. Menis, P. Skog, M. Rossi, T. Ota, D. W. Kulp, D. Bhullar, O. Kalyuzhnyi, C. Havenar-Daughton, W. R. Schief, D. Nemazee, S. Crotty, Precursor frequency and affinity determine B cell competitive fitness in germinal centers, tested with germline-targeting HIV vaccine immunogens. *Immunity* **48**, 133–146.e6 (2018).
49. P. U. Prinz, A. N. Mandler, I. Masouris, L. Durner, R. Oberneder, E. Noessner, High DGK- α and disabled MAPK pathways cause dysfunction of human tumor-infiltrating CD8+ T cells that is reversible by pharmacologic intervention. *J. Immunol.* **188**, 5990–6000 (2012).
50. E. K. Moon, L. C. Wang, D. V. Dolfi, C. B. Wilson, R. Ranganathan, J. Sun, V. Kapoor, J. Scholler, E. Pure, M. C. Milone, C. H. June, J. L. Riley, E. J. Wherry, S. M. Albelda, Multifactorial T-cell hypofunction that is reversible can limit the efficacy of chimeric antigen receptor-transduced human T cells in solid tumors. *Clin. Cancer Res.* **20**, 4262–4273 (2014).
51. X. P. Zhong, E. A. Hainey, B. A. Olenchock, M. S. Jordan, J. S. Maltzman, K. E. Nichols, H. Shen, G. A. Koretzky, Enhanced T cell responses due to diacylglycerol kinase zeta deficiency. *Nat. Immunol.* **4**, 882–890 (2003).
52. B. A. Olenchock, R. Guo, J. H. Carpenter, M. Jordan, M. K. Topham, G. A. Koretzky, X. P. Zhong, Disruption of diacylglycerol metabolism impairs the induction of T cell energy. *Nat. Immunol.* **7**, 1174–1181 (2006).
53. K. Okkenhaug, A. Bilancio, G. Farjot, H. Priddle, S. Sancho, E. Peskett, W. Pearce, S. E. Meek, A. Salpekar, M. D. Waterfield, A. J. Smith, B. Vanhaesebroeck, Impaired B and T cell antigen receptor signaling in p110delta PI 3-kinase mutant mice. *Science* **297**, 1031–1034 (2002).
54. Y. Kunisaki, A. Nishikimi, Y. Tanaka, R. Taki, M. Noda, A. Inayoshi, K. Watanabe, F. Sanematsu, T. Sasazuki, T. Sasaki, Y. Fukui, DOCK2 is a Rac activator that regulates motility and polarity during neutrophil chemotaxis. *J. Cell Biol.* **174**, 647–652 (2006).
55. M. J. Barnden, J. Allison, W. R. Heath, F. R. Carbone, Defective TCR expression in transgenic mice constructed using cDNA-based α - and β -chain genes under the control of heterologous regulatory elements. *Immunol. Cell Biol.* **76**, 34–40 (1998).
56. J. S aez de Guinoa, L. Barrio, M. Mellado, Y. R. Carrasco, CXCL13/CXCR5 signaling enhances B-cell receptor-triggered B-cell activation by shaping cell dynamics. *Blood* **118**, 1560–1569 (2011).
57. J. P. Butler, I. M. Tolic-Norrelykke, B. Fabry, J. J. Fredberg, Traction fields, moments, and strain energy that cells exert on their surroundings. *Am. J. Physiol. Cell Physiol.* **282**, C595–C605 (2002).
58. K. Mandal, I. Wang, E. Vitiello, L. A. Orellana, M. Bolland, Cell dipole behaviour revealed by ECM sub-cellular geometry. *Nat. Commun.* **5**, 5749 (2014).
59. A. Serg e, N. Bertaux, H. Rigneault, D. Marguet, Dynamic multiple-target tracing to probe spatiotemporal cartography of cell membranes. *Nat. Methods* **5**, 687–694 (2008).
60. L. Guillou, A. Babataheri, P. H. Puech, A. I. Barakat, J. Husson, Dynamic monitoring of cell mechanical properties using profile microindentation. *Sci. Rep.* **6**, 21529 (2016).
61. L. Guillou, A. Babataheri, M. Saitakis, A. Bohineust, S. Dogniaux, C. Hivroz, A. I. Barakat, J. Husson, T-lymphocyte passive deformation is controlled by unfolding of membrane surface reservoirs. *Mol. Biol. Cell* **27**, 3574–3582 (2016).
62. B. Fabry, G. N. Maksym, J. P. Butler, M. Glogauer, D. Navajas, J. J. Fredberg, Scaling the microrheology of living cells. *Phys. Rev. Lett.* **87**, 148102 (2001).

Acknowledgments: We thank M. Mellado and C. R. Jimenez-Saiz (CNB-CSIC) for the critical review of the manuscript, and M. Bolland (Iphig, Grenoble) for providing tools and suggestions for TFM experiments. We acknowledge the PICT-IBISA imaging platform at Institut Curie, a member of the French National Research Infrastructure France-BiImaging (ANR-10-INBS-04). **Funding:** S.V.M.-C. is supported by an FPI contract from the Spanish Ministry of Economy (MINECO; BES-2014-068006). This work was supported by grants from the MINECO (BFU2013-48828-P), from the Worldwide Cancer Research (WCR; grant reference number 15-1322), and from MCIU/AEI/FEDER EU (RTI2018-101345-B-I00) to Y.R.C. J.H. has benefited from the financial support of the LabeX LaSIPS (ANR-10-LABX-0040-LaSIPS), managed by the French National Research Agency under the "Investissements d'avenir" program (no. ANR-11-IDEX-0003-02), and from PEPS CNRS funding. **Author contributions:**

S.V.M.-C. designed parts of the study, performed experiments, analyzed the data, and assisted in manuscript preparation; S.R.G. and S.R.-G. performed some experiments, analyzed the data, and assisted in manuscript preparation; A.M.-R. and B.A. performed in vitro antigen presentation and in vivo immunization experiments, assisted in the data analysis, and provided input into the project; R.L. and I.M. provided DGK ζ ^{-/-} and DGK α ^{-/-} mice, DGK ζ constructs, and input into the project; J.P., A.-M.L.D., and P.P. performed and analyzed the TFM experiments and provided input into the project; J.H. performed and analyzed the MFP experiments and provided input into the project; and Y.R.C. designed and supervised all aspects of the work and wrote the manuscript. **Competing interests:** The authors declare that they have no competing interests. **Data and materials availability:** All data needed to evaluate the conclusions in the paper are present in the paper or the Supplementary Materials.

Submitted 28 January 2019
Resubmitted 29 July 2019
Accepted 31 March 2020
Published 14 April 2020
10.1126/scisignal.aaw8214

Citation: S. V. Merino-Cortés, S. R. Gardeta, S. Roman-Garcia, A. Martínez-Riaño, J. Pineau, R. Liebana, I. Merida, A.-M. L. Dumenil, P. Pierobon, J. Husson, B. Alarcon, Y. R. Carrasco, Diacylglycerol kinase ζ promotes actin cytoskeleton remodeling and mechanical forces at the B cell immune synapse. *Sci. Signal.* **13**, eaaw8214 (2020).

Diacylglycerol kinase ζ promotes actin cytoskeleton remodeling and mechanical forces at the B cell immune synapse

Sara V. Merino-Cortés, Sofia R. Gardeta, Sara Roman-García, Ana Martínez-Riaño, Judith Pineau, Rosa Liebana, Isabel Merida, Ana-Maria Lennon Dumenil, Paolo Pierobon, Julien Husson, Balbino Alarcon and Yolanda R. Carrasco

Sci. Signal. **13** (627), eaaw8214.
DOI: 10.1126/scisignal.aaw8214

Balancing B cell signals

Diacylglycerol kinases (DGKs) catalyze the conversion of the lipid signaling molecule DAG into phosphatidic acid (PA), both of which have distinct effects. Merino-Cortés *et al.* found that the DGK ζ isoform was critical in promoting signaling required for the optimal function of B cells. Compared with wild-type B cells, DGK ζ -deficient B cells exhibited decreased mechanical forces at the plasma membrane, impairing the ability of these cells to form stable contacts with antigen-presenting cells, extract antigen, and present it to T cells. As a result, mice with DGK ζ -deficient B cells showed diminished antibody responses in germinal centers. These data suggest that DGK ζ regulates the balance in signaling between DAG and PA that is required for optimal B cell function.

ARTICLE TOOLS

<http://stke.sciencemag.org/content/13/627/eaaw8214>

SUPPLEMENTARY MATERIALS

<http://stke.sciencemag.org/content/suppl/2020/04/10/13.627.eaaw8214.DC1>

RELATED CONTENT

<http://stke.sciencemag.org/content/sigtrans/11/542/eaai9192.full>
<http://stke.sciencemag.org/content/sigtrans/12/571/eaao7194.full>
<http://stke.sciencemag.org/content/sigtrans/11/533/eaah6692.full>
<http://stke.sciencemag.org/content/sigtrans/11/532/eaal1506.full>

REFERENCES

This article cites 62 articles, 35 of which you can access for free
<http://stke.sciencemag.org/content/13/627/eaaw8214#BIBL>

PERMISSIONS

<http://www.sciencemag.org/help/reprints-and-permissions>

Use of this article is subject to the [Terms of Service](#)

Science Signaling (ISSN 1937-9145) is published by the American Association for the Advancement of Science, 1200 New York Avenue NW, Washington, DC 20005. The title *Science Signaling* is a registered trademark of AAAS.

Copyright © 2020 The Authors, some rights reserved; exclusive licensee American Association for the Advancement of Science. No claim to original U.S. Government Works

C.3 Collaborative Research article 3

CELL BIOLOGY

Pinching the cortex of live cells reveals thickness instabilities caused by myosin II motors

Valentin Laplaud^{1,2}, Nicolas Levernier³, Judith Pineau⁴, Mabel San Roman⁴, Lucie Barbier², Pablo J. Sáez², Ana-Maria Lennon-Duménil⁴, Pablo Vargas², Karsten Kruse⁵, Olivia du Roure^{1*}, Matthieu Piel^{2*}, Julien Heuvingsh^{1*}

The cell cortex is a contractile actin meshwork, which determines cell shape and is essential for cell mechanics, migration, and division. Because its thickness is below optical resolution, there is a tendency to consider the cortex as a thin uniform two-dimensional layer. Using two mutually attracted magnetic beads, one inside the cell and the other in the extracellular medium, we pinch the cortex of dendritic cells and provide an accurate and time-resolved measure of its thickness. Our observations draw a new picture of the cell cortex as a highly dynamic layer, harboring large fluctuations in its third dimension because of actomyosin contractility. We propose that the cortex dynamics might be responsible for the fast shape-changing capacity of highly contractile cells that use amoeboid-like migration.

INTRODUCTION

Dynamic cytoskeletal networks associated with the cell surface define the shape of mammalian cells (1, 2). In particular, the actin cortex, a thin network of actin filaments just beneath the plasma membrane, plays a central role in shaping the cell surface (3) and in defining its mechanical properties (4, 5). The actin cortex comprises, in addition to actin filaments, motors, membrane and actin linker proteins, actin nucleators (6) and cross-linkers, and regulatory proteins (7), which, together, render animal cell shape highly dynamic and able to adapt to external stimuli in a variety of physiological contexts such as cell migration or tissue morphogenesis.

Despite its central importance in cellular morphogenesis, the actin cortex remains poorly characterized (8). Its physical dimension (thickness) was only recently measured in cultured mammalian cells, using optical methods (9–11), but whether and to which degree this thickness varies in time is not known. So far, cell cortex mechanics has been probed through shallow indentation of the cell with an atomic force microscope (12) or through the twisting of ferromagnetic beads attached to the cell surface (13), but it is difficult in these experiments to separate the contribution of the cell cortex from the contribution of the rest of the cytoskeleton and cell organelles.

Since its discovery, there is a tendency to consider the cortex as a uniform two-dimensional (2D) structure, and its spatial and temporal heterogeneities remain largely unexplored (4, 8). This is, at least, partly due to experimental limitations in imaging a structure whose thickness is smaller than the optical resolution and also to the fact that contact probing can only be realized from the outside of the cell. In this work, we circumvent this obstacle by using a pair of probes (magnetic beads), one located inside the cell and the other on the outside. The attraction between the beads is controlled by an

external magnetic field, allowing us to slightly pinch the cortical layer. We can, in this manner, measure with unprecedented spatial accuracy and temporal resolution the thickness and dynamics of the cell cortex.

RESULTS

The magnetic pincher: A robust method to measure the physical properties of the cell cortex in live cells

Inspired by our previous work in which we probed thin layers of actin networks assembled in vitro between superparamagnetic beads (14, 15), we develop a new experimental setup in which two magnetic beads pinch the cell cortex, one being inside the cell and the other outside (Fig. 1A, beads 1 and 2). In the present work, we probe the cortex of primary bone marrow–derived dendritic cells from mice. These cells display amoeboid motility: a migration mode independent of focal adhesions, stress fibers, or large lamellipodial protrusions, which mostly rely on the fast remodeling of their actin cortex (16–19). Dendritic cells can also ingest large quantities of extracellular material including fluid (macropinocytosis) and particles (phagocytosis). This environment sampling activity allows them to take up antigens, which is the basis of their immune function and, in the present case, enables entry of large magnetic beads, independently of specific receptor engagement. Cells loaded with uptaken beads and mixed with freely floating beads are placed in an external homogeneous magnetic field. The field induces a tunable attractive force between the beads, which then pinch the cell cortex between them (Fig. 1B). Constant low force experiments provide thickness measurements, while varying the force gives access to mechanical properties. The experiment is facilitated by the spontaneous organization of magnetic beads into pairs or chains when exposed to a magnetic field. Transmission electron microscopy (TEM) imaging and fluorescent labeling confirm that ingested beads are surrounded by an endomembrane that has not fused with lysosomes (fig. S1, A to C) and that the cortex is pinched between the internal and external beads (Fig. 1B).

A first important point is to determine the accuracy of the measured distance between the beads. The beads are monitored in 3D at a frequency of 1.25 Hz over typically 5 to 15 min with transmitted

¹Physique et Mécanique des Milieux Hétérogènes, ESPCI Paris, PSL University, CNRS, Univ Paris, Sorbonne Université, Paris, France. ²Institut Curie and Institut Pierre Gilles de Gennes, PSL University, CNRS, Paris, France. ³Department of Theoretical Physics, University of Geneva, Geneva, Switzerland. ⁴Institut Curie, INSERM U932, PSL University, Paris, France. ⁵Departments of Biochemistry and Theoretical Physics and NCCR for Chemical Biology, University of Geneva, Geneva 1211, Switzerland.

*Corresponding author. Email: olivia.durore@espci.fr (O.d.R.); matthieu.piel@curie.fr (M.P.); julien.heuvingsh@espci.fr (J.H.)

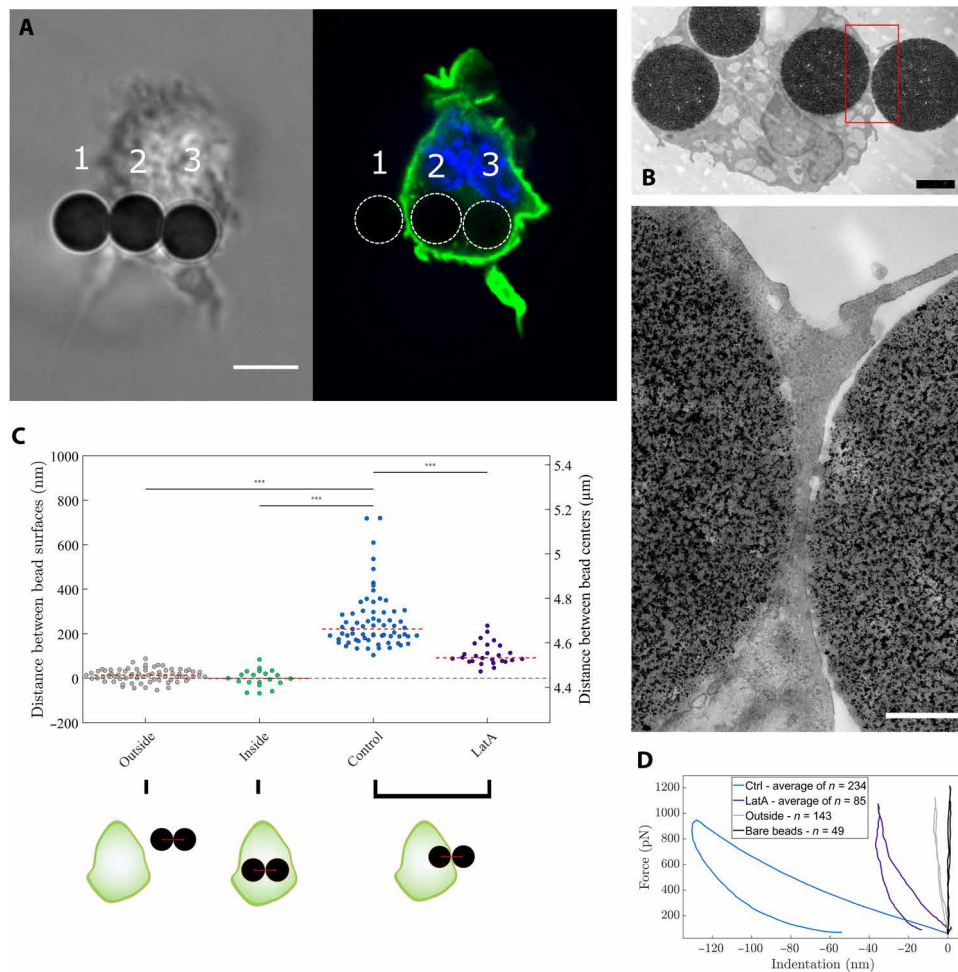


Fig. 1. Measurement of cortex thickness using magnetic beads. (A) Bright-field (left) and fluorescence (right) images of a dendritic cell expressing LifeAct-GFP (green) and stained with Hoechst (blue), with internalized magnetic beads aligned by a magnetic field. The cortex is pinched between bead 1 (inside the cell) and 2 (outside). Scale bar, 5 μm . (B) TEM of the cortex of a cell pinched between two magnetic beads. Scale bars, 2 μm (black, top) and 500 nm (white, bottom). (C) Distances between bead surfaces for pinching in control cells (blue, $n = 67$ cells, $N = 10$ independent experiments), pair of beads observed outside (gray, $n = 69$, $N = 2$) and inside (green, $n = 20$, $N = 13$), and pinching in cells treated with 500 nM LatA (purple, $n = 26$, $N = 5$). Each point is the median of a 5- to 15-min measurement at 1.25 Hz on a single cell. (D) Average force-indentation curves for bare beads (black, $n_c = 49$ compressions, $n = 16$ bead pairs), serum-coated beads outside of cells (beige, $n_c = 143$, $n = 11$), beads pinching the cortex of control cells (blue, $n_c = 234$, $n = 20$ cells, $N = 5$), and 500 nM LatA-treated cells (LatA, purple, $n_c = 85$, $n = 7$, $N = 1$), obtained from increasing the magnetic field from 5 mT (70 pN) to 50 mT (~ 1000 pN) in 1 s and decreasing it back.

light. The measurement accuracy on the distance between the center of two beads is approximately 2 nm (20) in the plane of observation and around 45 nm in the perpendicular direction (see the Supplementary Materials), resulting in an accuracy of 7 nm in the distance between bead centers. Subtraction of the bead diameter from the distance between the two centers gives the distance between the bead surfaces and thus the thickness of the pinched layer. We measure the beads to be highly monodispersed in size (fig. S1D), thus ensuring the precision of the distance between the bead surfaces. Overall, our measurement accuracy on the absolute thickness of the pinched layer is 31 nm (see the Supplementary Materials), which is $\sim 15\%$ of the reported thickness of the cell cortex (9). In addition, the thickness variation in time can be determined with a much better accuracy (7 nm, as the uncertainty on the bead diameters does not enter into this calculation) at >1 Hz, more precisely than any method used so far to estimate cortical thickness.

Dendritic cell cortical layer has a median thickness of 253 nm and a Young's modulus of 7 kPa

To determine the cortical layer thickness, a small magnetic field of 5 mT is applied and produce a constant attractive force (~ 70 pN) between the beads. This force holds the beads in contact with the outer membrane and the inner face of the cell cortex so that the distance between the surfaces accurately reflects the cortex thickness. To estimate this thickness and control for potential artifacts, we perform three types of experiments:

1) We compare measurements of distances between two beads outside the cell, two beads inside the cell, and two beads pinching the cortex (Fig. 1C). While the distance between the surfaces of two beads inside or outside the cell is, on average, undistinguishable from zero, the distance measured for the cortical layer has a median value of 220 nm (Fig. 1C, blue). This measurement is consistent with measurements in HeLa cells with subpixel-resolution fluorescence imaging (9).

2) We increase the magnetic field, and thus the attraction force (up to 1 nN), to check whether the structure pinched between the beads is deformable (Fig. 1D). Increasing the force between beads gives relative measures, which are precise down to a few nanometers. This shows that bare beads are stiff and nondeformable (less than 1-nm indentation), and beads used in the live-cell experiment show a minimal indentation (below 10 nm), which is due to the coating layer of serum (Fig. 1D, gray). In contrast, the cortical layer between a bead inside and a bead outside the cell is indented by more than 100 nm (Fig. 1D, blue), highlighting that a deformable object is being pinched. Upon force release, the distance between the beads relaxed, with a slight hysteresis, revealing the viscoelastic nature of the compressed material.

3) We compare control cells and cells in which the actin cortex has been disassembled using a high dose of latrunculin A (LatA) (Fig. 1, C and D). Treatment with 500 nM LatA disassembles the actin cortex, as evidenced by LifeAct-GFP (green fluorescent protein) imaging and phalloidin staining in fixed cells (fig. S1, E and F). The remaining layer, measured at 92 nm (Fig. 1C, purple), which is significantly thinner than in untreated cells, is thicker than the distance between two beads inside the cell and can be reversibly indented by about 40 nm (Fig. 1D, purple). This indicates that there is still material pinched between the beads when cells are treated with LatA. It might contain a combination of membrane, polysaccharide chains such as glycocalyx, proteins that link the membrane to the actin cortex such as ezrin/radixin/moesin, and other cytoskeletal components such as septins or intermediate filaments (2, 21).

Increasing the magnitude of the magnetic field while monitoring the variation of the cortex thickness allows force-indentation curves to be extracted. On the range of deformation that we probed (up to 25%), the mechanical response is linear (fig. S7E and Supplementary Materials) and the force indentation curves can be fitted with an appropriate model (22), taking into account the contact geometry of two beads deforming a thin layer (see the Supplementary Materials). The median of the estimated Young's modulus using the fit parameters is 7 kPa for control cell cortices and 18 kPa for the layer remaining after LatA treatment. The value of 7 kPa is in accordance with measures of in vitro dense actin networks (20, 22, 23) and compatible with the elastic modulus of whole cells (24).

The deformation of the cortex at low force in the constant field pincher experiments will induce a slight underestimation of the cortex thickness that we can calculate to be 13% using the value of 7 kPa (see the Supplementary Materials). We thus estimate the median thickness of the undeformed cortical layer to be 253 nm.

In conclusion, pinching the cortex with a pair of magnetic beads provides an accurate measure of the cell cortex thickness in live cells and a measure of its material properties. We evidence that dendritic cells have a thin and stiff cortical layer mostly composed of actin filaments, with properties comparable to the reported values in other cell types.

The actin cortex thickness displays large nonperiodic local instabilities

We next ask whether the cell cortex has a constant thickness, or whether thickness fluctuates in time. To address this question, we use time-resolved measures for single live cells comparing different bead configurations (Fig. 2A). Our measurement is extremely steady for beads outside the cells (control) and shows moderate fluctuations for inside beads, compatible with cell internal activity (25). In contrast,

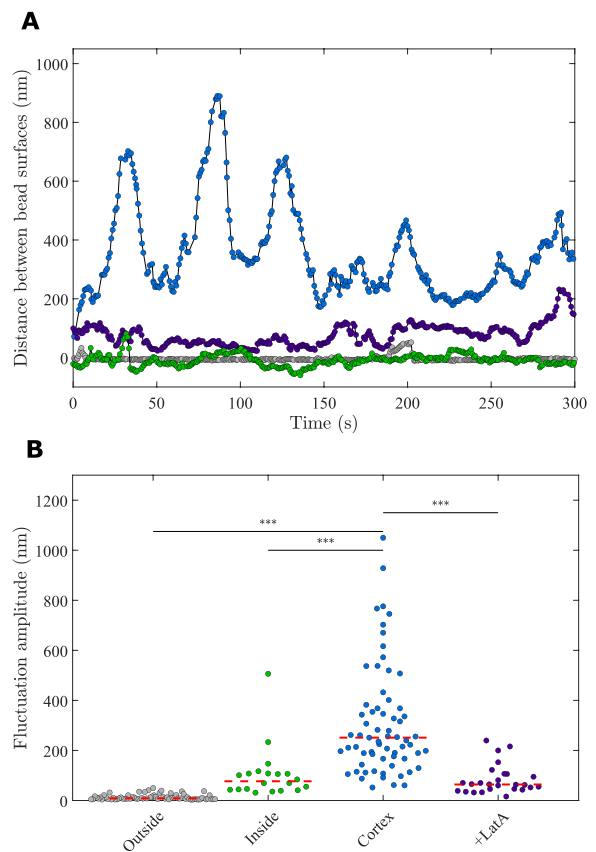


Fig. 2. Cortex thickness fluctuates in time. (A) Typical temporal evolution of the cortex thickness of control cells (blue) and LatA-treated cells (purple) compared to the temporal evolution of the distance between bead surfaces inside (green) or outside (gray) cells. Acquisition rate is 1.25 Hz. Large fluctuations are visible in the measured cortex thickness of control cells (blue) but not in the other signals. (B) Amplitude of the cortex thickness fluctuations in control cells (blue, $n = 67$, $N = 10$) compared to the fluctuations of the distance between bead surfaces in LatA-treated cells (purple, $n = 26$, $N = 5$) and pairs of beads inside (green, $n = 20$, $N = 13$) or outside (gray, $n = 69$, $N = 2$) cells.

we observe large and fast fluctuations (several hundred nanometers in a few tens of seconds) for bead pairs pinching the cortex of a live cell. Most of these fluctuations are lost when cells are treated with LatA (Fig. 2A, quantified in Fig. 2B; see details in fig. S2A), showing that they are driven by the activity of the actin network. Internalized beads do not change the thickness or the fluctuations of the cortex, as these measurements do not vary with the number of beads ingested by the cells (fig. S2D). No periodicity is observed in the fluctuations of cortex thickness, as shown by the absence of peaks in the autocorrelation function (fig. S2F), and of any emerging frequency in the Fourier analysis (fig. S2E). Characteristic time scales for fluctuations can nonetheless be extracted, the median of their distribution being 20 s. In some rare cases ($n = 4$ for control cells), the cortical layer is pinched at two different locations by two independent bead pairs (fig. S2G). No correlation between the signals of the two bead pairs is observed (fig. S2H), showing that thickness fluctuations are local rather than resulting from a global cell contraction. Cumulative distribution (fig. S2B) confirms the trend of large fluctuations in cortex thickness, and these fluctuations are strongly diminished

when analyzing bead pairs inside cells or at the cortical layer of actin-depolymerized cells. This analysis further reveals an asymmetry in these active cortex fluctuations: Fluctuations associated with a thickness increase are larger than fluctuations associated with a thickness decrease (fig. S2C). The existence of this asymmetry implies that fluctuations that increase the thickness can be considered as “peaks,” reflecting transient augmentation in the thickness of the cortical layer. We can thus extract a frequency by counting the number of peaks above a relevant threshold (see the Supplementary Materials). Control cell cortices exhibit, on average, 0.86 peaks per minute, while this number drops to 0.19 for cells treated with LataA (Fig. 3E). Together, these results show that the cortex is not a static structure with a constant thickness but is, on the contrary, a very dynamic object with large fluctuations in the direction perpendicular to the membrane. These fluctuations, nevertheless, remain below the resolution of classical imaging techniques, explaining why they had never been observed before. These measures therefore reveal a novel picture of the actin cortex as an unstable active layer that displays nonperiodical events of thinning and thickening.

Cortex fluctuations depend on actin polymerization and actomyosin contractility

While actin cortex thickness is mostly regulated by structural properties such as filament length (10), fast fluctuations more likely rely

on active processes such as actin assembly and contractility. We thus investigate the role of actin nucleators, Arp2/3 and formin, and of the myosin II motors in this process. We treat the cells with small inhibitors after they had ingested the beads, as bead ingestion requires an active actin cytoskeleton.

Confocal imaging of LifeAct-GFP-expressing cells after drug treatment shows the expected effects of inhibition of actin nucleators on surface ruffles, formin inhibition having the most pronounced effect (Fig. 3A and fig. S3F). Actin nucleation impairment from formin or Arp2/3 inhibition leads to a moderate but significant reduction of cortex thickness and to a strong decrease of the amplitude of cortex thickness fluctuations (Fig. 3, C and D). This decrease is also visible in the cumulative distribution of thickness above the median (fig. S3A). In parallel with the decrease in amplitude, the number of peaks (larger than 100 nm) observed per minute dropped to almost half of the control value (Fig. 3E). This tendency is more pronounced for the largest peaks (larger than 600 nm) with a threefold reduction for Arp2/3 and formin inhibition (Fig. 3F). Formin inhibition, which almost completely abolished membrane ruffles visible on microscopy images, had a more limited effect on cortical thickness and fluctuations measured with the magnetic pincher. We performed a quantitative analysis of the fluctuation of the fluorescence signal in the cortex (fig. S4). It showed that fluctuations of the fluorescence signal are dominated by large actin structures, which are mostly suppressed by formin inhibition.

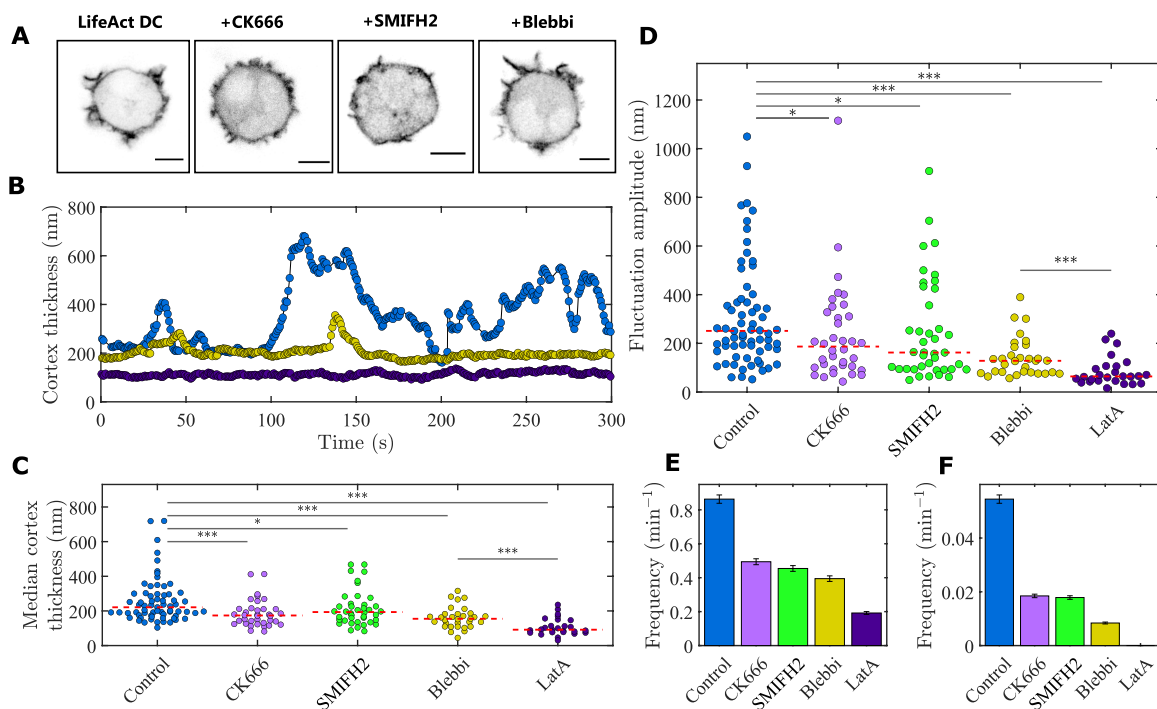


Fig. 3. Inhibition of myosin II affects cortex thickness and fluctuations more drastically than inhibition of nucleators. (A) Confocal imaging of actin in live LifeAct dendritic cells treated with DMSO, 50 μ M CK666, 12.5 μ M SMIFH2, and 50 μ M blebbistatin (left to right). After treatment by CK666, protrusions appear to be sharper; SMIFH2 treatment strongly reduces the number of protrusions; blebbistatin treatment slightly affects protrusion morphology. (B) Typical temporal evolution of the cortex thickness in control cells (blue), blebbistatin-treated cells (yellow), and LataA-treated cells (purple). (C) Median cortex thickness for control cells (blue, $n = 67$, $N = 10$) and cells treated with CK666 (light purple, $n = 36$, $N = 4$), SMIFH2 (green, $n = 40$, $N = 5$), blebbistatin (yellow, $n = 31$, $N = 5$), and LataA (dark purple, $n = 26$, $N = 5$). Control and LataA data are the same as in Fig. 1. (D) Amplitude of the cortex thickness fluctuations for control and treated cells [the same conditions as in (C)]. Myosin II inhibition has the strongest effect on fluctuations after LataA treatment but does not affect the morphology of the cell protrusions (A), leading to the conclusion that the measured fluctuations are not the signature of protrusion but rather fluctuations of the thickness of the underlying cortex. Control and LataA data are the same as in Fig. 2. (E) Frequency of peaks above 100 nm for control and treated cells. The reduced number of peak events in blebbistatin-treated cortices as well as with Arp2/3 and SMIFH2 inhibition is in agreement with the trend on fluctuation amplitude shown in (D). (F) Frequency of peaks larger than 600 nm for control and treated cells.

Inhibition of myosin II motors using blebbistatin has, unexpectedly, a stronger effect than inhibition of actin nucleators on the properties of the cortex measured by the magnetic pincher. Cortical thickness is decreased by about one-third, and the amplitude of fluctuations is divided by two (Fig. 3, B to D), giving a cumulative probability of thickness variation close to the one of actin-depleted cells (fig. S3A). The frequency of actin-dependent protrusions is the lowest of all inhibition conditions, with 0.39 protrusions per minute (Fig. 3E) and a sixfold decrease in the frequency of peaks larger than 600 nm (Fig. 3F). As blebbistatin is phototoxic (26), we used the ROCK inhibitor Y27632 (Y27) to image the cells with a reduced motor activity. This small molecule reproduced the effect of blebbistatin on cortex thickness and associated fluctuations (fig. S3D). However, we observed only a limited effect on the ruffling activity of the dendritic cell membrane as compared to nontreated cells, with the quantitative fluorescence fluctuations analysis (figs. S3, E and F, and S4, C and E). Performing an analysis excluding regions of the cortex with large protrusions showed fluctuations in fluorescence intensity that depended more on myosin activity and less on formin (fig. S4, D and F) than the direct analysis (fig. S4, C and E). However, the measured reduction of fluctuations by the drugs was still different from the effects observed with the magnetic pincher for which myosin II inhibition had the largest consequences.

Together, the results on small-molecule inhibitors suggest that the submicrometer fluctuations in cortical thickness observed here do not result from the large surface ruffles but rather correspond to fluctuations in the thickness of the cortical layer itself. These submicrometer fluctuations are hard to detect from fluorescence microscopy images, whose signal is dominated by larger structures, more dependent on actin nucleators than on myosin II activity.

A minimal physical description of the cortex recapitulating the effect of myosin II on thickness fluctuations

Initial theoretical analysis of the actin cortex proposed that its thickness results from a balance between nucleation at the plasma membrane and bulk disassembly (27). A more recent analysis introduced the effect of modulation of filament length (10). However, none of these studies accounts for our observation of active submicrometer fluctuations of cortical thickness caused by myosin II activity. We thus turn to an extension of the minimal description in (24) that accounts for stress anisotropies (28). Here, the cortex is treated as an active viscous gel, with a constant influx of material at the membrane (representing polymerization) and homogeneous disassembly. The contractile property of the cortex is captured as an active stress that can be different in the directions tangential and perpendicular to the membrane due to the alignment of actin or myosin filaments (Fig. 4A). When the anisotropy in the contraction is low, a stable profile of actin density forming a compressed layer of constant thickness near the membrane emerges. However, when the anisotropy in the active stress exceeds a threshold so that the tangential stress is strong enough and stronger than the perpendicular one, the density profile becomes unstable. The cortex contracts laterally in an inhomogeneous manner, leading to local densification of actin. This induces the formation of peaks growing perpendicularly to the cortex plane. These peaks are not stable: They slide laterally and merge with each other, while new ones appear (Fig. 4B). The dynamical behavior of the fluctuations does not settle into a periodic state and is, on the contrary, aperiodic and chaotic, which matches our experimental observations. The amplitude of the fluctuations is of the same order

of magnitude as the cortex thickness, and the frequency of those fluctuations is given by the characteristic depolymerization time of the cortex (~seconds), which also matches our experimental measures. The thickness fluctuations we observed in our experiments are thus a generic feature of actin networks assembling on a surface and exhibiting anisotropic contractility, which points to a major effect of contractility on cortex thickness stability.

To further analyze the analogy between our experimental results and the results of the theoretical analysis, we concentrate on the correlation between the cortical layer thickness and its fluctuation amplitude. In control cells, the amplitude of fluctuations in each single cell is strongly correlated with the thickness of the cortex (Fig. 4D, i). Although both cortical thickness and its fluctuation amplitude are reduced by the inhibition of actin nucleators (Fig. 4C, ii, and fig. S4B, i), this does not affect the correlation between the two (high correlation coefficient, low P value, and slopes of the same order as for control cells, between 1.5 and 2; fig. S4, A and B). On the contrary, myosin II inhibition, which also reduces both the thickness of the cortex and the amplitude of fluctuations, has a strong effect on the correlation between the two parameters, with a lower correlation coefficient and a slope of only 0.67 (Fig. 4D, iii). In the case of LatA, the correlation completely disappears ($P = 0.55$). Coming back to the simulations, we vary the active stress and measure the cortex median thickness and its fluctuation amplitude in the same way as in the experiments (Fig. 4F). As only one length scale is present in the theoretical analysis, changing the resting size of the cortex by modifying the polymerization speed will affect in the same way both the cortex median thickness and the amplitude fluctuation. Thus, in both our experiments and theory, the contractile nature of the cortex controls the correlation between cortex thickness and its fluctuation amplitude. This finding suggests that the mechanism captured by the theory can explain the fluctuations in cortex thickness observed in live cells.

DISCUSSION

A large number of cell types display patterns of activity in the cell cortex in the form of polymerization waves, global contraction, or unorganized flares of activity (29, 30). These patterns are explained by a dual mechanism of activation and inhibition in regulatory pathways in interplay with the actin cytoskeleton (30–32). Myosin-dependent waves of Rho guanosine triphosphatase activity have been observed in adherent cells (33) and pulsatile patterns in embryos (34). Cortical flows could also entrain some larger structures embedded in the cortex and result in myosin-dependent local increase in the cortical thickness. Although we cannot rule out that these mechanisms contribute to the fluctuations of cortical thickness, the intrinsic dynamics of an active gel layer displayed in the presented model is sufficient to capture most of the characteristics of the fluctuations that we observed.

Collectively, our data propose a fundamentally new picture of the cell cortex in live cells as a fluctuating entity, whose thickness varies on a time scale of tens of seconds with spatial amplitude of hundreds of nanometers. This picture emerges through the new method presented here that provides a time-resolved measurement of the cortex thickness of live cells with an unprecedented spatial accuracy of a few tens of nanometers. We found the amplitude of thickness fluctuations to be comparable to the median value of the thickness. These results are not specific to primary mouse dendritic cells, as the cortex of *Dictyostelium discoideum* displays a similar behavior (see the Supplementary Materials and fig. S7). Fluctuations mostly result

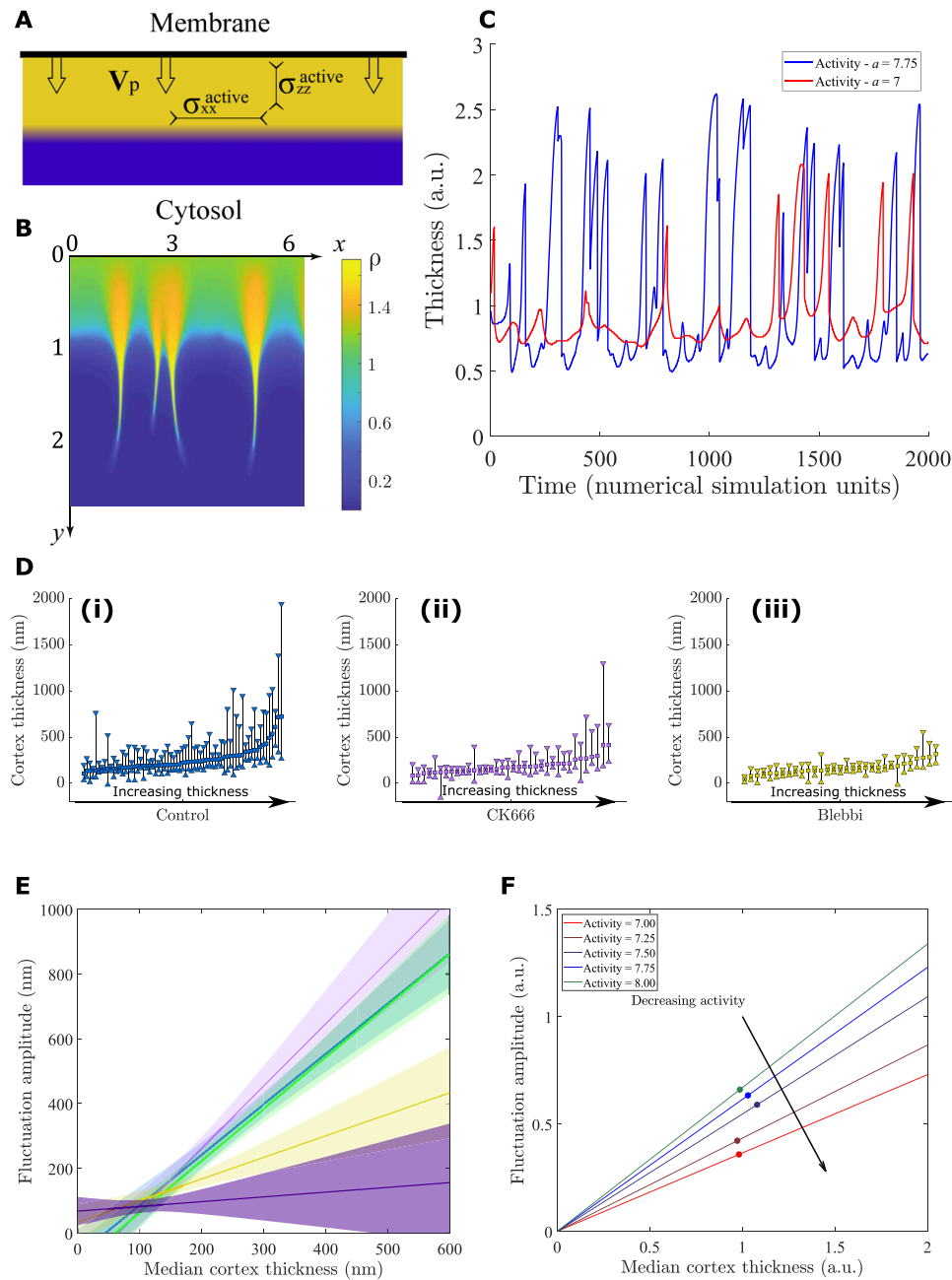


Fig. 4. A minimal theoretical description of the cortex captures the role of contractility in thickness fluctuations. (A) Illustration of the physical description of the cortex introducing the polymerization from the surface and the active stresses in the directions tangential (σ_{xx}) and perpendicular (σ_{yy}) to the membrane. (B) Snapshot of a numerical simulation using the cortex theoretical description illustrated in (A). The cortex locally deforms into protruding peaks because of the stress anisotropies in the actomyosin material. (C) Temporal evolution of the cortex thickness at one arbitrary spatial coordinate from a simulation at low contractile activity ($a = 7$, red) and at a higher contractile activity ($a = 7.75$, blue). The time unit is defined as the inverse of the gel's disassembly rate k (see Materials and Methods). (D) Representation of the cortex median thickness and fluctuation amplitude from experiments on control cells (i), CK666-treated cells (ii), and blebbistatin-treated cells (iii). Cells are sorted in ascending value of the median thickness (square). The length of the vertical line between the thickness first decile (upward triangle) and last decile (downward triangle) represents the fluctuation amplitude. The thickness fluctuations appear larger for larger cortex thicknesses for control cells but not for blebbistatin-treated cells. (E) Slopes from linear regression of fluctuation amplitudes as a function of cortex thickness from the experiments for control cells (blue) and cells treated with SMIFH2 (green, overlapping control), CK666 (light purple), blebbistatin (yellow), and LatA (dark purple). The colored area of each curve represents half the 95% confidence interval. The correlation of fluctuation amplitude with cortex thickness is markedly stronger for control and nuclear inhibitor compared to myosin II inhibition. (F) Slopes for the theoretical relation between thickness and fluctuation amplitude calculated from simulations at varying activity (dots). a.u., arbitrary units.

from the contractile activity of myosin II motors, which produces instabilities in the cortex, inducing large shifts perpendicular to the plasma membrane. They are intrinsically different from ruffles, which dominate the signal in fluorescence microscopy images. As our measure is local, it does not distinguish whether these shifts are due to bumps or wrinkles, but depicts the cortex as a dynamically embossed structure.

What are the putative functions of these cortical fluctuations that cells could modulate through the regulation of myosin II? One possible role could be to dynamically generate a rough plasma membrane surface that would augment the effective area of the cell surface and regulate membrane tension. Pulling membrane tethers from adherent fibroblasts revealed the existence of membrane reservoirs that depend on actin filaments (35). Gauthier *et al.* (36) proposed that these reservoirs come from submicrometer membrane wrinkles in the plasma membrane. The fluctuations in cortex thickness here reported could provide such a reservoir. Another possible function of a wrinkled or bumped cortex could be to provide dents on the outer surface of the cell to increase its friction with the substrate. Nonadherent cells can migrate faster than adherent cells, but the way forces are transmitted to the substrate in this migration mode is still mysterious. Having a dynamically rough surface could help dendritic cells generate propulsion forces in low adhesion environments. Last, the myosin-produced instabilities we evidenced give rise to fluctuations in thickness close to its median value. When these instabilities become too strong, the cortex could rupture, which could either induce local detachment of the plasma membrane called blebs or even lead to large-scale cell polarization (19, 34, 37). This local membrane detachment from the cortex has been proposed to be responsible for initiating cell protrusions, including lamellipodia (38). It is thus tempting to speculate that the cortex fluctuations we observed with the magnetic pincher could serve to facilitate nucleation of cellular protrusions and more generally contribute to the fast cell shape changes observed in fast-migrating amoeboid cells such as dendritic cells.

Increasing the magnetic force between the beads provides a measurement of the cortex mechanical properties. A complete study of these properties is beyond the scope of the present paper, but we are able to provide an estimate of 7 kPa for the elastic modulus of the cortex. No nonlinear behavior was detected even for cortices with up to 20% mean deformation (see the Supplementary Materials). This estimation of the elastic modulus of the cell cortex is similar to measurements obtained with atomic force microscopy using tips that are considered to probe the mechanics of the cortex itself (24). Although *in vitro* rheological studies on dilute entangled or cross-linked actin filament suspensions (39) report elastic modulus in the range of a few tens of pascals, it was shown that dense actin filament networks grown from a surface exhibit an elastic modulus of several kilopascals (20, 22, 23). The modulus reported here is thus in accordance with these measures. The filament networks in these studies regularly exhibit nonlinear behaviors such as stress stiffening that are explained by either the large extension of entropic filaments in dilute networks (39) or the limited connectivity of branched networks (20). The absence of nonlinear behavior in the present work suggests that the filament network in the cortex is too dense and well connected to display these characteristics. The moderate hysteresis observed during compression and release is the signature of some viscoelastic behavior that can be due to cross-linkers and motors binding and unbinding to the actin filaments. Overall, the precise determination of both cortex thickness and material properties is a promising

avenue to elucidate the quantitative contribution of the cortex mechanics to the global deformation of the cell in response to external mechanical stresses.

In conclusion, we believe that our observations not only provide measures of the physical properties of the cell cortex with unprecedented accuracy but also draw a novel picture for this subcellular entity as an active polymorphic layer dynamically thinned and thickened on a submicrometer scale as a result of actomyosin contractility. This could explain the propensity of the actin cortex to break upon activation of contractility, a phenomenon used by cells to polarize and move.

MATERIALS AND METHODS

Materials

The superparamagnetic beads (Dynabeads M-450) were purchased from Invitrogen (Carlsbad, CA, USA). Dimethyl sulfoxide (DMSO) was purchased from Sigma-Aldrich (St. Louis, MO, USA); SMIFH2, (R)-(+)-blebbistatin, CK666, and LatA were purchased from Tocris Bioscience (Bristol, UK).

Magnetic setup

The setup is mounted on an Axio A1 inverted microscope (Carl Zeiss, Germany) with an oil-immersion 100× objective [1.4 numerical aperture (NA)] mounted on a piezo-controlled translator (Physik Instrumente, Karlsruhe, Germany). The magnetic field is generated by two coaxial coils (SBEA, Vitry, France) with mu metal core (length, 40 mm; diameter, 26 to 88 mm; 750 spires). The coils are powered by a bipolar operational power supply amplifier 6A/36V (Kepco, Flushing, NY) controlled by a data acquisition module (National Instruments, Austin, TX). The maximum field generated is 100 mT with a gradient less than $0.1 \text{ mT} \cdot \text{mm}^{-1}$ over the sample. The chains of beads are formed with a constant field of 5 mT. Time-lapse images are recorded with an Orca Flash4 complementary metal-oxide semiconductor camera (Hamamatsu Photonics, Hamamatsu, Japan). No fluorescent images were taken during the magnetic pincher experiments to avoid phototoxicity when using sensitive drugs (e.g., blebbistatin). The setup was heated at 37°C using the box and the cube from Life Imaging Systems (Basel, Switzerland). The setup is controlled by a custom LabVIEW interface that ensures the synchronicity between piezo position, magnetic field imposition, and image acquisition.

Cells

Immature mouse bone marrow-derived dendritic cells were obtained by differentiation of bone marrow precursors for 10 to 11 days in dendritic cell medium [Iscove's modified Dulbecco's medium, fetal calf serum (10%), glutamine (20 mM), penicillin-streptomycin (100 U ml^{-1}), and 2-mercaptoethanol ($50 \mu\text{M}$)] supplemented with granulocyte-macrophage colony-stimulating factor (50 ng ml^{-1})-containing supernatant obtained from transfected J558 cells, as previously described (40).

Mice

LifeAct-GFP mice were a gift from M. Sixt (IST, Austria) (41) and bred in Institut Curie animal facilities. In general, 6- to 10-week-old mice were used as source for bone marrows to generate dendritic cells as described above. For animal care, the European and French National Regulation for the Protection of Vertebrate Animals used

for Experimental and other Scientific Purposes (directive 2010/63; French decree 2013-118) was strictly followed. The present experiments, which used mouse strains displaying nonharmful phenotypes, did not require a project authorization and benefited from guidance of the Animal Welfare Body, Research Center, Institut Curie.

Cell fluorescent imaging

Spinning disc images were acquired on a Leica DMI8 microscope (Leica, Wetzlar, Germany) with an Orca Flash4 camera and a 100× objective. The setup was heated at 37°C using the box and the cube from Life Imaging Systems. Acquisition was done using the MetaMorph software. Confocal images were acquired using a laser scanning microscope (Leica TCS SP8) with a 40× oil immersion objective (1.4 NA), a HyD detector (Leica), and the LAS-AF software.

Sample preparation

Dynabeads M450 were washed three times in Milli-Q water and stored in dendritic cell medium. Cells were incubated at 5×10^5 cells/ml, with coated Dynabeads (1:1 ratio) for 1 hour at 37°C in dendritic cell medium supplemented with 20 mM Hepes (Sigma-Aldrich). After 1 hour, $27 \pm 4\%$ of the cells have ingested at least one bead. Observation was done in homemade polydimethylsiloxane (PDMS) chambers coated with 1% bovine serum albumin (Sigma-Aldrich). Cells were observed during a maximum of 1.5 hours with no measured differences between the beginning and the end of the experiment.

For TEM experiments, cells were plated on μ -dishes with a glass bottom containing an imprinted 50- μ m cell location grid (Biovalley, ref. 81148). Cells were fixed in 2.5% glutaraldehyde in 0.1 M Na-cacodylate buffer (pH 7.4) for 1 hour, postfixed for 1 hour with 1% buffered osmium tetroxide, dehydrated in a graded series of ethanol solution, and then embedded in epoxy resin.

Drug treatment

CK666 and blebbistatin were used at 50 μ M, SMIFH2 at 12.5 μ M, and LatA at 500 nM, and the same quantity of DMSO was used in control experiments. PDMS chambers were preincubated with drugs 30 min before cell loading. Drugs were added to cell suspension at least 30 min before the beginning of the experiment.

Data and statistical analysis

Data relating to cortex thickness measurement come from 10 independent experiments for control, 4 independent experiments for CK666-treated cells, 5 independent experiments for SMIFH2-treated cells, 5 independent experiments for blebbistatin-treated cells, and 5 independent experiments for LatA-treated cells. For “inside” and “outside” data (Fig. 1), the pairs of beads were observed when the wanted situation occurred during the previously described experiments. Data relating to cortex mechanical properties come from five independent experiments for control and one experiment for LatA-treated cells. Indentation curves of bare beads and serum-coated beads (Fig. 1) come from one experiment.

To determine the significance of the differences between distributions (Figs. 1 to 3 and figs. S2, S3, and S7), we used Wilcoxon rank sum test. In fig. S2D, the slope is represented as $\pm 95\%$ confidence interval on the fit and the *P* value is extracted directly from the fitting algorithm. In fig. S5, the *P* value of the linear fits is extracted directly from the fitting algorithm. In fig. S8, the slope value is represented as $\pm 95\%$ confidence interval on the fit.

Determination of the bead distance

Image analysis was carried out using ImageJ (National Institutes of Health, USA) and Matlab (MathWorks, MA, USA). The in-plane position of each particle is determined by a weighted average of gray levels (fig. S5A), giving an accuracy of 2 nm as was done for in vitro work (14, 20). This accuracy can be obtained because the size of the Airy disc spans a few tens of pixels and because we tune the intensity of the incoming light to use the whole range of the 16-bit depth of the camera. A large number of information bits can thus be used to find the subpixel location of the center of the bead.

The position of the bead in the vertical direction is measured using the diffraction pattern on several images at different heights (42). Three images were recorded in quick succession (50-ms interval) at a height distance of 300 nm by moving the objective with a piezo-controlled translator. The diffraction patterns were compared to a reference (a depthograph), which was regularly updated. These depthographs are obtained by generating Z-stacks of immobilized beads and concatenating the central pixel lines of each bead image. Individual depthographs from independent beads are then averaged together to create the final reference.

A similar central pixel line is taken from a bead image on each of the three successive images and correlated onto the final depthograph (fig. S6B). The horizontal distance between the centers of two beads is taken as the average of these three measures. The precision on this procedure is estimated at 45 nm by cross-correlating independent depthographs and computing the average error. This leads to a precision of 7 nm on the 3D distance between the bead centers.

To ensure the quality of the tracking in the Z direction, data points are removed when a jump in Z (>700 nm) between two time points (0.8 s) is detected to avoid false measurements. Artefactual isolated points in the 3D distance curves were also removed (less than 0.05% for Z and 3D artefactual points). To ensure precision in the measurements of amplitude fluctuations of frequency of peaks, curves with too much removed data (>50%) or that are too short (<120 s) were not considered for analysis (1% of total curves).

Fluctuation and peak analysis

The amplitude of fluctuations is computed as the difference between the 90th and 10th decile of a dataset. The asymmetry of a curve corresponds to $(a - b)/(\text{fluctuations amplitude})$ (fig. S2A).

To ensure the validity of the fluctuation quantification, we study the cumulative distribution of the measured thickness for being below a certain value (fig. S2B). The median thickness is removed from each cell, and the shown curve is the mean of the cumulative distribution of each cell. The same trend of large fluctuations for the cortical thickness layer remains apparent. These fluctuations are strongly diminished when looking at a pair of beads inside the cell or at the cortical layer of actin-depolymerized cells. An asymmetry is also apparent in the cortical layer fluctuation, with larger fluctuations increasing the size of the cortical layer and smaller fluctuations decreasing its size. The upper decile of thickness is 1.7 times more distant from the median than the lower decile (asymmetry = 27%). This asymmetry is not present, with both beads inside the cells or with actin-depleted cells (fig. S2C).

To detect peaks, the signal is first smoothed using a Savitzky-Golay algorithm. The peaks are then detected as local maxima with a minimum prominence of 15 nm. Before computing statistics, peaks with a gap in time or in height (>5 s or >60% of prominence between two consecutive points) are removed from the data (less than 25%).

To avoid being dominated by noise, and to concentrate on actin-induced fluctuations, we considered only the peaks above a threshold of 100 nm for further analysis (fig. S2I).

Confocal image analysis

To analyze actin intensity at the cell cortex, each cell is first “unfolded” using a homemade MATLAB algorithm. On each image of the video, the cell is identified with intensity thresholding and isolated from the rest of the image by putting all noncell pixel intensity to zero. The cell center is found using an Euclidian distance transform on the binarized cell image. Then, a coordinate system change is operated from cylindrical to Cartesian. As pixels have a size and do not land perfectly in an (X, Y) grid from an (R, θ) grid, each “new pixel” intensity is computed as the weighted average of up to four old pixel intensities. The result is a video where the cell cortex appears linear (fig. S4A).

Cortex intensity value on each image is then taken as the maximum of vertical pixel line (fig. S4A, yellow lines and red dots) at 35 different positions along the cortex. From each position, a time curve is obtained (fig. S4B) and is analyzed in the same way as cortex thickness by measuring intensity median over time and intensity fluctuation between the first and last decile (fig. S4C). Spatial fluctuations (fig. S4E) are quantified as the standard deviation of the measured intensity distribution (35 points) on one image. In 10-min videos, spatial fluctuations are measured on one image every 30 s to ensure independent measurements through renewal of the actin cortex.

To assess the influence of protrusions in these intensity measurements, the same analysis was conducted after removing measurement points that were in protrusions (e.g., position 1 in fig. S4A). These points were identified by quantifying the number of nonzero pixels that extend from the maximum toward the exterior of the cell (fig. S4A, cyan lines on positions 2 and 4).

Theoretical description of the cortex

For the theoretical analysis, we use the following physical description of the cortex as an active gel leading (28). We consider that the cortex is growing into the half-space $z \geq 0$ at the surface ($x, y, z = 0$) because of polymerization. We note that ρ is the density of the actin gel and $v = (v_x, v_y, v_z)$ is the velocity field. For the sake of simplicity, we assume invariance along the y direction and $v_y = 0$. Three equations determine the temporal evolution of the cortex

$$\partial_t \rho + \partial_x(\rho v_x) + \partial_z(\rho v_z) = -k\rho \tag{1}$$

$$\eta [2\partial_{xx} v_x + \partial_{xz} v_z + \partial_{zz} v_x] = \partial_x \Pi_x(\rho) \tag{2}$$

$$\eta [2\partial_{zz} v_z + \partial_{xz} v_x + \partial_{xx} v_z] = \partial_z \Pi_z(\rho) \tag{3}$$

The first equation accounts for mass conservation and the two last ones for force balance. Here, k denotes the gel’s disassembly rate, η is the viscosity, and $\Pi_{x,z}$ are the components of the nonviscous contribution to the total stress in the gel. The latter has two contributions: an effective hydrostatic pressure and the contractile stress generated by active processes in the gel. Both components depend on the gel density, and we write (27, 28)

$$\Pi_{x,z} = -a_{x,z} \rho^3 + b\rho^4$$

with $b > 0$ accounting for positive hydrostatic pressure and $a_{x,z} > 0$, which reflects contractility of the active stress component.

These equations are complemented by the boundary conditions $v_z(z = 0) = v_p$ and $v_x(z = 0) = 0$, where v_p denotes the polymerization speed. See (28) for a discussion about more general boundary conditions including friction between the cortex and the membrane. Note that the sole length scale of this description is $l = v_p k^{-1}$. This implies that for a given value of $a_{x,z}/\eta$ and b/η , the amplitude of the fluctuations and the median thickness are proportional.

The set of previous equations generates spontaneously chaotic protrusions from the cortical layer if the active parameter a_x is large enough (28). Figure 4 (B, C, and F) is obtained by solving numerically the above equations. To this end, we used a discrete Euler scheme: In each time step, we first determine the velocity field through the force balance equations, where we use Fourier decomposition along x and finite differences along z . We then update the density. The contribution of $\partial_z(\rho v_z)$ is obtained by an upwind finite-difference scheme in real space. To improve the stability of the scheme, we have added a small diffusion term with diffusion constant $D = 10^{-3}$ to the mass conservation equation. In all simulations, we use $\Delta x = 0.004$, $\Delta z = 0.007$, and $\Delta t = 0.0005$. Last, we define the thickness of the cortex by the smallest z value for which the actin density dropped to half of its value at $z = 0$. Note that choosing another criterium does not affect the qualitative behavior of our results.

SUPPLEMENTARY MATERIALS

Supplementary material for this article is available at <http://advances.sciencemag.org/cgi/content/full/7/27/eabe3640/DC1>

[View/request a protocol for this paper from Bio-protocol.](#)

REFERENCES AND NOTES

1. T. D. Pollard, J. A. Cooper, Actin, a central player in cell shape and movement. *Science* **326**, 1208–1212 (2009).
2. P. Chugh, E. K. Paluch, The actin cortex at a glance. *J. Cell Sci.* **131**, jcs186254 (2018).
3. G. Salbreux, G. Charras, E. Paluch, Actin cortex mechanics and cellular morphogenesis. *Trends Cell Biol.* **22**, 536–545 (2012).
4. A. Diz-Muñoz, O. D. Weiner, D. A. Fletcher, In pursuit of the mechanics that shape cell surfaces. *Nat. Phys.* **14**, 648–652 (2018).
5. M. Fritzsche, C. Erlenkämper, E. Moendarbary, G. Charras, K. Kruse, Actin kinetics shapes cortical network structure and mechanics. *Sci. Adv.* **2**, e1501337 (2016).
6. M. Bovellan, Y. Romeo, M. Biro, A. Boden, P. Chugh, A. Yonis, M. Vaghela, M. Fritzsche, D. Moulding, R. Thorogate, A. Jégou, A. J. Thrasher, G. Romet-Lemonne, P. P. Roux, E. K. Paluch, G. Charras, Cellular control of cortical actin nucleation. *Curr. Biol.* **24**, 1628–1635 (2014).
7. M. Biro, Y. Romeo, S. Kroschwald, M. Bovellan, A. Boden, J. Tcherkezian, P. P. Roux, G. Charras, E. K. Paluch, Cell cortex composition and homeostasis resolved by integrating proteomics and quantitative imaging. *Cytoskeleton* **70**, 741–754 (2013).
8. T. M. Svitkina, Actin cell cortex: Structure and molecular organization. *Trends Cell Biol.* **30**, 556–565 (2020).
9. A. G. Clark, K. Dierkes, E. K. Paluch, Monitoring actin cortex thickness in live cells. *Biophys. J.* **105**, 570–580 (2013).
10. P. Chugh, A. G. Clark, M. B. Smith, D. A. D. Cassani, K. Dierkes, A. Ragab, P. P. Roux, G. Charras, G. Salbreux, E. K. Paluch, Actin cortex architecture regulates cell surface tension. *Nat. Cell Biol.* **19**, 689–697 (2017).
11. M. P. Clausen, H. Colin-York, F. Schneider, C. Eggeling, M. Fritzsche, Dissecting the actin cortex density and membrane-cortex distance in living cells by super-resolution microscopy. *J. Phys. D Appl. Phys.* **50**, 064002 (2017).
12. R. Vargas-Pinto, H. Gong, A. Vahabikashi, M. Johnson, The effect of the endothelial cell cortex on atomic force microscopy measurements. *Biophys. J.* **105**, 300–309 (2013).
13. B. Fabry, G. N. Maksym, J. P. Butler, M. Glogauer, D. Navajas, J. J. Fredberg, Scaling the microrheology of living cells. *Phys. Rev. Lett.* **87**, 148102 (2001).
14. T. Pujol, O. du Roure, M. Fermigier, J. Heuvingh, Impact of branching on the elasticity of actin networks. *Proc. Natl. Acad. Sci. U.S.A.* **109**, 10364–10369 (2012).

15. R. Belbahri, J. Planade, M. B. Sanders, A. Guillotin, O. du Roure, A. Michelot, J. Heuvingh, Mechanical stiffness of reconstituted actin patches correlates tightly with endocytosis efficiency. *PLoS Biol.* **17**, e3000500 (2019).
16. J. Renkawitz, K. Schumann, M. Weber, T. Lämmermann, H. Pflücke, M. Piel, J. Polleux, J. P. Spatz, M. Sixt, Adaptive force transmission in amoeboid cell migration. *Nat. Cell Biol.* **11**, 1438–1443 (2009).
17. T. Lämmermann, B. L. Bader, S. J. Monkley, T. Worbs, R. Wedlich-Söldner, K. Hirsch, M. Keller, R. Förster, D. R. Critchley, R. Fässler, M. Sixt, Rapid leukocyte migration by integrin-independent flowing and squeezing. *Nature* **453**, 51–55 (2008).
18. P. Vargas, J. Maiuri, M. Bretou, P. J. Sáez, P. Pierobon, M. Maurin, M. Chabaud, D. Lankar, D. Obino, E. Terriac, M. Raab, H.-R. Thiam, T. Brocker, S. M. Kitchen-Goosen, A. S. Alberts, P. Sunareni, S. Xia, R. Li, R. Voituriez, M. Piel, A.-M. Lennon-Duménil, Innate control of actin nucleation determines two distinct migration behaviours in dendritic cells. *Nat. Cell Biol.* **18**, 43–53 (2016).
19. Y.-J. Liu, M. Le Berre, F. Lautenschlaeger, P. Maiuri, A. Callan-Jones, M. Heuzé, T. Takaki, R. Voituriez, M. Piel, Confinement and low adhesion induce fast amoeboid migration of slow mesenchymal cells. *Cell* **160**, 659–672 (2015).
20. P. Bauër, J. Tavaoli, T. Pujol, J. Planade, J. Heuvingh, O. Du Roure, A new method to measure mechanics and dynamic assembly of branched actin networks. *Sci. Rep.* **7**, 15688 (2017).
21. M. P. Serres, M. Samwer, B. A. Truong Quang, G. Lavoie, U. Perera, D. Görlich, G. Charras, M. Petronczki, P. P. Roux, E. K. Paluch, F-actin interactome reveals vimentin as a key regulator of actin organization and cell mechanics in mitosis. *Dev. Cell* **52**, 210–222.e7 (2020).
22. Y. Marcy, J. Prost, M.-F. Carlier, C. Sykes, Forces generated during actin-based propulsion: A direct measurement by micromanipulation. *Proc. Natl. Acad. Sci. U.S.A.* **101**, 5992–5997 (2004).
23. P. Bieling, T.-D. Li, J. Weichsel, R. McGorty, P. Jreij, B. Huang, D. A. Fletcher, R. D. Mullins, Force feedback controls motor activity and mechanical properties of self-assembling branched actin networks. *Cell* **164**, 115–127 (2016).
24. P.-H. Wu, D. R.-B. Aroush, A. Asnacios, W.-C. Chen, M. E. Dokukin, B. L. Doss, P. Durand-Smet, A. Ekpenyong, J. Guck, N. V. Guz, P. A. Janmey, J. S. H. Lee, N. M. Moore, A. Ott, Y.-C. Poh, R. Ros, M. Sander, I. Sokolov, J. R. Staunton, N. Wang, G. Whyte, D. Wirtz, A comparison of methods to assess cell mechanical properties. *Nat. Methods* **15**, 491–498 (2018).
25. M. Guo, A. J. Ehrlicher, M. H. Jensen, M. Renz, J. R. Moore, R. D. Goldman, J. Lippincott-Schwartz, F. C. MacKintosh, D. A. Weitz, Probing the stochastic, motor-driven properties of the cytoplasm using force spectrum microscopy. *Cell* **158**, 822–832 (2014).
26. A. Mikulich, S. Kavaliuskiene, P. Juzenas, Blebbistatin, a myosin inhibitor, is phototoxic to human cancer cells under exposure to blue light. *Biochim. Biophys. Acta* **1820**, 870–877 (2012).
27. J.-F. Joanny, K. Kruse, J. Prost, S. Ramaswamy, The actin cortex as an active wetting layer Active Matter. Guest editors: Ramin Golestarian, Sriram Ramaswamy. *Eur. Phys. J. E* **36**, 52 (2013).
28. N. Levernier, K. Kruse, Spontaneous formation of chaotic protrusions in a polymerizing active gel layer. *New J. Phys.* **22**, 013003 (2020).
29. Y. Yang, M. Wu, Rhythmicity and waves in the cortex of single cells. *Philos. Trans. R. Soc. B Biol. Sci.* **373**, 20170116 (2018).
30. W. M. Bement, M. Leda, A. M. Moe, A. M. Kita, M. E. Larson, A. E. Golding, C. Pfeut, K.-C. Su, A. L. Miller, A. B. Goryachev, G. von Dassow, Activator-inhibitor coupling between Rho signaling and actin assembly make the cell cortex an excitable medium. *Nat. Cell Biol.* **17**, 1471–1483 (2015).
31. P. N. Devreotes, S. Bhattacharya, M. Edwards, P. A. Iglesias, T. Lampert, Y. Miao, Excitable signal transduction networks in directed cell migration. *Annu. Rev. Cell Dev. Biol.* **33**, 103–125 (2017).
32. D. S. Pal, X. Li, T. Banerjee, Y. Miao, P. N. Devreotes, The excitable signal transduction networks: Movers and shapers of eukaryotic cell migration. *Int. J. Dev. Biol.* **63**, 407–416 (2019).
33. M. Graessl, J. Koch, A. Calderon, D. Kamps, S. Banerjee, T. Mazel, N. Schulze, J. K. Jungkurth, R. Patwardhan, D. Solouk, N. Hampe, B. Hoffmann, L. Dehmelt, P. Nalbant, An excitable Rho GTPase signaling network generates dynamic subcellular contraction patterns. *J. Cell Biol.* **216**, 4271–4285 (2017).
34. M. Nishikawa, S. R. Naganathan, F. Jülicher, S. W. Grill, Controlling contractile instabilities in the actomyosin cortex. *eLife* **6**, e19595 (2017).
35. D. Raucher, M. P. Sheetz, Membrane expansion increases endocytosis rate during mitosis. *J. Cell Biol.* **144**, 497–506 (1999).
36. N. C. Gauthier, T. A. Masters, M. P. Sheetz, Mechanical feedback between membrane tension and dynamics. *Trends Cell Biol.* **22**, 527–535 (2012).
37. V. Ruprecht, S. Wieser, A. Callan-Jones, M. Smutny, H. Morita, K. Sako, V. Barone, M. Ritsch-Marte, M. Sixt, R. Voituriez, C. P. Heisenberg, Cortical contractility triggers a stochastic switch to fast amoeboid cell motility. *Cell* **160**, 673–685 (2015).
38. E. S. Welf, C. E. Miles, J. Huh, M. K. Driscoll, T. Isogai, J. Noh, A. D. Weems, J. Chi, T. Pohlkamp, M. Dean, R. Fiolka, A. Mogilner, G. Danuser, A unified role for membrane-cortex detachment during cell protrusion initiation. bioRxiv 696211 [Preprint]. 9 July 2019. <https://doi.org/10.1101/696211>.
39. M. L. Gardel, J. H. Shin, F. C. MacKintosh, L. Mahadevan, P. Matsudaira, D. A. Weitz, Elastic behavior of cross-linked and bundled actin networks. *Science* **304**, 1301–1305 (2004).
40. H.-R. Thiam, P. Vargas, N. Carpi, C. L. Crespo, M. Raab, E. Terriac, M. C. King, J. Jacobelli, A. S. Alberts, T. Stradal, A.-M. Lennon-Duménil, M. Piel, Perinuclear Arp2/3-driven actin polymerization enables nuclear deformation to facilitate cell migration through complex environments. *Nat. Commun.* **7**, 10997 (2016).
41. J. Riedl, K. C. Flynn, A. Raducanu, F. Gärtner, G. Beck, M. Bösl, F. Bradke, S. Massberg, A. Aszodi, M. Sixt, R. Wedlich-Söldner, Lifeact mice for studying F-actin dynamics. *Nat. Methods* **7**, 168–169 (2010).
42. C. Gosse, V. Croquette, Magnetic Tweezers: Micromanipulation and force measurement at the molecular level. *Biophys. J.* **82**, 3314–3329 (2002).
43. L. D. Landau, E. M. Lifshitz, *Theory of Elasticity* (Pergamon Press, 1960), vol. 64, pp. 176–177.
44. R. S. Chadwick, Axisymmetric indentation of a thin incompressible elastic layer. *SIAM J. Appl. Math.* **62**, 1520–1530 (2002).

Acknowledgments: We thank P. Belska for preliminary experiments on the magnetic pincher; R. Voituriez for useful discussions; X. Benoit Gonin and O. Brouard for technical support on the setup; A. Mathur, M. Deygas, H. Moreau, D. Sanseau, G. Delgado, and Z. Alraies for additional cell culture; and N. Srivastava for help on *D. discoideum* culture and handling. **Funding:** This work was supported by the Institut Pierre-Gilles de Gennes-IPGG (Equipement d'Excellence, "Investissements d'avenir," program ANR-10-EQPX-34 and Laboratoire d'Excellence, "Investissements d'avenir" program ANR-10-IDEX-0001-02 PSL and ANR-10-LABX-31). V.L. was supported by Inserm (16DOC011UPDE / FDU_2016001) and by ANR grant (ANR-19-CE13-0030-01) to M.P. K.K. was supported by SNSF grant (205321_17599). **Author contributions:** O.d.R., M.P., and J.H. designed the research; V.L., O.d.R., and J.H. developed the cortex pinching experiments; V.L. carried out all the cortex pinching experiments and analyzed the resulting data; L.B. and P.J.S. performed differentiation and culture of dendritic cells under the supervision of P.V.; J.P. carried out all confocal imaging experiments; M.S.R. performed electronic microscopy experiments; V.L. performed live-cell spinning disc imaging; V.L., L.B., and P.J.S. carried out and analyzed immunofluorescence experiments; K.K. and N.L. developed the theoretical analysis; N.L. performed and analyzed cortex simulations; V.L., O.d.R., M.P., and J.H. interpreted experimental data with the contribution of P.V. and A.-M.L.-D.; V.L., O.d.R., M.P., and J.H. wrote the manuscript. **Competing interests:** The authors declare that they have no competing interests. **Data and materials availability:** All data needed to evaluate the conclusions in the paper are present in the paper and/or the Supplementary Materials.

Submitted 17 August 2020
Accepted 20 May 2021
Published 2 July 2021
10.1126/sciadv.abe3640

Citation: V. Laplaud, N. Levernier, J. Pineau, M. S. Roman, L. Barbier, P. J. Sáez, A.-M. Lennon-Duménil, P. Vargas, K. Kruse, O. du Roure, M. Piel, J. Heuvingh, Pinching the cortex of live cells reveals thickness instabilities caused by myosin II motors. *Sci. Adv.* **7**, eabe3640 (2021).

Pinching the cortex of live cells reveals thickness instabilities caused by myosin II motors

Valentin Laplaud, Nicolas Levernier, Judith Pineau, Mabel San Roman, Lucie Barbier, Pablo J. Sáez, Ana-Maria Lennon-Duménil, Pablo Vargas, Karsten Kruse, Olivia du Roure, Matthieu Piel and Julien Heuvingsh

Sci Adv 7 (27), eabe3640.
DOI: 10.1126/sciadv.abe3640

ARTICLE TOOLS

<http://advances.sciencemag.org/content/7/27/eabe3640>

SUPPLEMENTARY MATERIALS

<http://advances.sciencemag.org/content/suppl/2021/06/28/7.27.eabe3640.DC1>

REFERENCES

This article cites 42 articles, 8 of which you can access for free
<http://advances.sciencemag.org/content/7/27/eabe3640#BIBL>

PERMISSIONS

<http://www.sciencemag.org/help/reprints-and-permissions>

Use of this article is subject to the [Terms of Service](#)

Science Advances (ISSN 2375-2548) is published by the American Association for the Advancement of Science, 1200 New York Avenue NW, Washington, DC 20005. The title *Science Advances* is a registered trademark of AAAS.

Copyright © 2021 The Authors, some rights reserved; exclusive licensee American Association for the Advancement of Science. No claim to original U.S. Government Works. Distributed under a Creative Commons Attribution NonCommercial License 4.0 (CC BY-NC).

Appendix D

Résumé en Français

Les lymphocytes B sont les cellules productrices d'anticorps, ce qui en fait des acteurs centraux de la réponse immunitaire adaptative. *In vivo*, leur activation a lieu dans les organes lymphoïdes secondaires où ils entrent en contact avec des antigènes à la surface de cellules dendritiques ou de macrophages sub-capsulaires. Le contact entre un antigène et un récepteur de cellule B qui lui est spécifique déclenche la signalisation du lymphocyte B et la formation d'une synapse immunologique avec l'autre cellule. La synapse immunologique est une plate-forme de communication où le lymphocyte B recueille des informations à la surface de l'autre cellule en accumulant l'antigène au centre du contact et en réorganisant ses organelles, ce qui permettra in fine l'extraction d'antigène et la production d'anticorps spécifiques. La synapse immunologique est une structure très organisée, où l'antigène est concentré au centre du contact, entouré d'un cercle d'actine, de myosine, et de molécules d'adhésion. En même temps, la réorganisation des organelles résulte en la polarisation du lymphocyte B, caractérisée par la relocalisation du centrosome au centre de la synapse immunologique, le transport rétrograde du noyau, et le transport de lysosomes vers la synapse immunologique le long des microtubules. L'extraction de l'antigène peut être réalisée par deux voies différentes : l'application de forces mécaniques sur l'antigène ou la sécrétion polarisée de protéases au niveau de la synapse immunologique. Ces deux voies sont intimement liées au cytosquelette, l'extraction mécanique reposant sur la contractilité de l'actomyosine (d'après des observations antérieures du laboratoire), et la sécrétion polarisée reposant sur la réorganisation polarisée des réseaux de microtubule et d'actine. Ce travail se concentre sur le rôle du cytosquelette dans ces deux voies, en étudiant (1) les structures d'actine qui génèrent des forces à la synapse immunologique et leur régulation et (2) le rôle du cytosquelette dans la régulation de la dynamique de formation de la synapse immunologique et la polarisation des lymphocytes B.

Dans une première partie, nous avons utilisé un substrat déformable couvert d'antigène permettant son extraction par voie mécanique, ainsi que la mesure des forces appliquées par la cellule par microscopie de force de traction. Ce projet a été

initié avant mon arrivée au sein de l'équipe, et avait déjà révélé que les lymphocytes B appliquent des forces sur le substrat spécifiquement en présence d'antigène. Deux types de forces ont été observées : des forces tangentielles, centripètes, à la périphérie de la synapse immunologique, et des forces locales, relevant soit de mouvements 3D, soit de mouvements de torsion, dans la région centrale, liées à des patchs d'actine. En utilisant de l'imagerie 3D, nous avons pu montrer que ces forces correspondaient bien à des mouvements 3D (protrusion ou invagination). L'étude approfondie des structures d'actine a révélé que celles-ci sont promues et stabilisées en présence d'antigène, et sont enrichies en phospho-Cortactin, un marqueur d'ILPs (Invadosome-like Protrusions), déjà décrit dans les lymphocytes T. De plus, une colocalisation partielle avec des patchs de clathrin indique que ces structures seraient des sites privilégiés pour l'internalisation de l'antigène clathrin-dépendente. Enfin, nous avons montré que la génération de forces à la synapse immunologique du lymphocyte B, la formation et stabilité des structures d'actine et l'extraction de l'antigène du substrat mou sont régulés par la contractilité du réseau d'actomyosine, car l'inhibition de la myosine II abroge tous ces processus, alors que sa sur-activation grâce à un agoniste du canal calcique des lysosomes TRPML1 augmente tous ces processus. Avec ces résultats, nous avons montré qu'il existe une organisation spatio-temporelle des forces régulée par la contractilité de l'actomyosine à la synapse immunologique du lymphocyte B, et que celle-ci contrôle l'extraction et l'internalisation de l'antigène au niveau de protrusions semblables à des invadosomes.

Dans un second temps, nous nous sommes concentrés sur l'établissement de la polarité du lymphocyte B, qui est un processus essentiel à l'extraction protéolytique de l'antigène, mais aussi à sa dégradation afin d'être présenté à des lymphocytes T lors de la coopération T/B. Cette étude représente un défi technique car ce processus ne dure que 10-15min, et commence dès le premier contact du lymphocyte avec l'antigène. Nous avons conçu un système microfluidique pour reconstituer des synapses immunologiques entre un lymphocyte B et une goutte d'huile recouverte d'antigène, et contrôler le temps et l'orientation du contact. Ce système est constitué de pièges microfluidiques où l'on peut capturer une goutte, puis un lymphocyte B, tout en imageant le processus en direct. Les gouttes d'huiles sont un nouvel outil très intéressant pour représenter la cellule présentatrice d'antigène, car ce sont des objets 3D, et que le ligand (ici l'antigène) est mobile à leur surface. Nous pouvons donc suivre dans le temps l'accumulation de l'antigène au centre du contact.

Nous avons établi les échelles de temps de polarisation des principaux acteurs de la synapse immunologique du lymphocyte B : l'actine, la production de diacylglycérol (DAG) à la synapse immunologique à la suite de la signalisation des récepteurs du

lymphocyte B, le centrosome, les lysosomes, l'appareil de Golgi et le noyau. Cette première approche nous a permis de définir que suite au contact du lymphocyte B avec la goutte couverte d'antigène, il y a un pic de polymérisation de l'actine à la synapse immunologique après 3 minutes, suivi d'un pic de production de DAG après 4 minutes. Le centrosome est repositionné au niveau de la synapse immunologique après 4.5 minutes, suivi de l'appareil de Golgi (7 minutes) et des lysosomes (11.5 minutes). Le noyau a une trajectoire plus complexe, puisqu'il effectue d'abord une rotation, alignant son invagination caractéristique des noyaux de lymphocytes avec la synapse immunologique, puis est transporté vers l'arrière de la cellule dans les temps longs. Il semble que les processus observés se séparent en deux catégories : les événements liés à la formation de la synapse immunologique (polymérisation de l'actine, production de DAG) sont les plus précoces, et les événements liés à la polarisation globale du lymphocyte B (centrosome, appareil de Golgi, lysosomes, noyau) sont plus tardifs.

Nous avons ensuite évalué la dépendance de ces processus à l'actine, la myosine et les microtubules. La dépolymérisation de l'actine par traitement avec de la Latrunculin A limite considérablement la capacité de la cellule à accumuler de l'antigène au centre du contact, et donc à amplifier la signalisation des récepteurs de lymphocyte B et produire du DAG. Cependant, les lymphocyte B sont toujours capables de polariser le centrosome ainsi que le noyau, certainement grâce à de la signalisation résiduelle suffisante au contact goutte-cellule. Dans les cellules traitées avec de la Latrunculin A, le centrosome est dès le début éloigné du noyau, auquel il est normalement attaché par de l'actine centrosomale. Dans les cellules contrôles, cette actine est dégradée suite à l'activation du lymphocyte B pour permettre au centrosome de s'approcher de la synapse immunologique, et au noyau de s'en éloigner. La polarisation du centrosome et du noyau est plus rapide en l'absence d'actine polymérisée, ce qui suggère que la dégradation de l'actine centrosomale est un élément limitant de la vitesse de polarisation. De plus, nous avons observé que l'orientation du noyau (de son invagination) et celle du centrosome par rapport à l'axe goutte-cellule évoluent de la même façon lorsque l'on image ces deux organelles simultanément. Cela indique que seuls les microtubules, via le complexe LINC et leurs moteurs moléculaires, sont responsable de l'orientation et du transport rétrograde du noyau dans le cadre de la synapse immunologique du lymphocyte B.

Nous avons également étudié l'effet de la régulation de la contractilité de l'actomyosine sur la formation de la synapse immunologique et la polarisation du lymphocyte B. L'inhibition de la myosine II (par traitement avec de la par-nitroBlebbistatin) ou l'activation de la contractilité (par traitement avec MLSA1, un agoniste du canal calcique des lysosomes TRPML1) ne semblent pas avoir d'impact sur la polarisation du centrosome et du noyau, et n'ont qu'un impact très léger sur la

polymérisation de l'actine à la synapse immunologique, l'accumulation d'antigène et la production de DAG suite à la signalisation des récepteurs de lymphocyte B.

La dépolymérisation des microtubules (traitement avec du Nocodazole) induit de forts changements dans le lymphocyte B. En effet, cela déclenche la libération et l'activation de GEF-H1, qui active RhoA et par conséquent peut augmenter la contractilité ainsi que l'activité des formines. Nous avons observé de fortes déformations des cellules, ainsi que des zones de polymérisation d'actine intense hors de la synapse immunologique. Cela ne semble par avoir significativement impacté l'accumulation de l'antigène, car de petites protrusions d'actine peuvent encore se former, et l'antigène peut s'accumuler par diffusion. Cependant, la dépolymérisation des microtubules affecte également la production de DAG, qui a également lieu à des sites hors de la synapse immunologique. Enfin, la forme du noyau, sa polarisation ainsi que la polarisation du centrosome sont fortement impactées par l'absence de microtubules.

Afin de découpler l'effet de la dépolymérisation des microtubules de son effet important sur la contractilité, qui déforme de façon intense et rapide la cellule, nous avons combiné le nocodazole avec un inhibiteur de la myosine II, la para-nitroBlebbistatin. Nous avons observé que la cellule ne présente plus de déformations rapides ni de blebbs, mais qu'une majorité de cellules se déforment toujours. Les cellules présentent une élongation progressive dans l'axe goutte-cellule, et toujours des sites de polymérisation de l'actine hors de la synapse immunologique, qui pourraient expliquer ce phénotype.

Nous avons défini des échelles de temps pour la polarisation d'acteurs majeurs de la synapse immunologique et de la fonction du lymphocyte B, et observé une séparation temporelle entre les événements liés à la formation de la synapse immunologique (réarrangement de l'actine et production de DAG à la synapse immunologique), et les événements liés à l'établissement d'une polarité globale du lymphocyte B (réorientation du centrosome, de l'appareil de Golgi, des lysosomes et du noyau). Il apparaît que la polymérisation de l'actine n'est indispensable que pour la formation d'une synapse immunologique capable de générer une forte signalisation, et production de DAG, mais qu'elle n'est pas nécessaire à l'établissement de la polarité du centrosome et du noyau. En revanche, les microtubules sont indispensables à la fois pour l'établissement d'un axe de polarité du noyau et du centrosome, mais également pour la maintenance de la structure de la synapse, en particulier de la polymérisation polarisée de l'actine. Ces défauts sont dû à l'activation de la myosine II et des formines suite à la l'activation de GEF-H1 lors de la dépolymérisation des microtubules. L'inhibition de la myosine II permet de rétablir une polarisation du noyau, mais celle-ci est liée à une élongation de la cellule causée par la polymérisation d'actine à différents sites, et non à son transport

spécifique. Les microtubules sont donc responsables de l'établissement de la polarité, mais également de la maintenance de la polymérisation polarisée de l'actine à la synapse immunologique, à travers leur capacité à réguler GEF-H1 et donc l'activation des formines. Grâce à un nouvel ensemble d'outils expérimentaux et analytiques, nous fournissons une caractérisation systématique de la dynamique de polarisation des organelles et des interactions organelles-cytosquelette pendant la polarisation des cellules B.

Nos résultats décrivent le rôle du cytosquelette dans différents contextes d'activation des lymphocytes B, de formation de synapse immunologique et d'extraction d'antigène, et mettent en évidence la polyvalence des lymphocytes B qui adaptent leur comportement aux conditions de présentation de l'antigène.

